DISSERTATION

The nonperturbative feats of local electronic correlation:

The physics of irreducible vertex divergences

Ausgeführt zum Zwecke der Erlangung des akademischen Grades eines
Doktors der technischen Wissenschaften (Dr. techn.)

unter der Anleitung von

Associate Prof. Dr. Alessandro Toschi

E138 – Institut für Festkörperphysik

eingereicht an der Technischen Universität Wien
Fakultät für Physik

durch

Dipl.-Ing. Patrick Chalupa-Gantner

Matrikelnummer 01125539
Fabrikgasse 2A/13, 2603 Felixdorf

Wien, August 2022

Abstract

The theoretical study of strongly correlated electron systems is both a fascinating and, at the same time, also a very challenging task. In particular, within the quantum field theoretic description of interacting many-electron systems, no small parameter can be defined a priori according to which a perturbation expansion could be safely formulated. As it turns out, already in situations of intermediate coupling among the electrons, this can have remarkable consequences: the breakdown of self-consistent perturbation theory, which manifests itself in the divergences of the two-particle irreducible vertex functions as well as the associated crossings of the physical with unphysical solutions of the (intrinsically multivalued) Luttinger-Ward functional. The occurrence of these nonperturbative effects poses considerable challenges to the state-of-the-art many-body theory and to the numerical applicability of several forefront approximation schemes.

In this thesis, one aspect of the breakdown of perturbation theory, namely the divergences of the irreducible vertex functions, is analyzed in different respects. In particular, as a first step, the appearance of these nonperturbative manifestations throughout the parameter spaces of several fundamental many-electron models is investigated and systematically discussed for cases with and without particle-hole symmetry. Thereafter, on a more fundamental level, the physical origin of the divergences of the irreducible vertex functions is unveiled. To this end, the way the formation of the local magnetic moment and its Kondo screening impact the generalized susceptibility in the charge channel is carefully analyzed. This study reveals the emergence of characteristic structures in Matsubara frequency space that originate vanishing eigenvalues, which are associated with the appearance of irreducible vertex divergences. As a remarkable byproduct of this analysis, an alternative criterion for the determination of the Kondo temperature on the two-particle level is identified. Further, the physical implications of the occurrence of irreducible vertex divergences are studied. As it turns out, the sign change of the associated eigenvalues of the generalized susceptibility in specific scattering channels can lead to effectively *attractive* contributions in these sectors. Ultimately, these contributions are responsible for the divergence of the isothermal compressibility, observed in the proximity of the Mott metal-to-insulator transition of the Hubbard model solved by the dynamical mean-field theory. From a more methodological perspective, different algorithmic strategies for circumventing the computational problems posed by the breakdown of self-consistent perturbation theory are reviewed. Because of its potential for future method development, a particular emphasis is given to the multiloop functional renormalization group (mfRG) scheme for the fundamental case of the Anderson impurity model, where its performance and physical content are studied from weak- to strong-coupling. Finally, the multifaceted perspectives for future studies, inspired by the main results presented in this thesis, are outlined in the final chapter.

Deutsche Kurzfassung

Die theoretische Untersuchung stark korrelierter Elektronensysteme ist eine faszinierende und gleichzeitig auch sehr herausfordernde Aufgabe. Insbesondere lässt sich in der quantenfeldtheoretischen Beschreibung wechselwirkender Vielelektronensysteme a priori kein Parameter definieren, nach dem eine Störungsentwicklung verlässlich formuliert werden könnte. Wie sich herausstellt, kann dies bereits in Situationen mittlerer Kopplung zwischen den Elektronen bemerkenswerte Folgen haben: den Zusammenbruch der selbstkonsistenten Störungstheorie, der sich in den Divergenzen der zweiteilchen-irreduziblen Vertexfunktionen sowie den damit verbundenen Kreuzungen der physikalischen mit unphysikalischen Lösungen des (mehrwertigen) Luttinger-Ward-Funktionals manifestiert. Das Auftreten dieser nichtperturbativen Effekte stellt die heutige Vielteilchentheorie sowie die Anwendbarkeit modernster Approximationschemata vor immense Herausforderungen.

In dieser Arbeit wird ein Aspekt des Zusammenbruchs der Störungstheorie, nämlich die Divergenzen der irreduziblen Vertexfuntionen, in vielerlei Hinsicht analysiert. Als ersten Schritt wird das Auftreten dieser nichtperturbativen Manifestationen in mehreren fundamentalen Vielelektronenmodellen für verschiedenste Parameter untersucht und systematisch für Fälle mit und ohne Teilchen-Loch-Symmetrie diskutiert. Danach wird auf einer grundlegenderen Ebene der physikalische Ursprung der irreduziblen Vertexdivergenzen geklärt. Zu diesem Zweck wird sorgfältig analysiert, wie sich die Bildung des lokalen magnetischen Moments und dessen Kondo-Abschirmung auf die generalisierte Suszeptibilität im Ladungskanal auswirken. Diese Analyse offenbart die Entstehung charakteristischer Strukturen im Matsubara-Frequenzraum, die verschwindende Eigenwerte hervorrufen, welche wiederum mit dem Auftreten irreduzibler Vertexdivergenzen verbunden sind. Als bemerkenswertes Nebenprodukt dieser Analyse wird ein alternatives Kriterium zur Bestimmung der Kondotemperatur auf der Zweiteilchen-Ebene identifiziert. Des Weiteren werden die physikalischen Implikationen des Auftretens irreduzibler Vertexdivergenzen untersucht. Wie sich herausstellt, kann der Vorzeichenwechsel der Eigenwerte der generalisierten Suszeptibilität in bestimmten Streukanälen zu effektiv *attraktiven* Beiträgen in diesen Sektoren führen. Letztendlich sind diese Beiträge für die Divergenz der isothermen Kompressibilität verantwortlich, die in der Nähe des Mott Metall-zu-Isolator-Übergangs des Hubbard-Modells, gelöst durch die dynamische Molekularfeldtheorie, beobachtet wird. Außerdem werden verschiedene algorithmische Strategien zur Umgehung der methodologischen Hürden betrachtet, die der Zusammenbruch der selbstkonsistenten Störungstheorie darstellt. Aufgrund des Potenzials für die zukünftige Methodenentwicklung wird der multiloop-funktionalen Renormierungsgruppe (mfRG) für den fundamentalen Fall des Anderson Störstellenmodells besondere Beachtung geschenkt, wobei deren Performanz sowie deren physikalischer Inhalt von schwacher bis starker Kopplung untersucht werden. Im abschließenden Kapitel werden die vielfältigen Perspektiven für zukünftige Studien skizziert, die von den hier präsentierten Ergebnissen inspiriert sind.

Contents

CHAPTER 1

Introduction

Preparing a great espresso is no easy task[1]. On the one hand, one needs to have a good understanding of the tools needed to make it. This mainly concerns the portafilter machine and the coffee grinder. On the other hand, its quality is dramatically influenced by various parameters, such as temperature, pressure, grinding sets, and many others. Nevertheless, hunting for the perfect solution to this complex problem, depending on so many factors as well as the subtle interplay among them, is a fascinating challenge for many people – and if it works out, a very rewarding one.

Arguably, this recalls the challenges posed by the physics of interacting many-electron problems. In fact, for systems of strongly correlated electrons the electronic interaction can no longer be neglected, e.g. due to insufficient screening of the Coulomb repulsion. In the theoretical description of these problems, it is hence impossible to treat the electrons individually without considering the presence and the mutual influence of all other electrons. In such cases, the electronic correlation needs to be explicitly accounted for. As an example, consider the double occupancy, i.e., the expectation value for two electrons with different spins to occupy the same site (e.g., of the lattice system under consideration). If the interaction among the electrons is sizable, this quantity will significantly differ from the product of the two individual occupancies ($\langle n_{i,\uparrow} n_{i,\downarrow} \rangle \neq \langle n_{i,\uparrow} \rangle \langle n_{i,\downarrow} \rangle$). Of course, this property generally characterizes all quantities of interest in the study of interacting electrons, featuring collective behaviors, which cannot be deduced solely through the analysis of the mere elementary constituents of these systems. This concept has been summarized best by P. W. Anderson in his famous article "More is Different" [1], "*The behavior of large and complex aggregates of elementary particles, it turns out, is not to be understood in terms of a simple extrapolation of the properties of a few particles.*". While the electronic correlation makes the theoretical treatment of strongly correlated electron systems significantly more challenging, it is also in these systems that a plethora of intriguing physical phenomena are found. As E. Dagotto writes in Ref. [2]: "*It is the diversity of behavior, namely the many*

---

[1]For a scientific approach to this problem, consider e.g. M. I. Cameron, *et al.* , *Systematically Improving Espresso: Insights from Mathematical Modeling and Experiment*, Matter **2**, 631-648 (2020) or Chapters 15-17 of *The Craft and Science of Coffee* (Academic Press, 2016) edited by B. Folmer. For a more practical perspective the author of this thesis recommends the YouTube channel of James Hoffmann.

possible metallic, insulating, magnetic, superconducting, and ferroelectric phases of strongly corre-
lated systems, that makes these types of investigations so exciting". In many cases, an intricate
competition of different phases is observed, depending on slight changes in one of the
systems parameters, such as doping, pressure, temperature, and many others. A single
glance at e.g., the phase diagram of cuprates (see for example Ref. [2] or Ref. [3]) impres-
sively illustrates this fact. However, in the study of strongly correlated electron systems,
many of these intriguing phenomena are not yet completely understood on a microscopic
level, despite the tremendous international research effort. For instance, unconventional
superconductivity [3–5], one of the many "perfect espressi" strongly correlated electron
systems have to offer, remains one of the most exciting puzzles to date. Progress on many
frontiers, both theoretically and experimentally, will be needed to tackle this challenge.

In this thesis, we focus on a crucial aspect of the theoretical description of electronic
correlation. Namely, on the physical and algorithmic implications of the fundamental
nonperturbative nature of interacting electron systems in condensed matter physics.

We recall that due to the vast number of degrees of freedom in many-electron systems,
a quantum field theoretic (QFT) description is indispensable. This formalism, described
in details in textbooks such as Refs. [6–9], shares many similarities with the perturbative,
Feynman-diagrammatic, formalism of quantum electrodynamics (QED). There is however
one crucial difference: For solid-state systems, no small parameter can be defined a priori,
such as the fine-structure constant for QED. In fact, when the electronic interaction is not
sufficiently screened, the corresponding energy scales can be of the same order of magni-
tude as the kinetic energy (or of other relevant energy scales of the system). This makes
a perturbative many-body treatment not rigorously justified and potentially dangerous.
A self-consistent perturbative treatment might even completely fail to describe pivotal as-
pects of the system under investigation, featuring what we define as "the breakdown of
perturbation theory" [10–12]. In particular, fundamental equations of the many-electron
theory, such as the Bethe-Salpeter (BSE) or the parquet equations (both introduced below),
can become *non-invertible* for specific parameter sets. This corresponds to divergences of
the building blocks of these equations [10] – the two-particle irreducible vertex functions.
The analysis of these divergences will be the central topic of this thesis. As it turns out,
their appearance is related [12] to an intrinsic multivaluedness [11] of the Luttinger-Ward
functional (LWF), a central quantity for the description of many-electron problems. In spite
of the increasing interest for this topic in the last years [10–28], some fundamental ques-
tions remained unanswered, particularly concerning the physical origin and the physical
implication of the breakdown of perturbation theory.

The aim of this thesis can be concisely summarized as the investigation of the following
four questions:

- In which cases are the different manifestations of the breakdown of perturbation the-
  ory (irreducible vertex divergences and crossings of solutions of the LWF) appearing,
  and how are they connected?

- What is the underlying physical mechanism that triggers the perturbative breakdown?

- Are there physical implications of the appearance of irreducible vertex divergences?

- What are the algorithmic implications of the breakdown of the perturbative expansions, and are there possible strategies for circumventing them?

The structure of the thesis is organized as follows:

Chapter 2 serves as an introductory chapter, where all the basic concepts needed for the subsequent discussions are recalled. This concerns, on the one hand, the many-electron models of interest for this thesis and, on the other hand, the QFT formalism on the two-particle level, necessary for studying the breakdown of perturbation theory. Finally, the analytical and numerical methods used to compute the quantities of interest are also mentioned or briefly discussed.

Chapter 3 focuses on the first central question of this thesis. Here, the subject of the divergences of the irreducible vertex functions is introduced and thoroughly discussed[2]. Subsequently, the other relevant manifestation of the breakdown of perturbation theory, i.e., the multivaluedness of the LWF, is concisely reviewed and the connection among both nonperturbative aspects is then summarized. Eventually, the numerous manifestations of the breakdown of perturbation theory in different many-electron models are discussed in detail, highlighting their ubiquity in the many-electron physics.

Chapter 4 presents an important theoretical advancement obtained in the course of this thesis. Specifically, we discuss how fundamental physical effects of many-electron systems are encoded in the QFT description on the two-particle level and, in particular, in the frequency structures of the generalized susceptibilities. Thanks to this progress, qualitative and quantitative insights on the two-particle scattering processes are gained allowing for a clear-cut answer to the second central question of this thesis.

Chapter 5 targets the third main question of this thesis, i.e., the physical implications of the irreducible vertex divergences. After discussing how the crossing of a divergence of the irreducible vertex, can be, to a certain extent, interpreted as a sign-flip of the effective electronic interaction, we identify a specific physical phenomenon, which is directly linked to the breakdown of perturbation theory: the increase of the isothermal compressibility in the proximity of the critical endpoint of the Mott metal-to-insulator transition (MIT) in the Hubbard model, solved by dynamical mean-field theory.

Chapter 6 discusses the last question listed above: the challenges posed by the breakdown of perturbation theory to algorithmic methods and possible workarounds. Several

---

[2]Since the topics of the divergences of irreducible vertex functions as well as the multivaluedness of the LWF are comparably new subjects, not yet encoded in textbooks or review articles, some sections of this thesis have partly a review character (namely, parts of Chapter 3 and Secs. 6.1 and 6.2). In these parts, in order to provide a self-contained reading material, recent literature results are concisely summarized and corresponding figures, where necessary, replotted.

cutting-edge approaches for the description of many-electron systems are summarized, with a primary focus on the so-called multiloop functional renormalization group, whose convergence and physical properties are investigated in great detail.

Finally, in **Chapter** 7, the main achievements of this thesis are summarized and the most relevant future directions for the research on these topics are outlined.

At the end of the thesis, a list of publications is provided, together with a short summary of the personal contributions of the author to these publications. Throughout the thesis, vertical bars mark parts taken from already published work of the author of this thesis. Please note that these parts were slightly modified, if necessary, to better match the text.

Models, formalism and methods

I fought the law and the law won
I fought the law and the law won
– The Clash

In this chapter, we present the basic definitions as well as the models and methods central to the discussion of the following Chapters 3 to 7. First, the fundamental many-electron models considered in this thesis are introduced. A particular emphasis is given to the Anderson impurity model since it represents the model used most frequently throughout this work. Second, definitions and properties of the two-particle quantities of interest are concisely discussed, focusing on the most relevant aspects for the nonperturbative phenomena studied afterward. Finally, the diagrammatic approximations and numerical approaches employed to compute two-particle quantities are briefly illustrated.

The primary topic of this thesis is to discuss the various aspects of the breakdown of self-consistent perturbation theory, addressed in Chapter 3. This goal is also reflected in the structure of this present chapter. In particular, we provide a comprehensive discussion of the basic formal concepts needed for investigating[1] the divergences of the irreducible vertex functions as well as the multivaluedness of the Luttinger-Ward functional. Other topics, instead, such as e.g., the particulars of the continuous-time quantum Monte-Carlo (CT-QMC) algorithm, are only defined to the necessary extent.

2.1 Models

In the following section we introduce the three many-electron models, which will be studied throughout the thesis. Each model is designed to describe a specific physical

---

[1] Please note that parts of the present chapter (especially Sec. 2.1.1, 2.2 and 2.3.1.2) were already reported in the *Master thesis* of the author [29]. They are to a small part reproduced here in order to provide a complete and self-contained description of the topics relevant for this thesis.

problem, ranging from dilute magnetic ions dissolved in host metals, up to correlated lattice systems. For a comprehensive introduction we recommend the following textbooks [9, 30, 31], which also represented the basis for the following discussion.

2.1.1   Anderson impurity model

The Anderson impurity model (AIM) is one of the most fundamental models in the field of correlated many-electron systems. It was originally introduced by P. W. Anderson [32] in order to describe magnetic impurities in non-magnetic metallic hosts. In his paradigmatic work the AIM was introduced and treated by a self-consistent Hartree-Fock method in order to identify the parameter sets for which a magnetic impurity, i.e., a singly occupied impurity site, would be realized. The structure of the Hamiltonian of the AIM, which is given below, reflects the central idea of Ref. [32] that is to distinguish between free conduction-band electrons and a local interacting site, where both elements are connected by a hybridization term. In the case of interest for this thesis, the impurity site has a single non-degenerate level, as in Ref. [32]. Extensions to degenerate impurity levels are of course possible [9, 30, 32], they are, however, not considered here.

The Hamiltonian of the AIM reads as follows [30]:

$$
\begin{aligned}
\mathcal{H} \;=\; & \sum_{\sigma} \epsilon_d c_{d,\sigma}^{\dagger} c_{d,\sigma} + U n_{d,\uparrow} n_{d,\downarrow} \\
& + \sum_{\mathbf{k},\sigma} \epsilon_{\mathbf{k}} c_{\mathbf{k},\sigma}^{\dagger} c_{\mathbf{k},\sigma} \\
& + \sum_{\mathbf{k},\sigma} (V_{\mathbf{k}} c_{d,\sigma}^{\dagger} c_{\mathbf{k},\sigma} + V_{\mathbf{k}}^{*} c_{\mathbf{k},\sigma}^{\dagger} c_{d,\sigma})
\end{aligned}
\tag{2.1}
$$

In the first line the impurity site terms are given, where ϵ_d corresponds to the one-particle energy of the impurity level and U is the local interaction strength, which contributes only if the site is doubly occupied. $c_{d,\sigma}^{\dagger}/c_{d,\sigma}$ creates/annihilates an electron on the impurity site and $n_{d,\sigma}$ is given by $c_{d,\sigma}^{\dagger} c_{d,\sigma}$. The second line describes the energy of the non-interacting conduction electrons with $\epsilon_{\mathbf{k}}$ being the dispersion relation and $c_{\mathbf{k},\sigma}^{\dagger}$ and $c_{\mathbf{k},\sigma}$ being the corresponding creation and annihilation operators, respectively. The wavevector $\mathbf{k}$ is restricted to the first Brillouin zone. In the third line the hybridization onto/off the impurity site ($V_{\mathbf{k}}/V_{\mathbf{k}}^{*}$) is given.

The specific AIM considered throughout this thesis is characterized by the following simplifications and parameters choices: The hybridization strength is assumed to be $\mathbf{k}$-independent, $V_{\mathbf{k}} = V$, where V is set to $V = 2$ and energy is measured in units of $V/2 = 1$. The non-interacting density of states (DOS) $\rho(\epsilon)$ for the conduction electrons is chosen to be box-shaped, $\rho(\epsilon) = 1/2D \, \Theta(D - |\epsilon|)$, where D is the half bandwidth, which is set to $D = 10$. Throughout ρ_0 refers to the constant value of the DOS $\rho(|\epsilon| < D) = \rho_0 = 1/2D$. The AIM is considered in the half-filled case, $\epsilon_d = -U/2$. These choices ensure that the
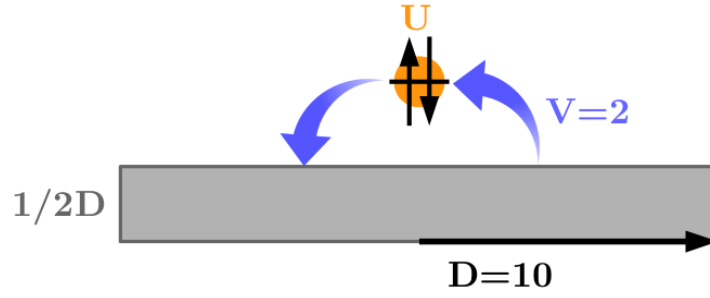
Figure 2.1: A sketch of the Anderson impurity model, showing the basic elements of the Hamiltonian in Eq. (2.1) in a schematic fashion: A box-shaped density of states (grey), hybridization onto/off the impurity site from/to the electron bath (blue) and the interacting doubly-occupied impurity site (orange). Figure taken from [29].

hybridization function $\Delta(\nu)$,

$$\Delta(\nu) = \sum_{\mathbf{k}} \frac{V^2}{i\nu - \epsilon_{\mathbf{k}}} \simeq \int \rho(\epsilon) \frac{V^2}{i\nu - \epsilon} = -i\frac{V^2}{D} \arctan \frac{D}{\nu} \, , \qquad (2.2)$$

as well as the non-interacting Green's function,

$$G_0(\nu) = \frac{1}{i\nu - \Delta(\nu)} \, , \qquad (2.3)$$

are purely imaginary. A sketch of the AIM with these specific parameter choices can be found in Fig. 2.1.

In the following, we summarize some important physical effects that are described by the AIM. Our discussion mainly concerns the formation of a local magnetic moment on the impurity site and its interplay with the conduction electrons, which will play an important role throughout this thesis. A thorough review of the physics of the AIM and the related Kondo problem can be found for example in the textbooks by A. C. Hewson [30] or P. Coleman [9]. We start by considering simple limiting regimes of the AIM, and focus on the question in which cases a magnetic impurity site is found.

2.1.1.1 Atomic limit

The atomic limit (AL) of the AIM is obtained by only considering the impurity terms in Eq. (2.1) (corresponding to setting $V = 0$), for which the Hamiltonian can be diagonalized straightforwardly. In this case,, the Hilbert space reduces to four states, which are shown schematically in Fig. 2.2. The non-magnetic states of an empty or doubly occupied impurity site have the energies 0 or $2\epsilon_d + U$, respectively. The magnetic states of a single electron with spin $\uparrow$ or $\downarrow$ in the impurity orbital have the energy ϵ_d. By setting $\epsilon_d = -U/2$ (ensuring perfect particle-hole symmetry), the magnetic states become the degenerate ground-states of the atomic limit of AIM.

Physically, the study of the AL proves to be quite insightful, since it describes a situation
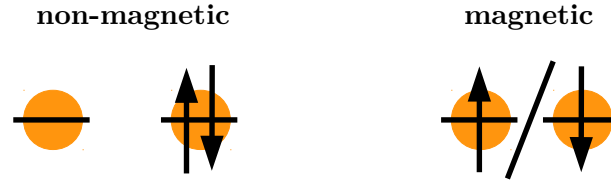
Figure 2.2: Isolated interacting impurity with a single non-degenerate orbital (orange), which can be at most doubly occupied. The energetically degenerate magnetic states are formed by the singly occupied impurity site with spin $\sigma = \uparrow, \downarrow$.

of a perfect local moment, which is not perturbed by any hybridization with conduction electrons. The magnetic response function in such a case shows an almost perfect textbook $\chi_m \sim 1/T$ Curie-behavior in the whole temperature range below $T \sim U$ (see further Sec. 4.1).

For this reason, throughout this work, the AL will provide for a valuable benchmark case, upon which results for the full AIM can be compared with[2]. From a practical point of view, the AL also has the advantage of being analytically treatable, see in particular Refs. [23, 33]. Note, that the AL case of the AIM coincides with the one of the Hubbard model (introduced in Sec. 2.1.3 below), where it represents the limiting case of vanishing hopping t.

2.1.1.2 Non-interacting case

The other extreme limit of the Hamiltonian given in Eq. (2.1) is realized by setting $U = 0$. Physically, considering this limit corresponds to study the interplay of the conduction electrons with a non-interacting impurity level, which represents an impurity scattering center. This problem goes back to pioneering studies of "virtual bound states" by Friedel and co-workers [30]. It effectively results in an excess density of states $\delta \rho(\epsilon)$ around the impurity level energy ϵ_d[3]. For the case relevant to this thesis, i.e., a flat conduction band and a $\mathbf{k}$-independent hybridization V, the change in the local density of states of the impurity site , $\delta \rho(\epsilon)$, is given by Eq. (1.58) of Ref. [30]

$$\delta \rho(\epsilon) = \frac{\Delta_0/\pi}{(\epsilon - \epsilon_d)^2 + \Delta_0^2} \, , \tag{2.4}$$

where $\Delta_0 = \pi \rho_0 |V^2|$ represents the width of the Lorentzian-shaped $\delta \rho(\epsilon)$, which is related to Eq. (2.2) by $\Delta(\nu) \approx -i\mathrm{sgn}(\nu)\Delta_0$ for small ν. For the parameters of the specific AIM, $\Delta_0 = \pi/5 \approx 0.63$, holds.

This broadening of the DOS leads to important physical effects, such as a renormalization of the specific heat and the magnetic susceptibility, but it does not yield a Curie-Weiss contribution to the magnetic response [30].

---

[2]Note that in some instances the AL will also synonymously be referred to as Hubbard atom (HA).

[3]Actually, the excess $\delta \rho(\epsilon)$ is centered around a shifted energy level $\tilde{\epsilon}_d$, see Eqs. (1.56) and (1.57) in Ref. [30]. The details of this shift, are however not relevant here, and hence neglected.

2.1.1.3 The local moment regimes of the AIM

Evidently, the physics described by the full AIM is significantly richer than the one of the two limiting cases considered above. In P. W. Anderson's original calculation [32] the question of the local moment formation was studied by using a Hartee-Fock treatment. For this mean-field case the condition $U > U_c = \pi\Delta_0$ [9, 30, 32] was identified to control whether a magnetic solution, i.e., a singly occupied impurity site, was present or not.

Beyond the mean-field picture, this problem can be treated in the strong-coupling limit by using a *Schrieffer-Wolff* transformation [9, 30]. This is applicable, e.g., for the following parameter set [30]: $\epsilon_d + U \gg \epsilon_F$, $\epsilon_d \ll \epsilon_F$ and $|\epsilon_d + U - \epsilon_F|$, $|\epsilon_d - \epsilon_F| \gg \Delta_0$, where ϵ_F is the Fermi-energy [30]. In particular, for the specific AIM studied throughout this thesis these constrains hold since in most cases $U > 2$ is considered and

$$\Delta_0 = \pi\rho_0 V^2 = \pi/5 < 1 \; ; \; \epsilon_d = -U/2 \;.$$

The main results of this canonical transformation can already be obtained by projecting the Hamiltonian onto the subspace of a singly-occupied impurity site, see Sec. 1.7 of [30]. In this way, the occupation of the impurity site is fixed and an effective Hamiltonian is obtained, which describes a spin model, the so-called "s-d" model[4]. The most relevant part of this Hamiltonian is given in the following and describes the interaction of the local moment on the impurity site with the spins of the conduction electrons, see Eq. (1.64) of Ref. [30]. The part not shown, merely represents a potential-scattering term (which vanishes for half filling) and the energy of the conduction electrons [30].

$$\mathcal{H}_{s-d} = \sum_{\mathbf{k},\mathbf{k}'} J_{\mathbf{k},\mathbf{k}'}\left(S^+ c^\dagger_{\mathbf{k},\downarrow} c_{\mathbf{k}',\uparrow} + S^- c^\dagger_{\mathbf{k},\uparrow} c_{\mathbf{k}',\downarrow} + S_z(c^\dagger_{\mathbf{k},\uparrow} c_{\mathbf{k}',\uparrow} - c^\dagger_{\mathbf{k},\downarrow} c_{\mathbf{k}',\downarrow})\right) \tag{2.5}$$

Here, $J_{\mathbf{k},\mathbf{k}'}$ represents the coupling constant between the impurity spin and the spin of the conduction electrons, which originates from the original hybridization term of the AIM after the projection onto the singly-occupied subspace. In particular, for a $\mathbf{k}$-independent hybridization explicitly reads (cf. Eq.(1.73) of [30]):

$$J_{\mathbf{k},\mathbf{k}'} = V^2\left(\frac{1}{\epsilon_d + U - \epsilon_{\mathbf{k}'}} + \frac{1}{\epsilon_{\mathbf{k}} - \epsilon_d}\right) , \tag{2.6}$$

which effectively describes an antiferromagnetic coupling of the magnetic moment of the impurity site, with the spins of the bath electrons. While the relation with the s-d model is important for relevant aspects of the physics described by the full AIM, naturally the full AIM represents a physically more complex case, as it also describes charge fluctuations.

2.1.1.4 The Kondo problem and the AIM

In general, the study of impurity magnetic moment interacting with the conduction electrons at different temperature scales represents a fascinating and insightful problem. In

---

[4] Note that this mapping is formally and conceptually similar to the mapping of the half-filled Hubbard model at strong coupling to an Heisenberg model.
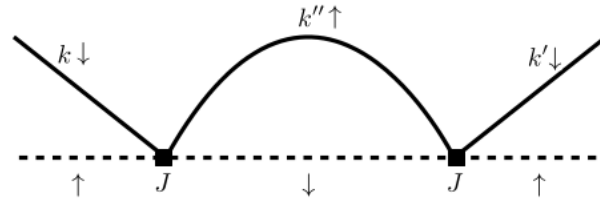
Figure 2.3: An example for a second order spin flip process, which is responsible for the temperature-dependent scattering amplitudes, eventually driving the logarithmic increase at low-T in the electrical resistivity. A conduction electron with wave vector $\mathbf{k}$ and spin down ($\downarrow$) is scattered into an intermediate state $\mathbf{k}'' \uparrow$, where the spins of both, the conduction electron and the impurity are flipped. The conduction electron is then scattered to the final state $\mathbf{k}' \downarrow$. Figure taken from [29].

fact, this underlies the so-called Kondo effect, as well as the Kondo problem, i.e., the highly non-trivial $T \to 0$ limit of the Kondo effect. In the following, we provide a brief historic summary targeted at the introduction of the famous *Kondo temperature* (sometimes also referred to as Kondo scale), which will be highly relevant for later chapters. We start by recalling the Kondo effect.

What is nowadays known as the Kondo effect goes back to the theoretical explanation of the experimentally observed resistivity minimum in metallic alloys of non-magnetic metals containing small amounts of transition metals. For low-temperatures, instead of a monotonically decreasing resistivity (as one would expect based on the conventional electron-phonon and electron-electron contributions, which typically yield a $\propto T^5$ and a $\propto T^2$ contribution, respectively), one finds an increase which shows a $\propto -\ln(T)$ behavior. As J. Kondo first showed in 1964 [34], the $-\ln(T)$ term in the resistivity appears due to the interaction of the conduction electrons with localized magnetic moments. In his work, he used second order perturbation theory for the s-d model (see Eq. (2.5)), sufficient to also describe spin-flip processes, which are shown diagrammatically in Fig. 2.3. The solid lines represent the conduction electron, while the local moment of the impurity site is shown as a dashed line. There are of course further examples of such a second order scattering process, which altogether yield a temperature-dependent scattering amplitude [9, 30]. By considering a dilute random distribution of impurities in the metal, the resistivity of the conduction electrons is given by

$$R(T) = aT^5 + R_0 - c_{imp}R_1 \ln\left(\frac{k_B T}{D}\right), \tag{2.7}$$

, see Eq. (2.58) of Ref. [30], where the concentration of impurity sites in the metallic host is given by c_{imp}, and R_1 contains among other constants the coupling J (assumed here to be $\mathbf{k}$-independent). This expression yields a minimum of the resistivity ($T_{min} \propto c_{imp}^{1/5}$), which is weakly dependent on the concentration of impurities.

On a more general perspective, while this result correctly describes the resistivity minimum, it also poses a new problem, namely the $T \to 0$ behavior. Using the treatment described above, the limit $T \to 0$ leads to an artificial logarithmic divergences of the resis-

tivity and other response functions, such as the specific heat or the magnetic susceptibility, which is not observed in experiment. The study of the $T \rightarrow 0$ behavior of the Kondo effect became known as the Kondo problem, a long-standing problem of theoretical solid-state physics, whose development is briefly outlined in the following.

The approach followed by A. A. Abrikosov [35] consisted of summing up leading logarithmic terms of higher order scattering processes. However, this did not solve the problem, since the different physical response functions diverge even at a *finite* temperature in this case: The Kondo temperature, which in the framework of this treatment reads [30]:

$$k_B T_K \propto D e^{-1/2J\rho_0} \, . \tag{2.8}$$

Here, ρ_0 is the constant value of a box-shaped density of states and J is again the **k**-independent coupling strength.

In the so-called *Poor Man's scaling* method, P. W. Anderson found another way to attack this problem [36]. In this scaling approach the bandwidth D is gradually reduced, which is compensated for by a renormalization of the coupling strength J. However, for the antiferromagnetic case of interest, a divergence of the coupling J is found, as soon as the scaling reaches energies[5] of the order of $k_B T_K$.

Nevertheless, this intuitive approach helped to inspire the development of the nonperturbative renormalization group approach by K. G. Wilson [37], which eventually provided definite answers to the problem of the $T \rightarrow 0$ limit. In fact, it could be shown that the Kondo temperature actually represents a *crossover* temperature [9, 30]: While at higher temperatures ($T > T_K$ but lower than U) the local moment is free, displaying a $\propto 1/T$ Curie-behavior, it gets gradually screened by the conduction electrons as the temperature is reduced. For very low-temperatures of $T \lesssim T_K$ this results in a fully quenched local moment, as the conduction electron spins and the impurity moment tend to form a spin singlet state. This results in a temperature-independent contribution to the resistivity and a constant contribution to the magnetic susceptibility. Furthermore, in this low-temperature regime all physical quantities turn out to be universal functions of the energy scale $k_B T_K$. Moreover, as the work by P. Nozières from 1974 showed [38], in the very-low-temperature case, the problem can be analyzed as a Landau Fermi-liquid, due to the presence of a sharp Kondo resonance at the Fermi level, with a width of the order of $k_B T_K$. The resulting physical picture throughout the full temperature range is best illustrated by the phase-diagram shown in Fig. 2.4, which was taken from the textbook by P. Coleman [9], see Fig. 16.11 therein.

These findings were later confirmed by analytic results for the s-d model obtained by a Bethe-Ansatz approach [9, 30]. In fact, also the AIM can be treated in this way, which allows to obtain an analytic expression for the Kondo temperature of the AIM. In the case

---

[5]Throughout this work k_B is set to unity $k_B = 1$ and usually neglected in expressions, however in this part it is included explicitly for consistency with the referenced literature.
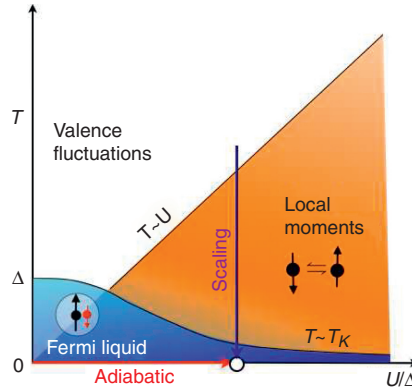
Figure 2.4: Phase-diagram of the Anderson impurity model, where the local moment regime is shown in orange, and the Fermi-Liquid regime is shown in blue. This figure was taken from Ref. [9], see Fig. 16.11 therein.

of $D \gg U$ (i.e., the wide-band limit) it reads

$$k_\mathrm{B} T_\mathrm{K} = 0.4107 \, U \left(\frac{\Delta_0}{2U} \right)^{1/2} e^{-\pi U/8\Delta_0 + \pi\Delta_0/2U} \tag{2.9}$$

This equation can be found in the textbook by A. C. Hewson [30] (Eq. (6.109) therein), where the numerical factor 0.4107 is derived from a comparison with numerical renormalization group calculations for the AIM performed by H. R. Krishna-murthy *et al.* [30, 39, 40]. The Kondo temperature can also be obtained numerically from calculations for the magnetic response function χ_m, which is discussed explicitly in Sec. 4.1. A comparison of the analytic expression for T_K given in Eq. (2.9) and the numerical results for the specific AIM used throughout this thesis can be found in Sec. 3.1.3.

This concludes the concise historic review of the local moment physics of the AIM and the Kondo problem. Let us point out that even nowadays, several decades after the solution by Krishna-murthy and Wilson, the AIM still plays an essential role in the description of the correlated electron systems. For instance, it represents a crucial part of the Dynamical Mean Field Theory (DMFT) solution of the Hubbard model [41], which is discussed below in Sec. 2.3.1. On the other hand also the Kondo problem in itself is still a very relevant research topic, for example for quantum dot applications, see e.g., Ref. [42]. Let us at this point also refer to a recent experiment performed by I. V. Borzenets *et al.* [43], where the spatial extent of the Kondo screening cloud could be experimentally observed and its size quantitatively estimated to be of the order of micrometers.

2.1.2 Periodic Anderson model

A natural extension of the Anderson impurity model with a single impurity site is the *periodic* Anderson model (PAM). The crucial difference to the AIM lies in the fact that now each lattice site is characterized by a strong local electrostatic interaction U and, at the same time, a hybridization with a non-interacting conduction band. The PAM plays an important role in modern solid-state physics, as its application range from e.g., studies

of heavy-fermion systems [9], to quantum criticality [44] and many more. Further, for large interaction values, it can be mapped to a spin-lattice model, the so-called Kondo lattice model [9]. While several versions of the corresponding Hamiltonian can be found in the literature [9, 30], we provide here the one relevant for the application of the PAM in Chapter 4, which can be found in the work by T. Schäfer *et al.* [44] (see Eq. (1) therein) or in a very similar version also in Ref. [41].

$$
\begin{aligned}
\mathcal{H} &= \sum_{i\sigma} \epsilon_f f_{i\sigma}^\dagger f_{i\sigma} + U \sum_i n_{f,i\uparrow} n_{f,i\downarrow} \\
&+ \sum_{\mathbf{k},\sigma} \epsilon_{\mathbf{k}} c_{\mathbf{k},\sigma}^\dagger c_{\mathbf{k},\sigma} \\
&+ V \sum_{i\sigma} (f_{i\sigma}^\dagger c_{i\sigma} + c_{i\sigma}^\dagger f_{i\sigma})
\end{aligned}
\tag{2.10}
$$

Similarly as for the AIM, the first line of Eq. (2.10) describes the locally interacting terms, which now also have a lattice site index i. $f_{i\sigma}^\dagger / f_{i\sigma}$ refers to the creation/annihilation operator for electrons on the interacting sites, ϵ_f is the corresponding energy and U the strength of the local interaction. In the second line, the term describing the non-interacting conduction electrons is given, where $\epsilon_{\mathbf{k}}$ is their dispersion relation. The last line corresponds to the hybridization term, where V is the **k**-independent hybridization strength.

For the most relevant application of the PAM in Chapter 4, its specifications read as follows: The PAM is considered on a two-dimensional lattice with nearest neighbor hopping only. The corresponding dispersion relation of the conduction electrons reads $\epsilon_{\mathbf{k}} = -2t[\cos(k_x) + \cos(k_y)]$, where t is the hopping amplitude and k_x and k_y are restricted to the first Brillouin zone $\in [-\pi, \pi]$ (the lattice constant a is put to unity throughout.) The interaction strength is fixed to $U = 4t$ and instead the hybridization V is varied.

2.1.3 Hubbard model

As the last of the three fundamental models of correlated electron systems considered in this thesis, the Hubbard model (HM) is discussed. Its introduction goes back to the works of J. Hubbard [45], J. Kanamori [46] and M. C. Gutzwiller [47]. In the one-band version, which will be of interest throughout this thesis, it already captures the important interplay between the kinetic (i.e., the hopping) and the potential (i.e., the interaction) energy of correlated lattice systems. While its expression might look deceptively simple, no analytic solution of the HM for the general case is known. Exact solutions exist only for the one-dimensional and the infinite-dimensional (or infinite lattice coordination number z) case, which is given by the DMFT solution (see Sec. 2.3.1) but not for the physically most relevant cases of two and three dimensions.

For a general introduction to the model, and its connection and importance to solid-state physics, we refer to introductory textbooks, such as e.g., [9] and [8] and for collections of pertinent works, see e.g., Ref. [48]. A comprehensive analysis more focused on the HM itself

can be found in Ref. [31] and many of the books of the Jülich "Modeling and Simulation" series, e.g., [49]. Let us also refer to some recent publications, where the current progress of several research groups working on the Hubbard model (mostly in its two-dimensional form) is summarized and different methods for its solution are benchmarked [50–53].
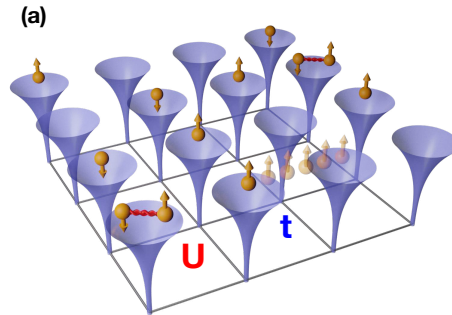
Figure 2.5: A sketch representation of the two-dimensional Hubbard model on a square lattice, where the hopping process (t, blue) and the local interaction (U, red) are shown. This figure was taken from the recent review on different numerical solutions of the HM [53], see Fig. 1 therein.

The Hamiltonian of the HM is given by the following expression [52]:

$$\mathcal{H} \;=\; -t \sum_{\langle ij \rangle, \sigma} c^\dagger_{i\sigma} c_{j\sigma} + U \sum_i n_{i\uparrow} n_{i\downarrow} \tag{2.11}$$

Unlike in the PAM or the AIM, the Hamiltonian of the HM considers only one species of electrons or sites arranged on a periodic lattice, where $c^\dagger_{i\sigma}/c_{i\sigma}$ creates/annihilates an electron with spin $\sigma = \{\uparrow, \downarrow\}$ on lattice site i. The first term concerns the kinetic energy part, where t is the hopping-matrix amplitude. In this thesis, we consider only nearest neighbor hopping (signaled by the $\langle ij \rangle$ in the sum), for which the model displays a perfect particle-hole symmetry at half-filling.

The second term of Eq. (2.11) instead represents the local interaction term, which (for the repulsive case $U > 0$) penalizes double-occupations on site i.

Fig. 2.5 illustrates the relevant contributions of the HM, as determined by the Hamiltonian given in Eq. (2.11). This figure was taken from Ref. [53], see Fig. 1 therein. Since the HM is used in slightly different versions throughout this thesis (e.g., on a Bethe lattice in Chapter 4 and on a square lattice in Chapter 5), its specifications are postponed to the corresponding instances in the later chapters.

2.2 Local two-particle formalism for many-electron systems

In this section, the focus lies on the introduction of the central quantities of interest for this thesis: the generalized susceptibilities. As will be discussed throughout the following chapters, the eigenvalues and eigenvectors of the generalized charge (and pairing as well magnetic) susceptibility represent the key to study the nonperturbative divergences of the irreducible vertex functions (s. Chapter 3), the fingerprints of the local moment formation

(s. Chapter 4) as well as the enhancement of the isothermal compressibility (s. Chapter 5)..
Additionally, in this section, we will also introduce the fundamental classes of two-particle
Feynman diagrams, i.e., two-particle reducible and -irreducible ones, and their mutual
relations in the form of the parquet- and the Bethe-Salpeter equations.

The following discussion is based mainly on Ref. [33] (and also Ref. [54]), where the
two-particle correlation functions have been introduced for the local problem, which is
also the most relevant case for this thesis. A more recent introduction of the two-particle
formalism of generalized susceptibilities and Feynman diagrams can be found in Ref. [51],
where the definitions are given for the more general **k**-dependent case. For textbooks
which introduce the many-body QFT formalism on a more general level (offering also a
detailed treatment of the one-particle level), we refer the interested reader to e.g., Refs. [6,
9, 30, 31]. More specialized treatments of particular aspects of the two-particle formalism
of interest for this thesis, can be found, for example, in the books of the Jülich "Modeling
and Simulation" series, e.g., [49], as well as Refs. [55–59].

We start our introduction of the two-particle (2P) formalism with the definition of the
local one-particle (1P) Green's function [33, 54]:

$$G_{1,\sigma_1\sigma_2}(\tau_1, \tau_2) = \langle T_\tau c^\dagger_{\sigma_1}(\tau_1) c_{\sigma_2}(\tau_2) \rangle \tag{2.12}$$

Here, T_τ represents the time-ordering operator, putting later times to the left, and the
thermal expectation value $1/Z \, \mathrm{Tr}(e^{-\beta \mathcal{H}} O)$ is denoted by $\langle O \rangle$, where Z is the partition function
$Z = \mathrm{Tr}(e^{-\beta \mathcal{H}})$ and $\beta = 1/T$ the inverse temperature. In Eq. (2.12), $c^\dagger_{\sigma_1}(\tau)$ and $c_{\sigma_2}(\tau)$ refer to
creation and annihilation operators of particles at imaginary time τ_n with spin $\sigma_n = \{\uparrow, \downarrow\}$.
While this explicit formulation is directly applicable to the *local* Green's functions, one
can easily introduce operators with additional indices representing, e.g., lattice sites i or
momenta **k**, orbitals l and others, see Refs. [54] or [51]. Hence, while we mostly focus on
the local case throughout this work, where necessary we will provide the definition for the
k-dependent case.

To provide an intuitive understanding for the 1P Green's function, one can consider the
following cases: For $\tau_1 > \tau_2$ a hole is created at the imaginary time τ_2 with spin σ_2, which
propagates through the system before being removed from it at τ_1. $G_{1,\sigma_1\sigma_2}$ hence represents
the transition amplitude for such a process, where the hole probes the system along its
propagation, allowing to gain essential information about the physics of the many-electron
system under consideration. For the other case of $\tau_1 < \tau_2$, the same is true for a particle
propagating through the system.

The natural next step, which represents a significant increase in the level of complexity,
is to consider the 2P Green's function, which describes the propagation of two particles (or
of a particle and a hole) [33, 51, 54].

$$G_{2,\sigma_1\sigma_2\sigma_3\sigma_4}(\tau_1, \tau_2, \tau_3, \tau_4) = \langle T_\tau c^\dagger_{\sigma_1}(\tau_1) c_{\sigma_2}(\tau_2) c^\dagger_{\sigma_3}(\tau_3) c_{\sigma_4}(\tau_4) \rangle \tag{2.13}$$

Usually, instead of directly working with the 2P Green's function, one extracts the so-
called generalized susceptibility from G_2 and G_1 since this is the object which can be most
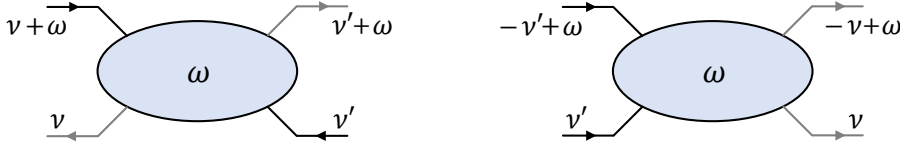
Figure 2.6: Two scattering processes are represented in their natural notation, where in both cases the energy ω is transferred and the outgoing propagator lines are shown in gray. Left panel: A particle and a hole scattering in particle-hole notation. Right panel: Two particles scattering with each other in particle particle notation.

directly related with physical response functions, as will be shown below.

The local generalized susceptibility $\chi_{\sigma_1\sigma_2\sigma_3\sigma_4}(\tau_1, \tau_2, \tau_3, \tau_4)$ is defined as follows [33, 51, 54]:

$$
\begin{aligned}
\chi_{\sigma_1\sigma_2\sigma_3\sigma_4}(\tau_1, \tau_2, \tau_3, \tau_4) \quad := \quad & G_{2,\sigma_1\sigma_2\sigma_3\sigma_4}(\tau_1, \tau_2, \tau_3, \tau_4) \quad\quad\quad (2.14) \\
- \quad & G_{1,\sigma_1\sigma_2}(\tau_1, \tau_2)G_{1,\sigma_3\sigma_4}(\tau_3, \tau_4)
\end{aligned}
$$

By exploiting the symmetries of the Hamiltonians of interest, the generalized susceptibility $\chi_{\sigma_1\sigma_2\sigma_3\sigma_4}(\tau_1, \tau_2, \tau_3, \tau_4)$ can be significantly simplified. The first step is to consider the absence of any terms in the Hamiltonians of the AIM, the PAM or the HM that break the time-translation invariance. Together with the boundary conditions for the Green's functions, the expression for the generalized susceptibility can be simplified as follows [33, 51, 54]: $\chi_{\sigma_1\sigma_2\sigma_3\sigma_4}(\tau_1, \tau_2, \tau_3, \tau_4) \rightarrow \chi_{\sigma_1\sigma_2\sigma_3\sigma_4}(\tau_1, \tau_2, \tau_3, 0) = \chi_{\sigma_1\sigma_2\sigma_3\sigma_4}(\tau_1, \tau_2, \tau_3)$, where τ_1, τ_2, τ_3 are restricted to the imaginary time interval $[0, \beta]$. As a second step, exploiting the SU(2)-symmetry of the Hamiltonians of Eq. (2.1), Eq. (2.10) and Eq. (2.11), significantly reduces the number of independent spin-combinations of $\chi_{\sigma_1\sigma_2\sigma_3\sigma_4}(\tau_1, \tau_2, \tau_3)$. More specifically, from the $2^4 = 16$ combinations, due to the conservation of the total spin, only 6 are possible [33, 51, 54]. These remaining 6 spin combinations can be further related to one another via the crossing-symmetry and the SU(2) symmetry [33, 51, 54]. In particular, in this work, the following spin components of $\chi_{\sigma_1\sigma_2\sigma_3\sigma_4}(\tau_1, \tau_2, \tau_3)$ are of interest:

$$
\chi_{\sigma\sigma'}(\tau_1, \tau_2, \tau_3) = \chi_{\sigma\sigma\sigma'\sigma'}(\tau_1, \tau_2, \tau_3) \quad\quad\quad (2.15)
$$

$$
\chi_{\overline{\sigma\sigma'}}(\tau_1, \tau_2, \tau_3) = \chi_{\sigma\sigma'\sigma'\sigma}(\tau_1, \tau_2, \tau_3) \qu\quad\quad\quad (2.16)
$$

where $\chi_{\overline{\sigma\sigma'}}(\tau_1, \tau_2, \tau_3)$ will only be relevant for Chapter 6. Note further that these considerations also simplify the 1P Green's function, defined in Eq. (2.12), $G_{1,\sigma_1\sigma_2}(\tau_1, \tau_2) \rightarrow G_{1,\sigma}(\tau, 0) = G_\sigma(\tau)$.

The generalized susceptibility $\chi_{\sigma\sigma'}(\tau_1, \tau_2, \tau_3)$ can be Fourier transformed to Matsubara frequency space, where $\nu = (2n + 1)\pi T$ denotes a fermionic and $\omega = 2n\pi T$ a bosonic Matsubara frequency [33, 51, 54]. For the purposes of this thesis, two possibilities to perform this transformation are considered, which relate to the so-called *particle-hole* (ph) and *particle-particle* (pp) notation. Those notations allow for a physically transparent descrip-

tion[6] of two different kinds of scattering processes, which are illustrated in Fig. 2.6. In the left panel the process of a particle scattering with a hole is depicted and the Matsubara frequencies are correspondingly given in the ph-notation. In the right panel two particles scatter and the diagram is shown in its natural pp-notation. In both diagrams in Fig. 2.6 a bosonic frequency ω is transferred (where hole propagators are associated with negative energies). It is worth noting that though indicated with the same symbol, the transfer frequencies for the ph- and the pp-processes are defined differently.

The generalized susceptibility in ph-notation $\chi_{ph,\sigma\sigma'}^{\nu\nu'\omega}$ reads [33, 51, 54] :

$$
\begin{aligned}
\chi_{ph,\sigma\sigma'}^{\nu\nu'\omega} &= \int_0^\beta d\tau_1 d\tau_2 d\tau_3 \, e^{-i\nu\tau_1} e^{i(\nu+\omega)\tau_2} e^{-i(\nu'+\omega)\tau_3} \\
&\times \chi_{\sigma\sigma'}(\tau_1, \tau_2, \tau_3) \\
&= \int_0^\beta d\tau_1 d\tau_2 d\tau_3 \, e^{-i\nu\tau_1} e^{i(\nu+\omega)\tau_2} e^{-i(\nu'+\omega)\tau_3} \\
&\times [\langle T_\tau c_\sigma^\dagger(\tau_1) c_\sigma(\tau_2) c_{\sigma'}^\dagger(\tau_3) c_{\sigma'}(0)\rangle \\
&- \langle T_\tau c_\sigma^\dagger(\tau_1) c_\sigma(\tau_2)\rangle \langle T_\tau c_{\sigma'}^\dagger(\tau_3) c_{\sigma'}(0)\rangle] \,.
\end{aligned}
\tag{2.17}
$$

In the pp-notation the generalized susceptibility is given as follows [33, 51, 54]:

$$
\begin{aligned}
\chi_{pp,\sigma\sigma'}^{\nu\nu'\omega} &= \int_0^\beta d\tau_1 d\tau_2 d\tau_3 \, e^{-i\nu\tau_1} e^{i(\omega-\nu')\tau_2} e^{-i(\omega-\nu)\tau_3} \\
&\times \chi_{\sigma\sigma'}(\tau_1, \tau_2, \tau_3) \,.
\end{aligned}
$$

As one can easily verify, both notations are related by a specific frequency shift: $\chi_{pp,\sigma\sigma'}^{\nu\nu'\omega} = \chi_{ph,\sigma\sigma'}^{\nu\nu'(\omega-\nu-\nu')}$ [33, 51, 54]. Note that in the following we focus on the ph channel and hence omit the subscript $\chi_{ph,\sigma\sigma'}^{\nu\nu'\omega} = \chi_{\sigma\sigma'}^{\nu\nu'\omega}$. Where necessary we provide the explicit expression for the pp channel.

The generalized susceptibility describes all scattering processes, in particular including also the independent propagation of the particle-hole or particle-particle pair. From a diagrammatic perspective, it is hence useful to split $\chi_{\sigma\sigma'}^{\nu\nu'\omega}$ into the following two parts [33, 51, 54]:

$$
\chi_{\sigma\sigma'}^{\nu\nu'\omega} = -\beta G_\sigma(\nu) G_\sigma(\nu+\omega) \delta_{\nu\nu'} \delta_{\sigma\sigma'} - G_\sigma(\nu) G_\sigma(\nu+\omega) F_{\sigma\sigma'}^{\nu\nu'\omega} G_{\sigma'}(\nu'+\omega) G_{\sigma'}(\nu')
\tag{2.18}
$$

Here, $F_{\sigma\sigma'}^{\nu\nu'\omega}$ represents the so-called *full* vertex (in the ph channel). It contains all possible vertex corrections, i.e., all 2P diagrams, where the propagating particle and hole interact with one another. The specific form of the first term of Eq. (2.18) can be understood

---

[6]Of course, all processes are included in $\chi_{\sigma\sigma'}(\tau_1, \tau_2, \tau_3)$, the notation merely concerns which scattering process is the one that is naturally described in the given notation, such that no frequency shifts are needed.

$$G_\sigma(\nu + \omega) \qquad G_\sigma(\nu + \omega) \qquad G_{\sigma'}(\nu' + \omega)$$

$$\chi_{\sigma\sigma'}^{\nu\nu'\omega} \quad = \quad -\beta\delta_{\nu\nu'}\delta_{\sigma\sigma'} \quad - \qquad \boxed{F_{\sigma\sigma'}^{\nu\nu'\omega}}$$

$$G_\sigma(\nu) \qquad\qquad G_\sigma(\nu) \qquad\qquad G_{\sigma'}(\nu')$$
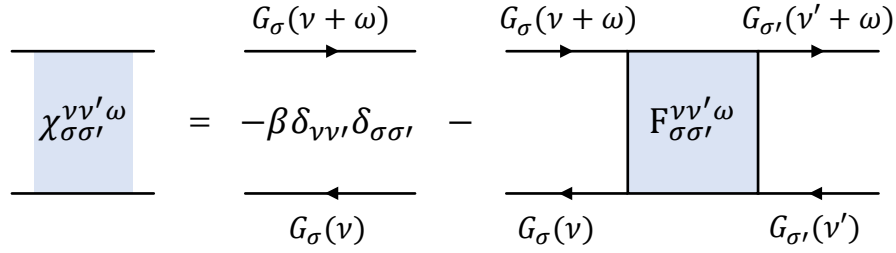
Figure 2.7: Diagrammatic representation of Eq. (2.18) for the generalized susceptibility in ph notation. The first diagram on the right-hand-side is the so-called "bubble"-term, which is a product of two 1P Green's functions. In the second term the full vertex $F_{\sigma\sigma'}^{\nu\nu'\omega}$ contains all vertex corrections.

from the definition of $\chi_{\sigma\sigma'}^{\nu\nu'\omega}$ in Eq. (2.14). In particular, by employing Wicks theorem for the $U = 0$ case, two products of 1P Green's functions are obtained, see Eq. (2.157) in Ref. [54]. In accordance with Eq. (2.14), the remaining disconnected part describes the independent propagation of a particle and a hole, the so-called "bubble"-term, which is the first diagram in Fig. 2.7, where Eq. (2.18) is represented diagrammatically. By using the definition $\chi_0^{\nu\nu'\omega} = -\beta G_\sigma(\nu)G_\sigma(\nu + \omega)\delta_{\nu\nu'}$,[7] Eq. (2.18) can be written in a more compact form [33, 51, 54]

$$\chi_{\sigma\sigma'}^{\nu\nu'\omega} = \chi_0^{\nu\nu'\omega}\delta_{\sigma\sigma'} - \frac{1}{\beta^2}\sum_{\nu_1\nu_2}\chi_0^{\nu\nu_1\omega}F_{\sigma\sigma'}^{\nu_1\nu_2\omega}\chi_0^{\nu_2\nu'\omega} \ . \tag{2.19}$$

Physically, in the correlated metallic regime, F can be interpreted as the amplitude of all scattering processes between a particle-hole pair [6, 33] and can also be related to Fermi-liquid parameters [6, 57].

Before discussing the connection of the generalized susceptibility to physical response functions, we will focus on the full vertex F, and its classification into different topological classes of 2P-Feynman diagrams, by the *parquet* or the Bethe-Salpeter equation. Here, the central quantities of interest–*the irreducible vertex functions*–will be defined, whose unexpected divergences, will be of primary interest throughout this thesis.

2.2.1 Parquet equations

The full vertex $F_{\sigma\sigma'}^{\nu\nu'\omega}$, referred to as F in the following part, includes all vertex corrections to the generalized susceptibility, i.e., all connected 2P-Feynman diagrams. These diagrams can be further classified according to the concept of *two-particle reducibility*, which is shown for an example case in in Fig. 2.8. Here, the part L on the left can be split from the part R on the right hand side by cutting two internal fermionic propagator lines, i.e., the two internal 1P Green's functions a and b (of course L and R could be merely the bare interaction diagram, or also more complicated connected diagrams as well). In this perspective, the concept two-particle reducibility represents a natural extension of the one-particle

---

[7]The expression in the pp notation can be obtained by the same frequency shift as before, $\chi_{pp,0}^{\nu\nu'\omega} = \chi_0^{\nu\nu'(\omega-\nu-\nu')} = -\beta G_\sigma(\nu)G_\sigma(\omega - \nu)\delta_{\nu\nu'}$
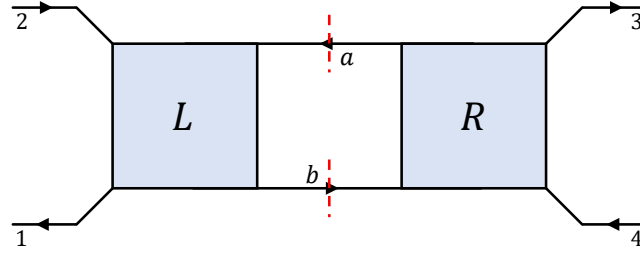
Figure 2.8: Example for a two-particle diagram which is reducible in the longitudinal particle-hole channel. By cutting the two internal Green's function lines a and b (signaled by the red dashed lines) it can be split into two parts, L and R.

reducibility, for which we refer to general textbooks such as e.g., Refs. [6–9]. However, at the higher level of complexity of the 2P level, several classes of two-particle reducible (2PR) diagrams can be distinguished, depending on the way the four legs (i.e., outgoing and ingoing propagator lines) are separated. The example shown in Fig. 2.8 refers to the longitudinal particle-hole channel (ph), where the pairs $(1, 2)$ are cut from $(3, 4)$. Reducible diagrams of the transverse particle-hole channel $(\overline{ph})$ are diagrams where $(1, 4)$ can be cut from $(2, 3)$. In line with the definition of the pp-notation, processes where $(1, 3)$ can be cut from $(2, 4)$, hence two incoming particles from two outgoing ones, are referred to particle-particle (pp) reducible, see also Fig. 2.9.

Due to particle-number conservation of the two-particle interaction considered, a 2PR diagram can only be reducible in one of the pp, ph or $\overline{ph}$ classes (see in particular pages 66-69 of Ref. [54] for a precise argumentation).

The second class of diagrams of F are those, which are *not* two-particle reducible, i.e., they cannot be separated by cutting two 1P Green's functions lines. The most straightforward example for such a diagram is the bare interaction diagram itself, another example (the so-called "envelope diagram") is shown below in Fig. 2.9. The diagrams belonging to this class are referred to as fully two-particle *irreducible* (fully-2PI).

Throughout this work we will indicate the fully 2PI diagrams with $\Lambda_{\sigma\sigma'}^{\nu\nu'\omega}$, and the ones reducible in channel $l = $ pp,ph, $\overline{ph}$ with $\Phi_{l,\sigma\sigma'}^{\nu\nu'\omega}$. On the basis of these definitions, the full vertex F can be exactly decomposed as follows,

$$F = \Lambda + \Phi_{pp} + \Phi_{ph} + \Phi_{\overline{ph}} \, , \tag{2.20}$$

which is known as *parquet* equation [33, 51, 54, 55]. Here, the spin indices $\sigma\sigma'$ were omitted, since the parquet equation holds for all spin components of the full vertex $F_{\sigma\sigma'}$ individually [33, 51, 54]. In Fig. 2.9 the parquet equation is represented diagrammatically, where for each diagram class an example of a low-order diagram is shown.

The parquet equation has great importance for practical applications, since it represents the starting point for several diagrammatic approaches [51]. As will be discussed in Sec. 2.3.2, together with the Bethe-Salpeter equations, a complete set of diagrammatic equations can be formulated, which can be solved based on a given input for the fully 2PI vertex Λ.
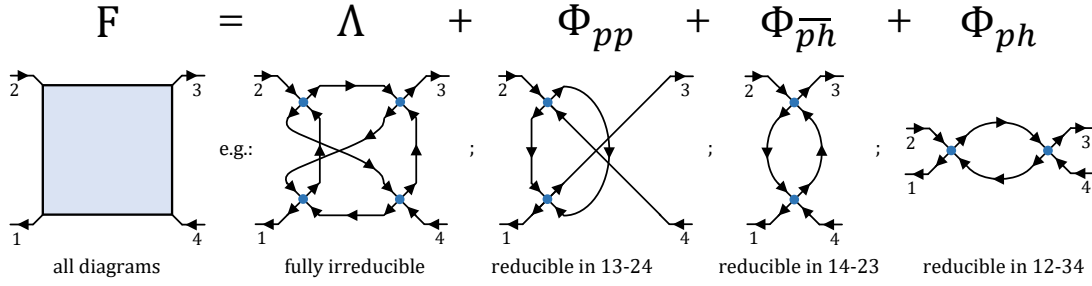
Figure 2.9: A representation of the parquet equation, an exact decomposition of the full 2P vertex F. In the first line the algebraic relation is shown (cf. Eq. (2.20)). In the second line, below each class (fully-2PI or 2PR in l), an example for a low order diagram is given. The bare interaction is represented by the blue dot with two incoming and two outgoing arrows. The diagrammatic example for the fully 2PI vertex Λ is the so-called "envelope diagram". In the last line, the two-particle reducibility is recalled. This figure is a inspired by Fig. 5 in Ref. [51], where, for pedagogical reasons, the bare interaction diagram is always drawn the same way for all examples (including the corresponding arrows).

2.2.2   Bethe-Salpeter equation

There exists also a different possibility of classifying the 2P reducible and 2P irreducible diagrams of the full vertex F [33, 51, 54]. Instead of classifying all reducible diagrams into the different classes $l = pp, ph, \overline{ph}$, one considers the reducibility with respect to a specific channel only. Since the 2P diagrams can only be reducible at most in one channel, this yields the decomposition $F = \Gamma_l + \Phi_l$, where Γ_l is the class of 2P diagrams which are *irreducible in channel l*. For example, when considering the ph channel, one would summarize the first three terms shown in Fig. 2.9 (Λ, Φ_{pp} and $\Phi_{\overline{ph}}$) as Γ_{ph}, and distinguish it from the last term, which is the corresponding reducible vertex Φ_{ph}.

As Γ_l contains all 2PI diagrams of channel l, Φ_l can be constructed from it by using the so-called Bethe-Salpeter equation (BSE) [33, 51, 54]

$$F = \Gamma_l + \int \Gamma_l GGF \ , \tag{2.21}$$

where the diagrams reducible in l are constructed by connecting Γ_l with F by two 1P Green's functions, such that the 2P-reducibility in l is ensured. A simple example is the second-order diagram for Φ_{ph} shown in Fig. 2.9, which can be obtained from the second term in Eq. (2.21), namely by considering the contribution originated by the bare interaction diagram for both, F and Γ_{ph}.

In the case of the BSE the spin components are however not completely independent (the $\int$ in Eq. (2.21) denotes the summation/integration over all internal degrees of freedom and hence mixes spin indices), unlike in the parquet decomposition case described in Sec. 2.2.1. In fact, the BSE e.g., for $F_{\uparrow\uparrow}$ and $F_{\uparrow\downarrow}$ in the ph channel are coupled, see Refs. [33, 54]. However, by introducing the *charge* $= \uparrow\uparrow + \uparrow\downarrow$ (c) and *magnetic* $= \uparrow\uparrow - \uparrow\downarrow$ (m) components these equations can be decoupled in the SU(2) symmetric case, where $F_c = F_{\uparrow\uparrow} + F_{\uparrow\downarrow}$ and $F_m = F_{\uparrow\uparrow} - F_{\uparrow\downarrow}$ and analogously for the generalized susceptibility χ and the irreducible
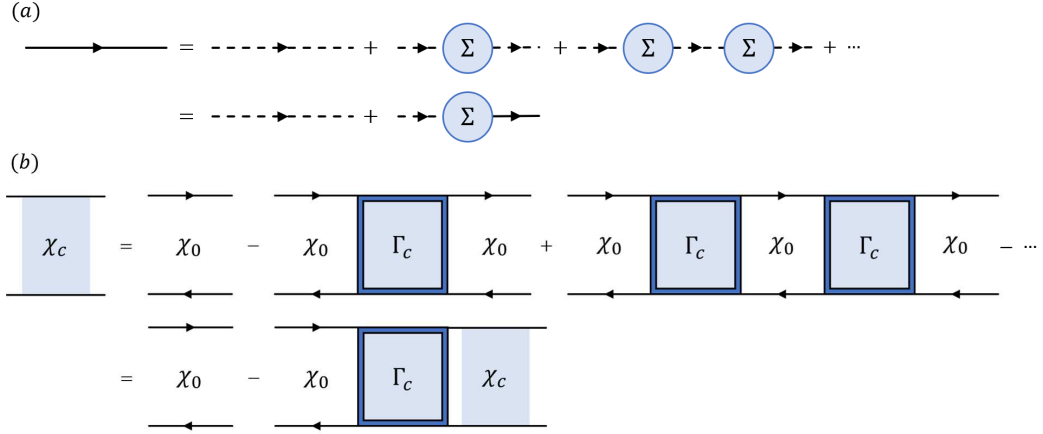
Figure 2.10: Diagrammatic representations of the Dyson equation (Eq. (2.23)) (a) and the BSE in the charge channel (Eq. (2.22)). Upper panel: The dashed line refers to a non-interacting G_0, the full to a full G.

vertex Γ. In the following we express the BSE in the decoupled form for the generalized susceptibilities, which can be obtained from Eq. (2.21) by using Eq. (2.19), see Refs. [33, 54] (Eq. (B6) in Ref. [33]).

In the ph channel the generalized susceptibility is related to the irreducible vertex $\Gamma_{ph,r} = \Gamma_r$ as follows [33, 51, 54]

$$\chi_r^{\nu\nu'\omega} = \chi_0^{\nu\nu'\omega} - \frac{1}{\beta^2} \sum_{\nu_1\nu_2} \chi_0^{\nu\nu_1\omega}\Gamma_r^{\nu_1\nu_2\omega}\chi_r^{\nu_2\nu'\omega} \ , \tag{2.22}$$

where $r = c, m$ refers to the charge or magnetic channel[8].

Structurally, one immediately notes that the BSE expresses the generalized susceptibility in terms of a geometric series of the irreducible vertex Γ in the form of a matrix multiplication[9]. Hence, while in the case of Eq. (2.19), the full vertex F is obtained from χ by a mere subtraction of χ_0 and division of the four legs (i.e., the four 1P Green's functions), this is not the case for the irreducible vertex. Formally, the BSE needs to be inverted in order to obtain the irreducible vertex Γ. In fact, this represents a perfect 2P analogue to the 1P case of the Dyson equation, which relates the Green's function and the (one-particle irreducible) self-energy Σ, as follows:

$$G = G_0 + G_0\Sigma G \ \rightarrow \text{inversion} \rightarrow \ \Sigma = G^{-1} - G_0^{-1} \ . \tag{2.23}$$

The structural similarity between the 1P Dyson equation and the 2P BSE also clearly emerges from the visual comparison of their diagrammatic representations in Fig. 2.10.

By inversion of Eq. (2.22), one thus obtains an explicit expression for the irreducible vertex in the charge and magnetic channel, which reads [33, 54]

---

[8]The $\overline{ph}$ channel is connected to the ph one by the crossing- and the SU(2) symmetry, and hence Γ_r for $r = c, m$ are the only independent functions for the two channels, see further Refs. [33, 54].

[9]Throughout, the summation over one (or more) fermionic Matsubara frequency indices goes along with one (or more) $1/\beta$ factors [33, 54].

$$\Gamma_r^{\nu\nu'\omega} = \left(\left[\chi_r^{-1} \right]^{\nu\nu'\omega} - \left[\chi_0^{-1} \right]^{\nu\nu'\omega} \right) \tag{2.24}$$

Similarly, in the particle-particle channel, we consider the $\uparrow\downarrow$ component, which reads as follows [33, 54][10] (see Eq. (B25) in Ref. [33]):

$$\tilde{\chi}_{pp,\uparrow\downarrow}^{\nu\nu'\omega} = -\frac{1}{\beta^2} \sum_{\nu_1\nu_2} \left(\chi_{pp,0}^{\nu\nu_1\omega} - \tilde{\chi}_{pp,\uparrow\downarrow}^{\nu\nu_1\omega} \right) \tilde{\Gamma}_r^{\nu_1\nu_2\omega} \chi_{pp,0}^{\nu_2\nu'\omega} \, , \tag{2.25}$$

where $\tilde{\chi}_{pp,\uparrow\downarrow}^{\nu\nu'\omega} = \chi_{pp,\uparrow\downarrow}^{\nu(\omega-\nu')\omega}$ and $\tilde{\Gamma}_r^{\nu_1\nu_2\omega} = \Gamma_r^{\nu_1(\omega-\nu_2)\omega}$. By inverting Eq. (2.25) for $\tilde{\Gamma}_r^{\nu_1\nu_2\omega}$ one gets [33, 54]

$$\tilde{\Gamma}_{pp,\uparrow\downarrow}^{\nu\nu'\omega} = \left(\left[(\tilde{\chi}_{pp,\uparrow\downarrow} - \chi_{pp,0})^{-1} \right]^{\nu\nu'\omega} + \left[\chi_{pp,0}^{-1} \right]^{\nu\nu'\omega} \right) \tag{2.26}$$

In Chapter 3, Eqs. (2.22), (2.24), (2.25) and (2.26) will play an important role for the investigation of divergences of the irreducible vertex functions.

2.2.3   Connection to physical response functions

After these general definitions we briefly discuss how the generalized susceptibility is related to experimentally accessible response functions.

For the already introduced charge and magnetic channel, the corresponding local physical response functions $\chi_c(\omega)$ and $\chi_m(\omega)$ are defined as follows [41, 54]:

$$\chi_c(\omega) = \frac{1}{2} \int_0^\beta d\tau e^{i\omega\tau} \langle [n_\uparrow(\tau) + n_\downarrow(\tau)][n_\uparrow(0) + n_\downarrow(0)] \rangle - \delta_{\omega,0} \langle n_\uparrow + n_\downarrow \rangle^2 \tag{2.27}$$

$$\chi_m(\omega) = \frac{1}{2} \int_0^\beta d\tau e^{i\omega\tau} \langle [n_\uparrow(\tau) - n_\downarrow(\tau)][n_\uparrow(0) - n_\downarrow(0)] \rangle - \delta_{\omega,0} \langle n_\uparrow - n_\downarrow \rangle^2 \tag{2.28}$$

These response functions encode the information whether a fluctuation in the charge or magnetic channel is long- or short-lived in (imaginary) time[11]. As a particularly simple example one can consider the local magnetic moment in the atomic limit case, where $\chi_m(\tau)$ (as well as $\chi_c(\tau)$) stays constant, as the spin operator (the charge operator) is a constant of motion in the AL, yielding after a Fourier-transform, a Kronecker-delta contribution at the Matsubara frequency $\omega = 0$. A detailed discussion of the temperature dependence of the local response functions in the charge and spin sector, for the AL as well as the AIM, can be

---

[10]For the pp channel there is also a coupling between different spin components in the BSE. This can however be decoupled in a different way, by using the crossing symmetry, which also underlies the expressions given here, see Refs. [33, 54], explicitly Appendix Bc. of Ref. [33], for more details. Alternatively, one can define a singlet and triplet channel for the pp channel analogously to the charge and magnetic one, which is however not relevant for this thesis [33, 54].

[11]For a more quantitative evaluation of the timescales of the physcial (e.g., screening) processes, an analytic continuation to real time/real frequencies would be needed. The latter would also allow for a direct comparison with, e.g., inelastic neutron scattering data, which is however not the subject of this thesis. We refer the interested reader to Refs. [60–63].

found in Sec. 4.1. In general, the physical response functions introduced above describe, within the linear response formalism, how the system reacts to a (not-too-strong) external dynamical or static perturbation. For details see, e.g., Chapter 6 in Ref. [64] and Chapter 6 of Ref. [65].

The important case of $\omega = 0$ corresponds to the static/isothermal response of the system [62, 66], and will be mostly relevant throughout this thesis.

The physical response functions can be computed from the generalized local ones introduced before, by performing a sum over all *fermionic* Matsubara frequencies [33, 51, 54]:

$$\chi_c(\omega) = \frac{1}{\beta^2} \sum_{\nu\nu'} \chi_c^{\nu\nu'\omega} = T^2 \sum_{\nu\nu'} \left(\chi_{\uparrow\uparrow}^{\nu\nu'\omega} + \chi_{\uparrow\downarrow}^{\nu\nu'\omega} \right) , \tag{2.29}$$

$$\chi_m(\omega) = \frac{1}{\beta^2} \sum_{\nu\nu'} \chi_m^{\nu\nu'\omega} = T^2 \sum_{\nu\nu'} \left(\chi_{\uparrow\uparrow}^{\nu\nu'\omega} - \chi_{\uparrow\downarrow}^{\nu\nu'\omega} \right) , \tag{2.30}$$

as the double sum over ν, ν' corresponds to taking equal times between pairs of fermionic operators, which is necessary to build the corresponding observables. From the diagrammatic point of view, this corresponds to closing the external fermionic lines of the diagrams shown in Fig. 2.7.

2.2.4 Properties of generalized susceptibilities

In this section we focus on the *eigenvalues* and *eigenvectors* of the local generalized charge ($r = c$) and magnetic ($r = m$) susceptibilities $\chi_r^{\nu\nu'\omega}$ in the ph channel and on the $\uparrow\downarrow$ component in pp notation ($r = \text{pp}, \uparrow\downarrow$). These eigenvalues and eigenvectors of $\chi_r^{\nu\nu'\omega}$ will play a central role in the investigation of the appearances of irreducible vertex divergences, discussed in Chapter 3.

Here, we first recall how symmetries of the underlying Hamiltonian (such as the SU(2) symmetry) and fundamental relations (such as the complex conjugation) are reflected in the properties of the generalized susceptibility $\chi_{\sigma\sigma'}^{\nu\nu'\omega}$. As a second step, we restrict ourselves to the static case ($\omega = 0$) and separately consider the half-filled and out-of-half-filled case.

In Table 2.1 we reproduce a subset of relations for the generalized susceptibilities, which can be found listed in Refs. [23, 54]. As mentioned above, these are a direct consequence of the general symmetries of the underlying Hamiltonian. For example, as discussed in the previous section, the SU(2) symmetry relates different spin-components of the generalized susceptibility $\chi_{\sigma\sigma'}^{\nu\nu'\omega}$ to one another. The "swapping" relation in Table 2.1 can be derived by applying the crossing symmetry twice, i.e., fully exchanging the outgoing and incoming particles [23]. Note that the last line holds only in the particle-hole symmetric case, which coincides with the half-filling ($\mu = U/2$) condition for the AIM. Also in the case of the HM, $\mu = U/2$ ensures particle-hole symmetry, since only nearest neighbor hopping terms are taken into account.

With the help of these general relations for $\chi_{\sigma\sigma'}^{\nu\nu'\omega}$ precise statements about its eigenvalues

Symmetry	Relation
SU(2)	$\chi_{\sigma\sigma'}^{\nu\nu'\omega} = \chi_{(-\sigma)(-\sigma')}^{\nu\nu'\omega} = \chi_{\sigma'\sigma}^{\nu\nu'\omega}$
Complex conjugation	$\left(\chi_{\sigma\sigma'}^{\nu\nu'\omega}\right)^* = \chi_{\sigma'\sigma}^{(-\nu')(-\nu)(-\omega)} \overset{\mathrm{SU(2)}}{=} \chi_{\sigma\sigma'}^{(-\nu')(-\nu)(-\omega)}$
Time reversal	$\chi_{\sigma\sigma'}^{\nu\nu'\omega} = \chi_{\sigma'\sigma}^{\nu'\nu\omega} \overset{\mathrm{SU(2)}}{=} \chi_{\sigma\sigma'}^{\nu'\nu\omega}$
Swapping (ph)	$\chi_{ph,\sigma\sigma'}^{\nu\nu'\omega} = \chi_{ph,\sigma'\sigma}^{(\nu'+\omega)(\nu+\omega)(-\omega)}$
Swapping (pp)	$\chi_{pp,\sigma\sigma'}^{\nu\nu'\omega} = \chi_{pp,\sigma'\sigma}^{(-\nu-\omega)(-\nu'-\omega)(\omega)}$
Particle-hole ($\mu = U/2$)	$\left(\chi_{\sigma\sigma'}^{\nu\nu'\omega}\right)^* = \chi_{\sigma\sigma'}^{\nu\nu'\omega}$

Table 2.1: Symmetry relations for the generalized susceptibility $\chi_{\sigma\sigma'}^{\nu\nu'\omega}$, see Refs. [23, 54]. If no subscript referring to the ph or the pp notation is given, the relation for $\chi_{\sigma\sigma'}^{\nu\nu'\omega}$ holds in the same way for both notations.

and eigenvectors can be made, as explained in the following. As anticipated before, we will now set $\omega = 0$ for a given channel r, since this is the case studied most frequently in the literature on the irreducible vertex divergences [10, 12, 13, 17–19, 21, 22, 26, 67, 68], and hence the most relevant for this work. Hereafter, we omit the bosonic frequency superscript ω to improve the readability, $\chi_r^{\nu\nu'(\omega=0)} = \chi_r^{\nu\nu'}$. In this way, $\chi_r^{\nu\nu'}$ can be regarded as a matrix in fermionic Matsubara frequency space. If no specific index regarding the notation is given, the ph notation is considered.

2.2.4.1   Half filling

Parts of this chapter, marked by a vertical bar, have already been published
*in the APS journal Phys. Rev. B. **101**, 155148 (2020).*

At half filling each lattice site (or the interacting site of the AIM) is on average occupied once: $\langle n_i \rangle = \langle n_{i,\uparrow} + n_{i,\downarrow} \rangle = 1$. As it can be seen in the last line of Table 2.1, for the Hamiltonians considered, this ensures that all matrix elements of $\chi_r^{\nu\nu'}$ are real as a result of the perfect particle-hole symmetry. Further, due to the time-reversal and SU(2) symmetry, $\chi_r^{\nu\nu'}$ is a symmetric matrix. Both properties are summarized in the following equations [26] (see Ref. [26] for the more general version for arbitrary ω).

$$\left(\chi_{\sigma\sigma'}^{\nu\nu'}\right)^* \overset{\mathrm{PH}}{=} \chi_{\sigma\sigma'}^{\nu\nu'} \tag{2.31}$$

$$\chi_{\sigma\sigma'}^{\nu\nu'} \overset{\mathrm{TR}}{=} \chi_{\sigma'\sigma}^{\nu'\nu} \overset{\mathrm{SU(2)}}{=} \chi_{\sigma\sigma'}^{\nu'\nu} \tag{2.32}$$

Mathematically, a real symmetric matrix can be spectrally decomposed in the following way:

$$\chi_r^{\nu\nu'} = \sum_i V_i^r(\nu)\,\lambda_i^r\,V_i^r(\nu')\,, \tag{2.33}$$

where λ_i^r are the eigenvalues and $V_i^r(\nu)$ the associated eigenvectors. Note that since $\chi_r^{\nu\nu'}$ is a real symmetric matrix for the particle-hole symmetric case, it can be diagonalized as $\chi_r = V^T D V$, where D is a diagonal matrix and V an orthogonal matrix. In this case the eigenvalues are guaranteed to be real and the eigenvectors $V_i^r(\nu)$ are real and form an orthonormal basis.

A second crucial equality can be found by using the complex conjugation in combination with the SU(2)- and the particle-hole symmetry [23, 26].

$$\chi_{\sigma\sigma'}^{\nu\nu'} \overset{\text{PH}}{=} \left(\chi_{\sigma\sigma'}^{\nu\nu'}\right)^* \overset{\text{CC}}{=} \chi_{\sigma'\sigma}^{(-\nu')(-\nu)} \overset{\text{TR}}{=} \chi_{\sigma\sigma'}^{(-\nu)(-\nu')} \tag{2.34}$$

A matrix with the property given in Eq. (2.34) is referred to as a *centrosymmetric* matrix. Since $\chi_r^{\nu\nu'}$ fulfills both Eq. (2.32) and Eq. (2.34) at half filling, it is a so-called *bisymmetric* matrix:

$$\chi_{\sigma\sigma'}^{\nu\nu'} = \chi_{\sigma\sigma'}^{(-\nu)(-\nu')} \quad \text{and} \quad \chi_{\sigma\sigma'}^{\nu\nu'} = \chi_{\sigma\sigma'}^{\nu'\nu} \tag{2.35}$$

This ensures that the matrix elements of $\chi_r^{\nu\nu'}$ are symmetric with respect to the diagonal $(\nu = \nu')$ and, at the same time, with respect to the secondary diagonal $(\nu = -\nu')$, see also the schematic representation in Fig. 2.11.

For the sake of a self-contained presentation, we summarize some mathematical literature on bisymmetric and centrosymmetric matrices [69–71] in the following, since these properties will be relevant throughout the thesis. First, we focus on centrosymmetric matrices before taking also the symmetry described in Eq. (2.32) into account in a second step.

Centrosymmetric matrices In the following we consider the centrosymmetric matrix H, a $2n \times 2n$ matrix, where n is the number of positive/negative fermionic Matsubara frequencies. As H is a centrosymmetric matrix it fulfills the following condition

$$JHJ = H \tag{2.36}$$

where J is the counteridentity matrix ($J^2 = \mathbb{1}$) given in Eq. (2.37)

$$J = \begin{pmatrix} 0 & \dots & 0 & 1 \\ \vdots & \cdot^{\cdot^{\cdot}} & \cdot^{\cdot^{\cdot}} & 0 \\ 0 & 1 & \cdot^{\cdot^{\cdot}} & \vdots \\ 1 & 0 & \dots & 0 \end{pmatrix} = \begin{pmatrix} \mathbb{0} & J \\ J & \mathbb{0} \end{pmatrix}. \tag{2.37}$$

If J is multiplied from the right, it inverts the columns of a matrix, if it is multiplied from the left, the rows are inverted. As one can easily see, for $\chi_{\sigma\sigma'}^{\nu\nu'}$ this implies

$$J\chi_{\sigma\sigma'}^{\nu\nu'}J = J\chi_{\sigma\sigma'}^{\nu(-\nu')} = \chi_{\sigma\sigma'}^{(-\nu)(-\nu')} = \chi_{\sigma\sigma'}^{\nu\nu'}, \tag{2.38}$$

which is true for our case, see Eq. (2.34).

If H is a centrosymmetric matrix, the following condition holds, where the submatrices A, B, C, D are $n \times n$ matrices

$$H = \left(\begin{array}{c|c} A & B \\ \hline C & D \end{array}\right) \stackrel{(2.36)}{=} JHJ$$

$$\left(\begin{array}{c|c} A & B \\ \hline C & D \end{array}\right) = \begin{pmatrix} \mathbb{0} & J \\ J & \mathbb{0} \end{pmatrix}\left(\begin{array}{c|c} A & B \\ \hline C & D \end{array}\right)\begin{pmatrix} \mathbb{0} & J \\ J & \mathbb{0} \end{pmatrix}$$

$$= \begin{pmatrix} \mathbb{0} & J \\ J & \mathbb{0} \end{pmatrix}\left(\begin{array}{c|c} BJ & AJ \\ \hline DJ & CJ \end{array}\right)$$

$$= \left(\begin{array}{c|c} JDJ & JCJ \\ \hline JBJ & JAJ \end{array}\right) \tag{2.39}$$

$$\Rightarrow D = JAJ \quad \& \quad B = JCJ. \tag{2.40}$$

This means that the centrosymmetric matrix H can be written in the following form

$$H = \left(\begin{array}{c|c} A & JCJ \\ \hline C & JAJ \end{array}\right). \tag{2.41}$$

Eigenvalues and Eigenvectors   Centrosymmetric matrices have a very useful property. Their eigenvalues can be obtained from the diagonalization of specific combinations of the submatrices A and C, corresponding to either symmetric or antisymmetric eigenvectors. Consider an eigenvector $\mathbf{v}$ of H

$$\begin{aligned} H\mathbf{v} &= \lambda\mathbf{v} & |\cdot J \to \\ JH\mathbf{v} &= \lambda J\mathbf{v} \\ HJ\mathbf{v} &= \lambda J\mathbf{v}, \end{aligned} \tag{2.42}$$

where we used Eq. (2.36) and $J^2 = \mathbb{1}$. From this it follows that $J\mathbf{v}$ is also an eigenvector of H corresponding to the eigenvalue λ, i.e.

$$J\mathbf{v} = a\mathbf{v}, \tag{2.43}$$

with $a \neq 0$, being the eigenvalue of J and since J is an orthogonal matrix: $a = \pm 1$. This leads to either antisymmetric or symmetric eigenvectors $\mathbf{v}$. In terms relevant for our discussion this means that

$$\mathbf{v} = \begin{pmatrix} v \\ Jv \end{pmatrix} \quad \text{or} \quad \begin{pmatrix} v \\ -Jv \end{pmatrix} \quad \text{with} \quad \begin{pmatrix} \text{neg. Matsubara} \\ \text{frequencies} \\ \hline \text{pos. Matsubara} \\ \text{frequencies} \end{pmatrix} \quad , \tag{2.44}$$

where $\mathbf{v}$ is a $2n \times 1$ vector and v is a $n \times 1$ subpart of it.

Next, we consider λ_S, an eigenvalue corresponding to a symmetric eigenvector $H\mathbf{v}_S = \lambda_S \mathbf{v}_S$

$$\begin{pmatrix} A & JCJ \\ C & JAJ \end{pmatrix} \begin{pmatrix} v \\ Jv \end{pmatrix} = \lambda_S \begin{pmatrix} v \\ Jv \end{pmatrix} \tag{2.45}$$

$$\Downarrow$$

$$(A + JC)v = \lambda_S v . \tag{2.46}$$

In a similar fashion one finds for λ_A, corresponding to an antisymmetric eigenvector

$$\begin{pmatrix} A & JCJ \\ C & JAJ \end{pmatrix} \begin{pmatrix} v \\ -Jv \end{pmatrix} = \lambda_A \begin{pmatrix} v \\ -Jv \end{pmatrix} \tag{2.47}$$

$$\Downarrow$$

$$(A - JC)v = \lambda_A v \tag{2.48}$$

This shows that the centrosymmetric matrix H has eigenvalues λ_S obtained from diagonalizing $A + JC$, which also gives the non-trivial parts v of the symmetric eigenvectors $\mathbf{v}_S$. On the other hand one observes that λ_A corresponds to antisymmetric eigenvectors obtained from the diagonalization of the submatrices $A - JC$.

In the following, a very elegant way to demonstrate this block structure of H is presented, which will proof to be very practical in Chapter 3.

Block-diagonalization Using the following orthogonal matrix Q ($QQ^T = \mathbb{1}$)

$$Q = \frac{1}{\sqrt{2}} \begin{pmatrix} \mathbb{1} & -J \\ \mathbb{1} & J \end{pmatrix} \tag{2.49}$$

one can block-diagonalize a centrosymmetric matrix H

$$
\begin{aligned}
QHQ^T &= \frac{1}{2}\begin{pmatrix} \mathbb{1} & -J \\ \mathbb{1} & J \end{pmatrix}\begin{pmatrix} A & JCJ \\ C & JAJ \end{pmatrix}\begin{pmatrix} \mathbb{1} & \mathbb{1} \\ -J & J \end{pmatrix} \\
&= \frac{1}{2}\begin{pmatrix} \mathbb{1} & -J \\ \mathbb{1} & J \end{pmatrix}\begin{pmatrix} A - JC & A + JC \\ C - JA & C + JA \end{pmatrix} \\
&= \frac{1}{2}\begin{pmatrix} 2(A - JC) & \mathbb{0} \\ \mathbb{0} & 2(A + JC) \end{pmatrix} \\
&= \begin{pmatrix} A - JC & \mathbb{0} \\ \mathbb{0} & A + JC \end{pmatrix}
\end{aligned}
\tag{2.50}
$$

revealing the previously discussed block structure.

Bisymmetric Matrices   As stated above, due to the SU(2)- and the time-reversal symmetry the centrosymmetric matrix H considered is in fact bisymmetric, see Eq. (2.35). This has important consequences for the submatrices A and C introduced earlier

$$
H = H^T
\tag{2.51}
$$

$$
\begin{pmatrix} A & JCJ \\ C & JAJ \end{pmatrix} = \begin{pmatrix} A^T & C^T \\ (JCJ)^T & (JAJ)^T \end{pmatrix} ,
\tag{2.52}
$$

as $J = J^T$ one finds $A = A^T$ immediately. For C the following equation holds

$$
C^T = JCJ \rightarrow C^T J^T = JC \rightarrow (JC)^T = JC .
\tag{2.53}
$$

This means that the combination of submatrices yielding the eigenvalues and the corresponding symmetric or antisymmetric eigenvectors, is itself symmetric, ensuring together with the particle-hole symmetry that the obtained eigenvalues are real

$$
(A \pm JC)^T = A^T \pm (JC)^T \overset{(2.53)}{=} A \pm JC .
\tag{2.54}
$$

The discussion of the general properties of bisymmetric matrices reported above and its specific impact on the generalized susceptibilities $\chi_r^{\nu\nu'}$ can be summarized as follows [26]: $\chi_r^{\nu\nu'}$ can be block-diagonalized into an antisymmetric and a symmetric block:

$$
Q\chi_r Q^T = \left(\begin{array}{c|c} A & 0 \\ \hline 0 & S \end{array}\right) ,
\tag{2.55}
$$

where A is the submatrix which contains eigenvalues λ_i^r of $\chi_r^{\nu\nu'}$ with strictly antisymmetric eigenvectors $V_i^r(\nu) = -V_i^r(-\nu)$ and S is the block which contains the symmetric ones $V_i^r(\nu) = +V_i^r(-\nu)$. Based on these insights the physical response (see Eqs. (2.29) and (2.30))

can be rewritten using Eq. (2.33):

$$\chi_r(\omega = 0) = \frac{1}{\beta^2} \sum_{\nu,\nu'} \chi_r^{\nu\nu'} = \sum_i \lambda_i^r w_i^r \ , \tag{2.56}$$

where w_i^r refers to a weight factor which is a strictly real non-negative number ($w_i^r \geq 0$), whose explicit expression in terms of the corresponding eigenvectors reads:

$$w_i^r = \Big[\frac{1}{\beta} \sum_\nu V_i^r(\nu)\Big]\Big[\frac{1}{\beta} \sum_{\nu'} V_i^r(\nu')\Big] \ . \tag{2.57}$$

Due to the summation of the eigenvectors $V_i^r(\nu)$, it is obvious that all weight factors corresponding to an antisymmetric eigenvector are zero. Hence the associated contributions $\lambda_i^r w_i^r$ of the entire antisymmetric block A to the physical response in Eq. (2.56) cancel and have no contribution at half filling [26].

The properties for the half-filled case are summarized below in Table 2.2 and a schematic representation of $\chi_r^{\nu\nu'}$ for the lowest Matsubara frequencies is shown in Fig. 2.11.

2.2.4.2   Out of half filling

In the more general case, where the system is not at half-filling, $\langle n_i \rangle = \langle n_{i,\uparrow} + n_{i,\downarrow} \rangle \neq 1$ and/or the underlying Hamiltonian is not particle-hole symmetric, the property of the last row of Table 2.1 is no longer guaranteed $(\chi_{\sigma\sigma'}^{\nu\nu'\omega})^* \neq \chi_{\sigma\sigma'}^{\nu\nu'\omega}$.

In the following, we focus first on the ph channel quantities $\chi_{r=c,m}^{\nu\nu'}$ for which the following equality is true [67]

$$\left(\chi_{\sigma\sigma'}^{\nu\nu'}\right)^* \ \overset{\text{CC}}{\underset{}{=}} \ \chi_{\sigma'\sigma}^{(-\nu')(-\nu)} \ \overset{\text{TR}}{\underset{}{=}} \ \chi_{\sigma\sigma'}^{(-\nu)(-\nu')} \ . \tag{2.58}$$

A matrix with this property is a so-called *centrohermitian* matrix [72], where all matrix elements are symmetric with respect to the center of the matrix under a complex conjugation. Further, since time-reversal and SU(2) symmetry evidently hold also out of half filling, Eq. (2.32) remains valid, and hence $\chi_{r=c,m}^{\nu\nu'}$ is a symmetric centrohermitian matrix. Note that this also means that $\chi_r^{\nu\nu'}$ is no longer a Hermitian matrix.

In this case, the generalized susceptibility is not guaranteed to be diagonalizable as $\chi_r = V^{-1}DV$, which is the generalization[12] of $\chi_r = V^T DV$ for matrices with complex entries. However, in all cases where it can be diagonalized, χ_r can be expressed as follows:

$$\chi_{r=c,m}^{\nu\nu'} = \sum_i V_i^{r-1}(\nu)\lambda_i^r V_i^r(\nu') \ , \tag{2.59}$$

where the eigenvalues λ_i^r can be either real or complex conjugate pairs [67, 72] (see also the Appendix of Ref. [73]) and $V_i^{r-1}(\nu)$ refers to an eigenvector of the V^{-1} matrix. The corresponding physical response can be then written as in Eq. (2.56) with the weights

---

[12]Note that $\chi_{r=c,m}^{\nu\nu'}$ is not a normal matrix ($[\chi_{r=c,m}^{\nu\nu'}]^* \chi_{r=c,m}^{\nu\nu'} \neq \chi_{r=c,m}^{\nu\nu'}[\chi_{r=c,m}^{\nu\nu'}]^*$), and thus cannot be diagonalized as V^*DV, with V being a unitary matrix $V^*V = \mathbb{1}$.

	PH symmetry given	PH symmetry broken
$\chi_{r=c,m}^{\nu\nu'(\omega=0)}$	bisymmetric	centrohermitian and symmetric
λ_i^r	$\in \mathbb{R}$	$\in \begin{cases} \mathbb{R} \\ \mathbb{C} \quad \text{as complex pairs } \lambda_i^r, \overline{\lambda_i^r} \end{cases}$
$V_i^r(\nu)$	$\in \mathbb{R}^n \begin{cases} V_i^r(\nu) = +V_i^r(-\nu) \quad \text{symmetric} \\ V_i^r(\nu) = -V_i^r(-\nu) \quad \text{antisymmetric} \end{cases}$	$\in \mathbb{C}^n$
w_i^r	$\in \mathbb{R}_{\geq 0} = \{x \in \mathbb{R} \mid x \geq 0\}$	$\in \begin{cases} \mathbb{R} \\ \mathbb{C} \quad \text{as complex pairs } w_i^r, \overline{w_i^r} \end{cases}$

Table 2.2: Properties of the static local generalized susceptibility $\chi_r^{\nu\nu'(\omega=0)}$, its eigenvalues λ_i^r, eigenvectors $V_i^r(\nu)$ and weights w_i^r in the charge and magnetic channel ($r = c, m$) for a case with (first column) and without (second column) particle-hole symmetry (PH). Note that for $\chi_{pp,\uparrow\downarrow}^{\nu\nu'(\omega=0)}$ the properties of the first column apply also without the PH symmetry, see Eq. (2.61) and (2.62).

defined as [67]

$$w_i^r = \Big[\frac{1}{\beta} \sum_\nu V_i^{r-1}(\nu)\Big]\Big[\frac{1}{\beta} \sum_{\nu'} V_i^r(\nu')\Big] . \tag{2.60}$$

We now consider the particle-particle channel for which an important difference in the swapping symmetry to the ph case, see Table 2.1, becomes crucial when considering the out-of-half-filling case. In fact, using the swapping symmetry (SP) for the pp channel in combination with the SU(2) symmetry the following equality can be found [23]:

$$\chi_{pp,\sigma\sigma'}^{\nu\nu'} \overset{\text{SP(pp)}}{=} \chi_{pp,\sigma'\sigma}^{(-\nu)(-\nu')} \overset{\text{SU(2)}}{=} \chi_{pp,\sigma\sigma'}^{(-\nu)(-\nu')} \tag{2.61}$$

which means that $\chi_{pp,\uparrow\downarrow}^{\nu\nu'}$ is a centrosymmetric matrix independently of the particle-hole symmetry. Even more so, taking the complex conjugation and the time-reversal symmetry into account, it can be shown that the static $\chi_{pp,\uparrow\downarrow}^{\nu\nu'}$ remains a real matrix also out of half filling:

$$\chi_{pp,\sigma\sigma'}^{\nu\nu'} \overset{(2.61)}{=} \chi_{pp,\sigma\sigma'}^{(-\nu)(-\nu')} \overset{\text{TR}}{=} \chi_{pp,\sigma'\sigma}^{(-\nu')(-\nu)} \overset{\text{CC}}{=} \big(\chi_{pp,\sigma\sigma'}^{\nu\nu'}\big)^* \tag{2.62}$$

Hence, for the static $\chi_{pp,\uparrow\downarrow}^{\nu\nu'}$ all properties and equalities of the highly symmetric half-filled case are still valid out of half filling. This demonstrates that the violation of the particle-hole symmetry does not directly affect the general properties of the static pp sector. With regard to Eq. (2.26), it is straightforward to see that the additional pp bubble term $\chi_{pp,0}^{\nu\nu'(\omega=0)} = -\beta G(\nu)G(-\nu)\delta_{\nu\nu'} = -\beta G(\nu)G^*(\nu)\delta_{\nu\nu'}$ is real.

In Table 2.2 we summarized all properties of $\chi_r^{\nu\nu'(\omega=0)}$ and the corresponding eigenvalues,-vectors and weights. In Fig. 2.11, $\chi_r^{\nu\nu'(\omega=0)}$ is sketched for the lowest Matsubara frequencies, illustrating the centrosymmetric and centrohermitian properties. Note that throughout this
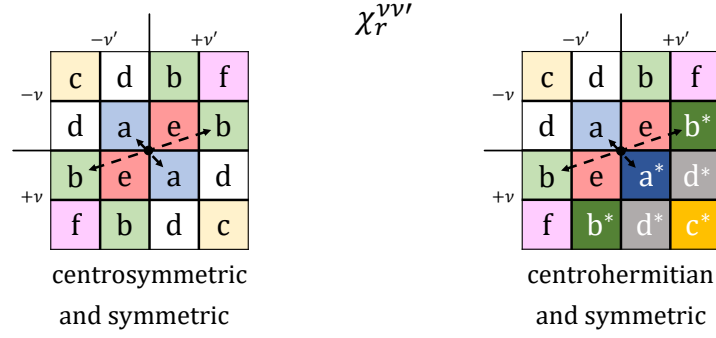
Figure 2.11: Schematic representation of the first matrix elements of $\chi_r^{\nu\nu'(\omega=0)}$, corresponding to the Matsubara frequencies $\nu^{(\prime)} = \pm\pi T, \pm 3\pi T$, for the half-filled (left) and the out-of-half-filled case (right). In the left panel, the matrix elements are symmetric with respect to the center of the matrix (centrosymmetric), in the right panel they are centrohermitian, i.e., symmetric under a complex conjugation. Additionally, for all cases the matrix is symmetric, which reduces the number of independent matrix elements, and ensures that in the right panel e and f are strictly real.

work, vertices and generalized susceptibilities are plotted with the diagonal running from the upper left to the lower right, i.e., a different convention as in topically related references such as [10, 33, 51]. This choice is made to underline the perspective of $\chi_r^{\nu\nu'(\omega=0)}$ as a matrix in fermionic Matsubara frequency space.

2.2.5 The Luttinger-Ward functional $\Phi[G]$

A central concept to quantum many-body field theory is the Luttinger-Ward functional (LWF) $\Phi[G]$, a universal functional of the full (sometimes also referred to as "bold", as opposed to the non-interacting or "bare") Green's function, which depends only on the interacting part of the underlying Hamiltonian [74], see also Ref. [31]. It is related to the thermodynamic grand potential $\Omega[G]$ in the following way [11, 75]:

$$\Omega[G] = \operatorname{Tr} \ln G - \operatorname{Tr}\left(G_0^{-1} - G^{-1}\right) G + \Phi[G] \,. \tag{2.63}$$

Based on the derivatives of the grand potential, static thermodynamic properties of the system under investigation can be calculated, while the LWF allows one to obtain dynamic quantities, such as the self-energy Σ and the Green's function G [11, 75]. The functional derivative of $\Phi[G]$ with respect to G yields [11, 75]

$$\beta \frac{\delta\Phi[G]}{\delta G} = \Sigma[G] \,, \tag{2.64}$$

which corresponds to the self-energy of the system if evaluated at the physical Green's function G, i.e., $\Sigma[G] = \Sigma$.

Based on the LWF, also the irreducible vertex $\Gamma_{\sigma\sigma'}^{\nu\nu'\omega}$ can be obtained by the functional derivative of Σ w.r.t. G [11, 12, 19, 55] . Note that in general, it is necessary to introduce symmetry breaking fields to perform such calculations, which prevents analytic treatments in most cases. For simple disordered models, however, which will be introduced and analyzed in Chapter 3, a simple expression can be given, which reads (see Eq. (11) of

Ref. [19]):

$$\Gamma_{\sigma\sigma'}^{\nu\nu'\omega=0} = \beta \frac{\delta\Sigma_\sigma(\nu)}{\delta G_{\sigma'}(\nu')} \tag{2.65}$$

While $\Phi[G]$ can in general not be obtained in closed form, it can be calculated by a diagrammatic perturbation expansion as the limit of an infinite series of skeleton diagrams [74], or in a nonperturbative manner by using a functional-integral approach, see Ref. [75].

The LWF plays an important role for fundamental quantum many-body theory, since e.g., approximations, which are based on an expression for the LWF, so-called "Φ"-derivable approximations, in which Σ and Γ are obtained as functional derivatives of a given approximation for $\Phi[G]$, are guaranteed to fulfill the conservation laws of the underlying microscopic theory [76]. Such approaches are referred to as "conserving" [51], where one of the best known examples is e.g., the self-consistent Hartee-Fock for Σ together with the random phase approximation (RPA) for the generalized susceptibility [11, 51]. Another example is the dynamical mean-field theory, see Sec. 2.3.1, where all local diagrams are included in the corresponding $\Phi[G]$ [51, 77]. In this respect, let us also note, that the functional derivatives of $\Phi[G]$ and the fulfillment of microscopic conservation laws are related to the validity of the so-called Ward identities, which are fulfilled in conserving theories, and broken if the approach is not conserving [51, 56].

2.3   Methods

After the introduction of the many-electron models most relevant for this thesis, providing the definitions for the two-particle correlation functions, and including a comprehensive discussion of their spectral properties, we now turn to a concise presentation of the methods used to treat these models and obtain the two-particle quantities of interest. In the first part we recall the basic idea underlying the well-known dynamical mean-field theory, specifying also the impurity solver employed throughout this thesis, before focusing on diagrammatic approaches that approximate the class of fully irreducible vertices: the parquet approximation and the functional renormalization group.

2.3.1   DMFT

The dynamical mean-field theory (DMFT) is one of the most important methods available to the field of strongly-correlated electron systems (for a detailed review see e.g., Ref. [41], for textbooks see e.g., Refs. [31, 49, 64] and for introductory articles summarizing key aspects of the DMFT see Refs. [78, 79]). This is due to the fact, that it allows for a nonperturbative treatment of correlated lattice systems. By using DMFT, intrinsically strong-coupling phenomena such as e.g., the Mott-Hubbard metal-insulator transition can be systematically described, see below.

The central approximation of the DMFT lies in neglecting the momentum dependence of the self-energy $\Sigma(\mathbf{k}, \nu) \rightarrow \Sigma(\nu)$. This approximation can be understood by considering
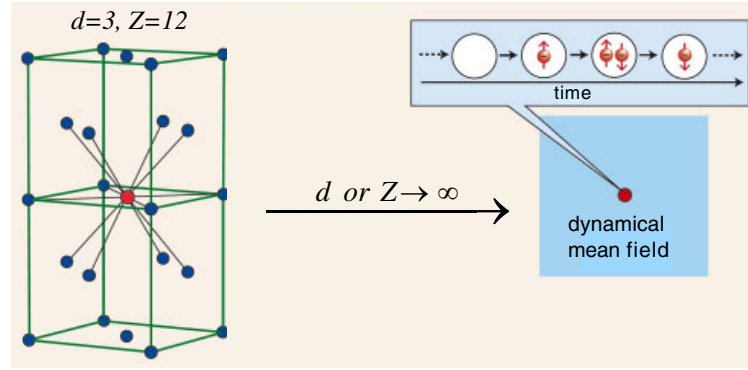
Figure 2.12: A schematic demonstration of the $d \to \infty$ limit (or equivalently of infinite coordination number), where a specific site of the lattice system (left) reduces to an interacting site in a dynamic mean-field (right). All temporal fluctuations of the interacting site are fully taken into account, as illustrated by the different occupations. Taken from Ref. [79] (see Fig. 4 therein).

the limit of infinite dimensions (or equivalently of infinite lattice coordination number), where it becomes exact. For $d \to \infty$, all nonlocal "bold" diagrammatic contributions to the self-energy collapse into local ones, yielding a crucial simplification, which allows for a numerical solution of the quantum many-body problem under investigation [80]. For pedagogical reasons, it is useful to consider a comparison to the classical Weiss mean-field theory of the Ising model [49]. There, as $d \to \infty$, the fluctuations of an individual neighboring spin become irrelevant. Instead a picture emerges of a spin, which interacts with an effective mean-field, originated by all the other neighboring spins. Analogously, in the solution of a quantum many-body problem on a lattice for $d \to \infty$, the effect of the rest of the system can be approximated by a time-dependent (dynamical) Weiss-field. As in the Weiss mean-field case, also for lattice models for $d \to \infty$ one needs to properly scale the different terms of the Hamiltonian in order to obtain a non-trivial limit [80]. Specifically, for the one-band Hubbard model introduced in Sec. 2.1.3, the hopping amplitude is scaled as $t \to \frac{t^*}{\sqrt{d}}$ [49, 80]. The interaction part of the Hamiltonian, instead, does not require any scaling, due to its purely *local* nature, $U \to U^*$ [49, 80]. The important difference of DMFT w.r.t. static/conventional mean-field theories, such as Hartree-Fock for lattice systems, lies in the *dynamic* nature of the Weiss field, as well as of the on-site correlations ($\Sigma(\nu)$), which ensures that *all* purely local temporal correlations are included. Fig. 2.12, taken from Ref. [79], visualizes this important difference schematically. The inclusion of these dynamical correlations allows for a non-trivial description of e.g., the decrease of the double occupancy ($\langle n_{i,\uparrow} n_{i,\downarrow} \rangle$) with U in the correlated case. In contrast to the DMFT description, a conventional (Hartree-Fock) mean-field theory, which would factorize the double occupancy, failing to describe its decrease as a function of U, see Ref. [49].

The DMFT equations, which are stated below, can be derived by mapping the lattice problem for $d \to \infty$ onto an auxiliary AIM [41, 81]. The idea behind this mapping can be understood in the following way: The DMFT method finds a suitably chosen auxiliary AIM (i.e., one fulfilling a self-consistency condition), which represents the local quantities of the lattice problem under consideration, embedded in the corresponding dynamical

Weiss-field [64]. Physically, one obtains in this way an embedded atom connected to a self-consistently determined bath, which is defined by the following local action [41, 49, 64] (or equivalently by the Hamiltonian defined in Sec. 2.1.1):

$$
\mathcal{S}_{\text{imp}} = -\int_0^\beta d\tau \int_0^\beta \sum_\sigma c_{d,\sigma}^*(\tau) \mathcal{G}_0^{-1}(\tau - \tau') c_{d,\sigma}(\tau') + U \int_0^\beta d\tau n_{d,\uparrow}(\tau) n_{d,\downarrow}(\tau) \tag{2.66}
$$

where the $c_{d,\sigma}^*(\tau)/c_{d,\sigma}^*(\tau)$ are now Grassman numbers, and the Fourier-transformed effective bare propagator reads $\mathcal{G}_0^{-1}(i\nu) = i\nu - \epsilon_d - \Delta(i\nu)$ (cf. Eq. (2.3)).

Based on the impurity action the impurity Green's function can be obtained in the path integral formalism as [49]:

$$
G_{\text{imp},\sigma}(i\nu) = -\frac{1}{Z} \int \prod_\sigma \mathcal{D}c_{d,\sigma}^* \mathcal{D}c_{d,\sigma} c_{d,\sigma}(i\nu) c_{d,\sigma}^*(i\nu) \exp(-\mathcal{S}_{\text{imp}}) \tag{2.67}
$$

with Z being the partition function, which in path integral formalism is given by [49]

$$
Z = \int \prod_\sigma \mathcal{D}c_{d,\sigma}^* \mathcal{D}c_{d,\sigma} \exp(-\mathcal{S}_{\text{imp}}) . \tag{2.68}
$$

Now, as the impurity Green's function of the AIM is used as a representation of the local Green's function of the lattice model, at self-consistency, one requires that the following expression holds [64]

$$
G_{\text{loc}}(i\nu) = \frac{1}{V} \sum_{\mathbf{k}} G(\mathbf{k}, i\nu) = G_{\text{imp}}[i\nu, \Delta] \tag{2.69}
$$

where V corresponds to the volume in the first Brillouin zone, and the $\mathbf{k}$-dependent Green's function of e.g., the one-band Hubbard model under consideration reads

$$
G(\mathbf{k}, i\nu) = \frac{1}{i\nu + \mu - \epsilon_{\mathbf{k}} - \Sigma(\mathbf{k}, i\nu)} . \tag{2.70}
$$

Using the central DMFT approximation of a $\mathbf{k}$-independent self-energy $\Sigma(\mathbf{k}, i\nu) = \Sigma_{\text{loc}}(i\nu)$ as well as that $\Sigma_{\text{loc}}(i\nu)$ is represented by the self-energy of the AIM: $\Sigma_{\text{loc}}(i\nu) = \Sigma_{\text{imp}}(i\nu) = \Sigma(i\nu)$, one can write down the following self-consistency equation based on Eq. (2.69) (see Eq. (11) of Chapter 3 of Ref. [64])

$$
G_{\text{imp}}[i\nu, \Delta] = \sum_{\mathbf{k}} \frac{1}{G_{\text{imp}}^{-1}[i\nu, \Delta] + \Delta(i\nu) - \epsilon_{\mathbf{k}}} . \tag{2.71}
$$

Here the Dyson equation $\Sigma(i\nu) = \mathcal{G}_0^{-1} - G_{\text{imp}}^{-1}$ and $\epsilon_d = -\mu$ was used.

In Fig. 2.13 we provide a sketch of the DMFT algorithm, which is iterated until the self-consistency condition is fulfilled. The bottleneck in this scheme is the calculation of the impurity Green's function based on $\mathcal{G}_0$, for which e.g., a continuous-time quantum Monte-Carlo (CT-QMC) algorithm can be used, as was done throughout this work. The details of the specific solver applied here can be found in Sec. 2.3.1.2.
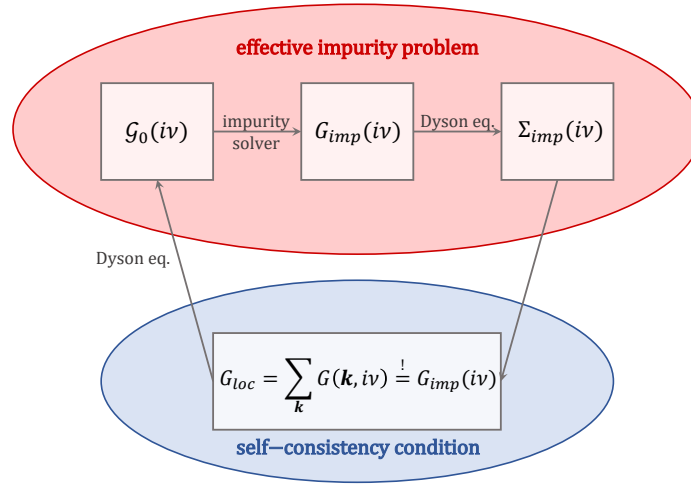
Figure 2.13: Schematic representation of the DMFT algorithm inspired by similar representations of Refs. [49, 54, 64]. At the start of the algorithm an initial guess for the impurity bath $\mathcal{G}_0$ is used. In the next step, an impurity Green's function is calculated by solving the impurity problem, see Eq. (2.67). Using $\Sigma_{\text{imp}} = \mathcal{G}_0^{-1} - G_{\text{imp}}^{-1}$ the local Green's function of the lattice problem under consideration $G_{\text{loc}} = \sum_{\mathbf{k}} G(\mathbf{k}, i\nu)$ is evaluated. From $G_{\text{loc}}^{-1} + \Sigma_{\text{imp}} = \mathcal{G}_{0,new}^{-1}$ a new effective bath is calculated until convergence of the scheme.

We conclude this subsection, by recalling that in finite dimensions, the DMFT assumption of considering a momentum independent self-energy is of course no longer exact, but nevertheless can be used as an approximation [49]. In this context, correlated effects in realistic materials can be treated by a combination of the density functional theory (DFT) with DMFT, frequently referred to as LDA+DMFT [49, 82, 83]. This consists of a merger of first-principles calculation of the correlated material, and a nonperturbative DMFT treatment of its local correlations.

2.3.1.1 Mott metal-insulator transition

As it should be clear from the discussion of the previous section, a crucial strength of DMFT is its capability to properly take local electronic correlation into account, even in cases where the interaction is strong and perturbative methods fail. In fact, this is clear already by considering other limiting cases where the DMFT becomes exact: the non-interacting case ($U = 0$, where Σ is trivially zero) *as well as* the atomic limit ($\Delta = 0$). Hence DMFT manages to describe the two limiting cases of isolated atoms as well as non-interacting electrons correctly [64].

This central property of DMFT is highly relevant when considering one of its most important successes: the description of a Mott metal-to-insulator (MIT) transition. This transition refers to a case where a paramagnetic metal becomes insulating, not because of a symmetry breaking (e.g., a long range magnetic order that is forming) but because of the interaction between electrons. In Fig. 2.14 we represent a sketch of the spectral function ($A(\omega) = -1/\pi \text{Im} G(\omega + i0^+)$) as obtained in DMFT across such a transition, taken from Ref. [78].
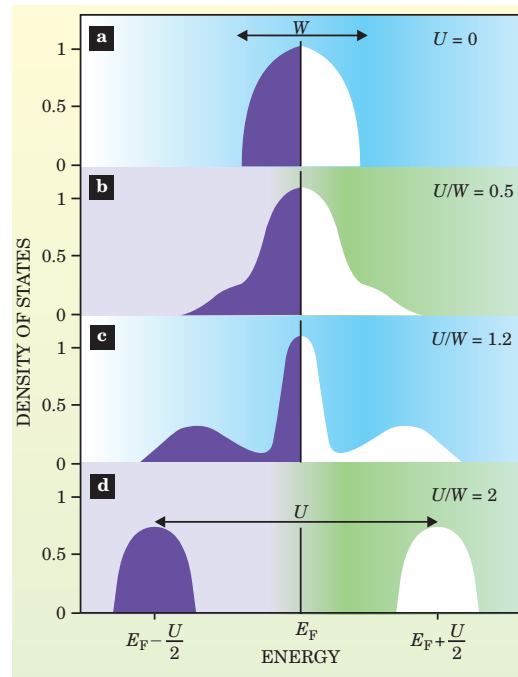
Figure 2.14: Evolution of the interacting density of states (the **k**-integrated spectral function) for the DMFT solution of a Hubbard model. As the interaction is increased, spectral weight from the quasiparticle peak at the Fermi-energy E_F is transferred to the lower and upper Hubbard bands, which leads to the characteristic three-peak structure (c) for strong interaction. For a large enough interaction value a Mott insulator is found (d). Taken from Ref. [78] (see Fig. 2 therein).

As can be seen in the top panel, for $U = 0$ a half-filled band metal is considered, where in this specific case the DOS is semi-circular. As the interaction is increased, the width of the central peak reduces, which describes the renormalization of the quasiparticle weight Z. For the strongly interacting case the so-called upper and lower Hubbard sub-band form (c), a crucial point that DMFT captures as opposed to e.g., DFT [64]. If the interaction compared to the bandwidth W is large enough (e.g., $U/W = 2$ in the specific case of Fig. 2.14) the quasiparticle peak around the Fermi-energy E_F vanishes (d). Physically, the kinetic energy gain of quasiparticle mobility (hopping) is here lower than the associated potential energy cost of creating doubly-occupied sites [49]. DMFT describes this transfer of spectral weight correctly, where the spectral weight of the quasiparticle peak $\sim Z$ is reduced as the MIT is approached, and instead the upper and lower Hubbard bands, which correspond to the atomic transitions described by the atomic limit, are formed [64].

In the DMFT description of a one-band Hubbard model the MIT is realized as a first-order transition with a critical endpoint at finite temperatures [41, 49, 64]. In Fig. 2.15 in the left panel a generic phase diagram representing this MIT is shown (taken from Ref. [64]). To the left of the hysteresis which is delimited by $U_{c1}(T)$ and $U_{c2}(T)$, a paramagnetic metal is found. For temperatures below the critical endpoint (red dot) this paramagnetic metal undergoes a transition into a paramagnetic insulator, the Mott phase, as the interaction is increased. For very low-temperatures an ordered phase is shown, which can be suppressed e.g., due to geometric frustration. In practical calculations however, the ordered phase is
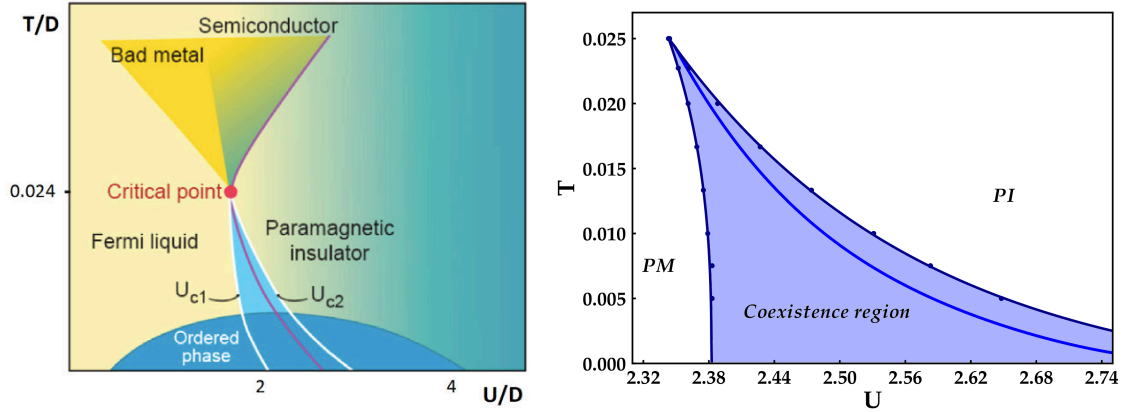
Figure 2.15: Left panel: Schematic representation of the MIT as obtained from DMFT for a Hubbard model, where a magnetically ordered phase is suppressed to low-temperatures. The first-order transition ends in a critical endpoint, for higher temperatures a crossover is found. The red line denotes the parameter sets where the minimum of the free energy is found, the blue region delimited by the white transition lines $U_{c1}(T)$ and $U_{c2}(T)$ represents the coexistence region. Taken from [64] (see Fig. 5 of Ch. 3). Right panel: Specific DMFT calculation for Hubbard model on a Bethe lattice (half-bandwidth $D = 1$) at half filling, where the coexistence region is shown in blue. The plot was provided by M. Pelz based on calculations performed throughout his Master thesis, see Ref. [84].

mostly disregarded by enforcing the symmetries of the paramagnetic phase. The hysteresis represents a coexistence region, where both, a metallic and an insulating phase can be found. This first order transition ends in a critical endpoint at T_c. For temperatures larger than T_c a crossover is found. In the right panel of Fig. 2.15 a specific calculation of the coexistence region of the Hubbard model on a Bethe lattice at half filling, performed by M. Pelz, is shown [84].

2.3.1.2 Quantum Monte Carlo

Throughout this thesis to obtain the one- and two-particle quantities a continuous-time quantum Monte-Carlo (CT-QMC) impurity solver is employed. Specifically, we use the solver provided by the open-access w2DYNAMICS package [85] in the 1.0.0 version. This is a CT-QMC algorithm in the hybridization expansion (CT-HYB), where we refer to the literature [86] for details on the method. In general we exploited the segment sampling method, which is suited for the density-density type interactions ($U n_\uparrow n_\downarrow$) of interest to this thesis, see Ref. [86] for details. In some specific parts (where mentioned explicitly) we also use worm sampling [87, 88] together with symmetric improved estimators [89], to significantly reduce the high-frequency noise for e.g., the self-energy.

2.3.2 Parquet approximation

The diagrammatic methodologies introduced in this and the following subsection will be used in several occasions throughout this thesis. Both are based on (*i*) a complete set of equations, which relates the one- and two-particle level, as well as (*ii*) an approximation for the fully 2PI vertex Λ. The goal of these approaches is always to obtain a self-consistent
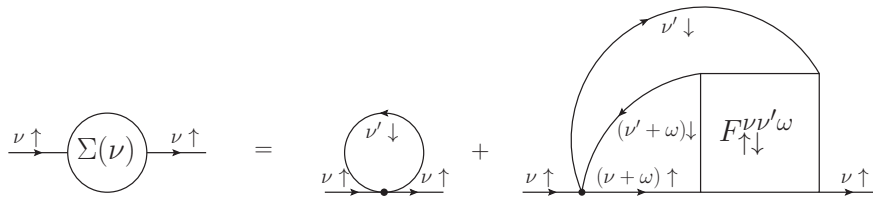
Figure 2.16: Diagrammatic representation of the Schwinger-Dyson equation (SDE), which relates the self-energy $\Sigma(v)$ to the full vertex $F_{\uparrow\downarrow}$. The first term on the right-hand side is the Hartree contribution. Taken from Ref. [33] (see Fig. 18 therein).

description of the relevant one- and two-particle quantities of the model of interest. In this section, we consider the parquet formalism (PA) [55], which is based on the parquet approach introduced in Sec. 2.2.1. By expressing the reducible vertices via the BSEs of Sec. 2.2.2 in terms of the full vertex F and the irreducible Γ_l's, one obtains a set of equations relating F and the 2PI vertices Γ_l and Λ to one another. At this point the Green's function and one of the vertex classes would be needed as an input to solve this set of equations [51]. The missing relations to obtain a closed set of equations, are those, which link the one- and the two-particle level: (*i*) the Dyson equation (Eq. (2.23)), which relates the propagators used in the BSEs, to the self-energy Σ and (*ii*) the so-called Schwinger-Dyson equation of motion (SDE), which relates the self-energy to the full vertex F. We recall, that the SDE is based on the Heisenberg equation of motion, obtained by deriving the interacting one-particle Green's function w.r.t. the imaginary time. In Matsubara frequency space, for local problems (such as the AIM or the DMFT solution of the HM), the SDE explicitly reads as follows [33, 54]:

$$\Sigma(v) = \frac{Un}{2} - \frac{U}{\beta^2} \sum_{v'\omega} G(v + \omega)G(v' + \omega)G(v')F_{\uparrow\downarrow}^{vv'\omega} , \qquad (2.72)$$

where n is the density of the system $n = \langle n \rangle = \langle n_\uparrow + n_\downarrow \rangle$. A diagrammatic representation of this equation is shown in Fig. 2.16. Let us note here, that more details of the SDE will be discussed in Chapter 6, when analyzing explicitly how the high-frequency asymptotic of $\Sigma(v)$ is linked to the symmetry of the full vertex $F_{\uparrow\downarrow}$.

Having obtained a complete set of self-consistent equations for the system under investigation, this can be solved starting from an input for one of the vertex classes. In the parquet based schemes, the natural choice is to perform the approximation on the "deepest" level of the corresponding diagrammatics, i.e., for the fully 2PI vertex Λ [33, 51]. The flow chart for this approach is shown schematically in Fig. 2.17, taken from Ref. [51].

In the PA, one approximates the fully 2PI vertex with its first order perturbative contribution, which is the bare interaction, $\Lambda = U$ [33, 55]. This ensures that the scheme is exact up to forth order in perturbation theory, since the next-to-leading contribution to Λ at small U is the "envelope"-diagram, shown in Fig. 2.9, which includes four bare interactions.

While we explicitly consider the local problem, note that this set of equations can be analogously formulated for the nonlocal case, see Ref. [51], in order to study, e.g., the
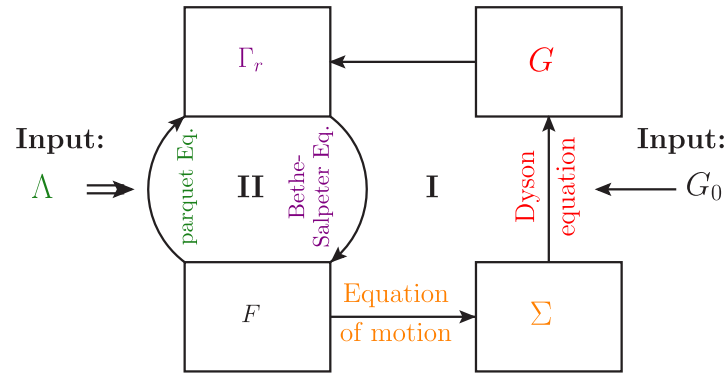
Figure 2.17: The left part of the flow diagram (II) concerns the set of equations, which connect the full vertex F to the irreducible ones: Γ_r and Λ. Starting from an input for Λ, this system of equations can be solved for a given propagator G. The complete set of equations, providing a self-consistent solution on the one- and the two-particle level, is shown in the right part of the diagram (I). From the full vertex F, using the SDE (i.e., the equation of motion), one obtains the self-energy Σ, and via the Dyson equation a new propagator G (where G_0 defines the system under investigation). Taken from Ref. [51] (see Fig. 6 therein).

Hubbard model in finite dimensions, and hence used to obtain a diagrammatic approximation including nonlocal correlations. See e.g., Refs. [90–92] for an application of this scheme, or Ref. [93] for a more recent formulation, where the parquet approach is combined with several numerical techniques to improve the computational performance, the so-called truncated unity parquet solver (TUPS). For a comparison of the TUPS version of the parquet approach using the parquet approximation, to other methods such as DMFT, numerically exact methods such as determinant quantum Monte-Carlo or diagrammatic Monte-Carlo and many others we refer to Refs. [52] and [94]. Moreover, it is important to emphasize here that one can also use the parquet approach beyond the simplest case of the PA, by including a different set of diagrams in the fully 2PI vertex Λ as a starting point of the method. One examples is the fully irreducible vertex of a converged DMFT solution, Λ_{DMFT}, a choice which defines the so-called DΓA approach [51, 95], discussed further in Chapter 6. As a last point, note that if the exact fully 2PI vertex Λ would be available, by using the parquet approach, all other quantities of interest could be obtained from it in an exact manner.

For the implementation of the iterative method to solve the set of PA-equations numerically, we refer to Ref. [96].

2.3.3 Multiloop fRG

*Parts of this chapter, marked by a vertical bar, have already been published in the APS journal Phys. Rev. Research **4**, 023050 (2022).*

The functional renormalization group (fRG) provides a versatile framework to study the scale-dependent behavior of a wide range of many-body problems (also outside of condensed matter physics, see [97] for a recent review) in an unbiased (i.e., not channel-

specific) way. For comprehensive reviews targeted at problems that are of interest to this thesis we refer to Refs. [98] and [99], a brief summary can be found in Chapter 11 of Ref. [64] or also in the Appendix D of Ref. [52]. Central to the fRG method is the introduction of a scale-dependent non-interacting propagator G_0^Λ, which enters the quadratic part of the action, see e.g., Eq. (2.66). Based on this $\mathcal{S}^\Lambda$ an effective action $\mathcal{S}_{\text{eff}}^\Lambda$ can be defined which acts as the generating functional for one-particle irreducible vertices, e.g., the self-energy Σ or the full vertex F. The fRG flow then refers to an exact functional flow equation for $\mathcal{S}_{\text{eff}}^\Lambda$, which can be expanded in terms of fields, yielding an infinite hierarchy of coupled differential (i.e., flow) equations [64], the so-called Wetterich equation [98, 100]. In this hierarchy, the flow equation for the one-particle irreducible (1PI) n-particle vertex, depends on the 1PI (n+1) vertex. In most practical applications, this system of coupled differential equations is truncated at the two-particle level, hence describing how the self-energy Σ and the full vertex F evolve as the scale Λ is changed from its initial value Λ_i to its final one Λ_f. The way this scale dependence is introduced is referred to as "cut-off", where in this work the following two cut-offs are considered:

$$G_0^\Lambda = \frac{\nu^2}{\nu^2 + \Lambda^2} G_0 \quad \text{with } \Lambda_i = \infty, \ \Lambda_f = 0 \ , \tag{2.73}$$

where G_0 is the non-interacting Green's function of the system. Since this cut-off is depending on the frequency ν it is called "frequency" cut-off, or also Ω flow. The second cutoff acts similarly as switching on an interaction, hence termed U cut-off or U flow.

$$G_0^\Lambda = \Lambda G_0 \quad \text{with } \Lambda_i = 0, \ \Lambda_f = 1 \ . \tag{2.74}$$

The fRG flow equation of Σ^Λ is determined by the full vertex F^Λ contracted with the so-called single-scale propagator $S^\Lambda = -G^\Lambda(\partial_\Lambda G_0^{\Lambda^{-1}})G^\Lambda$, which is related to the differentiated propagator $\dot{G} \equiv \partial_\Lambda G^\Lambda$ by $\dot{G} = S^\Lambda + G^\Lambda \dot{\Sigma}^\Lambda G^\Lambda$ [98]. For simplicity, we omit the superscript Λ in the following. The flow equation for F further involves the three-particle vertex $F^{(6)}$ [98]. If $F^{(6)}$ was known at all scales, the flow of Σ and F would be exact. This would imply, in particular, that every specific Λ dependence or cutoff choice, as in Eqs. (2.73) or (2.74), would yield the same result at the end of the flow. In practice, however, $F^{(6)}$ can hardly be treated numerically and its effect on the flow of Σ and F can only be accounted for approximately. As a consequence, the results of such truncated fRG flows will generically depend on the choice of the cutoff.

The most widely used fRG implementations neglect $F^{(6)}$ entirely, yielding approximate 1ℓ flow equations for Σ and F [98]. The contributions of $F^{(6)}$ that amount to self-energy derivatives can be added to the vertex flow by substituting $S \to \dot{G}$. This "Katanin substitution" [101] is labelled by $1\ell_K$ throughout. A further refinement, which effectively incorporates the three-particle vertex to third order in the renormalized interaction, is obtained by the two-loop (2ℓ) vertex corrections [101, 102].

Subsequently, the multiloop fRG extension (mfRG) [103–105] was introduced to incorporate all those contributions of $F^{(6)}$ to the flow of Σ and F ensuring that their right-hand
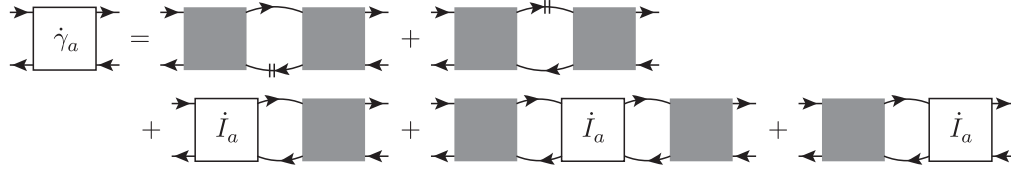
Figure 2.18: Diagrammatic representation of the multiloop flow equation for the reducible vertex in the ph channel $\dot{\Phi}_{\mathrm{ph}}$ ($\dot{\gamma}_a$ in the figure). In the first line the 1ℓ contributions are shown, where the single-scale propagator S is represented by the doubly-slashed propagator line. In the second line the first and last term represent Eq. (2.77a), while Eq. (2.77b) is shown in the center ($\dot{I}_a$ corresponds to $\dot{\Phi}_{\overline{\mathrm{ph}}}$ the notation of this thesis). The grey boxes represent the full vertex F. Taken from Ref. [105] (see Fig. 2a therein).

sides are *total* scale derivatives—which is not the case for the 1ℓ flow—thus guaranteeing by construction that the final results are independent of the choice of cutoff. In fact, the corresponding higher-loop terms of the mfRG represent the *minimal* additions to the conventional 1ℓ flow required to obtain cutoff-independent results. They also provide the *maximal* amount of diagrammatic contributions that can be added in a numerically feasible manner. Indeed, due to the iterative structure based on successive 1ℓ computations, these higher-loop contributions can be computed very efficiently [106].

The mfRG was shown to formally reproduce the diagrammatic resummation of the PA [104, 105] with the fully 2PI vertex $\Lambda = U$. An analogous approximation is performed in truncated fRG flows: Neglecting $F^{(6)}$, the vertex flow equation is of the form $\dot{F} = \sum_l \dot{\Phi}_l$ (note that l, which refers to the diagrammatic channels ph,pp,$\overline{\mathrm{ph}}$, needs to be distinguished from ℓ, which is the loop order). Thus, only the reducible parts are renormalized, while the fully irreducible part does not flow and remains at its initial value $\Lambda = U$.

In the following, the flow equations for the self-energy and the two-particle vertex are summarized, using a compact notation introduced in Ref. [105] (see Appendix A therein): A regular dot $\cdot$ refers to a sum over one internal frequency with a one-particle quantity, the $\circ$ refers to a matrix multiplication between two two-particle quantities.

One-loop flow The 'standard' fRG self-energy flow [98] reads

$$\dot{\Sigma}_{\mathrm{std}} = F \cdot S \ . \tag{2.75}$$

The first line of Fig. 2.18 shows an exemplary depiction of the 1ℓ flow of the reducible vertices, given by

$$\dot{\Phi}_l^{(1)} = F \circ \dot{\Pi}_{l,S} \circ F, \tag{2.76}$$

and $\dot{F} = \sum_l \dot{\Phi}_l$. $\dot{\Pi}_{l,S}$ corresponds to the differentiated two-particle propagator in channel l, with S used instead of $\dot{G}$.

The $1\ell_K$ flow with the Katanin substitution is obtained by replacing $S \to \dot{G}$, i.e., $\dot{\Pi}_{l,S} \to$

$\dot{\Pi}_l$, in Eq. (2.76). Since it includes self-energy (and not vertex) corrections from $F^{(6)}$, the results of the $1\ell_K$ flow are plotted between those for $\ell = 1$ and $\ell = 2$ in Chapter 6.

Multiloop flow   The multiloop flow further includes the contributions from $F^{(6)}$ which are generated by vertex corrections. These can be ordered by loops, leading to the expansion $\dot{\Phi}_l = \sum_{\ell \geq 1} \dot{\Phi}_l^{(\ell)}$ [103, 104]. Here, $\dot{\Phi}^{(1)}$ already includes the Katanin substitution to account for the self-energy corrections as above. The higher-loop terms, $\ell > 1$, are determined by

$$\dot{\Phi}_l^{(\ell)} = \dot{\Phi}_{\bar{l}}^{(\ell-1)} \circ \Pi_l \circ F + F \circ \Pi_l \circ \dot{\Phi}_{\bar{l}}^{(\ell-1)} \quad (\ell \geq 2) \tag{2.77a}$$

$$+ F \circ \Pi_l \circ \dot{\Phi}_{\bar{l}}^{(\ell-2)} \circ \Pi_l \circ F \qquad (\ell \geq 3), \tag{2.77b}$$

where $\Phi_{\bar{l}} = \sum_{l' \neq l} \Phi_{l'}$. Equation (2.77a) with $\ell = 2$ corresponds to the 2ℓ flow, while the so-called center part $\dot{\Phi}_{l,C}^{(\ell)} = F \circ \Pi_l \circ \dot{\Phi}_{\bar{l}}^{(\ell-2)} \circ \Pi_l \circ F$ of Eq. (2.77b) contributes only for $\ell \geq 3$. Both lines of the multiloop contributions to $\dot{\Phi}_l$ are shown in the second line of Fig. 2.18.

In order to fully generate all parquet diagrams, the self-energy flow also acquires a multiloop correction [104], where $\overline{ph}$ is for practical reasons renamed to xph in the following expression

$$\dot{\Sigma} = \dot{\Sigma}_{\text{std}} + (1 + F \circ \Pi_{\text{xph}}) \circ \dot{\Phi}_{\text{x}\bar{\text{ph}},C} \cdot G, \tag{2.78}$$

where $\dot{\Phi}_{\text{x}\bar{\text{ph}},C} = \sum_{\ell \geq 3} \dot{\Phi}_{\text{x}\bar{\text{ph}},C}^{(\ell)}$.

The above-mentioned procedure outlines the "traditional" way of viewing the mfRG equations as corrections to the fRG flow equations, which restore the total derivative by taking the effect of $F^{(6)}$ in the flow equations of Σ and F fully into account. Let us also highlight here the work by F. Kugler and J. von Delft [105], which offers a different perspective on the mfRG equations, in many ways closer to the concepts already presented in this thesis: As a starting point the parquet equation is used, see Sec. 2.2.1, which holds for any propagator. The idea of the authors was hence to replace $G \rightarrow G^{\Lambda}$ and derive the flow equations for the two-particle vertex, given above. Similarly, the SDE introduced in Sec. 2.3.2, was used to derive the flow equation for the self-energy together with the multiloop corrections mentioned above. In this way it becomes evident that solving the mfRG equations is equivalent to calculating the PA solution.

Equations (2.77a),(2.77b) and (2.78) define the mfRG procedure, which will be used in Chapter 6 of this thesis. The numerical solution of this system of differential equations, often referred to "flowing", is done by a Runge-Kutta solver, implemented in a C++ framework designed by N. Wentzell. Details on the implementation can be found in Refs. [94, 96, 106]. Let us note here that, similarly as in the PA case, the mfRG framework can also be used with a different irreducible vertex as a staring point, as it will be discussed explicitly in Chapter 6.

Aspects of the breakdown of perturbation theory

Turn and face the strange

– David Bowie

In this chapter, the central topic of this thesis is formally introduced: the divergences of the irreducible vertex functions. As an unmistakable hallmark of nonperturbative physics, they are found in many fundamental models of correlated electron systems already at intermediate coupling. Here we present an overview of their appearance, with a focus on the Anderson impurity model as well as the Hubbard model. The irreducible vertex divergences are also intrinsically connected to the multivaluedness of the Luttinger-Ward functional, which is reviewed in the second part of this chapter. In the last part, we eventually discuss the connection between these nonperturbative manifestations of the breakdown of self-consistent perturbation expansions.

Several of the most interesting phenomena observed in strongly correlated electron systems are beyond the description of perturbation theory. One example is the Mott metal-to-insulator transition (MIT), which was discussed in the previous Sec. 2.3.1.1. The central problem for condensed matter systems is that as soon as the interaction becomes sizable, e.g., due to insufficient electronic screening, there is no longer a clear expansion parameter, on the basis of which a perturbation theory could be safely formulated. In this chapter, we focus on a particular aspect of the way how the nonperturbative nature of electronic correlation becomes apparent in the quantum field-theoretical description of many-electron systems: the divergences of the irreducible vertices.

In the first part, we define the divergences of the two-particle irreducible (2PI) vertex functions and distinguish them from divergences of the full vertex F. We then provide an overview of their appearance in different many-electron models, with the main focus on the Hubbard model (HM) and the Anderson impurity model (AIM) (both defined in Sec. 2.1).

This manifestation of nonperturbative physics affects also a different quantity, central to the description of many-body problems: the Luttinger-Ward functional $\Phi[G]$ (LWF)
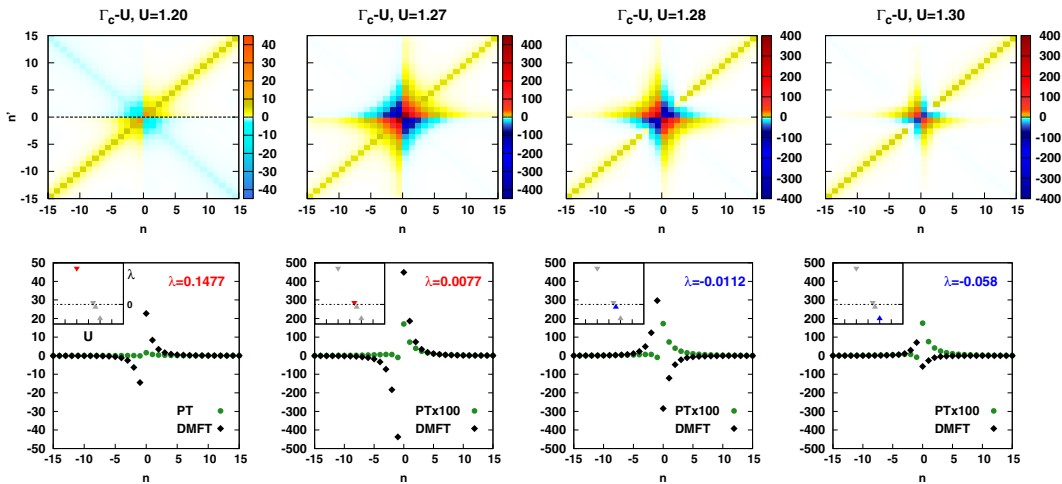
Figure 3.1: DMFT calculations for the Hubbard model on a square lattice for $T = 0.4t$, taken from Ref. [10] (see Fig. 1 therein). In the first row, plots of the static local irreducible vertex in the charge channel as a function of ν and ν' are shown, which diverges as U is increased from $U = 1.27$ (second column) to $U = 1.28$ (third column), where U is measured in units of $4t$. The second row panels demonstrate a comparison between the results obtained by second-order perturbation theory (green circles) and the DMFT results (black diamonds) for a cut along $\nu' = \pi T$ (n refers to the Matsubara index). As can be readily seen, not only the magnitude, but also the sign-structure is missed by perturbation theory (PT). The insets show the value of the corresponding singular eigenvalue of $\chi_c^{\nu\nu'(\omega=0)}$, see Eq. (3.1) and the corresponding discussion.

(see Sec. 2.2.5), which happens to be multivalued. In the second part of this chapter, we summarize some important aspects of the multivaluedness of $\Phi[G]$, which can lead to unphysical solutions for $\Sigma[G]$ at crossings of different branches of $\Phi[G]$, and discuss several instances where this problem appears.

Finally, in the last part of this chapter, we discuss the close connection between these two problems. As it turns out, they are in fact two sides of the same coin: the breakdown of self-consistent perturbation theory.

3.1   The divergences of the irreducible vertex functions

In the previous Sec. 2.2, the different classes of two-particle vertex functions were introduced. It is important to clarify that all of these vertex classes can in principle diverge for different reasons. An important example is the full one-particle irreducible vertex F, which is directly related to the generalized susceptibility (see Eq. (2.19)), and diverges at physical phase transitions, see for example Refs. [6, 33, 41, 57, 98]. However, here, we are interested in divergences exclusively affecting the irreducible vertex functions Γ_r, which are irreducible in channels $r = c, m, \mathrm{pp} \uparrow\downarrow$[1] as well as of the fully 2PI vertex Λ.

These divergences were first described in a work by T. Schäfer *et al.* [10] for the Hubbard model on a square lattice solved by DMFT at half filling, whose central result is shown in

---

[1]The $\uparrow\uparrow$ component in the pp sector is not considered, since no divergences of this quantity for $\omega = 0$ have been reported in the literature [19, 23].

Fig. 3.1. Already at intermediate interaction values (note that U is measured in units of $4t = 1$ in the referenced work), well below U_c of the corresponding MIT, a divergence of the irreducible vertex in the charge channel for the static case, $\Gamma_c^{\nu\nu'(\omega=0)}$, is observed (first row panels[2]). As it can be seen in Fig. 3.1, the behavior of Γ_c completely contradicts the predictions by second-order perturbation theory, shown in the second row of Fig. 3.1. Not only the order of magnitude is wrong, as one could have expected, but the sign-flip of the entire low-frequency structure in $\Gamma_c^{\nu\nu'}$ is missed by perturbation theory. The insets in the second row panels of Fig. 3.1 report an eigenvalue of the static generalized susceptibility in the charge channel $\chi_c^{\nu\nu'(\omega=0)} = \chi_c^{\nu\nu'}$, which crosses zero at the divergence of Γ_c. This connection can be understood by inserting the spectral decomposition for the half-filled case of $\chi_r^{\nu\nu'}$ (see Eq. (2.33)) into the inverted Bethe-Salpeter equation for the irreducible vertex in the charge or magnetic channel $r = c, m$ (see Eq. (2.24)):

$$\Gamma_{r=c,m}^{\nu\nu'(\omega=0)} = \left(\sum_i V_i^r(\nu) \left[\lambda_i^r\right]^{-1} V_i^r(\nu') - \left[\chi_0^{-1}\right]^{\nu\nu'} \right). \tag{3.1}$$

The same equation can also be written in matrix-product form for the pp$\uparrow\downarrow$ channel, in which case however the spectral decomposition for $\chi_{pp,\uparrow\downarrow}^{\nu(-\nu')} - \chi_{pp,0}^{\nu\nu'}$ needs to be considered [19, 22], see Eq. (2.26).

Eq. (3.1) represents indeed a crucial relation for the further discussion of this thesis: By increasing the interaction, the eigenvalues of $\chi_c^{\nu\nu'}$ (which are all positive at $U = 0$) get gradually suppressed, and some of them can even cross zero and become negative [12]. For repulsive U the same consideration applies to the pp$\uparrow\downarrow$ channel, for attractive U, this applies to the magnetic channel [26]. Evidently, each time an eigenvalue λ_i^r crosses zero, the irreducible vertex function diverges [10, 12, 13, 17–19, 21–23, 25, 26]. In practice, searching for singular eigenvalues of $\chi_r^{\nu\nu'}$ is also the way how the divergences of Γ_r are traced throughout the phase diagram of the model under investigation, see Refs. [19, 22, 29, 107] for further details on this topic. Let us at this point make a couple of important remarks concerning Eq. (3.1):

(i) Eq. 3.1 can also be written for $\omega \neq 0$, see e.g., Ref. [19] or Ref. [23]. However, in this thesis only the irreducible vertex divergences at $\omega = 0$ are considered since this is also the case analyzed most frequently in the literature [10, 12, 17–19, 21, 22, 25, 26]. The interested reader can find an analysis of the appearance of divergences of Γ_r also for the case $\omega \neq 0$ in Ref. [23].

(ii) Eq. 3.1 holds for *half filling*. Using Eq. 2.59, a similar expression can be formulated for a (diagonalizable) case out of half filling, however, not always the same conclusions can be drawn, which will be further discussed in Sec. 3.1.4.

(iii) As a last point, we note that a divergence of the irreducible vertices is indeed produced by singular eigenvalues of $\chi_r^{\nu\nu'}$, since the second contribution, $[\chi_0^{-1}]^{\nu\nu'}$ ($[\chi_{pp,0}^{-1}]^{\nu\nu'}$ in case of $r = pp \uparrow\downarrow$), is merely the nonsingular inverse of the bubble-term.

Turning back to Eq. (3.1), one must note that, close to a vertex divergence, the eigenvalue determining the divergence, e.g., $\lambda_{i=\alpha}$ is vanishingly small, and hence its inverse is clearly

---

[2]In the conventions of this thesis $\beta^2 \Gamma_c^{\nu\nu'(\omega=0)}$ is shown in Fig. 3.1, cf. Ref. [10] and Ref. [19].
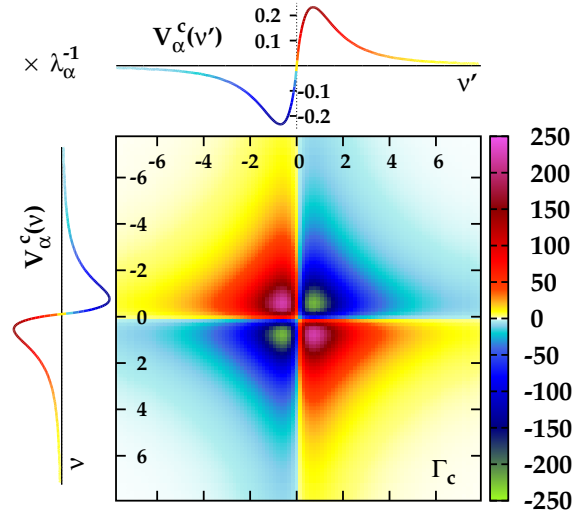
Figure 3.2: Demonstration of influence of the singular eigenvector $V_\alpha^c(\nu)$ onto the frequency structure of $\Gamma_c^{\nu\nu'}$ close to the singularity of λ_α. The parameters of the calculation for the AIM, defined in Sec. 2.1.1, are: $U = 3.321444$ and $\beta = 40$, which yields $\lambda_\alpha^c \simeq 0.00025$. The colors of the singular eigenvectors reported on the upper and left side of the main plot are not related to the colorbar, but merely serves as a guide to the eye. This figure is reproduced in the unit conventions of this thesis from Ref. [22].

larger than all other eigenvalues for $i \neq \alpha$[3]. This allows one to rewrite Eq. (3.1) in the following way [22]:

$$\Gamma_r^{\nu\nu'} \approx V_\alpha^r(\nu)\left[\lambda_\alpha^r\right]^{-1} V_\alpha^r(\nu') \ . \tag{3.2}$$

This relation clearly illustrates how, close to a vertex divergence, the magnitude of the irreducible vertex $\Gamma_r^{\nu\nu'}$ is mostly determined by $\left[\lambda_\alpha^r\right]^{-1}$ and its frequency structure by the corresponding eigenvector $V_\alpha^r(\nu)$. In Fig. 3.2 this connection is showcased for a specific calculation for the AIM very close to the zero-crossing of one $\lambda_{i=\alpha}^{r=c}$ [22]. It can be readily seen how the frequency structure of $\Gamma_c^{\nu\nu'}$ is completely controlled by the corresponding singular eigenvector plotted on top and to the left of Γ_c. Fig. 3.3 extends the analysis presented in Fig. 3.2 by comparing the full $\Gamma_c^{\nu\nu'}$ (left panel) and the tensor product $\lambda_\alpha^{-1}V_\alpha(\nu) \otimes V_\alpha(\nu')$ (center), where the corresponding difference is shown in the rightmost panel. The frequency structure of this remaining part shows two main features. On the one hand, a diagonal structure can be identified, which is originated by reducible vertices of other channels, see further Ref. [33]. On the other hand, highly fluctuating features are observed in the difference of $\Gamma_c^{\nu\nu'} - \lambda_\alpha^{-1}V_\alpha(\nu) \otimes V_\alpha(\nu')$, which can be attributed to noise of the QMC method that can become sizable for inversions of the BSE.

From this comparison, it becomes obvious that, close to a vertex divergence, also the symmetry properties of the eigenvectors corresponding to the singular eigenvalues will be directly reflected in the frequency structure of the divergences of $\Gamma_r^{\nu\nu'}$, which also allows

---

[3]This holds in the non-degenerate case, which is observed most frequently in cases discussed here, there are however situations where this is no longer true, see Sec. 3.1.3.
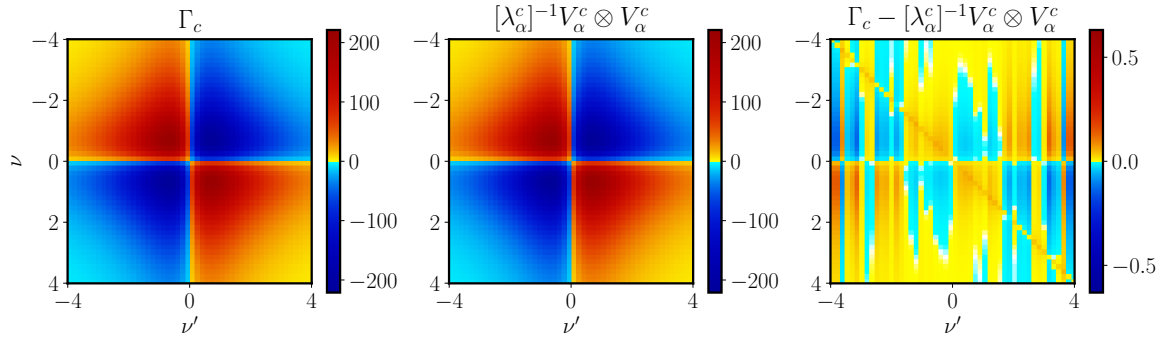
Figure 3.3: For the same parameter set used for the calculation shown in Fig. 3.2 a direct comparison of $\Gamma_c^{\nu\nu'}$ (left) and $[\lambda_a]^{-1}V_\alpha(\nu)\otimes V_\alpha(\nu')$ (center) is shown, whose difference is plotted in the right panel (note the difference in the colorbars on the right side of the corresponding plots).

for a categorization of the divergences, discussed further below.

Irreducible vertex divergences and the full vertex F After defining the divergences of the irreducible vertex functions let us point out a crucial aspect before discussing their appearance. As discussed above, the divergence of the irreducible vertex functions $\Gamma_r^{\nu\nu'}$ is caused by singular eigenvalues of the generalized susceptibility $\chi_r^{\nu\nu'\omega}$, i.e., by the inversion of the corresponding BSE (cf. Sec. 2.2.2) which contains singular contributions. The full vertex F, on the other hand, remains finite in such a case. How this happens can be analytically understood by reformulating Eq. (2.19) for the static local full vertex $F_r^{\nu\nu'}$ in channels[4] $r = c, m$ as follows:

$$
\begin{aligned}
F_r^{\nu\nu'} &= \left[\chi_0^{-1}\right]^{\nu\nu'} - \frac{1}{\beta^2}\sum_{\nu_1\nu_2}\left[\chi_0^{-1}\right]^{\nu\nu_1}\chi_r^{\nu_1\nu_2}\left[\chi_0^{-1}\right]^{\nu_2\nu'} \\
&= \frac{1}{\beta^2}\sum_{\nu_1\nu_2}\left[\underbrace{\left[\chi_r^{-1}\right]^{\nu\nu_1} - \left[\chi_0^{-1}\right]^{\nu\nu_1}}_{\text{Eq. (2.24)}}\right]\chi_r^{\nu_1\nu_2}\left[\chi_0^{-1}\right]^{\nu_2\nu'} \\
&= \frac{1}{\beta^2}\sum_{\nu_1\nu_2}\Gamma_r^{\nu\nu_1}\chi_r^{\nu_1\nu_2}\left[\chi_0^{-1}\right]^{\nu_2\nu'} .
\end{aligned}
\tag{3.3}
$$

From the first line, it becomes clear that the singular eigenvalues $\lambda_i^r \to 0$ of $\chi_r^{\nu\nu'}$ have a vanishing contribution to F, since $\chi_r^{\nu\nu'}$ enters directly instead of being inverted. The reformulation in the second and third line illustrates how the divergence of $\Gamma_r^{\nu\nu'}$, originated by $[\chi_r^{-1}]^{\nu\nu'}$, is compensated for by the matrix multiplication with $\chi_r^{\nu\nu'}$.

This fact is (presumably) also the reason why the divergences of the irreducible vertex functions were first fully described only in 2013[5] in Ref. [10].

---

[4]Note that the same argument can be made for the pp ↑↓ channel.

[5]In fact, the irreducible vertex divergences were observed for the first time 2011 in calculations performed in the group of M. Jarrell, see the first ArXiv version in Ref. [108]. This result was however discarded in the published version of this article [109]
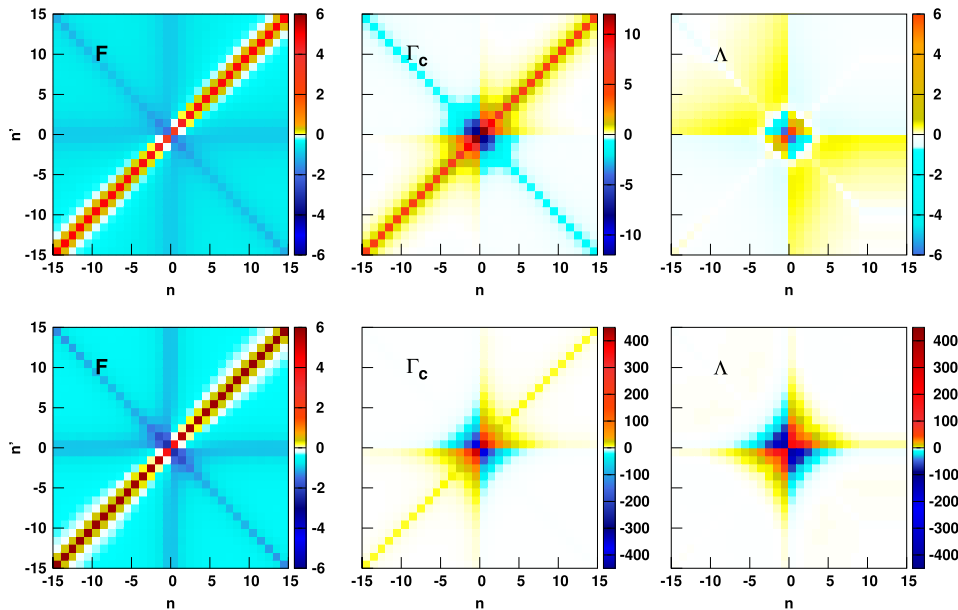
Figure 3.4: Results for the same model and parameters as in Fig. 3.1 for the local full vertex in the charge channel $F_c^{\nu\nu'}$ (left), the irreducible vertex in the charge channel $\Gamma_c^{\nu\nu'}$ (center) as well as the fully 2PI vertex $\Lambda_c^{\nu\nu'}$ as a function of $\nu^{(\prime)} = (2n^{(\prime)} + 1)\pi/\beta$. The bare interaction value is subtracted from the irreducible vertices. In the upper row the interaction value shown in the leftmost panel of Fig. 3.1, $U = 1.2$ (in units of $4t$), is used, where no divergence is close. In the bottom row the calculation for $U = 1.27$ is shown, where a divergence in both $\Gamma_c^{\nu\nu'}$ and $\Lambda_c^{\nu\nu'}$ is found, but not in the full vertex. Taken from Ref. [51].

The absence of divergences in F can also be analyzed from the perspective of the parquet equation [10, 18, 19, 51], introduced in Sec. 2.2.1. One possibility is to explicitly express the fully irreducible vertex Λ in terms reducible Φ_l and irreducible Γ_l vertices. In this case, the divergences of Γ_l are reflected in divergences of the fully 2PI vertex Λ and the corresponding reducible ones $\Phi_l = F - \Gamma_l$, rendering the full vertex F finite[6], as is explicitly shown in Chapter 3 of Ref. [110]. In Fig. 3.4, we showcase this aspect by hands of a calculation for the Hubbard model for the same parameter sets already used in Fig. 3.1, taken from Ref. [51]. From the comparison of the upper row (regular parameter set, $U = 1.2$ in Fig. 3.1) to the bottom row (diverging parameter set, $U = 1.27$ in Fig. 3.1) it is evident how the full vertex remains finite, while the irreducible vertices demonstrate a divergence.

Let us stress an important aspect at this stage: While the full vertex F remains finite *at the divergence of the local irreducible vertex*, the effects of electronic correlation that induce the appearance of singular eigenvalues are also affecting the full vertex F. In particular, while the divergence itself is compensated for, the suppression of the eigenvalues has a clear effect on F, which can be better noticed by reformulating Eq. (2.19) in the following way:

---

[6]We note that, alternatively, the reducible vertices in Eq. (2.20) can also be rewritten using $\Phi_l = F - \Gamma_l$, yielding an expression containing only full vertices F (for different spin combinations and frequencies) and irreducible ones, Λ and Γ_l. In this case a perfect compensation of divergences is observed, leaving the full vertex F finite. The explicit calculation is however not shown here.
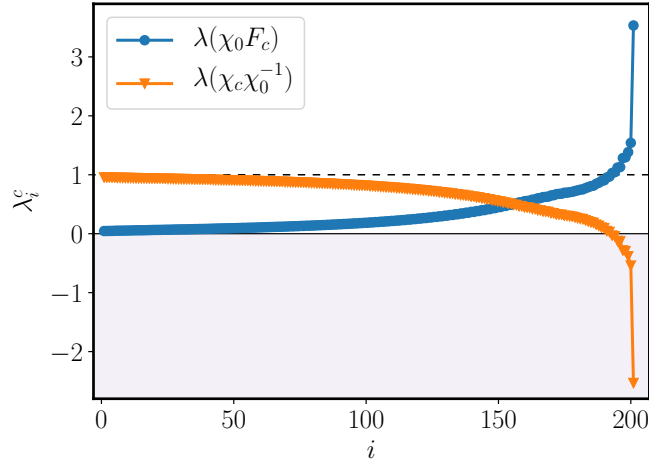
Figure 3.5: Full eigenvalue spectrum of $\chi_c \chi_0^{-1}$ (orange triangles) and $\chi_0 F_c$ (blue circles) for the AIM at $U = 5.75$ and $\beta = 60$. The negative eigenvalues of $\chi_c \chi_0^{-1}$ are compensated for by eigenvalues larger than 1 of $\chi_0 F_c$, see Eq. (3.4).

$$\frac{1}{\beta} \sum_{\nu_1} \chi_r^{\nu\nu_1} \left[\chi_0^{-1}\right]^{\nu_1\nu'} + \frac{1}{\beta} \sum_{\nu_1} \chi_0^{\nu\nu_1} F_r^{\nu_1\nu'} = \mathbb{1}^{\nu\nu'} \,. \tag{3.4}$$

From Eq. (3.4) it becomes clear that the eigenvalues of $\chi_r^{\nu\nu'}$, which cross zero and become more and more negative as the interaction is further increased (see e.g., the inset of rightmost panel in Fig. 3.1 and in more details Chapter 5), are reflected in large positive eigenvalues of F. This is demonstrated numerically for an example case of the AIM in Fig. 3.5, where the full spectrum of $\chi_c \chi_0^{-1}$ is plotted in comparison to $\chi_0 F_c$.

Note that, a priori, one could wonder how the eigenvalues of two different matrices (here $\chi_r^{\nu\nu'}$ and $F_r^{\nu\nu'}$) could actually be compared since the two matrices could have different eigenbases in general. However, one can show that in the specific case considered here, these matrices are simultaneously diagonalizable, and hence it is valid to directly link their eigenvalues as done above:

Suppose both A and B are diagonalizable matrices, where $A = V^{-1}DV$ and D is a diagonal matrix. Since these matrices sum to unity $A + B = \mathbb{1}$, the following statement is true:

$$
\begin{aligned}
A + B &= \mathbb{1} \\
&\Downarrow \quad \cdot V V^{-1} \\
\underbrace{VAV^{-1}}_{D} + VBV^{-1} &= VV^{-1} = \mathbb{1} \\
V^{-1}BV &= \mathbb{1} - D = \tilde{D}
\end{aligned}
\tag{3.5}
$$

where $\tilde{D}$ is again a diagonal matrix, which demonstrates that A and B are simultaneously diagonalized by V.

3.1.1   Manifestations of vertex divergences at half filling

In the following parts, we focus on the numerous manifestations of irreducible vertex divergences in different models. To this end, we present an overview of their appearances in this as well as the following Sec. 3.1.4, whereas in the former, we will address the particle-hole symmetric case (half filling); in the latter, we will focus on the results obtained for problems with broken particle-hole symmetry (out of half filling). A particular emphasis will be naturally given to results where the author of this thesis contributed to the calculation or the interpretation, while all the other findings of the literature, which are relevant for this work, are concisely reviewed.

Throughout, we consider two-particle calculations for the static case ($\omega = 0$), which is treated most frequently in the literature [10, 12, 17–19, 21, 22, 25, 26]. In general, for any model we are going to discuss, we first present the corresponding phase diagram. These explicitly show the parameter sets for which one (or more) eigenvalue of the generalized susceptibility in channel r crosses zero, corresponding to the so-called (vertex) divergence lines. Second, we characterize the irreducible vertex divergences by considering the symmetry of the corresponding singular eigenvectors. At the end of each subsection, a short summary of our analysis is given (colored boxes with bullet points), which highlights the relevant points for the discussion of this thesis (and allows for a quicker reading of this chapter).

3.1.1.1   Divergences in the atomic limit

The first model considered, due to its relative simplicity, is the atomic limit (AL), which has been defined in Sec. 2.1.1.1. At half filling ($\mu = -U/2$), the model is fully characterized by the temperature T and the interaction U, since there is no hopping term included in the Hamiltonian. The advantage of this simplified model is that analytic expressions for the full vertex F, the generalized susceptibility and the irreducible vertex are available [23, 33]. Nevertheless, the physics realized by this model is far from being trivial.

In Fig. 3.6 the T-U diagram of the AL for repulsive interaction U at half filling is shown, which was taken from Ref. [19]. As it turns out, two groups of lines along which the irreducible vertex diverges are found, which are shown as red and orange lines in the main panel of the figure. All divergence lines originate form $U = 0$ at $T = 0$, which means that there is *no* critical interaction value that needs to be reached before irreducible vertex divergences start to appear, as opposed to other cases discussed below.

The red divergence lines mark parameter sets where the static irreducible vertex in the *charge* channel $\Gamma_c^{\nu\nu'(\omega=0)}$ diverges. These divergences are driven by eigenvalues associated to eigenvectors with a particular frequency structure [19, 23]:

$$V_{\bar{\nu}}^c(\nu) = \frac{1}{\sqrt{2}}\left[\delta_{\nu\bar{\nu}} - \delta_{\nu(-\bar{\nu})}\right] \tag{3.6}$$

with $\bar{\nu} = (2\bar{n} - 1)\pi T$, being a fixed fermionic Matsubara frequency[7]. These eigenvectors

---

[7]Note that in Chapter 2 the fermionic Matsubara frequencies were defined as $\nu = (2n + 1)\pi T$, which does
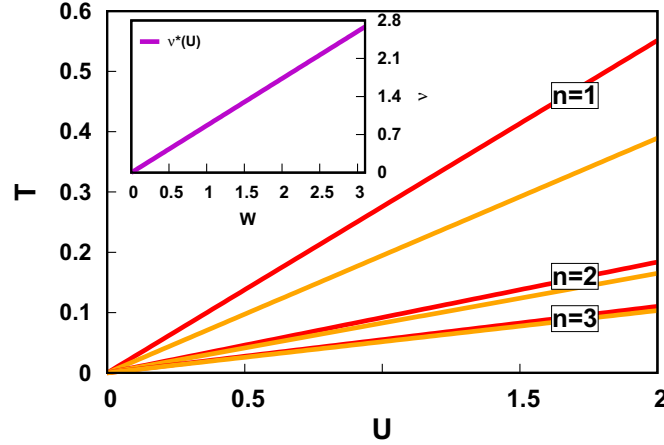
Figure 3.6: Phase diagram of the atomic limit at half filling for repulsive interaction. Along the red divergence lines, $\Gamma_c^{\nu\nu'(\omega=0)}$ diverges for a given Matsubara frequency $\nu = (2n - 1)\pi T = \bar{\nu}$, where n refers to the corresponding Matsubara index shown in the main panel. These divergences are determined by the energy scale ν^* (cf. Eq.(3.7)), shown in the inset (where W is a misprint in the original publication, is should be U). The orange lines mark the parameter sets where a simultaneous divergence of $\Gamma_c^{\nu\nu'(\omega=0)}$ and $\Gamma_{pp,\uparrow\downarrow}^{\nu\nu'(\omega=0)}$, i.e., in the charge and the particle-particle (singlet) channel is observed. The figure is taken from Ref. [19] (Fig. 8 therein).

are completely localized in Matsubara frequency space, and thus also the divergence of $\Gamma_c^{\nu\nu'}$ is observed only *at this specific frequency* $\bar{\nu}$, as discussed above, see Eq. 3.2. Due to the antisymmetric nature of $V_{\bar{\nu}}^c(\nu)$, the corresponding eigenvalues originate from the antisymmetric subspace of $\chi_c^{\nu\nu'}$, cf. Sec. 2.2.4. As shown in Ref. [19] (see Eqs. (44)-(46) therein) the analytic condition for vanishing eigenvalues along the red divergence lines can be explicitly written as:

$$\bar{\nu} = (2\bar{n} - 1)\pi T \;\; \overset{!}{=} \;\; \frac{\sqrt{3}}{2}U = \nu^* \tag{3.7}$$

$$\Downarrow$$

$$T_n \;\; = \;\; \frac{1}{(2\bar{n} - 1)\pi}\frac{\sqrt{3}}{2}U \;.$$

Hence, each time the frequency $\bar{\nu}$ becomes equal to the energy scale $\nu^* = U\sqrt{3}/2$ a divergence of $\Gamma_c^{\nu\nu'}$ occurs *at* this specific frequency (i.e., for $\Gamma_c^{(\nu=\pm\bar{\nu})(\nu'=\pm\bar{\nu})}$). This allows also to relate the red divergence lines shown in Fig. 3.6 to a given Matsubara index n (as explicitly shown in the reformulation in the second line of Eq.(3.7)). In this way, it becomes obvious that in the AL for each $U > 0$ infinitely many divergence lines are found for $T \rightarrow 0$, as the Matsubara frequencies become more and more dense. Equivalently, the red divergence lines can be rescaled to a single line, as shown in the inset of Fig. 3.6, using the factor $(2\bar{n} - 1)$. For completeness, let us note here that the energy scale ν^* corresponds to the inflection point of the one-particle Green's function of the AL, as discussed explicitly in

---

not differ crucially from the relation written here, apart from shifting the index n. The convention of Ref. [19] was used here, in order to match the convention used in the corresponding Fig. 3.6. In the conventions of this thesis, the first red divergence line would correspond to $n = 0$.

Refs. [22, 23].

At the same time, the phase diagram of Fig. 3.6 shows that a second kind of vertex divergence can be found. These take place simultaneously in the pp ↑↓ and the charge channel[8], and are represented by the orange lines in Fig. 3.6. Such divergences do *not* correspond to an eigenvector localized in frequency space, but to one that displays nonzero contributions at all Matsubara frequencies. More specifically, the singular eigenvalues associated to the orange lines, which are *symmetric* in Matsubara frequency, are determined by a more complicated equation, see Refs. [19, 23], and, as a result, no energy scale similar to ν^* can be defined. Nevertheless, infinitely many divergence lines also of this second kind are numerically found as $T \to 0$ [23]. They occur always *after* the red ones described above, becoming progressively nearer to them as T is reduced.

For the interested reader, let us make a wholehearted recommendation of Ref. [23], where the problem of vanishing eigenvalues and the corresponding eigenvectors for the atomic limit is analyzed in all details in a very transparent manner. In Ref. [23], other than half filling, no restrictions are made, e.g., also divergences for $\omega \neq 0$ are analyzed. Instead of going further into details, we summarize the crucial aspects of the results of the AL discussed above, which will be relevant throughout this thesis [19, 23]:

- In the half filled AL case, infinitely many divergence of the irreducible vertex function are found, which all emanate from $U = 0$ at $T = 0$. Hence, there is no critical interaction value for the vertex divergences of the AL.

- For repulsive interactions, these divergences are found in the charge and the pp ↑↓ sector, which are the channels with suppressed fluctuations in the AL. In the dominant magnetic channel, on the contrary, no divergences are observed for $\omega = 0$.

- The **red** divergence lines represent divergences of the irreducible vertex in the charge channel (Γ_c) and correspond to antisymmetric eigenvectors, which are localized in Matsubara frequency space and completely determined by the energy scale ν^*.

- The **orange** divergence lines mark parameter sets where divergences of the irreducible vertex functions in the charge and the pp, ↑↓ channel occur simultaneously (Γ_c and $\Gamma_{pp,\uparrow\downarrow}$). These are characterized by symmetric eigenvectors and are always observed after a red divergence line, i.e., at lower-T or larger-U.

---

[8]Note that for technical convenience, the divergence lines shown in Fig. 3.6 are calculated for the charge and the *singlet* channel, see Ref. [19], which is related to the pp ↑↓ one via $\chi_{\text{singlet}}^{\nu\nu'\omega} = [\chi_{pp,\uparrow\uparrow}^{\nu\nu'\omega} + 2\chi_{pp,\uparrow\downarrow}^{\nu\nu'\omega} - 2\chi_{pp,0}^{\nu\nu'\omega}]/4$, see Eq. (5c) in Ref. [23]. Since $\chi_{pp,\uparrow\uparrow}^{\nu\nu'(\omega=0)}$ does not show any singular eigenvalues for $\omega = 0$, the divergence lines of the singlet channel have a one-to-one correspondence to those of the pp↑↓ channel [19].

3.1.1.2 Divergences in disordered models

In the next part we summarize the problem of irreducible vertex divergences for disordered models, solved by DMFT. The advantage of these models is that the divergences can be analyzed analytically, as in the AL case, in spite of the presence of a nonzero hopping amplitude t. However, in contrast to the AL, these models essentially describe non-interacting electrons, between which interaction-like aspects, as the appearance of nonzero self-energies and vertex functions, are effectively introduced by averaging over random distributions of impurities. As a result, these models do display a MIT, and, in this way, the effect of metallic/Fermi-liquid behavior on divergence lines can be studied in a simplified way.

Irreducible vertex divergences have been reported for the Falicov-Kimball (FK) model in DMFT [13, 17, 19], as well as the binary-mixture (BM) model in DMFT in Refs. [19, 23, 26]. Here we focus on the BM, since this allows for particularly transparent calculations for the discussion made below in Sec. 3.2. The BM is characterized by the following Hamiltonian [19]:

$$H = -t \sum_{\langle ij \rangle, \sigma} c_{i\sigma}^{\dagger} c_{j\sigma} + \sum_{i,\sigma} \epsilon_i c_{i\sigma}^{\dagger} c_{i\sigma} \ , \tag{3.8}$$

where $\epsilon_i = \pm \frac{W}{2}$ is randomly distributed with equal probability and mimics the effect of an electron-electron interaction. W refers to the associated disorder strength. More details on this model and underlying calculations can be found in Ref. [19] (specifically, in Section III and Appendix D therein).

As in the AL case, also for the BM, frequency localized divergences of the irreducible vertex function are found, which are completely determined by a characteristic energy scale ν_{BM}^* [19]:

$$\nu_{BM}^*(W) = \frac{2W^2 - 1}{4W} \ . \tag{3.9}$$

More specifically, as soon as a Matsubara frequency ν is equal to ν_{BM}^*, a divergence of Γ_c occurs[9], the resulting divergence lines are shown in Fig. 3.7 and defined by the previous relation as [19] (see Eq. (20) therein):

$$T_n(W) = \frac{1}{\pi(2n-1)} \frac{2W^2 - 1}{4W} \ . \tag{3.10}$$

Hence, as for the red lines of the AL, all divergence lines can be rescaled to coincide by a factor $(2n - 1)$. Note that for the BM, the energy scale ν_{BM}^* can be related to the minimum of the Green's function $G(\nu)$ [19, 23].

However, the divergence lines for the BM demonstrate a crucial difference w.r.t. the ones of the AL: They start from a critical disorder strength $\widetilde{W} = 1/\sqrt{2}$, which is *smaller* than the one associated to the MIT ($W_{\mathrm{MIT}} = 1$). This property of the irreducible vertex

---

[9]Note that for the BM, $\Gamma_{\uparrow\downarrow}$ vanishes [19], hence the "charge" channel for the BM is given solely by the $\Gamma_{\uparrow\uparrow}$ contribution, i.e., $\Gamma_c = \Gamma_{\uparrow\uparrow}$.
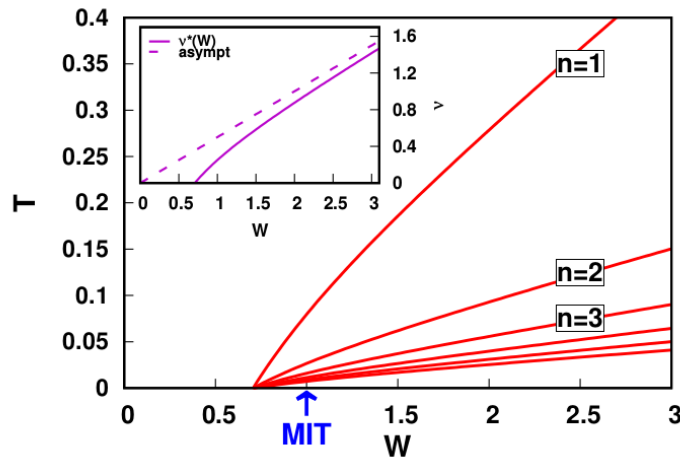
Figure 3.7: DMFT phase diagram of the binary mixture model at half filling as a function of disorder strength W and temperature T. The infinitely many red lines, which emanate from a critical disorder strength $\widetilde{W}$ lower than the one associated to the MIT (blue arrow), refer to divergences in the charge channel. These divergences are fully localized in frequency space, determined by the energy scale ν^*, which is shown in the inset. The figure is taken from Ref. [19] (Fig. 2 therein).

divergences of the BM is of particular significance, as a similar behavior is also observed in the HM. Let us note that for the BM the irreducible vertex divergences were also analyzed on the real frequency axis. As it turns out, only at the critical disorder strength $\widetilde{W}$, which represents an accumulation point, a divergence on the real axis is found, see Ref. [19] for details.

As mentioned before, as a next step of complexity, also the divergences of the DMFT solution of the Falicov-Kimball model were analyzed in the literature [13, 17, 19]. In fact, the DMFT solution of the FK model shares important similarities with the BM model, but yields a more complete description of the possible ways how vertex divergences can occur. In particular, on the one hand, one finds exactly the same localized divergences as in the BM case. On the other hand, the FK model also features divergences in the charge channel, which are not localized in frequency space, similar to those occurring along the orange lines in the AL.

Before considering the divergence lines for the substantially more complex Hubbard model, we summarize the results for the DMFT solution of disordered models:

- In the DMFT solution of the BM and the FK model, infinitely many divergences of two types are found, which are either localized or non-localized in Matsubara frequency space.

- For the BM and the FK model, the localized divergences show a similar dependence on an energy scale ν^*_{BM}, as in the AL case. These divergence lines start at a single critical disorder strength/interaction value for $T \to 0$, which is smaller than the one associated to the corresponding MIT.

3.1.1.3   Divergences in the Hubbard model

In this part we consider the divergences of the irreducible vertex functions in the HM solved in DMFT. We first discuss the results obtained for the HM on a square lattice, which was also the case first considered in the literature [10, 19].
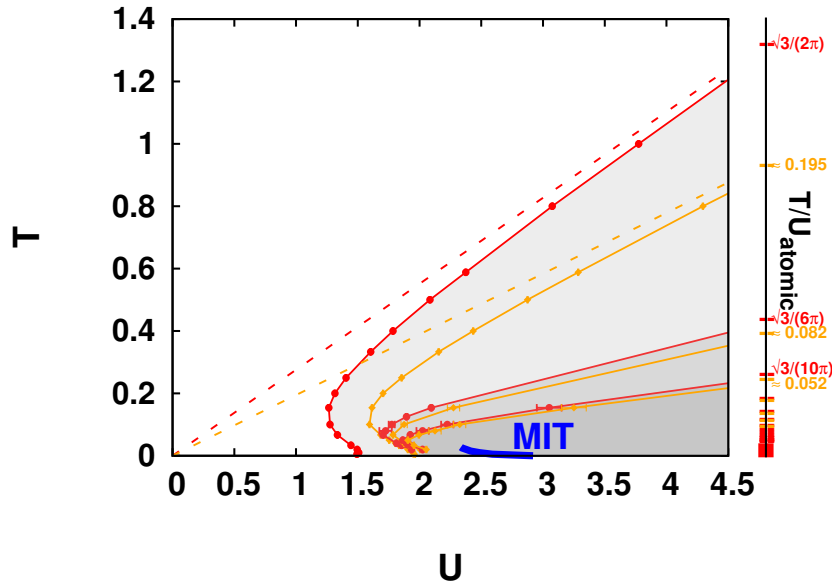

Figure 3.8: Phase diagram of the Hubbard model on a square lattice solved in DMFT, where the MIT is represented by the blue line. A finite set of divergence lines is shown, where along the red ones a divergence of the static $\Gamma_c^{\nu\nu'}$ is observed, while along the orange lines $\Gamma_c^{\nu\nu'}$ and $\Gamma_{pp,\uparrow\downarrow}^{\nu\nu'}$ diverge simultaneously. The first two divergence lines of the AL, see also Fig. 3.6, are plotted as dashed lines. The scale to the right of the main plots shows the ratios T/U for the AL divergences. Taken from Ref. [19] (Fig. 10 therein).

Similarly as for the AL and the disordered models, also for the HM solved in DMFT *infinitely* many divergence lines are found [19]. In the phase diagram of Fig. 3.8, the first six divergence lines are reported [19], while the Mott MIT is shown as the blue line (the shaded grey area illustrates the nonperturbative regime). Again two classes of divergences are observed: On the one hand, divergences of the static irreducible vertex in the *charge* channel $\Gamma_c^{\nu\nu'}$, which are associated to an *antisymmetric* singular eigenvector and marked as red lines throughout the phase diagram. On the other hand, divergences which take place simultaneously in the *charge* and the $pp\uparrow\downarrow$ channel, with a corresponding *symmetric* singular eigenvector. This kind of divergences are represented by orange lines in Fig. 3.8, in line with the color coding used for the AL.

Both types of divergence lines of the HM display a linear behavior at high-T and large-U, which can be understood by comparing them to the AL results [10, 19] discussed above. In particular, the dashed red and orange lines shown in Fig. 3.8 represent the first two divergence lines of the AL, which asymptotically coincide with the ones of the HM for large-U and high-T. Further, also the frequency structure of the associated singular eigenvectors in this regime is very similar to the ones of the AL [19] (cf. Sec. 3.1.3.2). Moreover, the scale to the right of the main plot in Fig. 3.8 reports the values for all ratios

T/U of the AL divergences, which determines the behavior of the HM divergence lines at large U.

As the temperature is reduced, the divergence lines of the HM show a bending ("re-entrance"), whose shape seems to suggest a relation to the MIT [10, 19]. The bending of the divergence lines is, however, incomplete, and hence the $T \to 0$ endpoints of the first divergence lines are found at *finite U* values, see more explicitly Appendix B of Ref. [19] and Fig. 13 therein. As in the case of the disordered models, the first vertex divergences are found already at interaction values significantly smaller than U_c of the MIT. However, other than in these simplified cases, there is not a single point at $T = 0$ where all divergence lines emanate from [19]. Moreover, with decreasing temperature, the frequency structure of the singular eigenvectors along the first red divergence line changes significantly (cf. Fig. 11 in Ref. [19] and in detail below Sec. 3.1.3.2), deviating strongly from the $\delta_{\nu\nu'}$-form observed in the AL (cf. Eq. (3.6)).

These results demonstrate important features, which provides the motivation for the subsequent studies presented[10] in Secs. 3.1.2 and 3.1.3:

- As in the AL case, the divergences for the DMFT solution of the HM appear in channels where the physical fluctuations are suppressed, i.e., for the specific case of repulsive interactions, in the charge and the pp sector. Thus a natural question arises: Are irreducible vertex divergences always affecting the scattering channels that are suppressed?

- So far, all models considered demonstrated a MIT (in the AL case, one can argue that this is located at $U = 0$). Is the MIT a necessary condition[11] to observe vertex divergences [10, 19]?

- Can the observed symmetry properties of the singular eigenvectors be understood on a more fundamental level?

3.1.2   Divergences in the Hubbard model on the Bethe lattice at half filling

In this part, by means of the DMFT (cf. Sec. 2.3.1), the local two-particle susceptibilities and irreducible vertex functions of both, the attractive and the repulsive Hubbard model (cf. Sec. 2.1.3) on the Bethe lattice (with a semielliptic DOS of half-bandwidth $D = 2t = 1$) are analyzed.

In all studies of models with *repulsive* interactions (summarized above) negative eigenvalues have exclusively occurred in physical channels that are *suppressed* upon increasing the interaction strength U, namely in the *charge* and in the *particle-particle* channels.

---

[10]Note that for practical reasons, both of these parts are formatted as subsections to allow for a better structured illustration. However, these cases are also studies performed at half filling, and hence topically part of Sec. 3.1.1.

[11]Note also the title of the first publication on irreducible vertex divergences [10]:"Divergent Precursors of the Mott-Hubbard Transition at the Two-Particle Level".

According to this observation, one may expect that vertex divergences in models with an *attractive* interaction will occur in the *magnetic* channel only. This would heuristically be consistent with the known "mapping" of the physical degrees of freedom (D.o.F./DOF) of the half-filled Hubbard model. Due to the intrinsic $O(4) = SU(2) \times SU(2)$ symmetry, the partial particle-hole, or also Shiba, transformation [111, 112]

$$c_{i\uparrow} \rightarrow c_{i\uparrow} \text{ and } c_{i\downarrow} \rightarrow (-1)^i c_{i\downarrow}^\dagger \tag{3.11}$$

acts as a mapping of all physical observables between $U < 0$ and $U > 0$. In particular, the two SU(2) spin ($\vec{S}$) and pseudospin ($\vec{S}_p$) sectors, which are related to the respective suppressed channels on the attractive and repulsive side, are transformed into each other[12]

$$
\begin{aligned}
S_x &= \frac{1}{2}[c_\uparrow^\dagger c_\downarrow + c_\downarrow^\dagger c_\uparrow] \leftrightarrow \frac{1}{2}[c_\uparrow^\dagger c_\downarrow^\dagger + c_\downarrow c_\uparrow] = S_{p,x} \\
S_y &= \frac{i}{2}[c_\uparrow^\dagger c_\downarrow - c_\downarrow^\dagger c_\uparrow] \leftrightarrow \frac{i}{2}[c_\uparrow^\dagger c_\downarrow^\dagger - c_\downarrow c_\uparrow] = S_{p,y} \\
S_z &= \frac{1}{2}[c_\uparrow^\dagger c_\uparrow - c_\downarrow^\dagger c_\downarrow] \leftrightarrow \frac{1}{2}[c_\uparrow^\dagger c_\uparrow + c_\downarrow^\dagger c_\downarrow - 1] = S_{p,z} .
\end{aligned}
\tag{3.12}
$$

This mapping of physical D.o.F. suggests that a similar "transformation" may as well apply to the vertex-divergences. However, as already noted in Refs. [33, 113], the mapping of generalized two-particle quantities, and especially of dynamical irreducible vertices, is more complex than Eq. (3.12) would suggest. In the following, we will see how this is reflected in the appearance and the nature of vertex divergences in the attractive Hubbard model.

3.1.2.1 DMFT results

The main outcome of our DMFT calculations are summarized in Fig. 3.9, where we report the location of the divergences of the static irreducible vertex $\Gamma_r^{\nu\nu'(\omega=0)}$ found for different values of the local attraction $U < 0$ and the temperature T (left side), compared against the corresponding results for the repulsive case $U > 0$ (right side), all in units of the half-bandwidth $D = 2t = 1$. In the large $|U|$ regime the numerical results are consistent with analytical calculations in the AL [23], (as seen above). Furthermore, in the whole repulsive sector, we also reproduce the outcome of the DMFT studies on the HM on a square lattice [10, 19], see Sec. 3.1.1.3, finding multiple lines in the U-T plane, where the irreducible vertex diverges. The small differences arise from the different lattices used in the DMFT calculations [19]. As already observed in Refs. [10, 19] and outlined above, the first divergences are located at moderate repulsion values, well before the MIT. With increasing interaction the occurrence of divergence lines becomes more dense, and the lines occur in alternating order starting with a divergence in the charge channel (red lines) followed by a simultaneous divergence in the charge and pp $\uparrow\downarrow$ channel (orange lines).

In the case of *attractive* interaction we find vertex divergences in the charge channel

---

[12]Here we assume for the explicit expression a site where $(-1)^i = 1$ holds. For a neighboring site on the lattice, one would have to consider the corresponding (-1), see further Ref. [113].
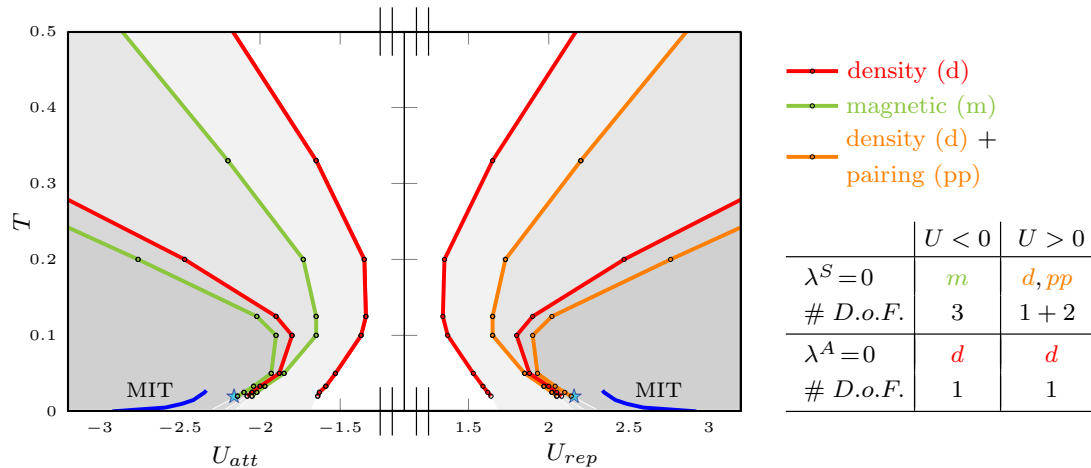
Figure 3.9: Left: Location of the divergences of the irreducible vertex in the different channels along the whole phase-diagram of the attractive *and* the repulsive half-filled Hubbard model on the Bethe lattice, computed in DMFT. The comparison of the negative and positive U sectors yields perfectly mirrored divergences in the density (i.e., charge in the conventions of this thesis) channel (red). The simultaneous divergences in the density and particle-particle channel (orange) in the repulsive model are mapped into divergences of the magnetic channel (green) on the attractive side. Stars refer to the position in the phase diagram of the data shown in Fig. 3.11. Right: Schematic sketch comparing the mapping of the singular eigenvalues λ^S [λ^A] associated to symmetric [antisymmetric] eigenvectors to the mapping of different physical degrees of freedoms (D.o.F.).

(red lines), which are perfectly mirrored with respect to the repulsive side. These occur in alternating order with lines of divergences in the magnetic channel (green lines), which mirror the orange divergence lines of the repulsive model. As a consequence, the location of the vertex divergences is highly symmetric when comparing the repulsive and the attractive sides of the phase diagram.

At first sight, this symmetry may appear rather surprising, because the physical properties of a given scattering channel in the repulsive and the attractive model are very different [112, 114, 115], as dictated by the mapping of the physical degrees of freedom (cf. Eq. (3.12) and Fig. 3.9). At a closer look, we can distinguish the situation of the three-fold degenerate divergences found at the orange and green lines, respectively, from that of the single degenerate divergences found at the red lines, occurring in the charge sector only. Specifically, the mapping of the combined divergences in the pp ↑↓ and charge sector (orange lines) into divergences of the magnetic sector (green lines) is fully matching our physical expectations: (i) divergences appear in the suppressed fluctuation channels and (ii) they are mapped consistently with the physical D.o.F., i.e., according to Eq. (3.12). At the same time, the perfect mirroring of the *charge* divergence lines (red) under the $U \leftrightarrow -U$ transformation looks puzzling, because (i) for $U < 0$, these divergences affect a scattering channel associated to a physical susceptibility, which is not suppressed but *enhanced* by the attractive interaction, and (ii) the physical degrees of freedom associated to the charge channel is mapped onto one of the three spin-components.
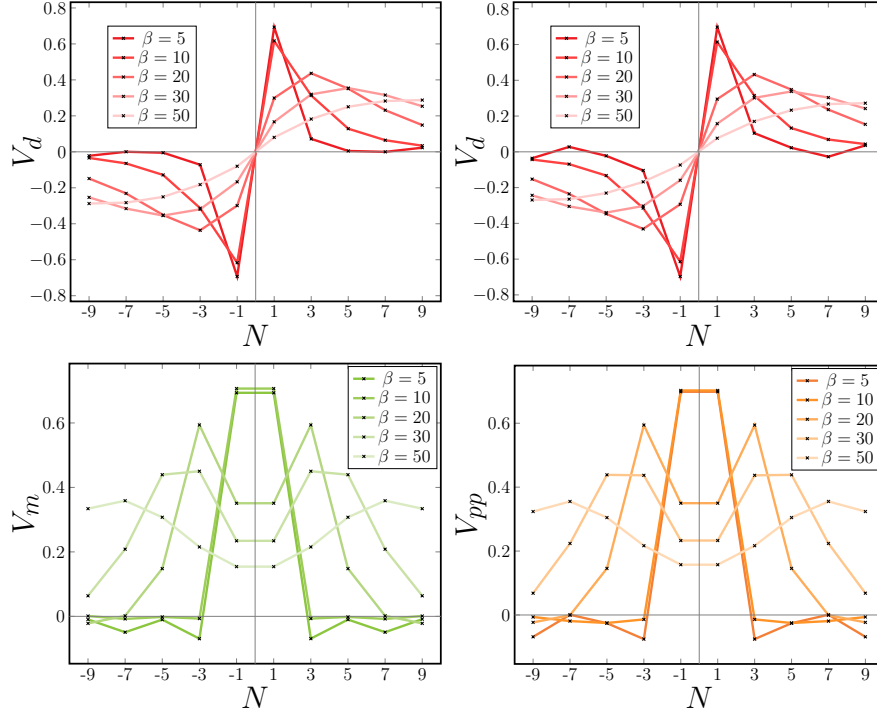
Figure 3.10: Comparison of the singular eigenvectors V_α^r in the repulsive and the attractive case, plotted as a function of the Matsubara index $N = \nu \frac{\beta}{\pi}$. The upper [lower] panels show perfectly identical singular antisymmetric [symmetric] eigenvectors located at different temperatures along the first [second] attractive (left) and first [second] repulsive (right) divergence line. The T-dependence will be studied explicitly in Sec. 3.1.3.2.

A first understanding of this apparent discrepancy is provided by the analysis of the symmetry of the eigenvectors associated to a vanishing eigenvalue (cf. Eq. (3.1)). In Fig. 3.10 we compare the shape of eigenvectors following the first and second divergence lines at different temperatures for $U \lessgtr 0$ (the T-dependence is studied explicitly below in Sec. 3.1.3.2). Evidently, the perfect mirroring of divergence lines is also reflected in identical shapes of the corresponding eigenvectors. The singular eigenvectors associated to *all* divergences in the charge sector only (red lines), display a completely *antisymmetric* frequency structure. In contrast, all other divergence lines (green and orange lines) are associated to frequency *symmetric* singular eigenvectors.

The symmetry of eigenvectors is essential in the calculation of the physical susceptibility, as discussed in Sec. 2.2.4 (cf. Eq. (2.56) and Eq. (2.57)). Due to the summation over Matsubara frequencies, the value of χ_r is *independent* of any antisymmetric eigenvector, irrespective of whether associated to a positive or a negative eigenvalue. Hence, the appearance of negative eigenvalues in a channel is *not* necessarily associated to a suppression of the respective physical susceptibility. While in the *repulsive* model the occurrence of divergences and the suppression of the respective channel coincide (maybe incidentally), our calculations of the *attractive* model provide a clear-cut counter-example: the crossing of several divergence lines in the charge sector is accompanied by an *enhanced* susceptibility.

To rationalize the results of our two-particle DMFT calculations on more general

grounds, we investigate the effect of the attractive-repulsive mapping on generalized two-particle quantities and its relation to the physical symmetries of the system under consideration.

3.1.2.2 The role of the underlying symmetries

As mentioned above, the mapping of the *generalized* two-particle quantities is far less obvious than the mapping of the physical degrees of freedom.

When considering purely local quantities, the single-particle Green's function $G(\tau_1, \tau_2)$ is identical for the repulsive ($U > 0$) and attractive ($U < 0$) half-filled model. On the other hand, the two-particle Green's function $G_{\uparrow\downarrow}(\tau_1, \tau_2, \tau_3, \tau_4)$ with anti-parallel spin orientation transforms [33, 54] according to

$$G_{\uparrow\downarrow}^{(U)}(\tau_1, \tau_2, \tau_3, \tau_4) = -G_{\uparrow\downarrow}^{(-U)}(\tau_1, \tau_2, \tau_4, \tau_3), \tag{3.13}$$

which, after Fourier transformation of all fermionic variables, reads

$$G_{\uparrow\downarrow}^{(U)}(\nu_1, \nu_2, \nu_3) = -G_{\uparrow\downarrow}^{(-U)}(\nu_1, \nu_2, -\nu_4) \tag{3.14}$$

with $\nu_4 = \nu_1 - \nu_2 + \nu_3$. After changing to the ph-notation, as defined in Eq. (2.17) ($\nu_1 = \nu$, $\nu_2 = \nu + \omega$, $\nu_3 = \nu' + \omega$, $\nu_4 = \nu'$) one can easily see how the transformation maps the generalized static ($\omega = 0$) susceptibility, $\chi_{\uparrow\downarrow}^{\nu,\nu'} = G_{\uparrow\downarrow}(\nu, \nu, \nu')$ of the $\uparrow\downarrow$ sector according to

$$\chi_{\uparrow\downarrow}^{\nu\nu'} \stackrel{U \leftrightarrow -U}{\Longleftrightarrow} -\chi_{\uparrow\downarrow}^{\nu(-\nu')}, \tag{3.15}$$

while $\chi_{\uparrow\uparrow}$ is obviously invariant under a partial particle-hole transformation.

Hence, in general, the Shiba transformation at the two-particle level will *mix* the different (particle-hole) channels of generalized susceptibilities and the associated irreducible vertices. *Only* the mapping of the generalized susceptibility expressed in the pp-notation

$$\chi_{pp,\uparrow\downarrow}^{\nu(-\nu')} - \chi_{0,pp}^{\nu\nu'} \stackrel{U \leftrightarrow -U}{\Longleftrightarrow} \chi_m^{\nu\nu'} \tag{3.16}$$

reflects [33, 54, 113] the transformation of the physical (spin/pseudospin) degrees of freedoms, discussed in Eq. (3.12), in a direct fashion.

As the location of divergence lines is directly encoded in the generalized susceptibilities, it will also be subject to the mixing of channels, explaining the differences w.r.t. the mapping of the physical degrees of freedom. To fully rationalize the results demonstrated in Fig. 3.9, we will focus on the symmetry properties of the generalized susceptibilities. In this respect we note that Eq. (3.16) already shows why the mirrored divergences of the pp $\uparrow\downarrow$ channel for $U > 0$ are observed in the magnetic channel for $U < 0$. Hence, the main question concerns the behavior of the particle-hole channels.

Since we consider the HM at half filling (with nearest neighbor hopping only), particle-hole symmetry is given, and thus the considerations made in Sec. 2.2.4.1 fully apply. As a reminder we recall the most relevant properties here: In this highly symmetric case, the

static generalized susceptibility is a bisymmetric matrix, which can be block-diagonalized by the orthogonal matrix Q (defined in terms of the counteridentity ($J^{\nu\nu'} = \delta_{\nu(-\nu')}$) and identity ($\mathbb{1}$) submatrices):

$$Q = \frac{1}{\sqrt{2}}\begin{pmatrix} \mathbb{1} & -J \\ \mathbb{1} & J \end{pmatrix} \quad , \quad Q\chi_r^{\nu\nu'}Q^T = \left(\begin{array}{c|c} A & \mathbb{0} \\ \hline \mathbb{0} & S \end{array}\right) . \tag{3.17}$$

The block-diagonalization of $\chi_r^{\nu\nu'}$ is associated with precise symmetry properties: the subspace denoted by A represents a submatrix with exclusively antisymmetric eigenvectors, while S is the subspace of purely symmetric eigenvectors. As a consequence, one can unambiguously attribute the occurrence of a red divergence line in $\chi_c^{\nu\nu'}$ (i.e., the corresponding vanishing eigenvalue) to the purely antisymmetric subspace A, while all other divergence lines will be accounted for by the symmetric subspace S.

A crucial ingredient for connecting the bisymmetry of the generalized susceptibilities to the mapping of divergence lines lies in the equivalence of the Shiba transformation for $\chi_{\uparrow\downarrow}^{\nu\nu'}$ to a matrix multiplication with the negative counteridentity matrix $(-J)$

$$\chi_{\uparrow\downarrow,(U)}^{\nu\nu'}(-J) = -\chi_{\uparrow\downarrow,(U)}^{\nu(-\nu')} = \chi_{\uparrow\downarrow,(-U)}^{\nu\nu'} . \tag{3.18}$$

Using $J^2 = \mathbb{1}$, the bisymmetric matrices $\chi_{\uparrow\uparrow}$ and $\chi_{\uparrow\downarrow}$ can be written as follows (the fermionic Matsubara frequency indices will be partly omitted in the following):

$$\chi_{\uparrow\uparrow}^{U>0} \quad = \quad \chi_{\uparrow\uparrow}^{U<0} = \chi_{\uparrow\uparrow} = \begin{pmatrix} A & JBJ \\ B & JAJ \end{pmatrix} \tag{3.19}$$

$$\chi_{\uparrow\downarrow}^{U>0} \quad = \quad \begin{pmatrix} C & JDJ \\ D & JCJ \end{pmatrix} \tag{3.20}$$

$$\chi_{\uparrow\downarrow}^{U<0} \quad \overset{\text{Eq. (3.18)}}{=} \quad \chi_{\uparrow\downarrow}^{U>0}(-J) = \begin{pmatrix} C & JDJ \\ D & JCJ \end{pmatrix}\begin{pmatrix} \mathbb{0} & -J \\ -J & \mathbb{0} \end{pmatrix}$$

$$= \quad \begin{pmatrix} -JD & -CJ \\ -JC & -DJ \end{pmatrix} . \tag{3.21}$$

Block-diagonalization (described in Sec. 2.2.4.1) of $\chi_{\uparrow\uparrow}$ and $\chi_{\uparrow\downarrow}$ for both cases leads to

$$Q\chi_{\uparrow\uparrow}Q^T = \begin{pmatrix} A - JB & \mathbb{0} \\ \mathbb{0} & A + JB \end{pmatrix} \qquad (3.22)$$

$$Q\chi_{\uparrow\downarrow}^{U>0}Q^T = \begin{pmatrix} C - JD & \mathbb{0} \\ \mathbb{0} & C + JD \end{pmatrix} \qquad (3.23)$$

$$Q\chi_{\uparrow\downarrow}^{U<0}Q^T = \begin{pmatrix} -JD - J(-JC) & \mathbb{0} \\ \mathbb{0} & -JD + J(-JC) \end{pmatrix}$$

$$= \begin{pmatrix} C - JD & \mathbb{0} \\ \mathbb{0} & -[C + JD] \end{pmatrix} \qquad (3.24)$$

This immediately shows that the antisymmetric block of $\chi_{\uparrow\downarrow}$, $(C - JD)$, is unchanged, whereas the symmetric one changes sign for $U > 0 \leftrightarrow U < 0$. Considering χ_c and χ_m for $U < 0$ and $U > 0$ the following expressions are obtained, where we use the trivial relation

$$Q\chi_{c^+,m^-}Q^T = Q(\chi_{\uparrow\uparrow} \pm \chi_{\uparrow\downarrow})Q^T = Q\chi_{\uparrow\uparrow}Q^T \pm Q\chi_{\uparrow\downarrow}Q^T \ ,$$

$$Q\chi_c^{U\gtrless 0}Q^T = \begin{pmatrix} [A-JB]+[C-JD] & \mathbb{0} \\ \mathbb{0} & [A+JB]\pm[C+JD] \end{pmatrix} \qquad (3.25)$$

$$Q\chi_m^{U\gtrless 0}Q^T = \begin{pmatrix} [A-JB]-[C-JD] & \mathbb{0} \\ \mathbb{0} & [A+JB]\mp[C+JD] \ . \end{pmatrix} \qquad (3.26)$$

In the charge channel case the $+$ sign corresponds to $U > 0$ the $-$ sign to $U < 0$, for the magnetic case it is the other way around. From Eqs. (3.25) and (3.26) three conclusions can be drawn:

(i) The antisymmetric block of $Q\chi_c^{U\gtrless 0}Q^T$ is independent of the sign of U. The diagonalization of $[A - JB] + [C - JD]$ will yield the eigenvalues and the corresponding antisymmetric eigenvectors of $\chi_c^{\nu\nu'}$. Their singularity corresponds to a red divergence line, independently of the sign of U. This is the mathematical reason for the perfect mapping of the red divergence lines reported in Fig. 3.9 and the equality of the singular eigenvectors shown in Fig. 3.10. Note that this statement is crucially dependent on the perfect particle-hole symmetry of the problem. Otherwise the bisymmetry property is lost.

(ii) The antisymmetric block of $Q\chi_m^{U\gtrless 0}Q^T$ is also independent of the sign of U. This means that, irrespective of the sign of U, the eigenvalues corresponding to antisymmetric eigenvectors of χ_m can be calculated by diagonalizing $[A - JB] - [C - JD]$. However, for the static cases considered so far none of these eigenvalues were found to be singular (see further Ref. [23]).

(iii) The symmetric parts of $\chi_c^{\nu\nu'}$ and $\chi_m^{\nu\nu'}$ are mapped in the following way: $[A + JB] +$

$[C + JD]$ is the symmetric blockmatrix of $\chi_c^{U>0}$ *and* $\chi_m^{U<0}$. This explains why the symmetric charge channel divergences for $U > 0$ are mapped to divergences with symmetric eigenvectors in the magnetic channel for $U < 0$. Analogously, $[A + JB] - [C + JD]$ is the symmetric blockmatrix of the enhanced channels $\chi_c^{U<0}$ *and* $\chi_m^{U>0}$.

Let us concisely summarize the considerations made so far: The antisymmetric sector A remains *invariant* under $U \leftrightarrow -U$ for all $\chi_r^{\nu\nu'}$. This explains why the red divergence lines ($\chi_c^{\nu\nu'}$) in Fig. 3.9 and their associated antisymmetric eigenvectors (Fig. 3.10) are perfectly mirrored on both sides of the phase diagram. At the same time one finds that the symmetric parts (S) of $\chi_c^{\nu\nu'}$ and $\chi_m^{\nu\nu'}$ are *mapped into one-another* for $U \leftrightarrow -U$, therefore connecting the symmetric divergences and the corresponding eigenvectors, appearing in $\chi_c^{U>0}$ (orange) and in $\chi_m^{U<0}$ (green). Let us stress at this point that the proof given here applies not only to singular eigenvalues, which are connected to divergence lines, but to *all* eigenvalues and eigenvectors of $\chi_r^{\nu\nu'}$. In this way, we have extended the mapping relation known for $\chi_{pp,\uparrow\downarrow}^{\nu\nu'}$ [33, 54, 113], see Eq. 3.16, to the entire particle-hole sector, clarifying the relation with the mapping of the physical D.o.F.: The antisymmetric subspace A of all channels r, which is not contributing to the physical susceptibility (cf. Eq. (2.56)), is *invariant* under the Shiba transformation, while the symmetric subspace is found to transform in accordance with Eq. (3.12).

As we have illustrated, the particle-hole symmetry plays a central role in determining the mirroring properties of the generalized susceptibilities. If one relaxes this constraint, the bisymmetry in the particle-hole sector is lost, and the eigenvalues are no longer necessarily real. At the same time, it is important to stress that even in the absence of particle-hole symmetry (e.g., out of half filling) $\chi_{pp,\uparrow\downarrow}^{\nu\nu'}$ remains [23] bisymmetric, as shown explicitly in Sec. 2.2.4.2, ensuring the validity of all associated properties (real eigenvalues as well as bisymmetry and associated properties).

3.1.2.3 Spectral representations of physical susceptibilities

The relation between generalized and physical susceptibilities emerging from our numerical and analytical analysis can be illustrated in a physically insightful way. As, for half filling, all eigenvalues of $\chi_r^{\nu\nu'}$ are real, we introduce a *susceptibility density* $\rho(\chi)$ defined (cf. Eq. (2.56)) as

$$\rho_r(\chi) = \sum_i \left| \sum_\nu V_i^r(\nu) \right|^2 \delta(\chi - \lambda_i^r) \geq 0 \tag{3.27}$$

from which the local physical susceptibility is readily obtained as an average over $\rho_r(\chi)$

$$\langle \chi_r \rangle = \int \chi \, \rho_r(\chi) \, d\chi \, . \tag{3.28}$$

This representation has several advantages: Equations (3.27) and (3.28) enable to distinguish immediately between positive ($\lambda^i > 0, \rho(\lambda^i) > 0$), negative ($\lambda^i < 0, \rho(\lambda^i) > 0$) and vanishing ($\lambda^i = 0$ or $\rho(\lambda^i) = 0$) contributions to the static response χ_r. Further, its
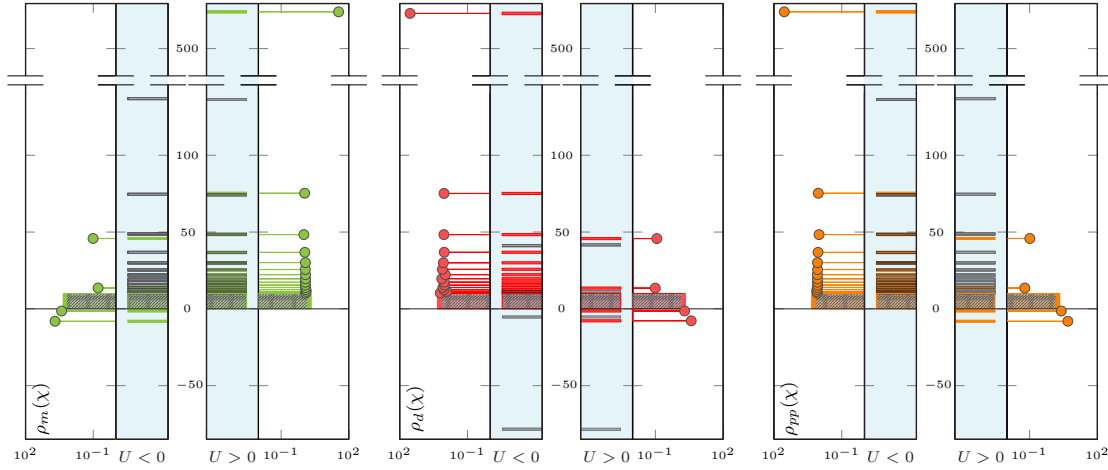
Figure 3.11: Comparison of susceptibility densities Eq. (3.28) for the magnetic (green), charge (ρ_d red), and pp (orange) sectors of the attractive $U < 0$ and repulsive $U > 0$ case, respectively. Each δ function in Eq. (3.28) is represented by horizontal bars (grey/colored if corresponding to an antisymmetric/symmetric eigenvector). The corresponding susceptibility densities $\rho_r(\chi)$ are plotted as colored circles. Data shown here was obtained for $T = 0.2$ and $U = 2.16$ in units of D. The position in the phase diagram is indicated by light blue stars in Fig. 3.9.

graphical conciseness is particularly suited to illustrate how the mapping of the generalized susceptibilities works for the different cases, highlighting the most relevant physical implications.

The introduced representation is applied here to analyze our susceptibility data after crossing four divergence lines at two mirrored positions in the phase diagram (light-blue stars in Fig. 3.9).

The corresponding results are shown in the three plots of Fig. 3.11, representing the three scattering channels. The positions of all eigenvalues λ_i^r are shown as bars in the light-blue shaded innermost panels of the three plots: *Gray bars* indicate eigenvalues associated to antisymmetric eigenvectors and thus to a vanishing ρ_r which does *not* contribute to χ_r. *Colored bars* account for eigenvalues associated to finite $\rho_r(\lambda_i^r)$ values, corresponding to symmetric eigenvectors whose weighted sum builds up the full χ_r. The actual value of the susceptibility density ρ_r for a given eigenvalue is indicated by the circle-symbols in the outermost panels of the plots in Fig. 3.11. The color-shaded regions slightly above $\chi \sim 0$ represent an increasingly denser distribution of small positive eigenvalues, arising from the high-frequency behavior of $\chi_r^{\nu\nu} \propto \frac{1}{\nu^2} \delta^{\nu\nu'}$. It can be shown that this (essentially non-interacting) large-ν feature induces a van Hove singularity in the $T \to 0$ behavior of $\rho_r(\chi) \simeq 1/\chi^{-3/2}$ for $\chi \to 0$, see the Appendix of Ref. [26].

The three plots of Fig. 3.11 graphically combine *all* aspects of the attractive-repulsive mapping of the generalized susceptibilities and allow for a comprehensive understanding at a single glance.

The location of the colored bars together with the corresponding values of $\rho_r(\chi)$ are transformed fully consistently with the mapping of the physical DOF. In accordance with

the results of Sec. 3.1.2.2, not only the physical susceptibility, but the entire distribution $\rho_r(\chi)$ of the identical charge and pp (pseudospin) sectors are mapped onto the magnetic (spin) sector and vice versa.

On the contrary, the positions of the gray bars of each channel are *unchanged* in the $+U$ and $-U$ cases, reflecting the perfect *invariance* of the antisymmetric subspaces of all generalized χ_r under the mapping. We note that the identical location of the gray bars in the magnetic and the pp channel reflects the fact that the *entire* generalized susceptibility sectors are transformed exactly as the physical degrees of freedom (compare Eq. (3.16)).

On the other hand, the different locations of gray bars in the charge sector compared to the other channels explain the non-trivial mapping properties of $\chi_c^{\nu\nu'}$ and of the corresponding irreducible vertices.

These general observations allow for a remarkable rationalization of the problem at half filling. Any suppressed local physical susceptibility can be associated to a *unique* susceptibility-density

$$\rho_{sup}(U) = \rho_m^{U<0} = \rho_c^{U>0} = \rho_{pp}^{U>0} .$$ (3.29)

Obviously, by replacing U with $-U$ in Eq. (3.29), a similar property holds for all enhanced susceptibility densities

$$\rho_{enh}(U) = \rho_{sup}(-U) = \rho_m^{U>0} = \rho_c^{U<0} = \rho_{pp}^{U<0} .$$ (3.30)

The comparison of the attractive and repulsive panels of each channel in Fig. 3.11 indicates as an overall trend that the suppression of a susceptibility is associated to a systematic shift of the *colored* bars toward smaller values, as well as to a change of the weight distribution, where the largest values of ρ_{sup} are associated with the smallest eigenvalues. This supports the physical picture that an interaction-driven suppression of a static local susceptibility is connected to an increasing number of negative eigenvalues and therefore with the crossing of multiple vertex divergences.

At the same time, this demonstrates why the "reverse" implication of the physical picture above is not correct. The perfect *invariance* of the gray bars under the mapping, whose physical content is totally decoupled from the static susceptibility, implies the perfect mirroring of all red divergence lines where only the charge channel is singular (Fig. 3.9). Hence, the occurrence of red divergence lines is *independent* of the behavior of the corresponding susceptibility as well as of the SU(2)×SU(2) symmetry properties of the model considered.

Finally, important quantitative information can also be gained from Fig. 3.11. By analyzing the behavior of the enhanced susceptibilities, it is evident that ρ_{enh} is dominated by the contribution of a *single* term: the one associated to *largest* eigenvalue λ^{max}. This property is illustrated in Fig. 3.12, where we compare the actual values of the static response functions χ_c and χ_m obtained from Eq. (3.28) with the case where the summation in Eq. (3.27) is reduced to the largest eigenvalue only. The contribution from the largest eigenvalue λ_{max} reproduces the trend across the entire repulsive and attractive regime very
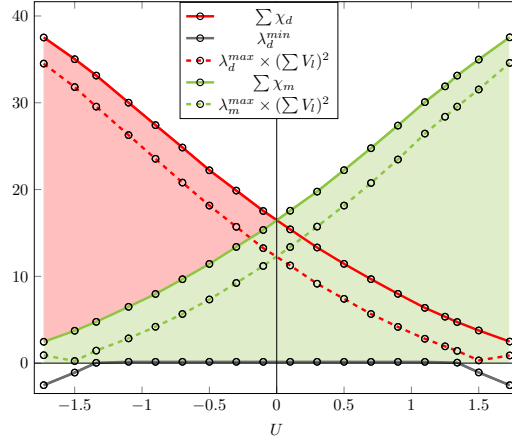
Figure 3.12: Comparison between the static charge $\chi_c(\omega = 0)$ (red) and magnetic $\chi_m(\omega = 0)$ (green) susceptibility and the contribution of the largest eigenvalue only, as a function of the attractive/repulsive Hubbard interaction U at $T = 0.2$. At the bottom of the plot, the lowest eigenvalue of $\chi_c^{\nu\nu'}$ is shown. The evolution of the lowest eigenvalues (λ_d^{min}, in dark gray) is completely decoupled from the behavior of the static susceptibility.

well and approximates to a great extent the actual value of the static susceptibilities χ_c and χ_m in their respective enhanced regions. Since the relation $V_{enh}^{max} = V_m^{max} = V_c^{max} = V_{pp}^{max}$ follows from Eqs. (3.25), (3.26) and (3.16), the value of *all* physical susceptibilities in their respective enhanced regions can be approximated by

$$\langle \chi_r \rangle \sim \lambda^{max} \left| \sum_\nu V_{enh}^{max}(\nu) \right|^2 . \tag{3.31}$$

According to this relation, the Curie-Weiss behavior of any static local susceptibility in the strong-coupling regime can be ascribed to the evolution of the corresponding λ^{max} and the associated eigenvector.

At the end of this section, it is useful to summarize the most relevant features emerging from the analysis of the divergence lines in the (attractive and repulsive) half-filled Hubbard model solved by DMFT.

- In the DMFT solution of the half-filled HM, infinitely many divergence lines are found, which can be grouped according to the symmetry of the underlying eigenvector.

- Divergences with an associated antisymmetric eigenvector are found in the *charge* channel (**red** lines), irrespective of the sign of U. Due to the antisymmetry of the eigenvector, the corresponding eigenvalues are not contributing to the physical response.

- Divergences with an associated symmetric eigenvector are found in those channels, where the physical response is suppressed. For repulsive interactions, this is realized simultaneously in the *charge* and the *pp* sector (**orange** lines),

> while for attractive interactions, divergences of this kind are found in the *magnetic* channel (**green** lines).
>
> - In all cases, the divergence lines are found already in the Fermi-Liquid metallic phase, for interaction values significantly smaller than those corresponding to the Mott-MIT. At high-T and large-U, the behavior of the vertex divergences can be understood to a great extent via a comparison to the atomic limit. In particular, in this regime, the divergence lines display a qualitatively similar linear behavior. For intermediate- to low-temperatures, however, this changes drastically. A bending of divergence lines towards higher values of U is found, with $T \to 0$ endpoints at finite interaction values. Unlike in the disordered models discussed in Sec. 3.1.1.2, these endpoints do not coincide for $T = 0$. Moreover, in contrast to the AL and BM/FK cases discussed above, no energy scale can be identified, that controls the behavior of at least one kind of divergence.

3.1.3 Divergences in the Anderson impurity model at half filling

*Parts of this chapter, marked by a vertical bar, have already been published in the APS journal Phys. Rev. B **97**, 245136 (2018).*

In this part, we consider the divergences found for the case of the AIM (defined in Sec. 2.1.1) at half filling. This allows for an investigation of the remaining question posed at the end of Sec. 3.1.1.3: whether or not the MIT represents a necessary condition for the appearance of irreducible vertex divergences. At the same time, the AIM enables us to directly investigate the interplay between the behavior of the divergence lines and the Kondo scale (cf. Sec. 2.1.1.4).

Note that in the following section the notation is slightly changed: The fermionic Matsubara frequencies are denoted by $i\nu_n[= (2n + 1)\pi T]$ in order to better illustrate the significant difference between the behavior of the quantities of interest as a function of Matsubara index n and the frequency $i\nu_n$. This slight modification of our notation also facilitates the distinction between finite temperature Matsubara frequencies $i\nu_n$ and their continuous imaginary frequency counterparts at $T = 0$: $i\nu$.

3.1.3.1 The T–U diagram

We start to illustrate our numerical results by reporting in the T–U diagram of the AIM (Fig. 3.13 left panel) the first (five) lines along which the two-particle irreducible vertex diverges. These correspond to the interaction values U at given temperatures T, where an eigenvalue of the generalized susceptibility vanishes, see Eq. (3.1), in the following denoted by $\widetilde{U}$. Specifically, the red lines mark irreducible vertex divergences taking place in the charge channel only, while orange lines represent divergences taking place in the charge
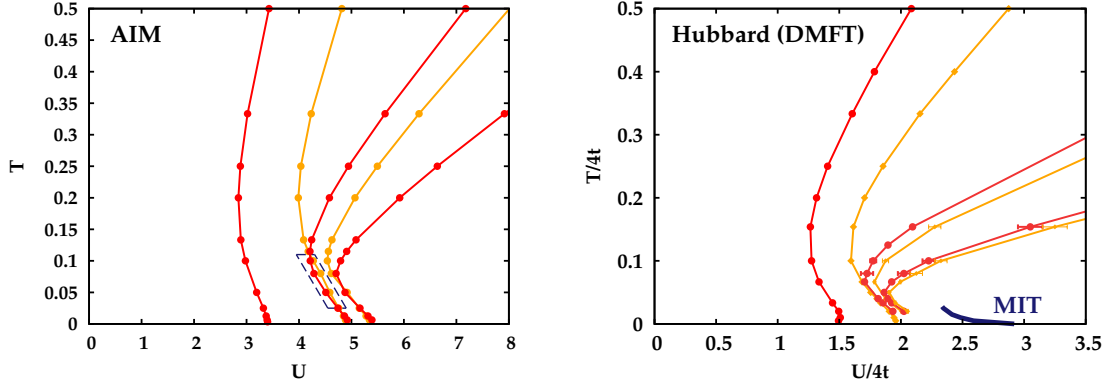
Figure 3.13: Left panel: $T - U$ diagram of the AIM at half filling, showing the first divergence lines along which the static ($\omega = 0$) irreducible vertex functions diverge. For red lines this divergence takes place in the charge channel, $\Gamma_c^{\nu_n \nu_{n'}}$, along the orange lines simultaneous divergences in the charge and the particle-particle up-down channel, $\Gamma_c^{\nu_n \nu_{n'}}$ and $\Gamma_{pp,\uparrow\downarrow}^{\nu_n \nu_{n'}}$, are observed. The dashed blue box marks the parameter region where the "atomic" ordering of divergence lines is violated (see text). Right panel: Reproduced Fig. 3.8 here for convenience and consistency with Ref. [22].

and the particle-particle up-down channel simultaneously (in agreement with the cases discussed so far).

Even from the first look at the data, the overall behavior of the divergence lines of the AIM appears qualitatively *very similar* to the one of the Hubbard model case [10, 19], shown in Figs. 3.8 (and 3.9), and reproduced for the square lattice case in the right panel of Fig. 3.13 (for convenience and consistency with Ref. [22]).

In particular, the similarity in the high-temperature/large interaction area of both T–U diagrams is not fully unexpected. In fact, here the divergence lines of both models display a rather linear behavior, which is consistent with the insights obtained from the results of the Hubbard atom case [19, 23]. The residual deviations can be ascribed to the fact that the atomic limit condition, i.e., U and T larger than all other energy scales, is not fully complied. In the case of the AIM, only for larger interactions than those shown in the left panel of Fig. 3.13 ($U \geq D = 10$), we recover a purely linear behavior (cf. Ref. [29]) as well as the perfect connection between the position in Matsubara frequency space of the divergence and the inflection point of Im $G(i\nu_n)$ [23], as expected for the atomic limit (for a more detailed analysis, see Appendix A of Ref. [22]).

At intermediate temperatures, the divergence lines show a progressively stronger non-linear behavior, starting to bend rightwards. Lowering the temperature further, one reaches the correlated metallic regime. Remarkably, in spite of the differences in the ground states of the two models (there is no MIT in the AIM), even there the results of the AIM and the Hubbard model remain qualitatively *very similar*. For both models the lines show a "re-entrance", i.e., a bending toward higher interaction values, as if the low-temperature intermediate interaction regime were "protected" against the non-perturbative mechanism originating the irreducible vertex divergences. Particularly remarkable, however, is that finite $\widetilde{U}$ values at $T = 0$ are observed in both cases, for the AIM the low-temperature
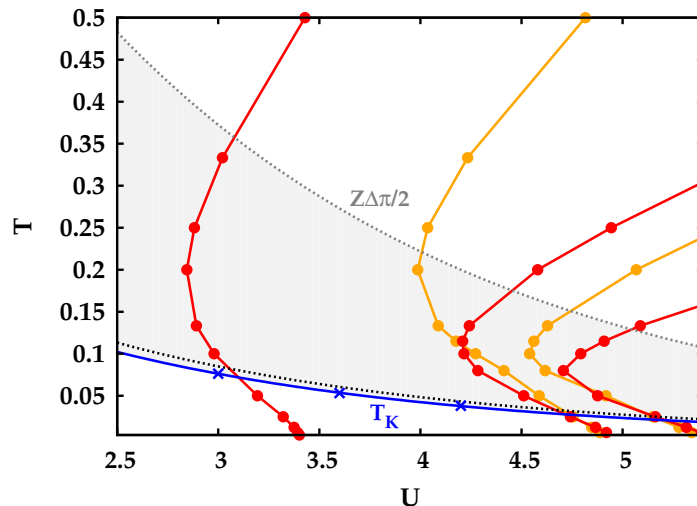
Figure 3.14: A zoom of the T–U diagram of the AIM (left panel Fig. 3.13) at half filling is shown. The blue-solid line marks the Kondo temperature (T_K), estimated from the rescaling of our numerical data for the magnetic susceptibility [39, 40], see Sec. 4.1. The black-dotted line represents an estimate for T_K obtained from an analytic expression [30] valid in the limit $D \gg U, T$, see Eq. (2.9). An additional scale related to the Kondo screening, the half-bandwidth of the $T \to 0$ Kondo peak ($\frac{\pi}{2} Z \Delta_0$) [30] is marked with a gray-dotted line, and is roughly five times larger than T_K. The light-gray shaded area can be regarded, thus, as the parameter region where the effects of the Kondo screening become visible.

behavior of the first line is investigated in detail in Sec. 3.1.3.3.

In the framework of the overall similarity discussed above, a specific difference can be noticed, however. This is highlighted by the dashed blue box in the left panel of Fig. 3.13 (see Fig. 3.14 below for a zoom): At intermediate temperatures, the second and third divergence line in the T–U diagram of the AIM cross, breaking the "atomic" line-order found in all cases analyzed so far (i.e., always an orange line after a red one, before the next red line). Nonetheless, the two divergence lines cross again at lower temperatures, restoring the typical line-order. We also observe that even the fourth and fifth line show such a peculiar crossing, though, to a much smaller extent. To verify the reliability of this observation several tests were performed using exact diagonalization (ED) calculations of the generalized susceptibility (see Ref. [29] for details). As it turns out, our ED analysis (not shown) has confirmed, within the numerical accuracy, the occurrence of such a line crossing. Although somewhat unexpected and not observed in other cases, the crossing of divergence lines is not in conflict with the theoretical understanding of vertex divergences [12], which is discussed in detail in Sec. 3.3. However, it remains to be understood why such a situation is apparently not realized in the correlated metallic regime of the Hubbard model solved by DMFT.

Finally, as for the theoretical understanding of the low-T regime of the AIM, it is important to estimate the Kondo scale T_K and its possible connection to the properties of the irreducible vertex divergences. In Fig. 3.14 a zoom of the T–U diagram of the AIM,
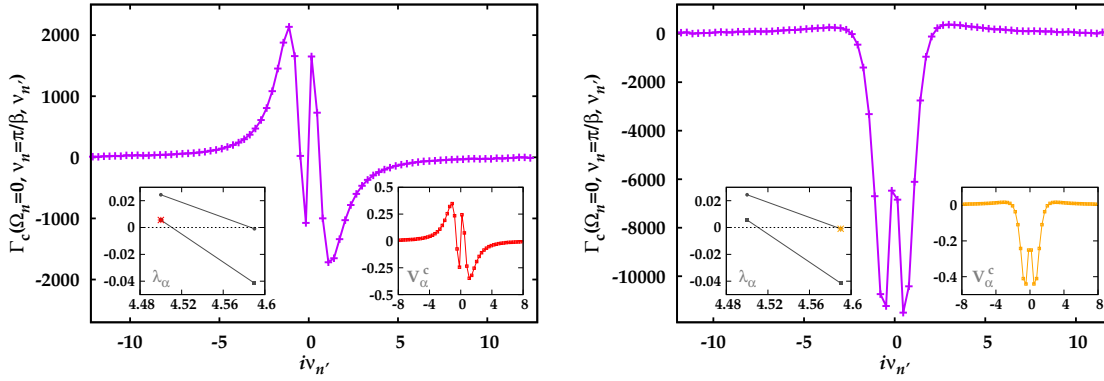
Figure 3.15: Cuts of the static irreducible vertex function in the charge channel, $\beta^2\Gamma_c^{\nu_n\nu_{n'}(\omega_n=0)}$, for a fixed Matsubara frequency, $\nu_n = \pi/\beta$ at $T = 0.05$ and two U values are shown. In the left insets the two eigenvalues of $(\chi_c/\chi_0)^{\nu_n\nu_{n'}}$ closest to zero are reported vs. U, in the right insets the eigenvector $V_\alpha^c(i\nu_n)$ corresponding to the lowest eigenvalue λ_α is shown as a function of $i\nu_n$. Left panel: At $U = 4.5$ the lowest eigenvalue is corresponding to the second red divergence line (red dot), hence $V_\alpha^c(i\nu_n)$ is antisymmetric. Right panel: For $U = 4.59$ the eigenvalue of the first orange line is the smallest (orange dot), $V_\alpha^c(i\nu_n)$ is symmetric.

shown in Fig. 3.13, is presented together with several estimates for the Kondo temperature T_K. In particular, the black dotted line represents the analytic estimate of Eq. (2.9), valid in the $D \gg U, T$ parameter regime [30] (cf. Sec. 2.1.1.4), while the blue line is determined through the universal scaling of the numerical susceptibility data [39, 40] (see Sec. 4.1 below). We note that the two procedures yield extremely close estimates of T_K. However, the Kondo temperature marks not a phase transition, but a smooth crossover, as discussed in Sec. 2.1.1.4. Indeed, the screening processes associated with it become active already at temperatures larger than T_K. For instance, we see that the temperature below which the effects of the Kondo resonance become visible in the spectrum is $T \lesssim Z\Delta_0\frac{\pi}{2}$, the half-bandwidth of the central peak [30] (Z refers to the quasiparticle weight factor, and was extracted from polynomial fits of $\Sigma(i\nu_n)$ for very low temperatures ($\beta = 300$)). We choose this scale to define the upper border of the corresponding crossover regime (shaded gray area in the T–U diagram of Fig. 3.14). It is quite visible, how the bending of the divergence lines is essentially occurring in this parameter region.

3.1.3.2   Classification of the singular eigenvectors

In order to make our study of the vertex divergences in the AIM more quantitative, we proceed with the analysis of the singular eigenvectors in the charge channel, associated to a vanishing eigenvalue of $\chi_c^{\nu_n\nu_{n'}}$ (see Eq. (3.1)). As illustrated in Fig. 3.2 and Fig. 3.3, their frequency structure controls the frequency dependence of $\Gamma_c^{\nu_n\nu_{n'}}$ in the proximity of – and especially at – a vertex divergence.

Since the perfect mapping, discussed in Sec. 3.1.2, is also applicable to the particle-hole symmetric AIM, the singular eigenvectors $V_\alpha^c(i\nu_n)$ and $V_\alpha^{pp,\uparrow\downarrow}(i\nu_n)$, associated to the orange divergence lines, are identical. For this reason $V_\alpha^{pp,\uparrow\downarrow}(i\nu_n)$ will not be shown in the

following. Additionally, note that below we will frequently display the eigenvectors of $\chi_c^{\nu\nu_1}[\chi_0^{-1}]^{\nu_1\nu'} = (\chi_c/\chi_0)^{\nu\nu'}$. This choice has specific practical reasons: locating vanishing positive eigenvalues of $(\chi_c/\chi_0)^{\nu\nu'}$ is significantly easier[13] than for $\chi_c^{\nu\nu'}$, see also Refs. [19, 22, 29]. Hence, since at half filling, the locations where the eigenvalues of both $(\chi_c/\chi_0)^{\nu\nu'}$ and $\chi_c^{\nu\nu'}$ become singular as well as the corresponding singular eigenvectors perfectly coincide [22, 29], it is more convenient to directly study $(\chi_c/\chi_0)^{\nu\nu'}$. Out of half filling, however, these properties are no longer guaranteed, see Ref. [107].

In general, the results for the AIM presented in the right insets of Fig. 3.15 and in Fig. 3.16 are qualitatively consistent with the AL and HM cases discussed above: Red divergence lines are associated to antisymmetric eigenvectors, while orange divergence lines have corresponding symmetric eigenvectors [22].

The symmetry of the singular eigenvectors is, as expected, well reflected in the frequency structure of the irreducible vertex. As another illustration of this connection, a cut of the irreducible vertex function in the charge channel, $\Gamma_c^{\nu_n=\pi T,\nu_{n'}}$ for two values of the interaction U at the same temperature ($T = 0.05$) is shown in Fig. 3.15. In fact, in spite of the proximity between the second red and the first orange divergence line for these parameters, it can be clearly seen how the frequency structure of the vertex function is almost perfectly antisymmetric/symmetric in the case where the lowest eigenvalue corresponds to a red/orange divergence line (left/right panel).

After discussing this general feature of the singular eigenvectors, we turn to their intriguing evolution with decreasing temperature, and start by going back to Fig. 3.16. There, eigenvectors corresponding to the five divergence lines (three red, two orange) shown in the left panel of Fig. 3.13 are compared for the same low temperature ($T = 0.025$). We further plot properly rescaled eigenvectors corresponding to the red lines at the highest temperature employed in the calculations ($T = 0.5$) in gray. The latter show an almost perfect agreement with the atomic limit: Eigenvectors, localized in Matsubara frequency space, which have finite weight almost only at one frequency [$\nu_n = (2n+1)\pi T$] equal to the energy scale ν^*. For example for the first divergence line (top panel) the gray eigenvector displays its by far largest contribution at the first Matsubara frequency ($n = 0$, $i\nu_n = \pi T$).

This specific property of frequency localization, characterizing the singular eigenvectors of the red divergence lines of the AL, and those of the HM and the AIM at high-T, gets lost when reducing the temperature. At $T = 0.025$ we note that their frequency decay is even slower than for the singular eigenvectors of the orange lines, which in the literature were always associated to "global" divergences [19]. In turn, this means that also the divergence of Γ_c is no longer restricted to a finite set of frequencies. Such a "frequency-broadening" of the red singular eigenvectors at low temperatures was so far only observed in the DMFT solution of the Hubbard model [19] (cf. Fig. 3.10), and seems to be associated with the presence of coherent quasiparticle excitations.

---

[13]This is due to the $1/\nu^2$ contribution originated by the bubble term, which creates many small, but never singular, eigenvalues of $\chi_c^{\nu\nu'}$.
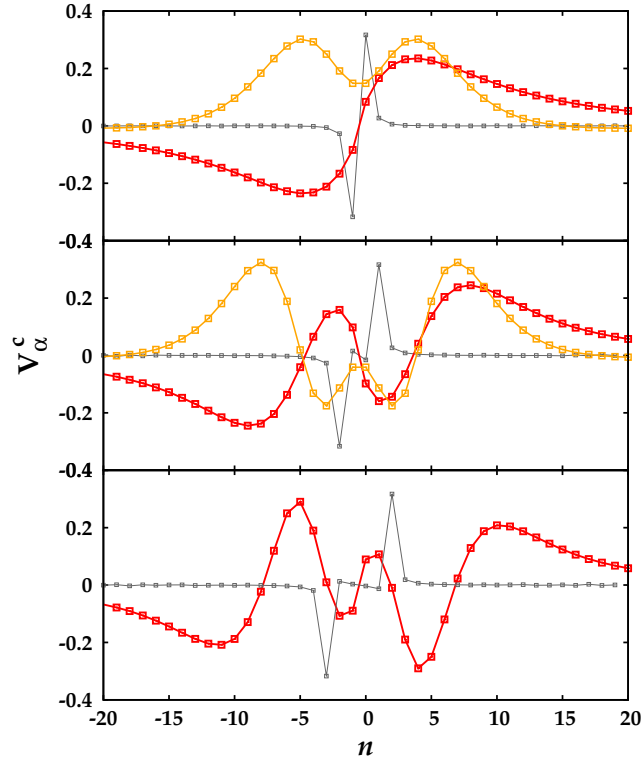
Figure 3.16: Singular eigenvectors of $(\chi_c/\chi_0)^{\nu_n \nu_{n'}}$ corresponding to the five divergence lines (left panel Fig. 3.13), shown as a function of Matsubara index n for the temperature $T = 0.025$. In gray the eigenvectors of the red divergence lines for a higher temperature, $T = 0.5$, properly rescaled, are plotted, indicating the broadening of $V_\alpha^c(i\nu_n)$ for lower temperatures. Top panel: Eigenvectors of the first red divergence line (red, antisymmetric) and the first orange divergence line (orange, symmetric). Middle (Bottom) panel: Same as top panel, but for the second (third) red and orange (red) divergence line.

For both kinds of singular eigenvectors, this general trend is analyzed in detail in Fig. 3.17: In the left panels the eigenvectors are plotted in terms of the Matsubara index n, while in the right panels several V_α^c for low temperatures are demonstrated as a function of Matsubara frequency $i\nu_n$. It can be easily seen, then, that for the eigenvectors corresponding to the first red (upper panels) and the first orange (lower panels) divergence line two regimes are distinguishable: (i) for $T \gg T_K$, the V_α^c are strongly peaked at a given Matsubara index $n_{\max}$, in perfect agreement with the results of the AL, see above. (ii) for $T \lesssim T_K$ the maximum contribution of the eigenvector moves to a higher index with decreasing temperature, i.e. to the right (Fig. 3.17 left panels). Remarkably, one notices instead that, as a function of Matsubara frequency, the maximum contribution of $V_\alpha^c(i\nu_n)$ remains localized at a given frequency $i\nu_{n_{\max}}$ in this regime (Fig. 3.17 right panels).

Finally, it is interesting to analyze in more detail the low-frequency structures of $V_\alpha^c(i\nu_n)$, which can be highlighted by comparing the red singular eigenvectors of different lines at the same low temperature, see Fig. 3.16. In particular, for the eigenvector of the second red divergence line (central panel of Fig. 3.16) an additional local maximum and minimum
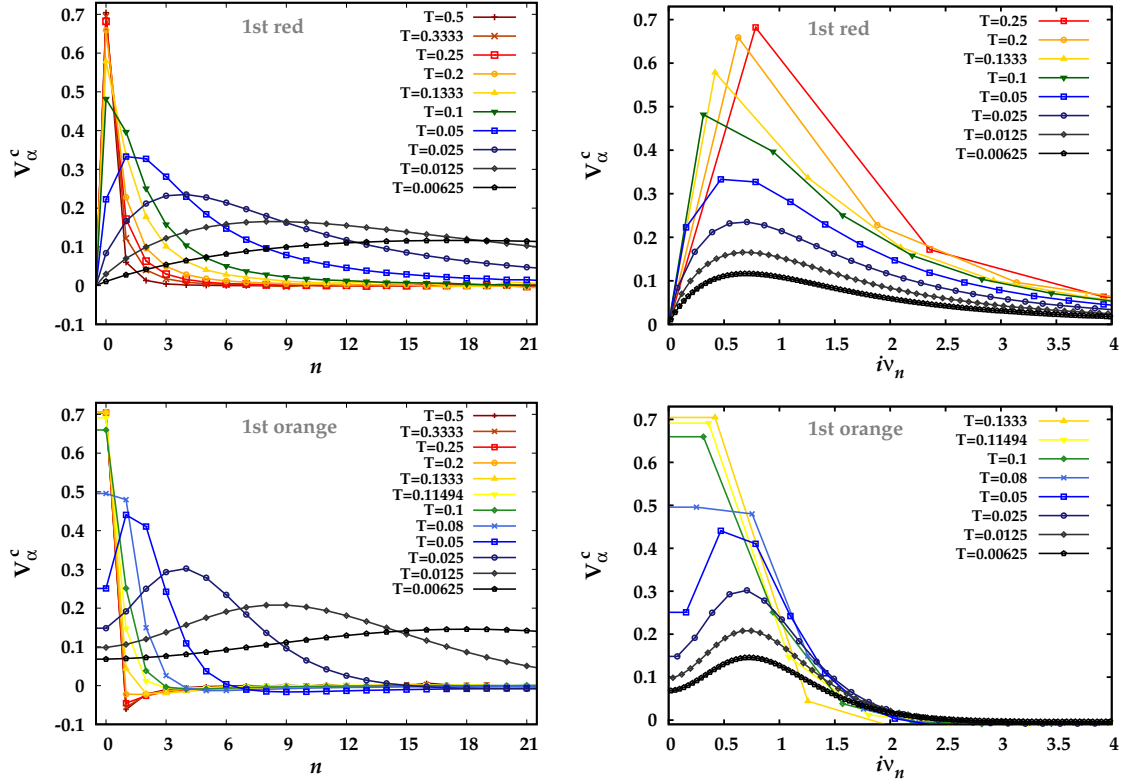
Figure 3.17: Left top panel: Singular eigenvectors $V_\alpha^c(i\nu_n)$ for several temperatures along the first red divergence line, plotted as a function of the Matsubara index n. Right top panel: Singular eigenvectors of the left top panel plotted as a function of Matsubara frequency $i\nu_n = (2n + 1)\pi T$ instead. Bottom panels: As top panels, but showing the data corresponding to the first orange divergence line.

appear at the lowest frequencies, leading to three "nodes" in their frequency components. In the case of the third red line (bottom panel) $V_\alpha^c(i\nu_n)$ has five "nodes". Extrapolating the behavior observed for the first three red divergence lines, one expects that the eigenvector of the n-th red divergence line will have $2n - 1$ "nodes". It is also interesting to note that for the eigenvectors of the first and second red divergence line the respective one or three nodes are also observed in the high-T regime (see the gray eigenvectors). This, however, no longer holds for the eigenvector of the third line.

Let us underline that the symmetry and node-structure of the singular eigenvectors become crucial in practical calculations, where vanishing eigenvalues of generalized susceptibilities need to be associated to the corresponding divergence lines. This consideration is especially important in cases of crossings as seen here for the AIM, or for large values of U, where the divergence lines become very dense in the phase diagram. Also, let us note that the T-dependent frequency structure of the associated singular eigenvectors (described above) can help to correctly locate a divergent parameter set along a divergence line that is being calculated, i.e., in the high- or the low-T regime (cf. Ref. [29]).
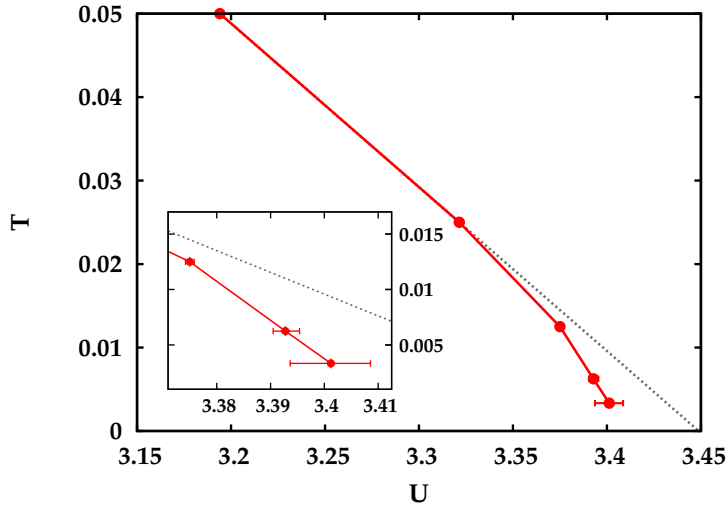
Figure 3.18: Zoom on the first red divergence line (cf. Figs. 3.13 and 3.14), showing the low-T behavior (for $T \ll T_K$), which demonstrates that, within the error bars obtained by a Jackknife analysis, the line bends toward the U-axis for $T \to 0$. Inset: Further zoom on the lowest temperatures, emphasizing the growth of the error bar with decreasing temperature.

3.1.3.3   Calculations in the low-T regime

In the last part of the analysis of the irreducible vertex divergences in the AIM we explicitly consider the low-temperature regime.

   We start by assessing the numerical accuracy of our results for the first red divergence line in the low-T range ($0.003\overline{3} < T < 0.05 < T_K \sim 0.07$). Our results are shown in Fig. 3.18, together with the corresponding error bars. The latter were obtained from a Jackknife error analysis [116] (for details we refer to the Appendix C of Ref. [22]). From the error bars in the main plot and the inset of Fig. 3.18 it can be inferred that the combined scaling (β^3 of the CT-QMC sampling (cf. Sec. 2.3.1.2) and β^2 of the Matsubara frequency box of the vertex function for $i\omega_n = 0$) prohibits us from obtaining informative results about the vertex divergences at temperatures lower than $T = 0.003\overline{3}$. However, the numerical precision for $T > 0.003\overline{3}$ was sufficient to accurately define the low-T behavior. In fact, we can compare our data with the dotted gray line, showing a linear extrapolation of the divergence line to $T \to 0$ using the (higher) temperatures $T = 0.05$ and $T = 0.025$. Even considering the growing error bars, the first divergence line shows a progressive leftwards deviation from the linear extrapolation when reducing the temperature. This is evidently completely inconsistent with an infinite value of $\widetilde{U}$ of the divergence line endpoint for $T \to 0$.

   That the temperatures considered are low enough to allow for a $T \to 0$ extrapolation is also supported by the behavior of the singular eigenvectors. We discuss here the case for the first red and orange divergence line, which is representative for all calculated divergences. In fact, for $T \ll T_K$ (e.g., for $T \leq 0.025$ for the first divergence) the eigenvectors do not only display a maximum at a T-independent value $i\nu_{n_{\max}}$, but as functions of $i\nu_n$, they
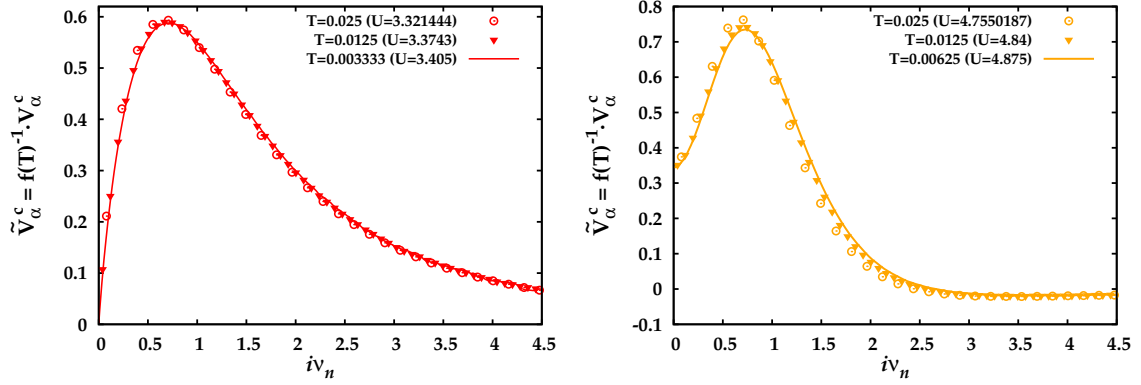
Figure 3.19: Left panel: Eigenvectors of the first red divergence line for a given temperature multiplied with the inverse of the scaling factor $f(T)$, which yields the eigenvector at $T = 0$ that governs the frequency structure of the eigenvectors at all temperatures in the $T \ll T_K$ regime. Right panel: As left panel, but for the first orange divergence line. Here, the minor discrepancies can be ascribed to a stronger U-dependence of the singular eigenvectors in comparison to those of the red lines (cf. Ref. [29]).

even show a perfect scaling in the whole low-T regime (see Fig. 3.19). This demonstrates that the low-T frequency structure of the singular eigenvectors, and hence, of the vertex divergences, is completely controlled by an underlying, T-independent, function: $\widetilde{V}_\alpha^c(iv)$, such that $V_\alpha^c(iv_n, T) = f(T)\widetilde{V}_\alpha^c(iv)$. Our numerical data indicates further that $f(T)$ simply represents the conversion factor needed, when taking the $T \rightarrow 0$-limit of the discrete sum of Matsubara frequencies defining the norm of the eigenvector ($\sum_{v_n} |V_\alpha^c(iv_n, T)|^2 = 1$): $f(T) = \sqrt{2\pi T}$. In Fig. 3.19 the correspondingly rescaled eigenvectors ($= \widetilde{V}_\alpha^c(iv)$) for the first red and orange divergence line are shown. These are extracted from the data for $V_\alpha^c(iv_n, T)$ by exploiting the low-T scaling relation:

$$\widetilde{V}_\alpha^c(iv) = \frac{V_\alpha^c(iv_n, T)}{f(T)} = \frac{V_\alpha^c(iv_n, T)}{\sqrt{2\pi T}} \tag{3.32}$$

In the case of $\widetilde{V}_\alpha^c(iv)$, iv represents continuous imaginary frequencies.

After these considerations for the case of the AIM we summarize the results and elaborate on the implications of the most important findings [22]:

- Consistent with the results for repulsive interactions of the AL and the DMFT solution of the HM, two kinds of divergences are observed in the AIM: Those occurring in the charge channel only (**red** divergence lines), and those affecting the charge and the pp↑↓ channel simultaneously (**orange** lines). The symmetries of the singular eigenvectors coincide with the one seen for the AL and the HM (antisymmetric eigenvectors corresponding to red divergence lines, symmetric ones to the orange kind). Note that these general results were confirmed in a later work by C. Melnick and G. Kotliar [25], where the irreducible vertex

divergences for the same AIM were compared to those of the PAM solved by DMFT.

- The similarity of the results between the AIM and the HM also extends to the low-T regime: In both cases a bending ("re-entrance") of divergence lines is observed as the temperature is reduced, featuring endpoints at finite U values as $T \rightarrow 0$. In particular, in the case of the AIM, the low-T behavior was studied in great detail. The analysis of the lowest-T results of the first divergence line, in comparison with the error bars of the QMC treatment, as well as the scaling behavior of the singular eigenvectors, provides robust numerical evidence that the divergence lines of the AIM end at finite U values for $T \rightarrow 0$[14]. Based on the results discussed so far, several conclusions can be drawn, which we summarize in the following. At the same time, we also formulate some outstanding questions that arise from these conclusions:

    - The striking resemblance between the HM and AIM results for all temperature regimes demonstrates clearly that the presence of the MIT does *not* represent a necessary condition to observe irreducible vertex divergences. Note that this similarity also rules out the so-called "ring-scenario" [19, 22], where two energy scales would take a similar role in the description of the divergences of the HM, as the energy scale ν^* for those of the BM/FK or the AL case.

    - Instead, the AIM results in the very low-T regime call for a reconciliation of well-defined Fermi-Liquid properties on the one hand, with nonperturbative divergence lines down to $T \rightarrow 0$ on the other hand. One could view this problem as an emergence of a nonperturbative Fermi-Liquid phase, whose precise meaning needs to be defined.

    - These results also inspire questions on the possible appearance of vertex divergences on the *real* frequency axis. Based on Eq. (3.1), the scaling of the singular eigenvectors described in Eq. (3.32) and their underlying symmetry properties, one can expect divergences of $\Gamma_{c;pp\uparrow\downarrow}^{(i\nu_n \rightarrow 0)(i\nu_{n'} \rightarrow 0)}$ for $T \rightarrow 0$ for *all orange* divergence lines. Instead, at zero frequency, the red divergences vanish due to the antisymmetric nature of the eigenvectors. So far, only for the BM/FK case, a vertex divergence for real frequencies was observed. However, this was found only *at* the accumulation point at $T = 0$, where all divergence lines coincide [19].

- The interplay between the divergences and the Kondo regime allows for a clear and physically transparent classification: At high-T the divergence lines display a linear behavior, with associated eigenvectors that are localized in Matsubara frequency space, in perfect agreement with the results of the AL. In the regime where the screening of the local moment becomes active (indicated

by the grey region in Fig. 3.14) the divergence lines start to bend and the nature of the eigenvectors is changing. For $T < T_K$ instead, a smooth behavior of the divergence lines is observed, the eigenvectors fully extend over the whole Matsubara frequency range, and even display a perfect scaling for $T \ll T_K$, see Eq. (3.32) and Fig. 3.19. In general, for both the HM and the AIM, the screening of the local moment seems to counter the appearance of vertex divergences, which will be discussed further in Chapter 4.

- Based on these insights, one can formulate a clear-cut prediction for the appearance of divergence lines in the coexistence region of the MIT of the HM, see Chapter IV of Ref. [22]. This was later confirmed by the DMFT calculations of the Master thesis of M. Pelz [84]. In this work, the divergence lines (or in fact the number of negative eigenvalues) in the coexistence region of the Hubbard model on the Bethe lattice solved in DMFT, both for the metallic and the insulating solution, was carefully investigated. In particular, the corresponding number of negative eigenvalues is shown as an intensity plot in Fig. 3.20 (figure taken from Ref. [84], see Fig. 5.1 therein). On a first glance one immediately notices how high the number of negative eigenvalues, and hence how dense the corresponding divergences lines, becomes at large interaction values. The results for the metallic solution indicate the presence of an accumulation point of divergence lines at $U_{c2}(T = 0)$. The insulating solution shows a different (and systematically larger) number of negative eigenvalues as compared to the metallic solution, in agreement with the first order nature of the MIT.
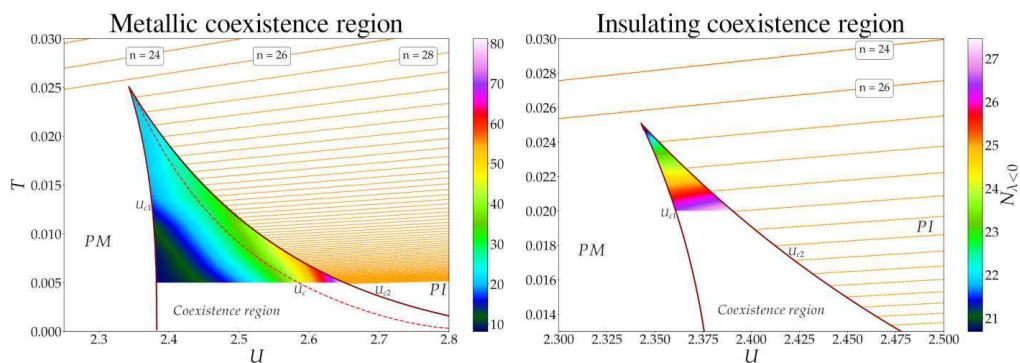

Figure 3.20: Number of negative eigenvalues for the metallic (left panel) and insulating (right panel) solution in the coexistence region of the MIT, shown as an intensity plot (colorscale on the right). The calculation was performed for a Hubbard model on the Bethe lattice (same units as in Sec. 3.1.2), solved by DMFT. The orange lines to the right of the coexistence regions for both solutions represent the divergence lines of the AL. Taken from Ref. [84] (see Fig. 5.1 therein).

---

[14]Let us here also refer to the project work of C. Schattauer [117] (performed in the group of A. Toschi and co-supervised by the author of this thesis), who analyzed the divergences of an AIM with a *single* bath site. Both, the low-T behavior of the first divergence line as well as the scaling of the associated singular eigenvectors, are also verified in this case, providing further numerical support for the conclusions drawn.

3.1.4 Manifestations of vertex divergences out of half filling

In the last section, the irreducible vertex divergences for different models at half filling were discussed in great detail. Here, instead, we consider the vertex divergences in cases out of half filling, where the perfect particle-hole symmetry is broken. For this analysis, it is essential to differentiate between the ph channels $r = c, m$ and the $\uparrow\downarrow$ component of the pp channel. As established at the end of Sec. 2.2.4.2, $\chi_{pp,\uparrow\downarrow}^{\nu\nu'(\omega=0)}$ remains real and bisymmetric (with real eigenvalues and perfectly (anti)symmetric eigenvectors), even if particle-hole symmetry is broken. Thus, for the $r = $ pp $\uparrow\downarrow$ channel, Eq. 3.1 stays valid and continues to determine the divergences of $\Gamma_{r=pp,\uparrow\downarrow}^{\nu\nu'(\omega=0)}$ also out of half filling. For the ph channels $r = c, m$, this is not the case, as the generalized susceptibility $\chi_{r=c,m}^{\nu\nu'}$ is now a symmetric centrohermitian matrix, see Sec. 2.2.4.2, with either real or complex conjugated pairs of eigenvalues. The associated eigenvectors are no longer guaranteed to be real or to demonstrate strict symmetry properties. Hence, for the $r = c, m$ channels, the defining Eq. 3.1 and the corresponding conclusions needs to be re-examined and several modifications need to be taken into account. First of all, as discussed in Sec. 2.2.4.2, the static generalized susceptibility can be written as $V^{-1}DV$ if it is diagonalizable, which is now no longer guaranteed a priori. When $\chi_r^{\nu\nu'}$ is diagonalizable, the analogous equation to Eq. 3.1 reads [67, 73]:

$$\Gamma_{r=c,m}^{\nu\nu'(\omega=0)} = \left(\sum_i V_i^{r-1}(\nu)\left[\lambda_i^r\right]^{-1}V_i^r(\nu') - \left[\chi_0^{-1}\right]^{\nu\nu'} \right), \qquad (3.33)$$

whereas, different from Eq. (3.1), λ_i^r is not guaranteed to be real. This has important consequences for the understanding obtained so far: Even if the real part of a specific eigenvalue $\lambda_\alpha^r = \text{Re}[\lambda_\alpha^r] + i\text{Im}[\lambda_\alpha^r]$ would vanish, Γ_r would not diverge, as long as the *imaginary* part $\text{Im}[\lambda_\alpha^r]$ is nonzero.

In the following we summarize the few existing numerical results, which demonstrate that there indeed exists a doping regime close to half filling, where divergences in the ph-channels are still found, because a subset of eigenvalues remains real. On the other hand, as soon as a doping becomes large enough, these eigenvalues become complex and no true divergence of the irreducible vertex can be found any longer.

A first understanding can already be gained by considering a 2×2 submatrix[15] of $\chi_{c,m}^{(\nu=\pm\pi T)(\nu'=\pm\pi T)}$:

$$\begin{pmatrix} a + ib & c \\ c & a - ib \end{pmatrix} \quad \Rightarrow \quad \lambda_{1,2} = a \pm \sqrt{c^2 - b^2} \,. \qquad (3.34)$$

From this simplified analysis (see Ref. [118]) one can already outline a plausible expectation. Since for the ph-channels out of half filling, the eigenvalues are either real or complex conjugate pairs, while they are strictly real at half-filling, when going out of half filling, the real eigenvalues need to "meet", i.e., become complex pairwise. In the quite recent literature

---

[15]Note that the off-diagonal element c stays real, due to the centrohermitian *and* symmetric property of the generalized susceptibility.
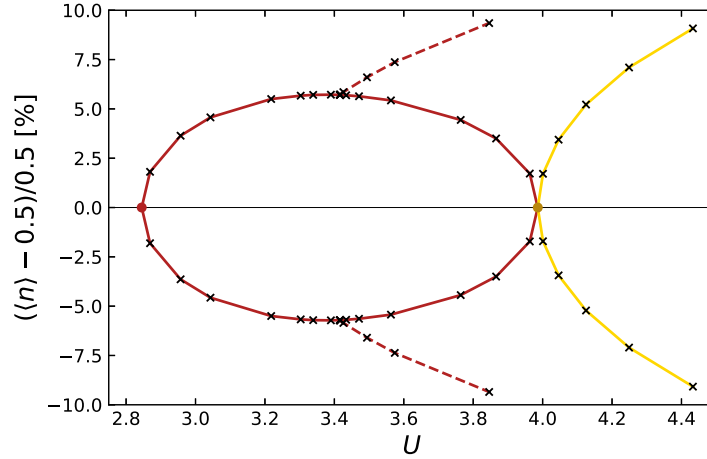
Figure 3.21: First two divergence lines of the AIM (cf. Fig. 3.13) for dopings close to half filling (in percent) at $T = 0.2$. The red divergence lines mark divergences in the charge channel. The orange point at half filling represents the orange divergence line at this temperature, which splits into the second red and the first yellow divergence line along which solely the pp↑↓ component diverges. The red divergence lines meet at $\approx 6\%$ doping, the dashed red line tracks the condition $\mathrm{Re}\lambda_\alpha^c = 0$. Taken from Ref. [107].

on this topic, this has been referred to as "splitting point" [118], "meeting" point [107] or "exceptional point" [119]. In particular, this wording reflects the fact that with increasing doping, starting at half filling, the real parts of $\lambda_{1,2}$ (for $|c| \geq |b|$) need to become closer in value. In fact, $\lambda_{1,2} = a \pm \Delta$ holds (with $\Delta^2 = c^2 - b^2$) for as long as the eigenvalues are still real ($|c| \geq |b|$). As the imaginary part b grows, the eigenvalues approach their meeting point, becoming equal in value, $\lambda_{1,2} = a$, where the matrix is formally *not* diagonalizable. Going further out of half filling, in the case of $|c| < |b|$, $\lambda_{1,2}$ form a complex conjugate pair of eigenvalues with $\lambda_{1,2} = a \pm i\tilde{\Delta}$ (with $\tilde{\Delta}^2 = b^2 - c^2$). Afterwards, the condition $\mathrm{Re}\lambda_{1,2} = 0$ does no longer correspond to an actual vertex divergence (but defines the so-called "pseudodivergence line", whose formal and physical implications need further investigations in the future).

3.1.4.1 Divergences in the AIM out of half filling

The first model considered is the AIM (defined in Sec. 2.1.1), identical to the one analyzed in Sec. 3.1.3, for dopings close to half filling at the fixed temperature $T = 0.2$. This analysis was performed by Leon Domazetovski in the context of a project work in the group of A. Toschi [107]. The results as a function of doping and U for the first two divergence lines (cf. Fig. 3.13) are presented in Fig. 3.21. The first red divergence lines moves toward higher values of U as the doping is increased, until it meets the second *red* divergence line at $\approx 6\%$ doping. Here, right after this meeting point, the eigenvalues become a complex conjugate pair, and no actual vertex divergences is found any longer, in agreement with the simplified 2×2 analysis made above. Note that at this meeting point, the generalized susceptibility is not diagonalizable. For higher dopings, one can track the parameter sets along which the real part of the eigenvalues vanish, which is shown as a dashed red line.
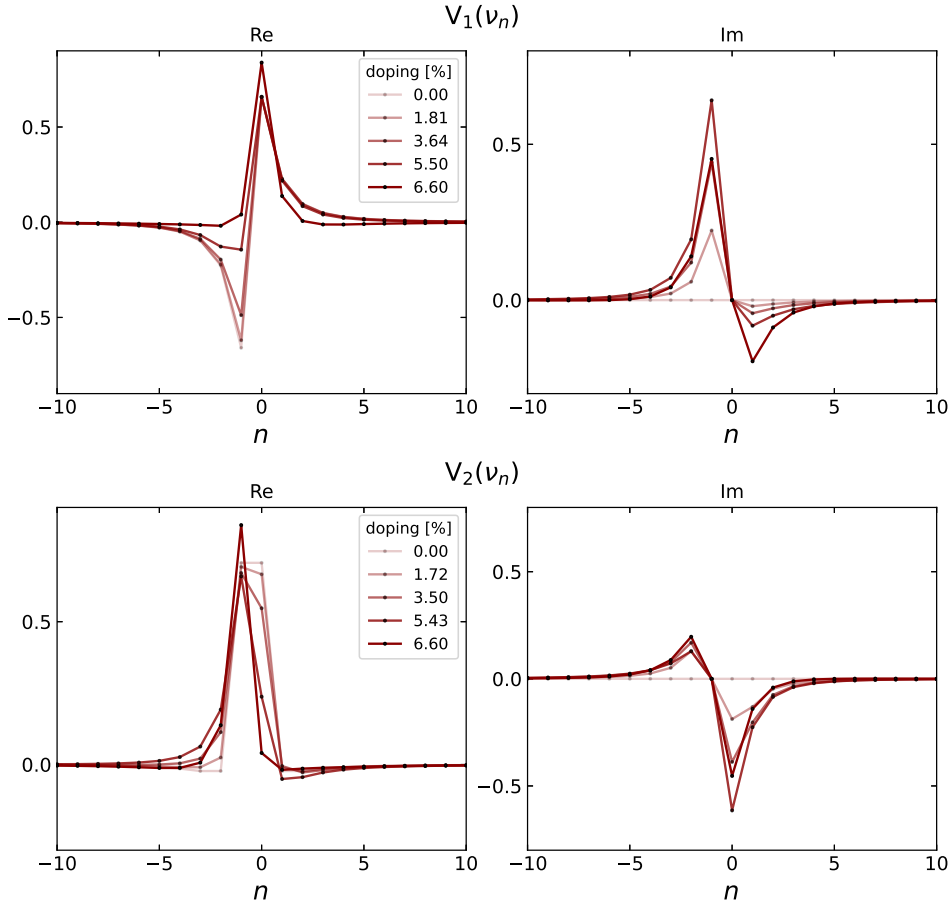
Figure 3.22: Eigenvectors of the first (upper panels) and second (lower panels) red divergence line, along which only the charge channel diverges for different dopings. The panels on the right represent the corresponding imaginary parts, which have nonzero contributions out of half filling. Taken from Ref. [107].

At the same time, due to the violation of particle-hole symmetry (see Sec. 2.2.4.2 and the argument above) the orange divergence line *splits* into the second red divergence line, along which only the charge channel diverges, and the *yellow* line, where a divergence of solely the pp↑↓ component is found. This yellow divergence line shows a similar behavior in doping as the first red divergence line, moving toward higher interaction values with increasing doping. However, as opposed to the red divergence lines, it always marks an actual vertex divergence, due to $\chi_{pp,\uparrow\downarrow}^{\nu\nu'}$ remaining a real bisymmetric matrix even out of half filling (see Sec. 2.2.4.2 and above).

As pointed out in Sec. 2.2.4.2, out of half filling, also the perfect symmetry properties of the singular eigenvectors in the ph-channels are lost. This can be seen in Fig. 3.22, where the eigenvectors along the first two red divergence lines are shown for different dopings. In the right panels the imaginary parts of the corresponding eigenvectors are shown, which have nonzero contributions out of half filling. As Fig. 3.22 illustrates clearly, only for half filing (0% doping), the eigenvectors display perfect symmetry properties.

For further details on the results of the AIM out of half filling we refer to Ref. [107].
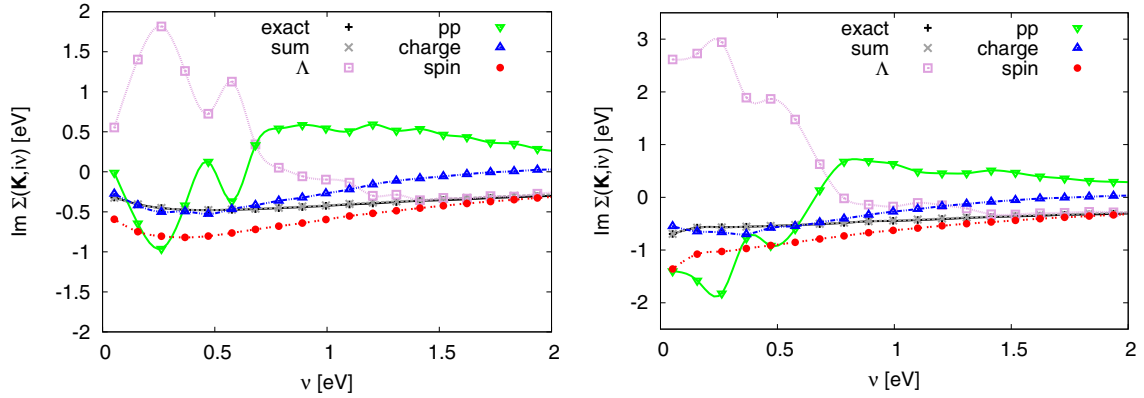
Figure 3.23: Parquet decomposition of the self-energy for the nodal (left panel) and the antinodal (right panel) momentum of a DCA calculation (8 cluster sites) for the Hubbard model on a square lattice with n=0.94, $\beta = 60$, $U = 1.75$. The parquet contributions (Λ, pp, charge, spin (=magnetic)) sum to the DCA solution for Σ (sum and exact). Taken from Ref. [18] (see Fig. 8 therein).

Let us at this point also refer to related works by D. R. Fus and H. Eßl, both working in the group of Alessandro Toschi, who performed a similar analysis for the AL case [118, 120], which yielded results in agreement with the AIM case presented here, and allowed for additional analytic insights.

3.1.4.2 Divergences in the Hubbard model out of half filling

We now consider the case of the Hubbard model (on a square lattice) out of half filling, and at this point also extend the analysis made so far by a crucial aspect: in the following we will review literature results including nonlocal correlation *beyond* DMFT. So far, only divergences in DMFT solutions of the Hubbard model (or disordered models) and for the purely local AL and AIM were considered. One should not get the wrong impression, however, that the irreducible vertex divergences are a phenomenon restricted to local physics. This is absolutely not the case, as was first shown in a work by O. Gunnarsson *et al.* [18] in 2016.

In this work the parquet decomposition idea was applied to the self-energy for the Hubbard model on a square lattice using both, DMFT and the dynamical cluster extension (DCA) [121]. Summarizing briefly the main idea of Ref. [18]: By decomposing the full vertex $F_{\uparrow\downarrow}$ in the second term of the Schwinger-Dyson equation (cf. 2.3.2) according to the parquet equation, introduced in Eq. (2.20), one can split the self-energy into four parts corresponding to the different diagrammatic channels: $\Sigma = \Sigma_\Lambda + \Sigma_{pp} + \Sigma_c + \Sigma_m$. The first term is originated by the fully irreducible vertex, the other terms by reducible vertices in channels $r = pp, c, m$. In principle, this procedure would allow to individually inspect the effects that the two-particle fluctuations, separated into the different fluctuation channels, have onto the one-particle self-energy (and thus also e.g., on the one-particle spectrum). Let us also refer to recent publications, where this idea is reviewed and compared to other approaches, such as the fluctuation diagnostics [122], which work in the same spirit [58, 59]. The fundamental problem of the parquet decomposition of the self-energy is that
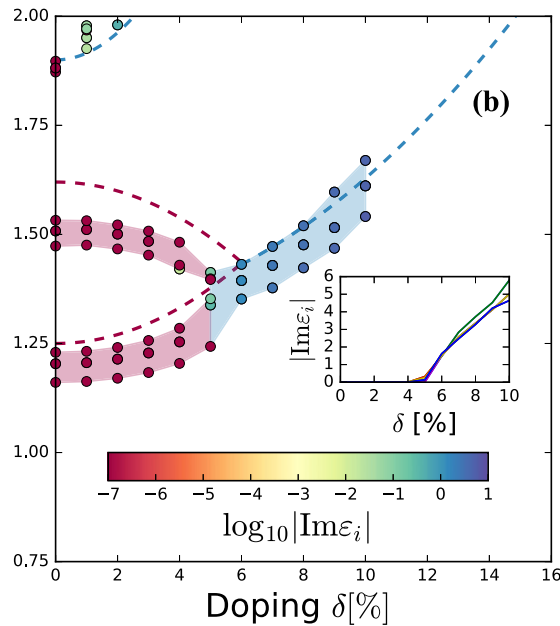
Figure 3.24: Divergence lines of the charge channel in the Hubbard model on a square lattice, solved by DMFT (dashed lines) and CDMFT(colored areas), as a function of U and doping δ. The color map represents the magnitude of the imaginary part of the associated eigenvalues. The inset depicts the behavior of the imaginary parts of those eigenvalues, associated with the colored areas, as a function of doping. Taken from Ref. [21] (see Fig. 1 therein).

possibly diverging irreducible vertices directly enter into the approach. In fact, this type of procedure breaks down in the nonperturbative regime. As an example, in Fig. 3.23, results of Ref. [18] showing a DCA calculation (8 cluster sites) for the underdoped case n=0.94 at $\beta = 60$ and $U = 1.75$ (in eV units) is presented, a parameter set where the momentum differentiation of the self-energy is found (see exact and sum data sets in Fig. 3.23). In the left panel the different contributions to the self energy at the nodal point ($\mathbf{k} = (\frac{\pi}{2}, \frac{\pi}{2})$) are shown, in the right panel at the antinodal point ($\mathbf{k} = (\pi, 0)$) [18]. As can be seen easily, the fully irreducible contribution (Λ) is fluctuating wildly, due to the proximity of divergences of the corresponding irreducible vertex function[16] [18]. The full self-energy, however, is well-behaved, because in the sum (grey crosses), the pp-contribution compensates for the uncontrolled Λ-contribution [18].This is related to the fact that the full vertex $F_{\uparrow\downarrow}$ remains finite, as discussed at the beginning of this chapter. The magnetic (spin) and charge contributions on the other hand appear well-behaved for the parameter set considered. While this is not surprising for the former, as the irreducible vertex function in the magnetic channel do not diverge for the repulsive model considered (see Sec. 3.1.2), the absence of an unstable behavior of the charge contribution needs additional considerations. In fact, this numerical outcome can be reasonably explained by assuming that the divergences of the charge channel have already been neutralized due to breaking particle-hole symmetry, which has been discussed above (cf. Eq. 3.33).

---

[16]As discussed in [18], it is mostly the momentum dependence of the generalized susceptibility, which triggers the divergence observed in the DCA results.

Another important study on vertex divergences of the HM beyond the single-site DMFT is represented by the work of J. Vučičević *et al.* [21]. In Fig. 3.24 the first three divergence lines of the Hubbard model (square lattice) solved by DMFT (dashed lines) and cellular DMFT (CDMFT) [121] (colored areas) as a function of U and doping for a fixed temperature of $T = 0.125$ (in units of $4t$) are shown, taken from Ref. [21]. Note that in this work only the charge channel has been considered. Similarly to the results for the AIM out of half filling, the DMFT solution (dashed lines) yields real eigenvalues for a limited doping region around half filling. In the case of the third divergence line ($U \approx 1.8$) already for small dopings the eigenvalue becomes complex. The first two divergence lines meet at around 6% doping, as in the AIM case. The CDMFT results, obtained for a 2×2 cluster, yield real and complex eigenvalues which are shown as colored areas in Fig. 3.24. These results demonstrate three important features: (*i*) Instead of one eigenvalue crossing zero, four eigenvalues cross zero at fairly similar parameter sets, which defines the colored areas. (*ii*) As also noted in Ref. [18], these divergence areas shift toward *lower* values of U as compared to the single-site DMFT results. (*iii*) They appear to be become neutralized by the increase of the imaginary parts of the associated eigenvalues already at dopings slightly closer to half filling.

The second point (*ii*) can be qualitatively understood by recalling the half-filling results for the vertex divergences of the AIM and the DMFT solution of the HM, summarized at the end of Sec. 3.1.3. Since in cluster approaches the MIT of the HM is shifted to lower values of U [51], also a possible accumulation point of divergences at U_{c2} is most likely shifted toward lower values of U. Assuming, that the distance between divergence lines at intermediate coupling does not change dramatically, one can expect to find divergence lines of the HM solved in cluster extensions of DMFT already at lower values of U, as compared to those of the single-site DMFT solution.

Eventually, all the (few) existing results for the irreducible vertex divergences out of half filling can be summarized as follows:

- When the condition of perfect particle-hole symmetry is released (e.g., by doping the system away from half filling), the local generalized ph-susceptibility acquires imaginary components, yielding a centrohermitian matrix. The latter is characterized by eigenvalues which can be either real or complex conjugated pairs. The appearance of an imaginary part in an eigenvalue with a vanishing real part evidently cuts off a possible irreducible vertex divergence.

- For repulsive interactions, divergence lines in the charge channel in doping regions close to half filling are still found (**red** lines). If the doping is large enough, however, these divergence lines meet pairwise, and the corresponding singular eigenvalues develop nonzero imaginary parts. After this exceptional point, where the generalized susceptibility is formally not diagonalizable, no actual divergences of the irreducible vertex in ph channels are found any longer. The corresponding singular eigenvectors become complex and lose
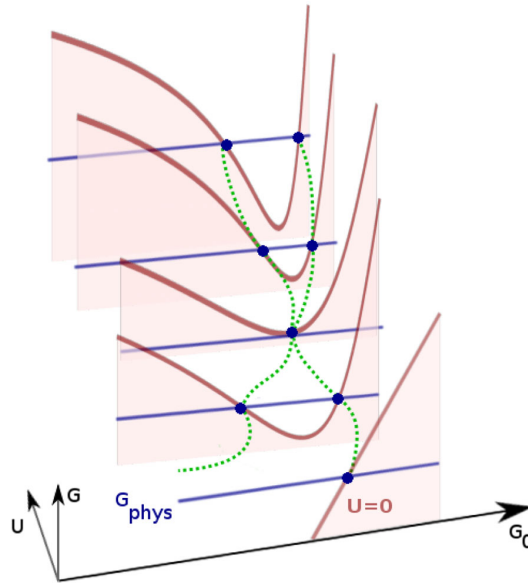
Figure 3.25: Simplified illustration of $G[G_0, U]$, where multiple G_0's (blue dots) correspond to the same physical G (blue lines) for different values of U (sheets). The dashed green lines represent the corresponding self-energies. A crossing of the physical branch, which is connected to the $U = 0$ sheet, and an unphysical solution, is demonstrated in the third sheet. Taken from Ref. [12] (see Fig. 1 therein).

the perfect symmetry properties of the particle-hole symmetric case.

- In the pp channel, the generalized susceptibility retains its symmetry properties, remaining a real bisymmetric matrix also out of half-filling. Hence, divergence lines along which only the pp↑↓ channel diverges are found, extending throughout the whole doping region (yellow lines).

- Irreducible vertex divergences are also found in cluster extensions of DMFT (DCA and CDMFT). They are shifted towards lower values of U, and the exceptional points of the ph-channel divergences appear to be slightly closer to half filling.

3.2   The mulivaluedness of the Luttinger-Ward functional

In Sec. 2.2.5, the Luttinger-Ward functional $\Phi[G]$ (LWF) was introduced, a fundamental quantity in the description of many-body systems. In this present section, we focus on a peculiarity of the LWF, which can have surprising consequences: $\Phi[G]$ turns out to be multivalued [11, 12, 14–16, 19–21, 23, 24, 27, 28]. As first described in the pioneering work by E. Kozik *et al.* in 2015 [11], due to this intrinsic property of $\Phi[G]$, the self-energy functional $\Sigma[G] = \beta \frac{\delta\Phi[G]}{\delta G}$ (cf. Eq. 2.64), is *not* single-valued. Put differently, for the *same* physical Green's function G, *several* $\Sigma[G]$'s can be found that correspond to it, only one of which is the physical one. As we discuss below, this is related to the fact that the map

$G_0 \to G$ is *not* injective.

An intuitive, but strongly simplified, sketch of the multivaluedness is presented in Fig. 3.25, taken from Ref. [12]. Here the full Green's function G and it's non-interacting counterpart G_0 are treated as simple numbers. The red lines illustrate the functional dependence $G[G_0]$ for different values of U, where the specific physical Green's function is represented by the blue line. At the point where the physical Green's function crosses the red line, a suitable non-interacting Green's function is found. For $U = 0$, only one solution can exist as $G = G_0$. At larger values of U, due to the multivaluedness of $\Phi[G]$, several G_0's may be in principle identified that fulfill the map $G_0 \to G$, and hence, consistent with the Dyson equation (cf. Eq. (2.23)), several possible Σ's (green dashed lines). These additional solutions are characterized by unphysical behaviors. However, their existence in itself does not pose a problem, until these unphysical solutions cross the physical one, i.e., an equality of the physical G_0 with one (or more) of the unphysical G_0's is found, as illustrated in the 3rd sheet in Fig 3.25. These so-called "branching"-points can have dramatic effects. For instance, (i) methods and algorithms that are based on diagrammatic resummations of $\Phi[G]$ might select the wrong branch. As observed in several applications [11, 14, 15, 21, 24, 27, 28], these methods do converge also after the branching points, but to an *unphysical* result. On the other hand, (ii) at these branching points, the irreducible vertex diverges [12, 19], suggesting the existence of a precise link between the two aspects, which is addressed further below in Sec. 3.3.

This rather abstract problem can be understood in a very transparent manner by going back to the BM model (see Sec. 3.1.1.2), which allows for analytic calculations, reproduced here from Ref. [19]:

In DMFT (i.e., the coherent potential approximation for the BM) the Green's function of the BM reads:

$$G(\nu) = \frac{1}{2}\left(\frac{1}{G_0^{-1}(\nu) + \frac{W}{2}} + \frac{1}{G_0^{-1}(\nu) - \frac{W}{2}} \right) , \tag{3.35}$$

where $G_0 = (\nu - \Delta(\nu))^{-1}$ and Δ is the self-consistently determined hybridization function (half filling is assumed in the calculation).

Using the Dyson equation one can express the self-energy as a functional of G_0:

$$\Sigma[G_0] = \frac{W^2}{4} G_0 , \tag{3.36}$$

which yields the exact solution. However, one can also calculate $\Sigma[G]$, i.e., as a functional of the full G:

$$\Sigma^2 + G^{-1}\Sigma - \frac{W^2}{4} = 0 \tag{3.37}$$
$$\Downarrow$$
$$\Sigma^{\pm}[G] = \frac{\pm\sqrt{1 + W^2 G^2} - 1}{2G}$$
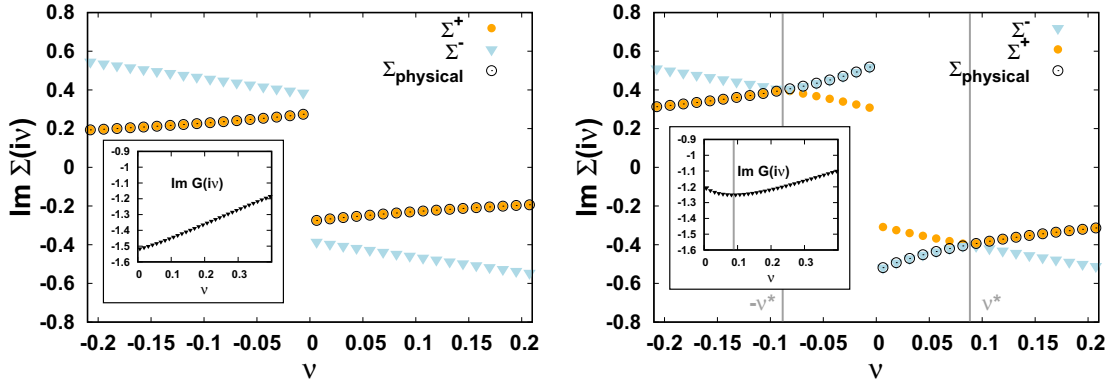
Figure 3.26: Physical self-energy (black circles) of the BM for weak ($W < \widetilde{W}$, left) and intermediate coupling ($W > \widetilde{W}$, right). Σ^+ and Σ^- refer to the two possible solutions of Eq. 3.37. In the right panel the physical Σ for $\nu < \nu^*_{BM}$ is given by Σ^-, while for $\nu > \nu^*_{BM}$, Σ^+ corresponds to the physical solution. The insets demonstrate the relation of ν^*_{BM} to the minimum of the Green's function, which is unique to the BM case [19] (see Sec. 3.1.1.2). Taken from Ref. [19] ((see Fig. 3 therein)).

which demonstrates that $\Sigma[G]$ is *not* single-valued. Instead, two solutions (referred to as "branches") are found, which *both* correspond to the physical Green's function. Let us note that this simple BM calculation already foreshadows an important aspect: When expressing Σ (or in more general cases, the diagrammatic expansion for the object of interest) as a function of G_0, no multivaluedness is found [11, 16, 19] (see further Sec. 6.1).

As mentioned, the existence of unphysical solutions alone is not problematic in itself, but it becomes problematic at a crossing of unphysical solutions with the physical one. In fact, the two self-energies $\Sigma^\pm$ coincide for $1 + W^2G^2 = 0$, which is exactly the defining equation for the energy scale ν^*_{BM}, see Eq. (3.9) [19]. The implications of this result is shown in Fig. 3.26. For weak disorder strength $W < \widetilde{W}$ (left panel) ν^*_{BM} is negative, i.e., $1 + W^2G^2 = 0$ is never fulfilled and no crossing exists. Indeed, the physical self-energy (defined by Eq. (3.36)) coincides for all frequencies with Σ^+. At larger disorder strengths $W > \widetilde{W}$ (right panel), a crossing occurs and for $\nu < \nu^*_{BM}$ the physical self-energy is given by the Σ^- branch. Only at higher frequencies $\nu > \nu^*_{BM}$, Σ^+ (which also has the correct high-frequency behavior), corresponds to the physical solution.

As outlined in Ref. [19], by calculating the irreducible vertex $\propto \frac{\delta\Sigma}{\delta G}$, one finds a divergence at the energy scale ν^*_{BM}, which defines the divergence lines of the BM presented in Fig. 3.7 (see Sec. 3.1.1.2). While the BM example is a special case, allowing for analytic calculations, it already illustrates the fundamental connection between the multivaluedness of $\Phi[G]$ and the divergences of the irreducible vertices, further discussed in Sec. 3.3.

After introducing the multivaluedness of $\Phi[G]$ and the corresponding multivalued $\Sigma[G]$ in general and for the simpler BM case, we need to clarify an important aspect: For analytic considerations on $\Phi[G]$, one can always restrict oneself to the physical solution [11]. The problem instead affects practical diagrammatic resummations. As seen in several cases, these approaches seem to select the wrong branch after the first crossing, where they still *converge,* but to *unphysical* results [11]. The underlying issue is that these methods produce

results corresponding to the perturbative branch, i.e., the one connected to $U = 0$ [14, 15, 27, 28] (Σ^+ in the simple BM example, see Ref. [19]). However, the *physical* solution is not always given by this branch, as seen for the simple BM example at larger disorder strength.

We split the subsequent presentation in this thesis along the following lines: In this section the appearance of the multivaluedness is addressed. The focus lies, in particular, on the locations of branching points of the LWF solutions in the phase diagrams of different models, as well as on their general connection to the divergences of the irreducible vertex function (see Sec. 3.3). We postpone to Sec. 6.1 instead, the treatment of the corresponding algorithmic implications: How does the multivaluedness affect numerical calculations and what can be done to find workarounds and enter parameter regimes beyond the branching points.

In the following, we summarize the appearance of the multivaluedness of $\Phi[G]$ for cases at half filling and out of half filling, respectively. In the literature, two strategies have been chosen for the *identification* of unphysical solutions. On the one hand (*i*), comparisons between results of diagrammatic resummations based on $\Phi[G]$ to those of benchmark methods are performed (such bold diagrammatic Monte-Carlo [123, 124] versus QMC, respectively). Where significant differences[17] are observed, a branching point is identified. On the other hand (*ii*), iteration schemes [11], or also "reverse" solvers [21], and even reformulated Hirsch-Fye methods [12], follow a different path. In these approaches the exact Green's function G is known a priori and instead G_0 candidates are identified that correspond[18] to this physical G. Evidently, in order to identify unphysical G_0's, one needs to allow for some freedom, e.g., real parts in cases where they should be zero due to symmetry reasons, see further Ref. [12] and the corresponding supplemental material.

3.2.1 The multivaluedness of the LWF at half filling

As already pointed out at the beginning of this section, the first observation and characterization of the multivaluedness was made in the work by E. Kozik *et al.* in 2015 [11]. In this work the multivaluedness was described for the AL, the AIM (both at half filling at out of half filling) and the HM (not discussed explicitly here, we refer the interested reader to Ref. [11]).

In Fig. 3.27 we show the results of Ref. [11] for the AL at half filling, where the double occupancy is plotted as a function of U for $\beta = 2$. Scheme A and B refer to iteration schemes, along strategy (*ii*) discussed above, where A represents the natural choice, which coincides with the results of diagrammatic Monte-Carlo calculations. Scheme B is an *ad-hoc* modification of Scheme A. The exact solution for the AL is known, and demonstrates a decreasing double occupancy with increasing interaction U. However, at a large enough interaction U_*, Scheme A converges, but yields increasing double occupancies – an evidently unphysical trend. Instead, after the branching point, Scheme B produces the expected

---

[17]Significant differences refer in this context to deviations in the results that go beyond numerical ones that can be attributed to choosing different methods.

[18]In particular, if a G_0, which was identified by such a "reverse" procedure, is used as an input for a numerically exact solver, the physical G is obtained again.
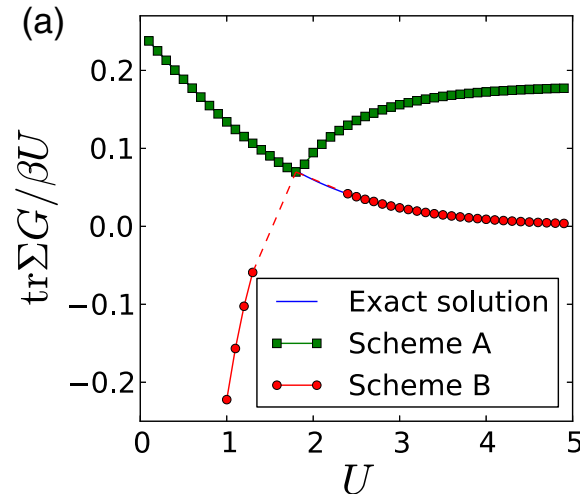
Figure 3.27: Calculations for the AL at $\beta = 2$, demonstrating the double occupancy as a function of U at half filling. Scheme A and B refer to iteration methods, see strategy (*ii*) above, the results of diagrammatic resummations coincide with those of Scheme A (not shown). A branching point is identified, after which Scheme A converges, but yields an increasing double occupancy. Taken from Ref. [11] (see Fig. 2 therein).

physical behavior (where no data is shown, Scheme B did not converge). Diagrammatic Monte-Carlo calculations were performed for the AL and reproduced the results of Scheme A, including convergence to unphysical results at large enough interaction (see Fig. 3 in Ref. [11]).

Naturally, the results of Ref. [11] triggered the interest of the many-body community, which lead to several studies where the multivaluedness was analyzed in simplified models. One example is the so-called "one-point"-model, where analytic calculations are possible, see Refs. [14, 15]. As opposed to the BM model, a full interaction term is taken into account in this model, but no Matsubara frequency dependence is considered. Since the LWF $\Phi[G]$ is a universal functional of the interaction term, this makes the results of the one-point model more comparable to the AL case. Nevertheless, similarly as for the BM, two branches of the self-energy are identified. Further, the multivaluedness in replica systems was studied [24], where is was linked to the nature of fermionic statistics. An analysis of the effect of self-consistency for the case of the AL can be found in Ref. [20].

3.2.2   The multivaluedness of the LWF out of half filling

The multivaluedness of $\Phi[G]$ has been also observed numerically for several cases out of half filling.

In Fig. 3.28 the result of Ref. [11] for the AIM is displayed, where the color map encodes the difference in the double occupancy between the exact solution (obtained by a numerically exact QMC impurity solver) and the solution of Scheme A, mentioned above. In this way, the locations of branching points as a function of the interaction U and the doing δ are identified. In general, the results are reminiscent of the AIM results for the divergences out of half filling. In a doping region close to half filling, one observes an
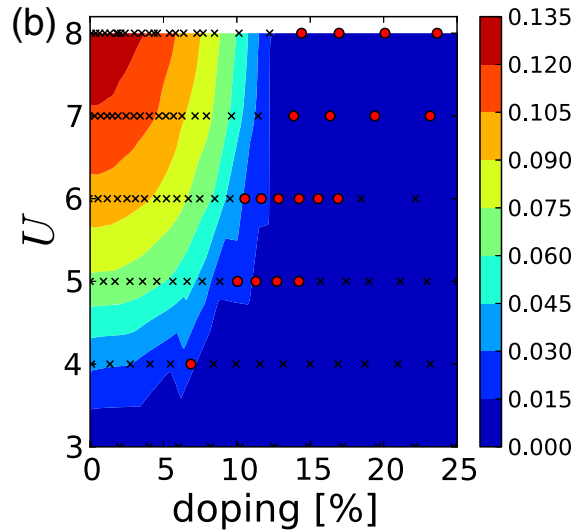
Figure 3.28: Identification of the branching points for the AIM as a function of U and doping δ, by using the iterative Scheme A of Fig. 3.27, see Ref. [11]. The red dots mark parameter regimes, where the calculation did not converge. Taken from Ref. [11] (see Fig. 2 therein).

extended region where a growing difference of the results of Scheme A w.r.t. the exact one is found. For large doping values Scheme A reproduces the physical solution, and no branching points are identified. As in the AL case, diagrammatic Monte-Carlo calculations were performed and indeed reproduced the results of Scheme A [11].

The direct link between the irreducible vertex divergences and the multivaluedness becomes even more apparent in Fig. 3.29, which was taken from Ref. [21]. These calculations were performed for a HM on a square lattice, using CDMFT (left) and the so-called nested-cluster scheme (NCS, see below) (right) for its solution. The colored red and blue areas, along which divergences of irreducible vertex are found, were already analyzed in Sec. 3.1.4. The color maps of both panels show the magnitude of the difference between an unphysical solution and the physical one, obtained by CDMFT. In the left panel, a reverse solver is used (strategy (ii)), identifying unphysical non-interacting Green's functions based on CDMFT calculations. If a branching point is encountered, the reverse solver jumps onto the wrong branch and yields unphysical results (in the right inset of the left panel the hybridization function of an unphysical result is shown, see Ref. [21] for details). At the red crosses, the iteration did not converge, similarly as in Fig. 3.28. In the right panel, the actual result of the NCS is shown, as compared to the CDMFT benchmark (strategy (i)). This cluster approach is an attempt to formulate a translationally invariant real-space cluster method, which is based on diagrammatic resummations for $\Phi[G]$ for different cluster sizes, see Ref. [21] for details. After the branching point, this method starts to yield an unphysical result, progressively deviating from the CDMFT result for Σ.

Altogether, both panels of Fig. 3.29 are relatively similar to Fig. 3.28 for the multivaluedness of the AIM. On the one hand, close to half filling, unphysical solutions are identified at large interaction values, while at lower interaction values only the physical solution is found, and hence no branching points are present. On the other hand, at higher doping
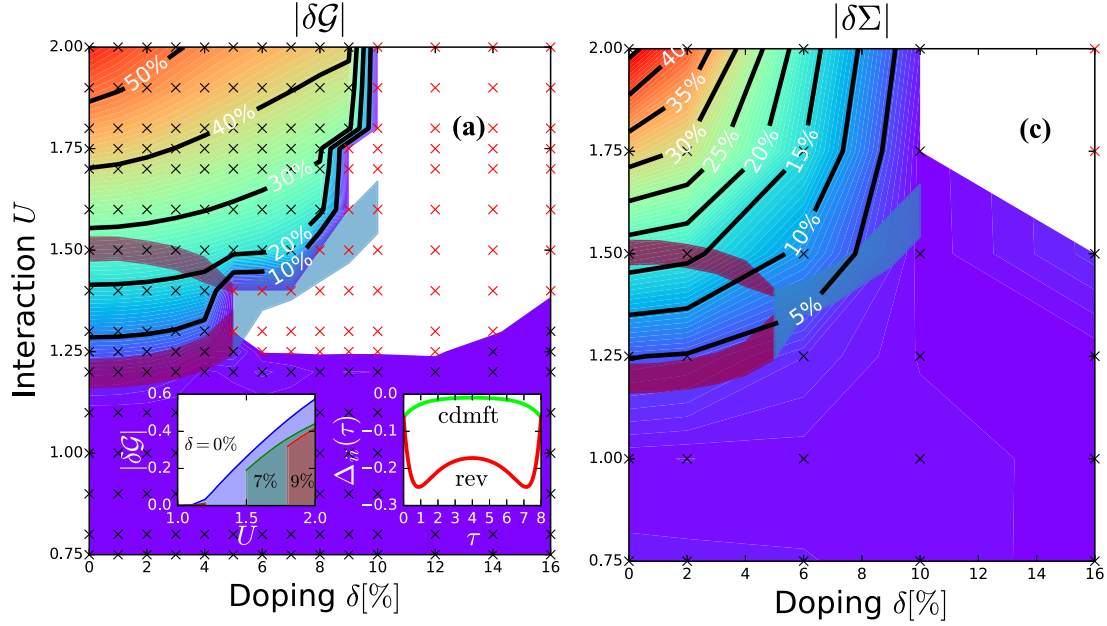
Figure 3.29: Results of Ref. [21], identifying the multivaluedness for the Hubbard model on a square lattice at $T/D = 0.125$ as function of U and doping δ (in units of $D = 4t$). The red and blue areas represent the parameter sets where vanishing eigenvalues are found without (red) and with (blue) a remaining imaginary part, see Sec. 3.1.4. In the left panel the difference in the local component of the non-interacting G_0 is shown, as obtained from the CDMFT benchmark (2×2 cluster) and a reverse solver (strategy (ii), see Ref. [21]). At the red crosses the reverse solver did not converge. In the right panel the difference between the CDMFT benchmark and the result of a NCS calculation, based on $\Phi[G]$ (see text), is shown. Taken from Ref. [21] (see Fig. 1 therein).

levels, an increasing difficulty in the convergence of both schemes (reverse CDMFT and NCS) is observed. For both cases, the first divergence area (red and blue branch) seems to delimit the two regimes, even in cases, where the divergence of the irreducible vertex itself is no longer observed (blue area, due to imaginary parts of associated eigenvalues).

3.3 Two sides of the same coin

In the last part of this chapter, we summarize the state-of-the-art theoretical understanding on the fundamental connection between the divergences of the irreducible vertex functions (cf. Sec. 3.1) and the branching of different solutions due to the multivaluedness of the LWF $\Phi[G]$ (cf. Sec. 3.2).

A first step in this direction was already showcased in the last section: for the BM model the multivaluedness of $\Sigma[G]$ and the divergence of Γ_c could be understood on an analytic level [19]. In general, however, it is not as straightforward to obtain the irreducible vertex from a functional derivative $\propto \delta\Sigma[G]/\delta G$. In this respect, the work of O. Gunnarsson et al. from 2017 [12] represents a very important achievement. In this work, the precise connection between the crossings of the physical and unphysical solutions and the divergences of the irreducible vertex functions could be demonstrated for the AL at half filling. As a first step, the authors managed to identify several unphysical G_0's,
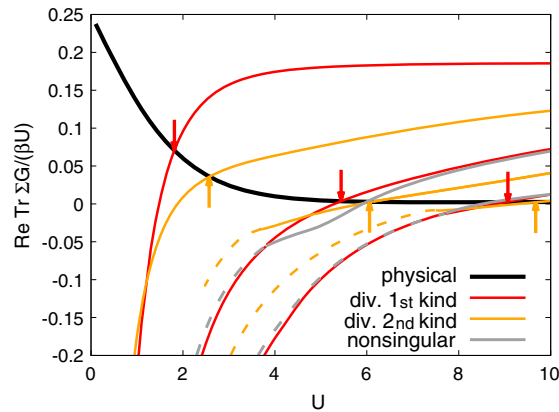
Figure 3.30: As Fig. 3.27, demonstrating the crossing of the physical (solid black line) with several unphysical solutions (red, orange and grey lines). The arrows represent the interaction values where divergences of the irreducible vertex functions in the AL occur. The color code corresponds to the one of Fig. 3.6. Taken from Ref. [12] (see Fig. 2 therein).

which is shown in Fig. 3.30 in the same manner as Fig. 3.27. Several crossings of the physical solution (black line) with unphysical solutions (red, orange and grey lines) are observed, where the first red one corresponds to the one crossing shown in Fig. 3.27 of Ref. [11]. Moreover, at the different crossings, the precise behavior in U how an unphysical G_0's becomes equal to the physical one for the different Matsubara frequencies ν could be identified (see Fig. 2 of Ref. [12]). This was crucial for the second step, where the authors succeeded in connecting this crossing-behavior in U for the different ν to the appearance of vertex divergences at these parameter sets. Indeed, the arrows in Fig. 3.30 represent the U values of the divergences observed in the AL for $\beta = 2$, which are in perfect agreement with the crossings of solutions. The analytic proof of this fundamental link can be found in the corresponding supplemental material (part I.A) of Ref. [12]. The main idea of the proof will be summarized here in a few words, allowing also to discuss its limitations:

The starting point is the generating functional $\mathcal{F}[G_0^{-1;U,\nu}]$ for the one-particle Green's function, at a parameter set close to a crossing of the physical G_0 with an unphysical G_0. $\mathcal{F}[G_0^{-1;U,\nu}]$ for one G_0 around the crossing can then be expressed by a Taylor expansion in terms of the other G_0. This expansion is then connected with the generalized susceptibility in the charge channel (as a functional derivative of the generating functional w.r.t. G_0^{-1}). By a suitable recasting of the equation, using the precise behavior in U how the G_0's cross for the different Matsubara frequencies, an eigenvalue equation is obtained. Vanishing eigenvalues were found corresponding to localized eigenvectors on the one hand, controlled by the energy scale ν^*, and non-localized eigenvectors on the other hand, depending on the precise crossing-behavior in U for the different frequencies ν. These singular eigenvalues and eigenvectors of course correspond to the previously discussed red and orange divergence lines of the AL (cf. Sec. 3.1.1.1), as reflected in the color coding of Fig. 3.30. Note that also the presence of grey lines corresponds to unphysical G_0's which do *not* become equal to the physical one at the crossing point.

In this way the crossings of solutions, fulfilling the map $G_0 \rightarrow G$, where G is the

physical Green's function, could be connected to the divergences of the irreducible vertex functions for the AL. The precise behavior in U for the different Matsubara frequencies even determines the kind of divergence that is found - localized or non-localized in frequency space.

On a more general perspective, the question arises whether such a connection exists also for more general situations. Considering, e.g., the results for the HM solved by CDMFT presented in Fig. 3.29, it seems that the direct link between the crossings of physical and unphysical solutions and the divergences of irreducible vertex divergences extends also to cases without particle-hole symmetry. Hence, in future studies, it remains to be seen how the formal relation presented here for the AL can be extended to describe, e.g., cases where the eigenvalues of $\chi^{\nu\nu'}$ have nonzero imaginary parts and form complex conjugated pairs. In fact, as Fig. 3.29 impressively demonstrates, also in cases where the divergence itself is absent, due to imaginary parts of the singular eigenvalues, a branching of the LWF is found. Further, an extension of the direct link described here for the AL, accounting also for the symmetry property of the associated singular eigenvectors, would be of interest (cf. the summaries of Secs. 3.1.1, 3.1.2 and 3.1.3). In this way, this extension of the proof of Ref. [12] would also apply to the irreducible vertex divergences of the AIM and the DMFT solution of the HM throughout the entire temperature regime.

As the last (rather specialist) topic let us recall the crossing of divergence lines, observed in the case of the AIM in Figs. 3.13 and 3.14. Based on the results for the crossings of the physical with unphysical solutions in the AL represented in Fig. 3.30, this can be rationalized. In particular, in Fig. 3.30 at $U \approx 1$, $\mathrm{Re}\,\mathrm{Tr}(\Sigma G/\beta U) \approx -0.1$, one observes a crossing of two unphysical solutions (here referred to as A). One can easily imagine a situation where this crossing (A) takes place between the first orange and the second red unphysical branch *at* the point where they cross *also* the physical solution. This would characterize a parameter set with two simultaneous divergences of two kinds – a crossing of a red and an orange divergence line, such as the ones observed in Figs. 3.13 and 3.14.

Physical origin of irreducible vertex divergences

You can't always get what you want
But if you try sometimes, well, you just might find
You get what you need
– The Rolling Stones

The previous chapter thoroughly discussed the ubiquitous presence of characteristic manifestations of the breakdown of self-consistent perturbation theory in correlated electron systems. This chapter focuses, instead, on a more fundamental topic, which represents one of the central questions of this thesis: *What is the underlying physical mechanism that triggers the perturbative breakdown*? To investigate this question, the impact of fundamental physical processes of the many-electron physics upon quantities of the two-particle level is studied in-depth in this chapter. Specifically, the precise way how the local magnetic moment formation and its Kondo screening are encoded in the Matsubara frequency structure of generalized susceptibilities will be clarified. These insights also allow, on a more quantitative level, to identify an alternative criterion for the determination of the Kondo temperature in the charge sector and, more generally, to precisely assess the limitations of self-consistent perturbative methods.

Parts of this chapter, marked by a vertical bar, have already been published in the APS journal
*Phys. Rev. Lett. **126**, 056403 (2021) and the corresponding supplemental material.*
To improve the pedagogical character of this chapter, both sources are mixed accordingly.

The quantum field theoretical (QFT) description of many-electron systems can be pursued at different levels of complexity, essentially depending on the number of added or removed electrons in the physical processes considered to define the corresponding Green's functions.

Presently, one can rely on a solid textbook interpretation [6, 8] of the QFT formalism describing the single-particle (1P) processes, measurable e.g., by (angular resolved) direct and inverse photoemission [125] or scanning tunneling microscopy [126, 127]. Crucial information about the metallic or insulating nature of a given many-electron problem, as well as quantitative information about the electronic mass renormalization Z and quasiparticle lifetime τ is encoded in the momentum/energy dependence of the electronic self-energy Σ. If the temperature T is low enough, even a quick glance at the low-energy behavior of Σ, either in real or in Matsubara frequencies, yields a qualitatively reliable estimate of the most important physical properties.

The situation is clearly different on the two-particle (2P) level, which can be experimentally accessed by e.g., inelastic neutron scattering [128, 129]. Due to the complex physical mechanisms at play, the related textbook knowledge is mostly limited to general definitions [6–9]. For this reason, corresponding analytical/numerical calculations are often performed with significant approximations or with a black-box treatment of the 2P processes. However, the last decade has seen a rapid development of methods at the forefront of the many-electron theory [51, 98, 121], for which generalized 2P correlation functions are the key ingredient. This is reflected in an increasing effort to develop the corresponding formal aspects and algorithmic procedures [18, 33, 51–53, 58, 59, 67, 94, 96, 98, 104, 105, 121, 122, 130–142]. At the same time, the rather poor physical understanding of the 2P processes remains largely behind the requirements of the most advanced QFT methods. Interesting progress has been recently reported [25, 57] on the relation of 1P Fermi-liquid parameters to 2P scattering functions. Ideally, however, one would like to be able to interpret the physics encoded at the 2P level with a similar degree of confidence as for the 1P processes.

In this chapter, we make a significant step forward in this direction: We identify the fingerprints of two major hallmarks of strong correlations in the generalized charge susceptibility. In particular, we pinpoint the frequency structures encoding the formation of local magnetic moments as well as of their Kondo screening. In this perspective, we also show how the Kondo temperature T_K corresponds to a specific property of the generalized charge susceptibility, allowing for an alternative, simple path of extracting its value directly from the lowest Matsubara frequency data.

We recall that the Kondo problem [30] provides a paradigm for a variety of physical effects [143–147] involving strong electronic correlations. Local moment formation and Kondo screening are also a crucial ingredient of the physics described by the dynamical mean-field theory (DMFT) [41] through the solution of a self-consistently determined auxiliary Anderson impurity model (AIM).

Learning how to extract important physical information from the generalized susceptibility represents a substantial improvement for the understanding of quantum many-electron physics at the 2P level. Further, having this information at hand also enables us to draw conclusions on two relevant theoretical questions: (i) The relation of the multifaceted manifestations [12] of the breakdown of perturbation theory, discussed in great detail in
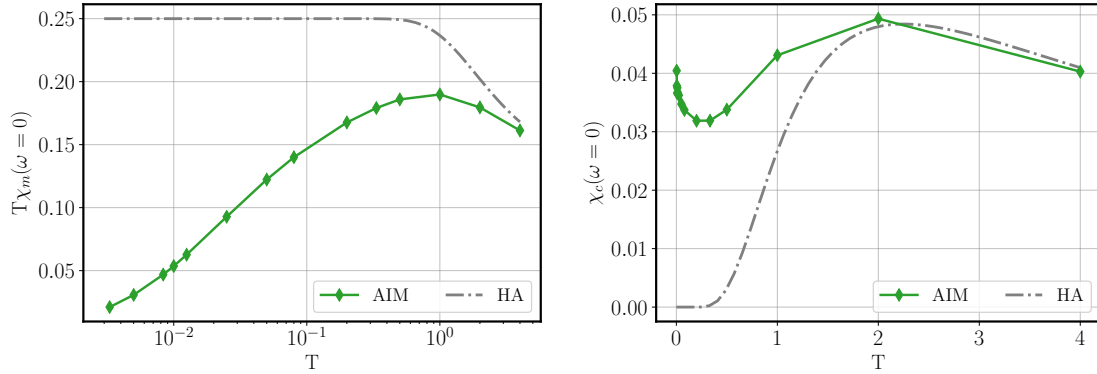
Figure 4.1: Behavior of the static magnetic (left) and charge (right) response function for the AIM (green diamonds) and the HA (grey dashed-dotted line) for an interaction value of $U = 5.75$ as a function of T. To facilitate the identification of the Curie-Weiss behavior $\propto 1/T$, $T\chi_m$ is plotted in the left panel.

Chapter 3, such as the divergences of the irreducible vertex functions [10, 12, 13, 17–19, 21–23, 25, 26] and the crossing of multiple solutions [11, 12, 14, 15, 19–21, 23, 24] of the Luttinger-Ward functional, with the local moment physics and its Kondo screening; (ii) the built-in limit of advanced perturbative approaches to describe these fundamental physical effects.

4.1 Response functions for the AIM

Before starting with the analysis of the generalized susceptibility we first present a concise overview of the behavior of the static response functions of the impurity site in the charge $\chi_c(\omega = 0) = \chi_c$ and the magnetic $\chi_m(\omega = 0) = \chi_m$ channel. This section serves hence as a short summary on the well-known and thoroughly studied response functions of the AIM for a half-filled case without external magnetic field, we refer e.g., to Refs. [9, 30, 39, 40] for more details. For the purposes of this chapter we also compare the results of the AIM to the ones of the Hubbard atom (HA) case (i.e., the atomic limit of the AIM, see Sec. 2.1), where simple analytic expressions are available [23, 33]. We recall that in the HA no hopping term is taken into account, hence representing the case of a single site with solely an on-site interaction U. In this way the HA case constitutes an "ideal realization" of the local moment physics, and therefore represents an important baseline for our considerations throughout this chapter.

   In Fig. 4.1 we show $T\chi_m$ (left panel) and χ_c (right panel) as a function of temperature for a sizable interaction value of $U = 5.75$ for both the AIM (green diamonds) and the HA (grey dashed-dotted line) case. Note that the specific value of $U = 5.75$ is also considered in the remaining sections of this chapter because it represents an interaction value for which the local magnetic moment in the AIM is already well-defined in a broad T-range, while, at the same time, self-consistent perturbative calculations (see below in Sec. 4.5) are still feasible. We note that in other contexts, U for the AIM is often expressed in terms of the

scale $\Delta_0 = \pi V^2 \rho_0$, see Sec. 2.1.1. Since in our case $\Delta_0 = \pi/5$, $U = 5.75$ corresponds to $U/\Delta_0 \approx 9.15$.

Starting this step-by-step analysis by inspecting the HA results for χ_m at high temperatures, one observes a well-defined and expected trend: The magnetic susceptibility rises as the local moment begins to form for $T \sim U$. For higher temperatures, in the so-called free-orbital regime [39, 40], all states are thermally populated, leading to $T\chi_m \simeq 1/8$ (not shown). In the local moment regime $T < U$, the susceptibility shows a Curie-Weiss $\propto 1/T$ behavior, which can be clearly noticed in the plot as a constant. Comparing the HA result with the QMC calculations for the AIM one observes a qualitatively similar trend at high-temperatures, as expected. However, the AIM contains also the physics of the Kondo screening, originated by the coupling to the conduction electron bath. This coupling leads to a deviation of the plain $\propto 1/T$ dependence found in the HA case. After the local moment is formed at about $T \approx 1$, where the maximum of $T\chi_m$ is found, the moment begins to get screened as the temperature is decreased. At low-T the screening of the local moment is fully effective, which leads to a constant-in-T behavior of χ_m, seen as a steep decrease of $T\chi_m$ in the left panel of Fig. 4.1.

While the local moment formation as well as its screening for magnetic response functions is a thoroughly studied topic, the corresponding behavior of χ_c is, in comparison, less frequently analyzed. The temperature dependence of χ_c is shown in the right panel of Fig. 4.1. At first, we focus again on the HA case: Here, one readily observes a significant decrease of the charge fluctuations as the local moment is formed at temperatures of the order of U (note the linear x-scale instead of the logarithmic one of the left panel). Similarly, also for the AIM a decrease is found in the temperature regime where χ_m shows predominantly a Curie-Weiss behavior. However, at low-temperatures the local moment is screened and hence the charge fluctuations get partially revived. This is reflected in the observed low-temperature increase of χ_c of the AIM, which is completely absent in the HA case.

It is important to recall here that the changes from one regime to the other are continuous crossovers in the AIM, i.e., there is no abrupt change of phase as that observed at the MIT in the Hubbard model. This also applies to the Kondo temperature T_K, which represents a crossover temperature. Thus, let us present the precise definition adopted throughout this work for computing T_K.

Specifically, the value of the Kondo temperature for the AIM has been determined from the overall temperature dependence of the static magnetic susceptibility $\chi_m(\omega = 0)$ on the impurity site. This (well-known) procedure was described in a work by H. R. Krishna-murthy, *et. al* [39, 40] and is also summarized in Ref. [30]. It is based on comparing the temperature evolution of $\chi_m(\omega = 0)$ for a fixed interaction value U to a universal renormalization group solution for a Kondo-Hamiltonian [39, 40]. Note that the constants used in Refs. [39, 40] are included in our definition of the static magnetic susceptibility, leading to $\chi_m = \chi_m^{\text{Refs. [39, 40]}}/(g\mu_B)^2$, where $g = 2$ and μ_B is the Bohr magneton. In practice, one must (*i*) compute $T\chi_m(\omega = 0)$ in a quite large temperature range and (*ii*) shift the data
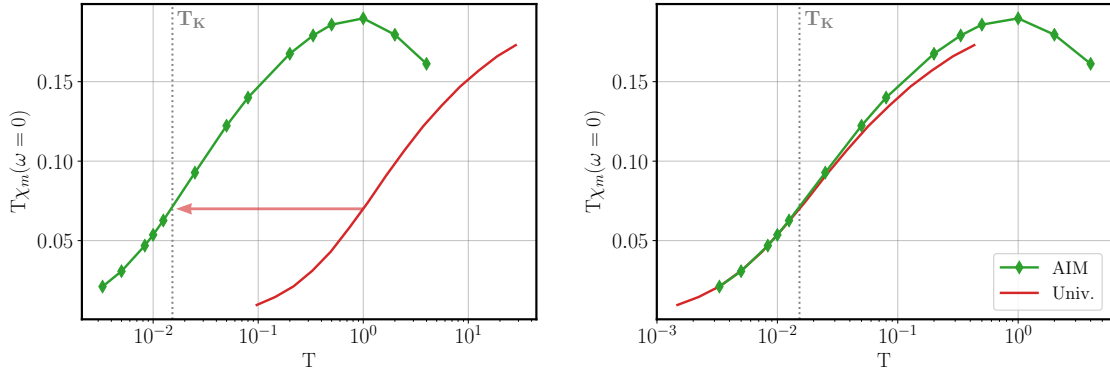
Figure 4.2: Extracting the value of T_K of the AIM for a given interaction value ($U = 5.75$) from the numerical data for the static local magnetic susceptibility $\chi_m(\omega = 0)$ (QMC, green), by shifting the universal result (red) onto it (highlighted by the red arrow), obtained from the renormalization-group solution of a Kondo-Hamiltonian [39, 40]. The value for T_K obtained in this way is shown as the vertical grey dotted line.

of the universal result [39, 40], plotted as a function of $\log(T/T_K)$ with $T_K = 1$, onto the numerical result for $T\chi_m(\omega = 0)$. This way, one obtains the effective Kondo temperature of the AIM for this value of U. The procedure is shown in Fig. 4.2 for $U = 5.75$, where the unshifted case is plotted in the left panel, the shifted one in the right. This shift is applied in such a way that the agreement between the universal result for the Kondo-Hamiltonian (red) and the numerical one for the AIM (green) is the most precise for low temperatures $T \lesssim T_K$. For the specific case of $U = 5.75$, the Kondo temperature results to $T_K \simeq 1/65 \approx 0.015$. Throughout this thesis this procedure was used to obtain the value of T_K for several interaction values of the AIM, in particular, also the ones depicted in Fig. 3.14, where they were shown to agree well with the analytic estimate of Eq. (2.9) for T_K corresponding to the wide-band limit of the AIM.

4.2 How to read two-particle quantities

After discussing the behavior of the response functions of the AIM, we now turn to the generalized susceptibilities, defined in Eq. (2.17). Note that a minor change of notation is made in the following. To facilitate the distinction between the static response functions $\chi_r(\omega = 0) = \chi_r$ and the generalized susceptibilities $\chi_r^{\nu\nu'}(\omega = 0)$ in channel r, the latter will be highlighted by adding a tilde: $\chi_r^{\nu\nu'}(\omega) \to \tilde{\chi}_r^{\nu\nu'}(\omega)$ throughout the rest of this chapter.

More on a physical note, it is worth underlining already at this stage that, for repulsive on-site interactions, the local generalized *charge* susceptibility $\tilde{\chi}_c^{\nu\nu'}(\omega) = \tilde{\chi}_{\uparrow\uparrow}^{\nu\nu'}(\omega) + \tilde{\chi}_{\uparrow\downarrow}^{\nu\nu'}(\omega)$ allows for a particularly high readability of the underlying physics at the 2P level. While this statement will be substantiated by the numerical analysis we discuss below, we can already note–on a general level–that correlation functions in the charge channel capture fundamental properties of any interacting electron system. In particular, they describe the fluctuations of its charge carriers, which are crucial, for example, to characterize the

different mobility properties of metallic and (Mott) insulating phases.

As already mentioned in Sec. 2.2.3, the corresponding physical charge response function, $\chi_c(\omega)$, can be directly obtained from the generalized susceptibility $\tilde{\chi}_c^{\nu\nu'}(\omega)$ by summing over the fermionic Matsubara frequencies ν, ν' (cf. Eq. (2.29)). For convenience we reproduce Eq. (2.29) here for the static case ($\omega = 0$) regarded throughout this chapter:

$$\chi_c = \chi_c(\omega = 0) = T^2 \sum_{\nu\nu'} \tilde{\chi}_c^{\nu\nu'} = T^2 \sum_{\nu\nu'} (\tilde{\chi}_{\uparrow\uparrow}^{\nu\nu'} + \tilde{\chi}_{\uparrow\downarrow}^{\nu\nu'}) \tag{4.1}$$

After this general considerations, we start by analyzing the arguably simple case of the Hubbard atom. In Fig. 4.3 (upper panels), we show an intensity plot of $\tilde{\chi}_c^{\nu\nu'}$ (normalized by T^2) for $U = 5.75$, half filling (where $\tilde{\chi}_c^{\nu\nu'}$ is real [23, 33], cf. Sec. 2.2.4.1) and different temperatures. At high temperature ($T_{\text{high}} = 2$, left panel), the overall frequency structure consists of a large positive-valued diagonal (yellow/red) and a weak negative cross structure (blue). This corresponds to a typical *perturbative* behavior [33, 96], dominated by the diagonal bubble term $\tilde{\chi}_0^{\nu\nu'} = \tilde{\chi}_{0,\uparrow\uparrow}^{\nu\nu'} = -\delta_{\nu\nu'}G(\nu)^2/T$: Correlation effects are washed out for $T \gtrsim U$, consistent with the feasibility of high-T expansions.

The situation changes radically when reducing T: in the intermediate ($T_{\text{int}} = 0.1$) and low ($T_{\text{low}} = 1/60 \approx 0.017$) temperature regime (central and right panel), one observes a strong *damping* of all diagonal elements of $\tilde{\chi}_c^{\nu\nu'}$. The effect is more pronounced at low frequencies, as the sign of $\tilde{\chi}_c^{\nu=\nu'}$ becomes even *negative* (bluish colors) for $|\nu| \lesssim \sqrt{3}/2\, U$ [23] (black square). This major feature is accompanied by the appearance of small *positive* off-diagonal elements (yellow). The net effect is a suppression of the physical susceptibility χ_c, see Eq. (4.1), which occurs when the thermal energy is no longer large enough ($T \sim \nu < U$) to counter the formation of a local moment driven by U, eventually yielding an exponentially small $\chi_c \sim e^{-U/2T}$ for $T \to 0$, as seen in Fig. 4.1.

As opposed to the HA case, we now consider the case of the perturbative random phase approximation (RPA, central row). The RPA results were obtained by using the simplest possible approximation for the irreducible vertex ($\Gamma_{\uparrow\downarrow}^{\nu\nu'} = U, \Gamma_{\downarrow\downarrow}^{\nu\nu'} = 0 \,\forall\, \nu, \nu'$) and the non-interacting G_0 of the AIM as propagator. Instead of sign changes of the diagonal of $\tilde{\chi}_c^{\nu\nu'}$, for all temperatures *no* qualitative deviations from the perturbative structure, i.e., from the one identified at high-T in the HA case, is observed.

Altogether, the low-T HA results illustrate, on a single glance, how the onset of a pure local moment is encoded in the charge sector: A progressive emergence of a non-perturbative sign structure in $\tilde{\chi}_c^{\nu\nu'}$ (strong negative diagonal, light positive background), which qualitatively appears as the *opposite image* of the perturbative one seen for the RPA (strong positive diagonal, light negative background). This also induces several negative eigenvalues of $\tilde{\chi}_c^{\nu\nu'}$, responsible for the breakdown of perturbative expansions [12] (see Sec. 3.1).

Let us now examine how this picture changes when the HA system is connected to an electronic bath, corresponding to the full Anderson impurity model. By comparing
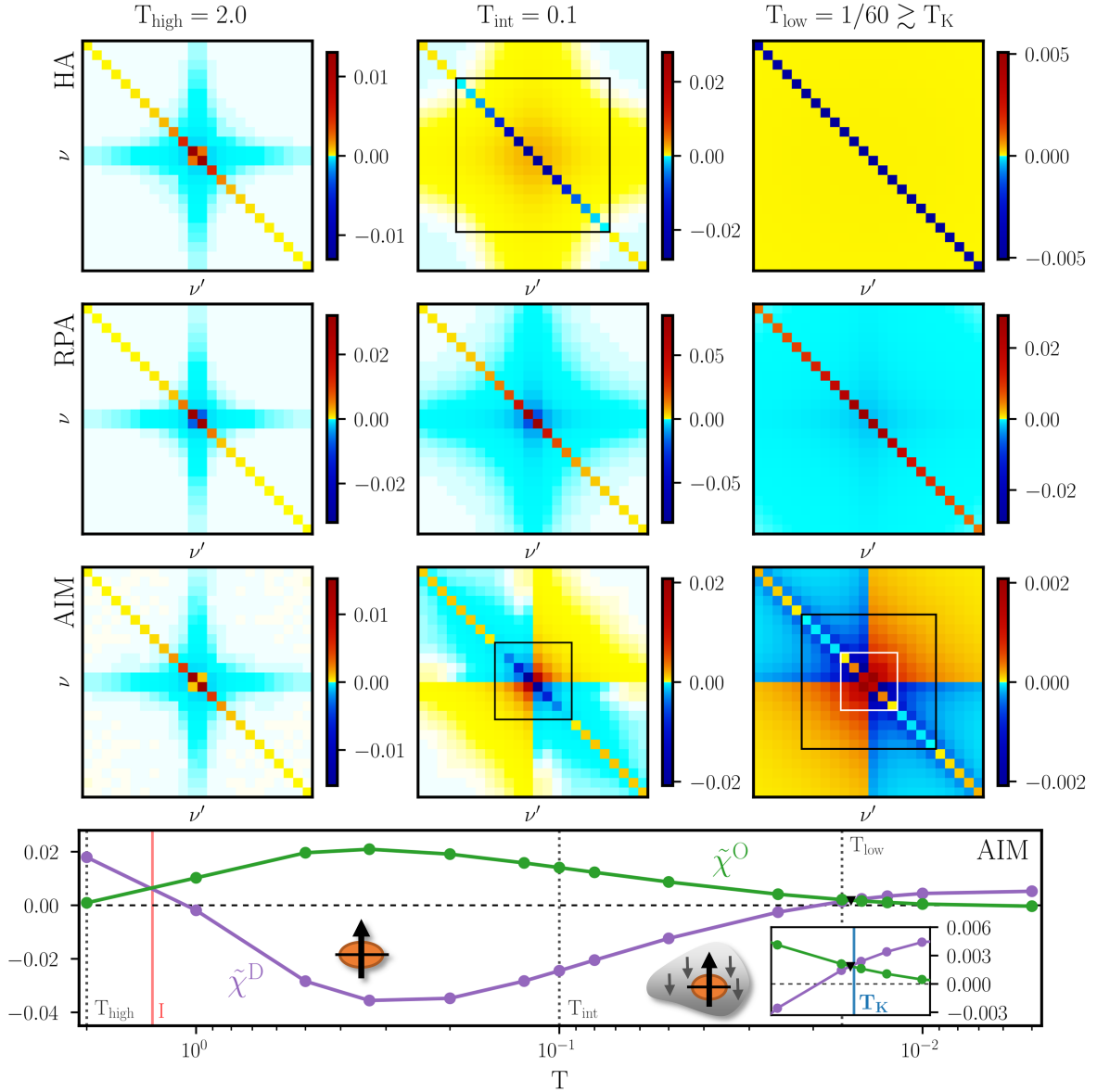
Figure 4.3: Upper part: Matsubara frequency structure of $T^2 \tilde{\chi}_c^{\nu\nu'}(\omega = 0)$ for the HA (top row), the RPA (center row) and the (numerically exact) QMC (bottom row) solution of the AIM for $U = 5.75$ and various temperatures. A fixed number of Matsubara frequencies is plotted (note that the readability is improved here by hiding the corresponding labels). The main frequency structures, as described in the text, are marked by black and white squares. Lower panel: Lowest Matsubara frequency elements of $T^2 \tilde{\chi}_c^{\nu\nu'}(\omega = 0)$: $\tilde{\chi}^D = T^2 \tilde{\chi}_c^{\pi T, \pi T}$ (violet) and $\tilde{\chi}^O = T^2 \tilde{\chi}_c^{\pi T, -\pi T}$ (green) as a function of temperature. They coincide at T_{high} at the divergence of Γ_c (red (I)), as well as at low-temperatures at $T \simeq T_K$ (black triangle). The inset shows a zoom for $T \sim T_K$ (vertical blue line). The local moment and the Kondo screened regime are sketched by the arrows without and with the surrounding screening cloud, respectively.

the results of $T^2 \tilde{\chi}_c^{\nu\nu'}$ (bottom-row panels of Fig. 4.3, computed with w2dynamics [85], see Sec. 2.3.1.2) to those of the HA, we observe almost no difference at T_{high}. This is not surprising, as thermal fluctuations prevail over both correlation (U) and hybridization (V) effects in this case. Upon lowering T to T_{int}, we enter the *local moment* regime of

the AIM, see also Fig. 4.1. This is reflected in a qualitatively similar evolution as seen in the HA: a progressive suppression of the diagonal entries of $\tilde{\chi}_c^{\nu\nu'}$, turning negative in the low-energy sector (black square), accompanied by positive, yet smaller, off-diagonal contributions, with an overall freezing effect on the local charge fluctuations (see Eq.(4.1) and more explicitly below). This is how the formation of a local moment affects the charge sector, thus representing its *fingerprint*. However, due to the screening effects of the bath, its features get weakened, explaining the quantitative differences to the HA (e.g., the reduced size of the black square).

The most interesting situation is encountered when reducing T further down to $T_{\text{low}} \gtrsim T_K$ (right panel), where the Kondo screening induces *qualitative* differences w.r.t. the HA. We observe that the low-frequency diagonal elements of $\tilde{\chi}_c^{\nu\nu'}$ (white square) are flipped back to positive, as in the perturbative regime and the RPA. This trend is driven by the low-energy correlations between electrons with antiparallel spins ($\tilde{\chi}_{\uparrow\downarrow}^{\nu=\nu'}$), as we explicitly show in Sec. 4.3. The weakening of their negative contribution increases the physical charge susceptibility χ_c, see Eq. (4.1), and simultaneously mitigates the magnetic response. However, in the intermediate frequency regime, the diagonal elements of $\tilde{\chi}_c^{\nu\nu'}$ are still negative, reflecting the underlying presence of a (partially screened) local moment. The fingerprint of the Kondo regime is, thus, the *onion*-like frequency structure of $\tilde{\chi}_c^{\nu\nu'}$, which is clearly recognizable in the rightmost bottom panel of Fig. 4.3: (i) a high-frequency perturbative asymptotic, (ii) a local moment driven structure (with suppressed diagonal) at intermediate frequencies, (iii) an inner core (with a similar sign structure as (i)) induced by the Kondo screening. A quick glance at the sign structure of $\tilde{\chi}_c^{\nu\nu'}$ therefore allows for an immediate understanding of the underlying physics. This nicely illustrates the balanced competition in the charge sector between the freezing effects of the local moment and the defreezing effects of its low-energy screening, which characterizes the Kondo regime.

The connection between the frequency structure of $\tilde{\chi}_c^{\nu\nu'}$ and the corresponding behavior of the physical response χ_c in the local moment and the Kondo regime, can also be traced in the results of partial summations of the generalized charge susceptibility. Specifically, we consider the ν, ν' summation of $\tilde{\chi}_c^{\nu\nu'}$ over frequency boxes of increasing sizes, as detailed by the following expression:

$$\chi_{\text{partial}}(\nu_{\text{max}}) = T^2 \sum_{\nu,\nu'=-\nu_{\text{max}}}^{\nu_{\text{max}}} \tilde{\chi}_c^{\nu\nu'} \tag{4.2}$$

Evidently, for $\nu_{\text{max}} \to \infty$, χ_{partial} corresponds to χ_c, and Eq. (4.2) reduces to Eq. (4.1). At the same time, by inspecting the results obtained for finite ν_{max}, the energy-selective effects of different nonperturbative/perturbative features in $\tilde{\chi}_c^{\nu\nu'}$ can be clearly individuated.

In Fig. 4.4 the result of this partial sum is displayed as a function of ν_{max} for the three different temperatures regimes discussed in Fig. 4.3.

At high-temperature (T_{high}), i.e., in the perturbative regime, χ_{partial} (red circles) is always *positive* and *increases* monotonically toward its asymptotic value for $\nu_{max} \to \infty$ (red dashed line).
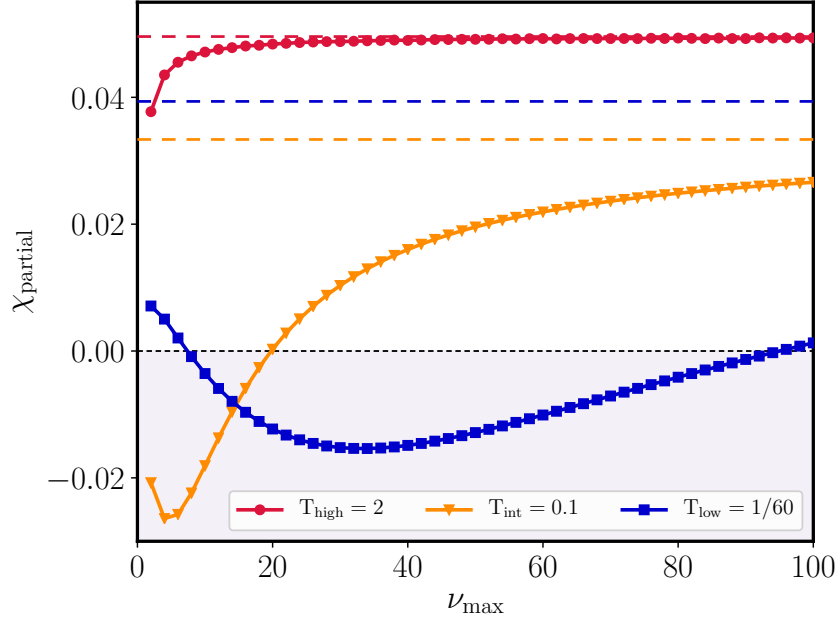
Figure 4.4: Partial frequency summation of $T^2 \sum_{\nu\nu'} \tilde{\chi}_c^{\nu\nu'}$ (cf. Eq. (4.2)) for the AIM at $U = 5.75$ over frequency boxes of increasing size ($\nu_{\max}$) for three different temperatures regimes (solid lines). The values of the physical response χ_c, which correspond to the $\nu_{\max} \to \infty$-limit, are depicted as dashed lines. The area where χ_{partial} is negative is highlighted by a grey background.

For intermediate temperatures (T_{int}) we enter the local moment regime of the AIM. As we discussed above, this results in large negative diagonal entries in $\tilde{\chi}_c^{\nu\nu'}$ at low-to-intermediate frequencies. Due to these negative contributions, χ_{partial} (orange triangles) is *negative* for small $\nu_{\max}$ and further *decreases* until, for a certain value of $\nu_{\max}$ a minimum is reached. Thereafter, the perturbative high-frequency asymptotics comes into play, slowly enhancing χ_{partial} until a positive value of χ_c is eventually obtained for $\nu_{\max} \to \infty$ (orange dashed line). Because of the initial *negative* low-frequency contributions to χ_{partial}, the final value of the physical charge response χ_c gets strongly suppressed w.r.t. the perturbative one.

At low-temperatures (T_{low}) in the Kondo regime $\tilde{\chi}_c^{\nu\nu'}$ displays the characteristic "onion-structure". This represents a clear hallmark of the competition between the two trends discussed above. χ_{partial} (blue diamonds) starts *positive*, due the positive low-frequency elements of the diagonal of $\tilde{\chi}_c^{\nu\nu'}$. χ_{partial} then *decreases* as a function of $\nu_{\max}$ until a minimum is reached, similarly as in the local moment regime. Eventually it increases again until a positive value is recovered for $\nu_{\max} \to \infty$. Due to the initial positive sign of the low-energy contributions to the frequency sum of Eq. (4.2), the final value of the physical response χ_c gets slightly *enhanced* w.r.t. the corresponding one in the local moment regime, where these positive low-energy contributions to the partial sum are absent.

Note, that the characteristic frequency structures in $\tilde{\chi}_c^{\nu\nu'}$ (i.e., the local moment and the onion structure) are also found for other values of U, as well as in other models, see further Appendix A.1.1.
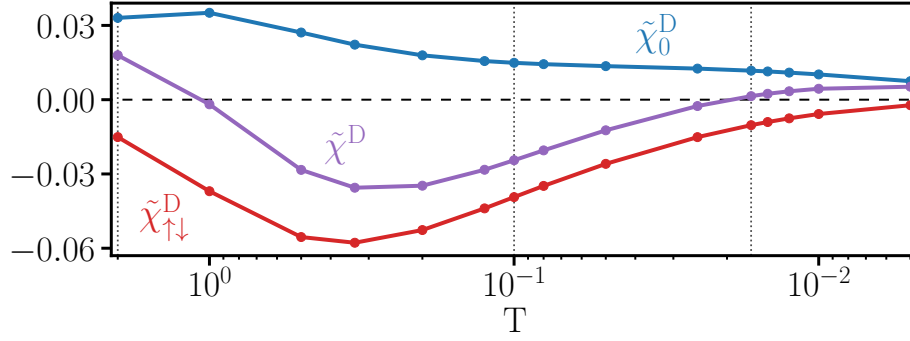
Figure 4.5: Behavior of the lowest-frequency diagonal element of $T^2 \tilde{\chi}^{\nu=\nu'}$ for the $\uparrow\uparrow$ (blue), the $\uparrow\downarrow$ (red) and the charge ($\uparrow\uparrow$ + $\uparrow\downarrow$) sector (violet, shown also in Fig. 4.3), for the AIM at $U = 5.75$ as a function of the temperature on a logarithmic axis. The vertical dotted lines mark the three temperatures also shown in Fig. 4.3.

4.3   How to extract the Kondo temperature in the charge sector

The behavior of $\tilde{\chi}_c^{\nu\nu'}$ described above is also reflected in the temperature evolution of its lowest frequency entries: the diagonal $\tilde{\chi}^D = T^2 \tilde{\chi}_c^{\pi T, \pi T}$ and the off-diagonal $\tilde{\chi}^O = T^2 \tilde{\chi}_c^{\pi T, -\pi T}$, shown in the lowest panel of Fig. 4.3. We can readily trace the sign changes marking the three regimes discussed above, associating the (negative) minimum of $\tilde{\chi}^D$ with the temperature at which the strongest local moment effects are observed.

As already mentioned in the previous section, it is mainly the correlation between antiparallel spins $T^2 \tilde{\chi}_{\uparrow\downarrow}^{\pi T, \pi T} = \tilde{\chi}_{\uparrow\downarrow}^D$ that underlies the behavior of $\tilde{\chi}^D$, which is verified in Fig. 4.5. The only remaining contribution to $\tilde{\chi}^D$ originates in the $\uparrow\uparrow$ sector. However, since on the diagonal there are no vertex corrections, $F_{\uparrow\uparrow}^{\nu=\nu'} = 0$, see e.g., Refs. [33] and [54], only the bubble term remains $T^2 \tilde{\chi}_{\uparrow\uparrow}^{\nu=\nu'} = T^2 \tilde{\chi}_0^{\nu\nu'} = -T\delta_{\nu\nu'} G(\nu)^2$, which is plotted as $\tilde{\chi}_0^D$ (blue line).

The screening induced enhancement of $\tilde{\chi}^D$ at lower temperatures has *remarkable consequences*: We find that crossing the Kondo temperature, as defined in a standard way from the behavior of the static magnetic response of the system, see Sec. 4.1 ($T_K = 1/65 \approx 0.015$ at $U = 5.75$), matches with high accuracy the equality of $\tilde{\chi}^D$ and $\tilde{\chi}^O$ observed at low-T (s. inset of Fig. 4.3, marked by black triangle). We emphasize that this criterion holds more generally. As shown in the phase diagram of the AIM in Fig. 4.6 (left panel), the condition $\tilde{\chi}^D = \tilde{\chi}^O$ (black triangles) perfectly traces T_K (blue line)[1] in the *entire* local moment regime $T, V < U$ (see also the logarithmic inset), i.e., where the definition of a Kondo scale is actually meaningful. Note that this is not the case for other criteria one could naturally think of, such as $\tilde{\chi}^D = -\tilde{\chi}^O$ or $\tilde{\chi}^D = 0$ see Appendix A.1.2.

Moreover, our simple 2P definition of T_K holds also beyond the single impurity problem. In Fig. 4.6, we show DMFT calculations for the periodic Anderson model (defined in Sec. 2.1.2) on a square lattice with nearest-neighboring hopping t (PAM, central) and for a Hubbard model (defined in Sec. 2.1.3) on a Bethe lattice with unitary half-bandwidth D (HM, right).
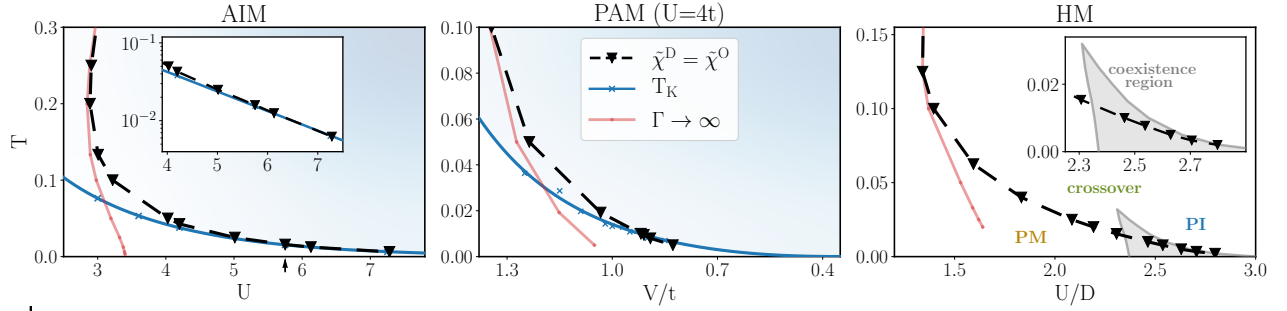
Figure 4.6: Phase diagram of the AIM (left), the PAM (DMFT) (middle), and the HM (DMFT) (right) as a function of the interaction U (hybridization V for the PAM, U fixed) and the temperature T showing the line where $\tilde{\chi}^{\mathrm{D}} = \tilde{\chi}^{\mathrm{O}}$ holds (black triangles dashed), i.e., the singularity of the 2×2 submatrix of $\tilde{\chi}_c^{\nu\nu'}$. The left and central panels show the agreement at low temperatures between T_{K} (blue solid line) and the condition $\tilde{\chi}^{\mathrm{D}} = \tilde{\chi}^{\mathrm{O}}$, clearly evident also in logarithmic scale (left inset). The local moment regime is represented by a bluish shadowed area in both panels. The red lines denote the (first) divergence of the irreducible vertex Γ_c. For the HM on the Bethe lattice the paramagnetic metallic (PM)/insulating (PI) phases are indicated together with their crossover. The coexistence region is shown in gray. The arrow on the abscissa (left) marks the interaction value used in Figs. 4.3, 4.5 and 4.7. The figure is reproduced from Ref. [68].

In particular, we observe that for the PAM, the *same matching* of the condition $\tilde{\chi}^{\mathrm{D}} = \tilde{\chi}^{\mathrm{O}}$ (black triangles) and T_{K} [44, 148] (blue line) is found in the local moment regime (i.e., when $V < t$, blue-shadowed area). Note that for the PAM the maximum of $\chi_m(\omega = 0)$ as a function of the temperature was used to determine the value of the Kondo temperature, see further the supplemental material of Ref. [44].

In the HM, the Kondo temperature characterizing the auxiliary AIM associated with the self-consistent DMFT solution, depends on the temperature itself: $T_{\mathrm{K}}^{\mathrm{HM}}(T)$. Hence, $\tilde{\chi}^{\mathrm{D}} = \tilde{\chi}^{\mathrm{O}}$ (black triangles) indicates that the temperature equals the effective Kondo temperature, i.e., $T_{\mathrm{K}}^{\mathrm{HM}}(T) = T$. Physically, it is natural to relate this condition to the onset of low-energy electronic coherence: For all temperatures below the $\tilde{\chi}^{\mathrm{D}} = \tilde{\chi}^{\mathrm{O}}$ condition, a conventional Fermi-liquid behavior of the physical response can be expected (e.g.: $\rho(T) \propto T^2$, $c_V(T) \propto T$, etc. [6]). This would also be consistent with the $\tilde{\chi}^{\mathrm{D}} = \tilde{\chi}^{\mathrm{O}}$ condition approaching the Mott Hubbard metal-insulator transition (MIT) at $U_{\mathrm{MIT}}(T = 0) = U_{c2}$ in the low-T limit (see also recent DMFT studies of the physics in the proximity of the MIT [149, 150]).

The equality of the elements of the innermost 2×2 submatrix of $\tilde{\chi}_c^{\nu\nu'}$ represents therefore a very simple, clear-cut 2P criterion for determining T_{K} in the charge sector.

4.4 A nonperturbative Fermi liquid

Beyond its physical relevance, our improved 2P understanding sheds light onto the non-trivial relation with the breakdown of perturbation theory [12], thoroughly introduced in

---

[1]For different interaction values T_{K} is extracted, as detailed in Sec. 4.1 (blue crosses), and then fitted using a function based on the analytical expression for T_{K} (cf. Eq. (2.9)) in the wide-band limit [30] ($A\sqrt{U\Delta_0}\exp\left(-B\frac{U}{\Delta_0} + C\frac{\Delta_0}{U}\right)$).

Chapter 3. At high T, where $\nu_0 = \pi T \gtrsim V, U, t$, the 2×2 submatrix encodes all relevant energy scales, the rest being nonsingular high-frequency asymptotics. In this case $\tilde{\chi}^{\mathrm{D}} = \tilde{\chi}^{\mathrm{O}}$ corresponds to a singular eigenvalue of the *entire* $\tilde{\chi}_c^{\nu\nu'}$ and hence to a divergence of the irreducible vertex function $\Gamma_c^{\nu\nu'} = [\tilde{\chi}_c^{\nu\nu'}]^{-1} - [\tilde{\chi}_0^{\nu\nu'}]^{-1}$, specifically to the first (I) one encountered when reducing the temperature (red line in Figs. 4.3 and 4.6) [10, 19, 22, 23, 26], shown also in several instances in Secs. 3.1.1, 3.1.2 and 3.1.3. For intermediate temperatures, the 2×2 submatrix is controlled by the local moment, leading to a strongly negative $\tilde{\chi}^{\mathrm{D}}$ and negative eigenvalues of the submatrix (as in the HA case). At T_{K} the eigenvalue flips sign and one finds again $\tilde{\chi}^{\mathrm{D}} > \tilde{\chi}^{\mathrm{O}}$ for $T \lesssim T_{\mathrm{K}}$, as in the perturbative regime (s. Fig. 4.3, lowest panel). Here, however, because of the onion-like structure of $\tilde{\chi}_c^{\nu\nu'}$, the positive-definiteness (and thus the invertibility) is guaranteed only for an inner submatrix describing the Fermi liquid regime, but not for the full $\tilde{\chi}_c^{\nu\nu'}$. This explains why divergences of irreducible vertex functions can occur also at low temperatures [22] even in the presence of a Fermi liquid ground state, as shown explicitly in Sec. 3.1.3. Indeed, such vertex divergences mark the distinction between a Fermi liquid in the weak- and in the strong-coupling regime, which mostly affect the intermediate frequency/energy domain.

4.5   Limitations of perturbative approaches

The direct link between the 2P fingerprints of local moments and vertex divergences, sets also precise physical limitations for self-consistent perturbative methods, where–per construction–Γ is finite (with the only exception of second-order phase transitions to long-range ordered phases, not relevant here). Hence, the impact of the characteristic physics emerging from the magnetic sector onto the charge channel, cannot be described by such self-consistent perturbative methods. We substantiate this statement by considering two advanced perturbative schemes, the functional renormalization group (fRG) [98] (in the $1\ell_K$ truncation, see Sec. 2.3.3) and the parquet approximation (PA) [55, 90–92, 96, 151–157], both introduced in Chapter 2, where per construction $\Lambda^{\nu\nu'} = U$ holds. The results obtained for the AIM with $U = 5.75$ and $T = T_{\mathrm{int}}$ are shown in Fig. 4.7. $\tilde{\chi}_c^{\nu\nu'}$ computed by the fRG and PA (upper panels) appear qualitatively different from the (numerically) exact one of Fig. 4.3 (AIM, bottom-row): The diagonal elements are all *positive* and substantially larger than the off-diagonal ones, resembling more the case of the RPA (central-row). This ensures the positive-definiteness of the entire $\tilde{\chi}_c^{\nu\nu'}$, preventing the strong suppression effects of the charge response, which characterize the local moment regime. This drawback qualitatively affects the physical description. In particular, the temperature dependence of the numerically exact charge susceptibility χ_c (Fig. 4.7 lower panel) exhibits a *clear minimum* for intermediate $T_{\mathrm{high}} > T > T_{\mathrm{K}}$, as discussed in Sec. 4.1. This emerges from the competition between the suppression induced by the local moment (see the extreme HA case) and the low-energy screening. Both features are *not* captured by the fRG (blue pentagons) and PA (brown squares), which display a monotonous behavior as T is decreased. At the same time, as we show in the following, the perturbative approaches are able to
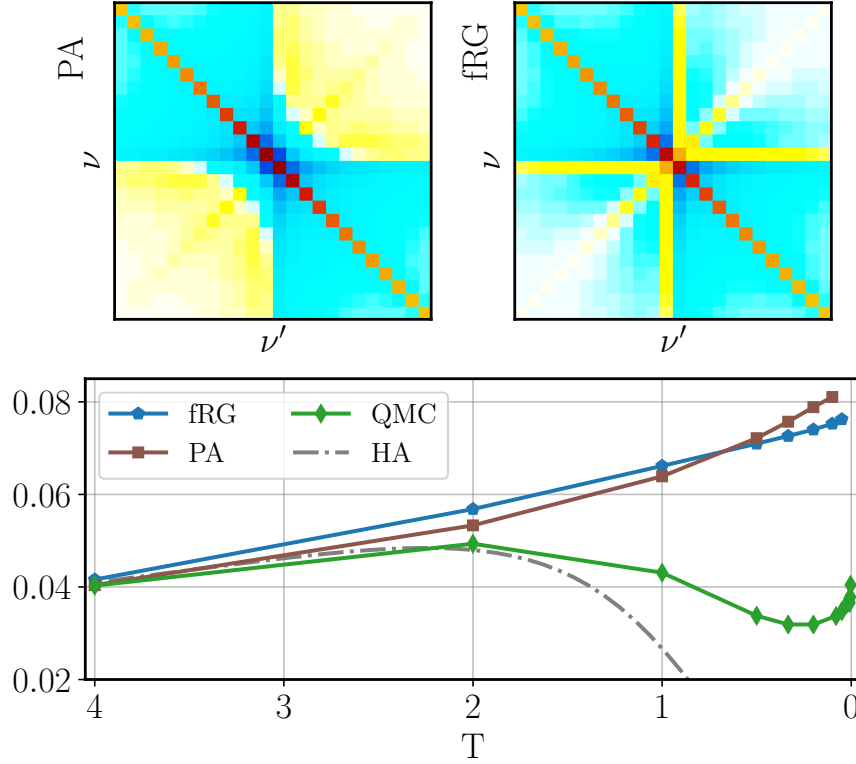
Figure 4.7: Generalized charge susceptibility $(T^2 \tilde{\chi}_c^{\nu\nu'})$ for the AIM, as obtained by means of PA and fRG (using the $1\ell_K$ truncation, see Sec. 2.3.3 for details) for $U = 5.75$ and $T = T_{\text{int}}$. The same color scale as in Fig. 4.3 (AIM, T_{int}) is used. Lower panel: static physical charge susceptibility χ_c computed with different approaches as a function of T.

capture the qualitatively correct behavior of the magnetic response, reflecting the absence of divergences of Γ in this sector.

To substantiate this understanding, we now focus on the static magnetic response $\chi_m(\omega = 0)$ as obtained from the PA as well as the fRG and extract the corresponding Kondo temperature, in a similar fashion as in Sec. 4.1. In the following we choose an interaction value of $U = 4.2$, which ensures that, as opposed to the $U = 5.75$ case shown above, low temperatures ($T < T_K$) are numerically accessible with our PA solver.

In the left panel of Fig. 4.8 the Kondo temperature is extracted from the PA data (brown). The corresponding result is incorrect at the quantitative level ($T_K^{\text{PA}} = 1/12 \gtrsim 2T_K$, where $T_K = 1/27$). Nonetheless, the PA method yields a qualitatively correct description of the local moment physics (namely of its overall temperature-dependence) in the magnetic channel. Similarly as in Fig. 4.2 the unshifted universal result is shown as the dashed red line, whereas the arrow illustrates the shift. In the same way the fRG $1\ell_K$ case (blue) is shown in the right panel of Fig. 4.8. Here one notices that, as in the PA case, the quantitative value is too large ($T_K^{\text{fRG}} = 1/8$). Further the qualitative description is no longer perfect, showing deviations from the universal result for $T < T_K$. Let us note at this point, that the multiloop fRG extension (mfRG) [104, 105] of the $1\ell_K$ contains all PA diagrams, as detailed in Chapters 2 and 6. This means that, if it is solved, the result coincides with the
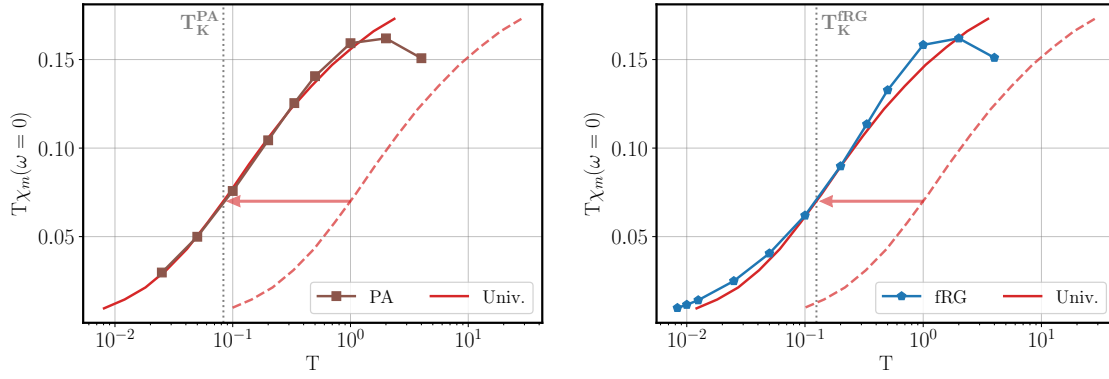
Figure 4.8: Extracting T_K in the standard way described in Sec. 4.1, for the PA (left panel) and the fRG (right panel) data for $U = 4.2$, where the respective result is shown as vertical dotted line for each method. Interestingly, the PA manages to describe the qualitatively correct behavior of $\chi_m(\omega = 0)$, albeit with a too high $T_K^{PA} \gtrsim 2T_K$. The fRG method with a 1ℓ-truncation, gives an even larger estimate for T_K and displays some qualitative deviations for $T < T_K$.

PA solution, removing the low-T discrepancies observed for $1\ell_K$ in Fig. 4.8.

To summarize, both perturbative methods describe the physics of the magnetic channel in a qualitatively correct way (with somewhat larger deviations in the $1\ell_K$-fRG case). This contrasts entirely their performance in the charge sector, where their description is fully incorrect, even at a qualitative level, as shown and discussed above. The false description of the impact of the local moment formation and its screening onto the charge fluctuations roots back to the absence of divergences of the corresponding irreducible vertex functions [10, 13, 17, 19, 21–23, 26] in both perturbative approaches. The same consideration applies to the paring channel (not shown). For completeness, in Fig. 4.9 the result for the physical local charge susceptibility χ_c is shown for $U = 4.2$ (solid lines), as a reference also the result for $U = 5.75$ is reproduced (dashed and transparent). In both cases it can be readily noticed that *both* perturbative methods fail in describing the minimum of $\chi(T)$ associated with the local moment regime of the AIM, as seen above.

To analyze this qualitative drawback in the description of local moment physics in greater detail, we provide a comparison for $U = 4.2$ of the low-frequency elements of $\tilde{\chi}_c^{\nu\nu'}$, $\tilde{\chi}^D = T^2\tilde{\chi}_c^{\pi T,\pi T}$ and $\tilde{\chi}^O = T^2\tilde{\chi}_c^{\pi T,-\pi T}$, for all methods considered, similarly as in Sec. 4.3. Fig. 4.10 shows the behavior of the diagonal frequency elements ($\tilde{\chi}^D$) (solid lines) for the numerically exact QMC solution (green, top panel), the PA result (brown, middle) and the fRG result (blue, bottom), as well as of the corresponding off-diagonal ones ($\tilde{\chi}^O$) (dashed lines). The QMC data (top panel) for $U = 4.2$ display qualitatively the same behavior as the QMC results for $U = 5.75$ shown in Fig. 4.3. In particular one readily notices the negative sign of $\tilde{\chi}^D$, which encodes the freezing of charge fluctuations in the local moment regime. The corresponding data for the perturbative methods show instead qualitative differences w.r.t. the QMC ones in the entire local moment regime as *no* sign change in $\tilde{\chi}^D$ (middle and bottom panels) is observed in the whole temperature regime. As a last point, we also
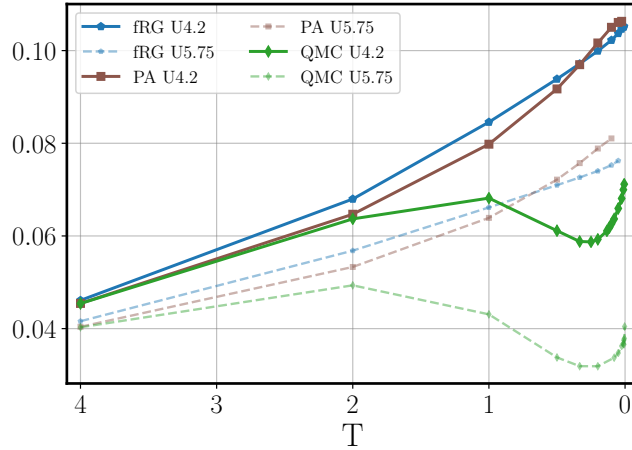
Figure 4.9: Temperature behavior of the physical static charge susceptibility χ_c for $U = 4.2$ (solid) and $U = 5.75$ (dashed) for the exact solution (QMC, green diamonds) and perturbative approaches (PA, brown squares and fRG, blue pentagons).

note that for the PA the largest deviations are found precisely for the temperatures where χ_c is mostly suppressed in the numerically exact solution.

4.6 Discussion and current developments

In this chapter, we have characterized how the local moment formation and its Kondo screening affect the generalized susceptibility in the charge channel [68]: On the one hand, the local moment leads to a strong suppression of the physical charge response χ_c. On the 2P-level this is reflected most evidently in suppressed or even negative diagonal elements of $\tilde{\chi}_c^{\nu\nu'}$, which together with an emerging off-diagonal frequency structure, yield negative eigenvalues of $\tilde{\chi}_c^{\nu\nu'}$. Each time a sign change of one of the eigenvalues of $\tilde{\chi}_c^{\nu\nu'}$ occurs, the irreducible vertex diverges, a feature that is –by construction– entirely absent in self-consistent perturbative approaches such as the (truncated) fRG and the PA. On the other hand, the screening of the local moment leads to a partial revival of the charge response χ_c. In the Kondo regime for $T \sim T_K$, we observed the formation of the "onion"-structure in $\tilde{\chi}_c^{\nu\nu'}$, where the negative diagonal entries flip sign again in the lowest-frequency range.

These quite general findings allow discerning the physical situation at hand by just a single glance at the Matsubara frequency structure of the local generalized susceptibility in the charge sector. Additionally, based on our results [68], we could identify a quantitative criterion for the Kondo temperature, namely that all elements of the lowest-frequency 2×2 submatrix of $\tilde{\chi}_c^{\nu\nu'}$ (for $\nu, \nu' = \pm\pi T$) are equal, and hence have a zero-eigenvalue.

At this point, one might wonder what happens, instead, in the *magnetic* channel on the 2P level. We recall that the magnetic channel is the dominant fluctuation channel of the AIM for repulsive interactions. As discussed in Sec. 4.1, with decreasing temperatures, χ_m changes from a $\propto 1/T$ Curie-behavior to one constant in T. To understand how this is reflected on the 2P level, we show a similar plot as in Fig. 4.3, but only for the AIM in
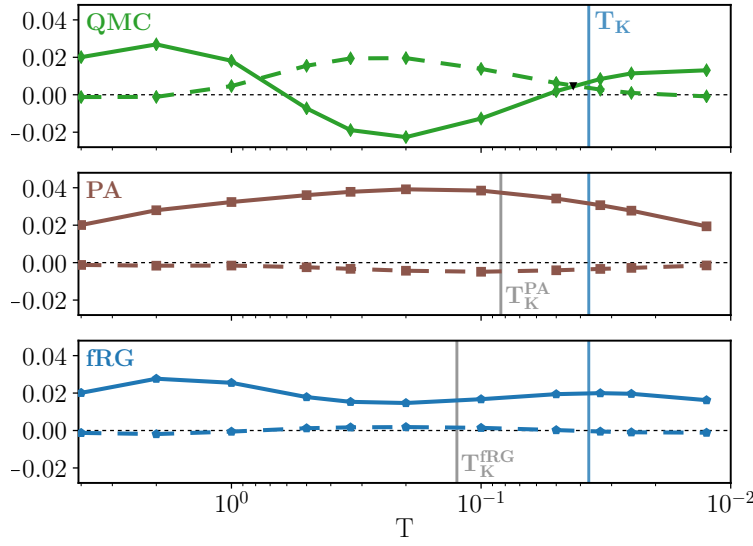
Figure 4.10: Comparison of $\tilde{\chi}^D$ and $\tilde{\chi}^O$ for the QMC (top), PA (middle), fRG (bottom) for $U = 4.2$ and different temperatures. Also shown as a vertical blue line in all panels is the Kondo temperature T_K as obtained from the numerically exact solution for $U = 4.2$. The grey vertical lines show the Kondo temperature as obtained from the approximative solutions (PA and fRG) described above.

both the charge (top row) and the magnetic (bottom row) channel in Fig. 4.11. Here one immediately notes the crucial difference between the two channels. While quantitative changes in the magnetic channel are visible, the main frequency structure remains the same as the temperature is decreased, even for very low temperatures $T_{\text{cold}} = 1/300 \ll T_K$. No change of sign or other crucial qualitative changes can be identified, apart from the finer Matsubara frequency grid, as opposed to the charge channel. Indeed, it is the "precise balance" in the charge channel, i.e., the delicate interplay between the strong suppression and its mitigation as T is reduced, which allows for a more immediate readability of the generalized two-particle quantities and, in particular, of their sign-structure.

Fig. 4.11 also shows results at lower T than those analyzed in Ref. [68] (see Fig. 4.3). In particular, turning back to the inspection of the charge channel, we note that the results for $\tilde{\chi}_c^{\nu\nu'}$ at $T_{\text{cold}} \ll T_K$, demonstrate how, for very low temperatures, the onion structure vanishes, and an apparently more "perturbative-looking" frequency structure seems to be recovered. In fact, by comparing the rightmost upper panel of Fig. 4.11 to the PA result of Fig. 4.7 one notices a striking qualitative similarity. This is also in agreement with the low-T results of Fig. 4.10, where the QMC data for the 2×2 submatrix become more similar to the ones of the fRG and the PA. Physically, this is related to the manifestation of the Fermi-liquid regime of the AIM, where the charge fluctuations become gradually revived. On the two-particle level, however, a crucial difference remains between the PA (or the fRG) and the QMC case. Although the fingerprint structure corresponding to the local moment formation is no longer directly visible in $\tilde{\chi}_c^{\nu\nu'}$, there are still negative eigenvalues for $T \ll T_K$ present (see Sec. 3.1.3), as opposed to the case of the self-consistent perturbative solutions of the fRG and PA (or also the perturbative case of $T_{\text{high}} \gg T_K$, which also shows a qualitatively similar structure). This feature distinguishes a Fermi-Liquid in
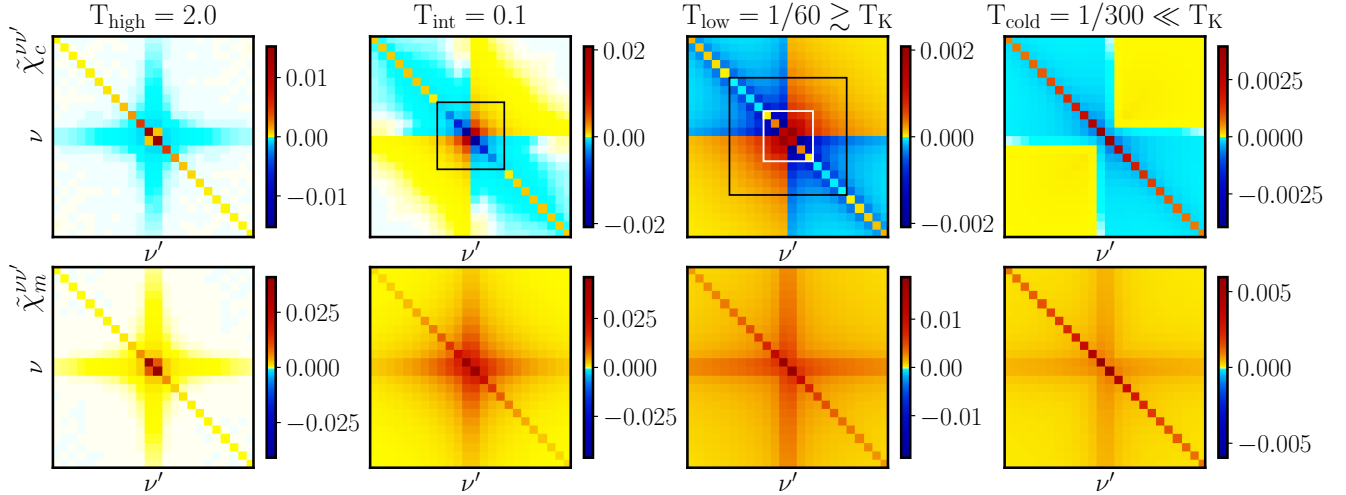
Figure 4.11: Similarly as in Fig. 4.3, AIM results for $T^2 \tilde{\chi}^{\nu\nu'}(\omega = 0)$ in the charge (upper) and the magnetic (lower) channel for a broad temperature range and fixed $U = 5.75$.

the perturbative from one in the nonperturbative regime. The negative eigenvalues of the low-T QMC solution are also reflected in the characteristic structure of the partial summation, introduced in Sec. 4.2, which is explicitly reported in Appendix A.1.1. From a more general perspective, this finding underlines that the "onion structure" in $\tilde{\chi}_c^{\nu\nu'}$ is a rather selective hallmark of the Kondo regime, i.e., of $T \sim T_K$.

To complete the description of our numerical results, we also consider smaller values of U, i.e., where less negative eigenvalues are present. In particular, in Fig. 4.12 we report $T\chi_m$ (left panel) and χ_c (right panel), similarly as in Fig. 4.1, for $U = 3.0$ and $U = 4.2$, as indicated in the phase diagram shown in the inset of the right panel. Evidently, $U = 3$ corresponds to a borderline case, where only the first divergence line is crossed for a limited T-range as T is varied. For both interaction values, the magnetic channel displays the behavior already discussed in Sec. 4.1, where $U = 3$ corresponds to a weaker local magnetic moment than $U = 4.2$. In the charge response for the case of $U = 4.2$, a clear minimum can be still identified, as already discussed throughout this chapter (see explicitly Fig. 4.9). In the borderline case of $U = 3$, one observes the precursor of the minimum of χ_c, which corresponds to the occurrence of an almost "stationary" point in the temperature range of the local moment formation. This analysis indicates that in the perturbative regime, where no vertex divergences are present, the suppression of the charge fluctuations is too weak to produce a minimum in the T-dependence of the local charge response. More systematic investigations of a possible strict link between the minimum formation and the presence of divergences in correlated metallic systems is left for future studies. A fist step in this direction, inspired by the results shown in this thesis, have been performed in Ref. [158], where the temperature-behavior of χ_c was studied for the DMFT solution of the Hubbard model (see also the discussion at the end of the section).

Finally, we turn to the central question of this chapter: *What is the underlying physical mechanism that triggers the perturbative breakdown?*

Based on the insights gained so far, the local moment formation can be clearly identified
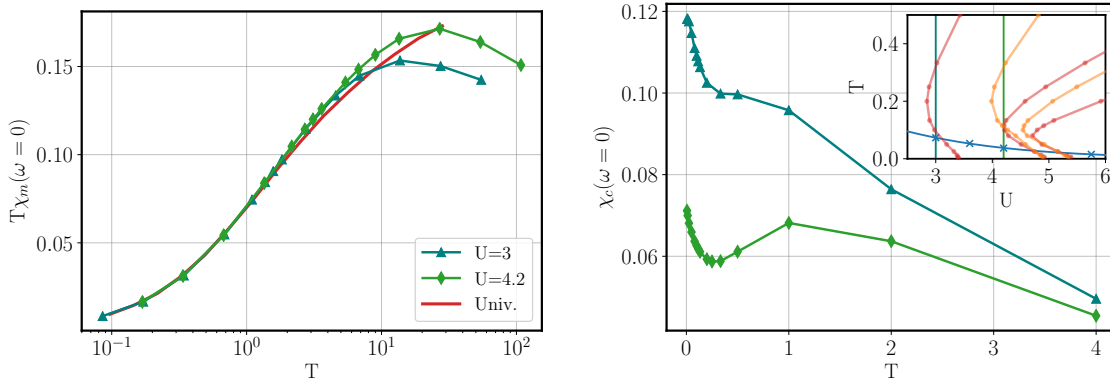
Figure 4.12: Temperature dependence of the physical response functions of the AIM in the magnetic (left) and the charge (right) channel for two different interaction values. Left panel: The magnetic response is plotted as $T\chi_m$, similarly as Figs. 4.1 and 4.2, to facilitate the identification of the local moment formation. At low temperatures, both data sets perfectly match the universal result (red line), see Sec. 4.1. Right panel: The inset shows the first divergence lines of the AIM (red and orange), described in Chapter 3, together with the two interaction values $U = 3$ (teal triangles) and $U = 4.2$ (green diamonds) plotted as vertical lines.

as the driving mechanism behind the singular eigenvalues of $\tilde{\chi}_c^{\nu\nu'}$ [68], as speculated already in early works [10, 12, 18, 22]. This fundamental physical effect, which dominates the local magnetic response, leads to a frequency dependent suppression of the diagonal entries of $\tilde{\chi}_c^{\nu\nu'}$ and a concomitant emergence of off-diagonal ones [18, 26, 68].

These findings strongly suggest the interpretation that the irreducible vertex is, intuitively speaking, acting as a "messenger". It exchanges essential physical information between the different diagrammatic channels and ensures the physical consistency between them. In the specific case studied in this chapter, the irreducible vertex carries over the information of the local moment formation from one channel to the other. As the fRG and PA results show, if the irreducible vertex is fixed to e.g. $\Lambda = U$, the messenger function is to a large extent deactivated –the messenger is "silenced"– and, consequently, the suppression of the charge response remains largely incomplete. This leads to the rather unphysical result of a well-formed local moment in the magnetic channel coexisting with still sizable local charge fluctuations. Evidently, a consistent treatment of both channels is necessary to describe nonperturbative physical situations in their entirety as, e.g., in the case of the Mott-MIT in the Hubbard model. Hence, the possibility of capturing the intense communication between channels, which characterize the phenomena described above, is beyond those theoretical descriptions, which do not allow for the occurrence of divergences of the irreducible vertex functions. For diagrammatic approaches for strongly correlated electron systems, these considerations support the choice of a DMFT starting point on the two-particle level [51], where the local moment formation is already accounted for consistently in all channels. The interplay of such approaches and the breakdown of self-consistent perturbation theory is discussed in Chapter 6.

The study of the local moment formation has been the subject of renewed interest
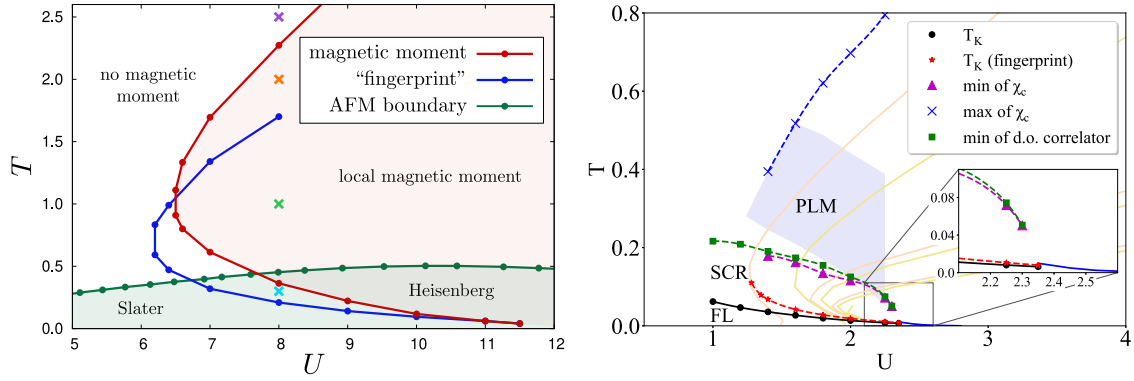
Figure 4.13: Comparisons of the "fingerprint"-criterion introduced in Sec. 4.3, and two independent criteria for the local moment formation (left) and T_K (right). Left: Plot taken from the work by E. Stepanov *et al.* [159] (Fig. 3 therein). The calculations are performed for a 3D Hubbard model on a cubic lattice, solved by DMFT, the blue line traces the $\tilde{\chi}^D = \tilde{\chi}^O$ condition, the red line represents the parameter sets where a sign change of the second derivative of the free energy is found [159]. Right: Plot is taken from the work by T. B. Mazitov and A. A. Katanin [158] (Fig. 4 therein). The calculations are performed for a Hubbard model on a square lattice, solved by DMFT. In this case the red line represents the condition based on the 2×2 submatrix of $\tilde{\chi}_c^{\nu\nu'}$ and the black line the calculation of T_K by shifting the magnetic response function $\chi_m(\omega = 0)$ [158], as in Sec. 4.1.

recently, see e.g., Refs. [62, 63, 158, 159]. In fact, the identification of an alternative route to calculate the Kondo temperature, introduced above, inspired several authors to perform precise comparisons for the Hubbard model case. Specifically, in the work by E. Stepanov *et al.* [159], the authors have introduced an effective local action, where the local moment formation is described by using the formalism of a spontaneous symmetry breaking. In this way, a precise criterion for the formation of the local moment could be formulated by considering the sign change of the second derivative of the free energy, i.e., when the free energy changes from a paraboloid-like to a "Mexican"-hat-shaped potential. In Fig. 4.13, we reproduce the comparison performed by E. Stepanov *et al.* for the three-dimensional Hubbard model on a cubic lattice, solved by DMFT, which shows satisfactory agreement in the large interaction, low-temperature regime, when the Mott MIT is approached. In an independent work by L. Gaspard and J. Tomczak [63] the agreement between our and E. Stepanov's criteria was confirmed for the Bethe lattice case of the Hubbard model (solved by DMFT). In this work both criteria also showed a convincing agreement with characteristic timescales of the decay of the magnetic susceptibility in imaginary time, which are the focus of the corresponding Ref. [63]. Eventually, in the work by T. B. Mazitov and A. A. Katanin [158] the same procedure as the one introduced in Sec. 4.1 for the AIM was used for the Hubbard model on a square lattice solved by DMFT. In this way, the Kondo temperature of the DMFT solution of the Hubbard model was extracted from the temperature-behavior of χ_m and again compared to the criterion of the generalized charge susceptibility introduced above. The result is shown in the right panel of Fig. 4.13.

As the authors of the corresponding publications note, and as we also mentioned before, the T_K criterion as obtained from $\tilde{\chi}^D = \tilde{\chi}^O$ is valid only in the low-temperature and

the intermediate-to-strong coupling regime. In fact, our "fingerprint"-criterion coherently applies in the parameter regions where a description of the local properties in terms of the Kondo physics becomes appropriate. To summarize, the consistent comparisons of Refs. [63, 158, 159] support the remarkable agreement of T_K and the "fingerprint"-criterion in the Kondo regime. In our opinion, this represents a clear hint for a profound and rigorous connection between the vertex functions (generalized susceptibilities, or also reformulated as full vertices F) and the Kondo temperature, which goes beyond the general one related to the numerical determination of T_K based on χ_m, see Sec. 4.1. In particular, we speculate that a specific analytic relation may exist between the Kondo singlet formation and the lowest-frequency entries of the vertex functions, analogous to the one between the quasiparticle weight Z and the low-frequency range of the self-energy. It remains left for future studies to investigate whether such an analytical connection can be formulated, e.g., by starting from newest NRG two-particle calculations of the scattering amplitude of Ref. [141] (see Fig. 9 therein).

Physical implications of irreducible vertex divergences

Here comes success, here comes success
Hooray success, hooray success
– Iggy Pop

The last chapters clearly demonstrated that irreducible vertex divergences should be expected as a general characteristic of interacting many-electron models. However, the physical implications of their appearance have not been discussed so far. This will be the main topic of this chapter, also answering the third central question of this thesis. To this aim, we first elaborate on the connection between the suppression of physical response functions and the vertex divergences, already partly addressed in Chapters 3 and 4. In particular, we investigate whether their role is purely linked to suppressive effects. As it turns out, this is not the case. In fact, the sign-flip of the singular eigenvalues, associated with crossing a divergence line, can also drive opposite effects, such as an effective attraction in given scattering channels. This mechanism can have dramatic implications: It underlies the enhancement and ultimately the divergence of the isothermal compressibility, which characterizes the occurrence of phase-separation instabilities in the proximity of the Mott transition.

So far, the discussion of vertex divergences has remained on a very conceptual and fundamental level. Chapter 3 focused on analyzing their occurrence in different models at half filling and out of half filling. This investigation clearly demonstrated that the appearance of irreducible vertex divergences is not a peculiar feature of one specific model but rather a ubiquitous property of strongly correlated electron systems. In Chapter 4, we discussed how the formation of a local magnetic moment originates negative diagonal entries in the static generalized charge susceptibility $\chi_c^{\nu\nu'(\omega=0)}$ and leads to vanishing eigenvalues, the origin of the vertex divergences. However, an important question remained unanswered: *Are there physical implications of the appearance of irreducible vertex divergences*?, which represents the third central question of this thesis. As outlined at the beginning of Chapter 3, the full vertex F remains finite at an irreducible vertex divergence since the generalized

susceptibility has a vanishing contribution there, ruling out the most natural connection with observable physical effects.

Nonetheless, in this chapter, we demonstrate that significant physical implications *exist*, and thus, entering the nonperturbative regime is not only a mere mathematical pathology of the QFT description of many-electron systems. In particular, as we will show, the eigenvalues and eigenvectors that determine the occurrence, the location, and the mathematical properties of the irreducible vertex divergences, also play an essential role for physical response functions.

First, by restricting ourselves to purely local physics, we discuss the interplay of the suppression of physical response functions and the suppression of eigenvalues of the corresponding generalized susceptibilities.

As a second step, we leave the purely local level and consider the *uniform* ($\mathbf{q} \to 0$) charge response of the system (in the framework of DMFT), which is related to the isothermal compressibility κ. As we will show, the negative eigenvalues of the local charge susceptibility can have significant effects on this quantity: they encode a sign-flip of the effective interaction, which leads to attractive contributions that enhance the uniform charge response. In some cases, e.g., in the proximity of the Mott MIT, these attractive contributions can even lead to a divergence of the isothermal compressibility κ. Note that this topic was first addressed in the Master thesis of M. Reitner [73] (which the author of this PhD thesis has co-supervised) and then extended in Ref. [67] (which represents the basis for this chapter).

5.1   Is it all just suppression?

Parts of this chapter, marked by a vertical bar, have already been published in the APS journal
*Phys. Rev. Lett. **125**, 196403 (2020) and the corresponding supplemental material.*
To improve the pedagogical character of this chapter, both sources are mixed accordingly.

As already mentioned in previous chapters, the possible link between irreducible vertex divergences in channel r and the corresponding suppression of the physical response in the same channel r was considered in several works [12, 18, 22, 26]. In this context, the more recent results obtained in the attractive case of the HM solved in DMFT (see Sec. 3.1.2), have cast some doubt on the generality of this interpretation, because of the occurrence of divergences in the enhanced charge sector of the attractive case [26]. On the other hand, as mentioned at the end of Ref. [26], the analysis of that study was limited by the particle-hole symmetry constraint, which we are going to release in the course of this chapter.

In particular, we will focus on the charge channel. Let us begin our discussion by briefly recapitulating the literature results for the half-filled case of Refs. [12, 18], relevant for our analysis. We start with the definition of the static local charge response $\chi_c^{\text{loc}}(\omega = 0)$, which can be obtained from $\chi_c^{\nu\nu'(\omega=0)}$ by a summation over all fermionic Matsubara frequencies, see Sec. 2.2.3. By recasting the corresponding summation for the general case without particle-hole symmetry in terms of the eigenbasis of $\chi_c^{\nu\nu'}$ (see Sec. 2.2.4 and in particular

Eqs. (2.56) and (2.59)), one obtains [67]:

$$\chi_c^{\text{loc}} = \frac{1}{\beta^2} \sum_{\nu\nu'} \chi_c^{\nu\nu'(\omega=0)} = \sum_i \lambda_i^c w_i^c \; . \tag{5.1}$$

Note that here a slightly different notation[1] is used: $\chi_c^{\text{loc}} = 2\chi_c^{\text{Eq. (2.27)}}$. Consequently, also the generalized susceptibility is defined here as $\chi_c^{\nu\nu'} = 2(\chi_{\uparrow\uparrow}^{\nu\nu'} + \chi_{\uparrow\downarrow}^{\nu\nu'})$. Further, the $\frac{1}{\beta^2}$ factor is directly included in the eigenvalues λ_i^c. Accordingly, the weights read as: $w_i^c = \left[\sum_\nu V_i^{c-1}(\nu)\right]\left[\sum_{\nu'} V_i^c(\nu')\right]$ (cf. Eq. (2.60)). Since we only consider the charge channel in this chapter, the c superscript will be omitted in the following.

In order to investigate the possible implications of the appearance of vertex divergences, we start with an observation, based on the findings of Chapters 3 and 4: The occurrence of sign-changes of the eigenvalues of the generalized susceptibility, at least of those with an associated symmetric eigenvector, was always found in cases where the corresponding response function was suppressed (cf. Sec. 3.1.2). By inverting this logic, one may ask how crucial the role of negative eigenvalues is for determining the correct behavior of the physical response function. In general, their importance was already noted when analyzing the two-particle calculations for the AIM, for which methods such as the fRG (in the $1\ell_K$ truncation) and the PA, which lack–per construction–the possibility to describe irreducible vertex divergences and sign-flips of the corresponding eigenvalues, did not capture the minimum of the charge response as a function of T (see Sec. 4.5).

A focused study of this role of the negative eigenvalues of $\chi_c^{\nu\nu'}$ has been performed in Ref. [12], where the authors considered a HM solved by DMFT on a square lattice ($4t = 1$ is the unit of energy). Fig. 5.1 illustrates their results for the local charge response χ_c^{loc} (black line) at half filling for an intermediate temperature of $\beta = 40$. Altogether one observes a progressive suppression of the charge response as a function of U, as one would expect. The local magnetic response increases with U as the local moment is formed, whereas charge fluctuations are significantly suppressed. The kink observed at about $U \approx 2.35$ was attributed to the MIT. As outlined in Eq. (5.1), χ_c^{loc} can be analyzed by using the eigenbasis of $\chi_c^{\nu\nu'}$. In Fig. 5.1 the sum of those contributions which correspond to positive eigenvalues, is illustrated as the orange area and "+" signs. The contribution related to negative eigenvalues is shown in blue and marked by "-" signs. This separation clearly demonstrates the role played by the eigenvalues of $\chi_c^{\nu\nu'}$: As the interaction increases, the positive eigenvalues reduce in value up until $U \approx 1.9$. After this point, negative contributions appear, which become crucial for the correct description of the suppressed response function. Neglecting them would lead to a significant overestimation of the local charge response (orange "+" for large U), and also the kink associated with the MIT would be absent. Naturally, at half filling, each appearance of a negative contribution corresponds to a zero-crossing of an eigenvalue and hence a divergence of $\Gamma_c^{\nu\nu'}$ (cf. Sec. 3.1). The inset shows the value of the eigenvalues with associated symmetric (antisymmetric) eigenvectors

---

[1]All changes of notation are made in order to relate the susceptibilities in a more elegant way to the isothermal compressibility, see below (otherwise a factor of 2 would appear in several terms) [67, 73], consistently with Ref. [67].
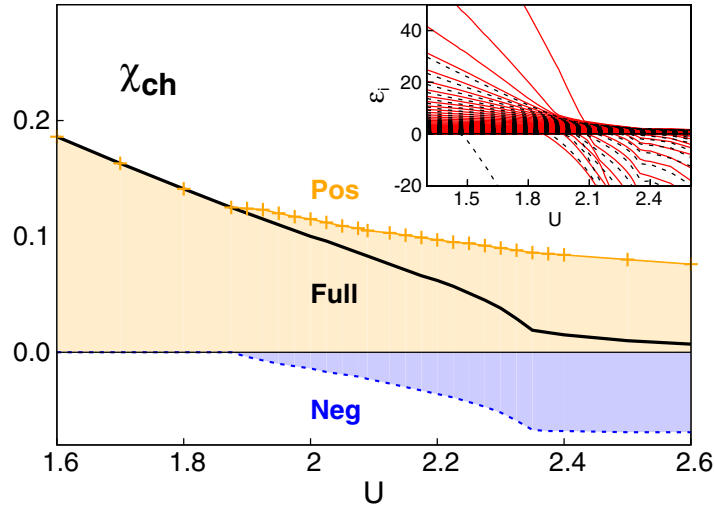
Figure 5.1: Local charge response (solid black line) for the HM solved by DMFT at $\beta = 40$ as a function of U. The yellow (blue) area corresponds to the summed contribution to χ_c^{loc} originated by positive (negative) eigenvalues (cf. Eq. (5.1)). The inset demonstrates the eigenvalues corresponding to a symmetric / antisymmetric eigenvector as a function of U (solid red / dashed black lines). For completeness, let us note that the authors did use the regular convention (cf. Sec. 2.2.3 and 2.2.4) for the $\frac{1}{\beta^2}$ factor and for χ_c^{loc}. The figure was taken from Ref. [12] (see Fig. 3 therein).

as solid red (dashed black) lines. Due to the perfect antisymmetry at half filling, eigenvalues which correspond to an antisymmetric eigenvector do not contribute in Eq. (5.1) (cf. 2.2.4.1). This means that the lowest U value where the first negative contributions appear is related to the first orange divergence line, in perfect agreement[2] with Fig. 3.8.

In this way it becomes apparent how the negative eigenvalues of $\chi_c^{\nu\nu'}$, at least those corresponding to a symmetric eigenvector, impact the physical response functions in the nonperturbative regime. The same perspective is also valid for the pp-$\uparrow\downarrow$ channel and the pairing fluctuations at repulsive U, or the magnetic ones in the attractive case [26] (cf. Sec. 3.1.2), i.e., for the channels whose local fluctuation are suppressed by the interaction.

However, also a different viewpoint is possible, as shown in Ref. [160]: Since the irreducible vertex $\Gamma_c^{\nu\nu'}$ is the core of a BSE, its multiple sign-changes (driven by those of λ_i, see Eq. (3.2)) could be interpreted as a flipping of a repulsive into an attractive interaction (or vice versa). Heuristically, if we consider a simple RPA-like expression [$\Gamma_c^{\nu\nu'} \to \Gamma_0 > 0 \, \forall \, \nu, \nu'$ (constant, as described in Sec. 4.2)] for the *lattice* charge (and similarly for the pairing) response, one gets:

$$\chi_{\mathbf{q}} = \frac{\chi_{\mathbf{q}}^0}{1 + \Gamma_0 \chi_{\mathbf{q}}^0} \ . \tag{5.2}$$

---

[2]Following the results discussed at the end of Sec. 3.1.3 one can even make a closer connection to the results discussed here: As shown in Fig. 3.20, the number of negative eigenvalues changes abruptly at the MIT, depending on which solution (metallic or insulating) is realized. These results are in perfect agreement with the kink in Fig. 5.1, which is only observed in the negative contributions.
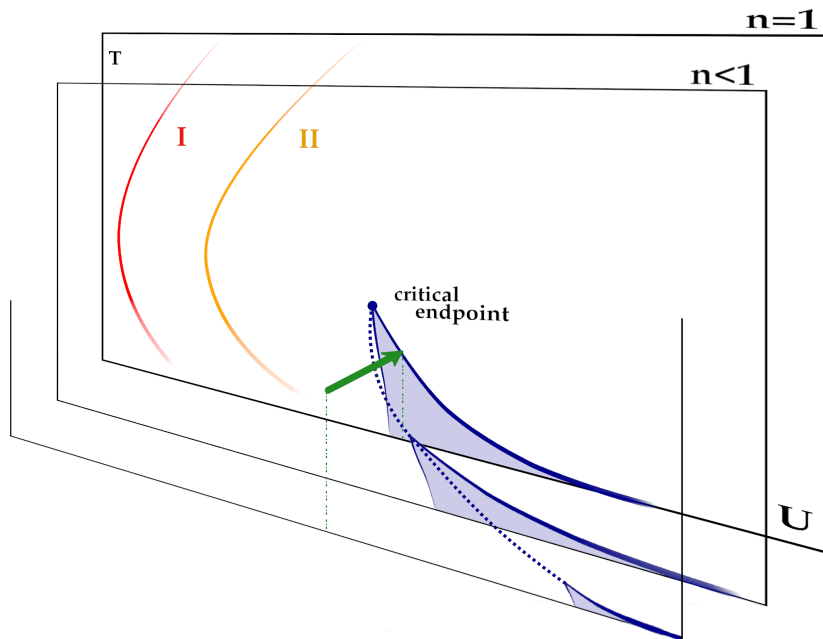
Figure 5.2: Sketch representation of the Hubbard model phase diagram in DMFT, based on Ref. [163]. The coexistence region of the MIT at $n = 1$ as well as the phase separation at $n < 1$ is represented by shaded blue regions, the corresponding critical endpoints by the blue dot / the blue dotted line. First(I)/Second(II) lines of divergences of Γ at half filling: red/orange curves. The calculations performed in this analysis are illustrated by the green arrow.

Hence, a sign-change of Γ_0 would induce an enhancement, instead of a suppression, of the corresponding susceptibility with increasing interaction.

Though intriguing, this interpretation [160] raises additional questions: It seems hard to be reconciled with the suppression of charge fluctuations at half filling discussed. Further, if taken too literally, it would lead to rather bizarre physical predictions: One might then expect the multiple divergences of Γ, found in the phase diagram of the Hubbard model (cf. Sec. 3.1), to be reflected in a series of maxima (maybe even of divergences) of the lattice charge and pairing susceptibilities by increasing U. However, such a peculiar oscillatory behavior has never been reported [160–169].

5.2 The isothermal compressibility κ

As known [160–163], DMFT calculations show only one major enhancement of the charge fluctuations: the uniform charge response, which corresponds to the isothermal compressibility κ, is strongly enhanced in the proximity of the critical endpoint of the MIT of the Hubbard model (blue dot, topping the blue-shaded area in the $n = 1$ plane of the phase diagram sketched in Fig. 5.2). Specifically, while at half filling the isothermal compressibility κ decreases monotonically with increasing U, a strongly enhanced compressibility is observed in the crossover region at *finite* doping on both sides of the MIT. In fact, κ even diverges along two curves in the parameter space embracing the critical endpoint of the

MIT (blue dotted line in Fig. 5.2, shown on one side only) and marking the onset of a phase separation at lower T [163].

As we will show, this behavior of κ is directly linked to the divergences of the irreducible vertex Γ_c and, specifically, to the first ones encountered [10, 19, 26] in the correlated metallic region, much before the MIT itself. The location is sketched as red (I) and orange (II) curves in the $n = 1$ plane of Fig. 5.2 (cf. Sec. 3.1.1.3).

In general, the compressibility κ can be defined (i) at the one-particle level, as the derivative of the density w.r.t. the chemical potential[3]$(\frac{dn}{d\mu})$or (ii) at the two-particle level, as the static limit ($\mathbf{q} \to 0$, $\omega = 0$) of the momentum and frequency dependent charge response function $\chi_{c,\mathbf{q}}^{\omega} = \chi_{\mathbf{q}}^{\omega}$, obtained through the lattice BSE in the DMFT framework [41]

$$\chi_{\mathbf{q}}^{\omega} = \frac{1}{\beta^2} \sum_{\nu\nu'} \left[\left[\chi_{\mathbf{q}}^0\right]_{\nu\nu'\omega}^{-1} + \Gamma_c^{\nu\nu'\omega} \right]^{-1}, \tag{5.3}$$

where the bubble term reads $\chi_{\mathbf{q}}^{0,\nu\nu'\omega} = -2\beta \sum_{\mathbf{k}} G(\mathbf{k},\nu)G(\mathbf{k}+\mathbf{q},\nu+\omega)\delta_{\nu\nu'}$. Here $\mathbf{q}$ is the transferred crystal momentum. In DMFT, where the self-energy and the irreducible vertex Γ are both extracted from a (self-consistently determined) auxiliary impurity model [41], the two definitions yield per construction the same value of κ (see Ref. [170] and [56, 57, 160]).

Let us briefly recall the derivation of the momentum and frequency dependent charge response function in DMFT obtained through the BSE, following Ref. [41]. We discuss its analytical properties for the Hubbard Model on a Bethe-lattice, by going into the eigenbasis of the generalized local two-particle susceptibility.

In the limit of infinite dimensions $d \to \infty$ the irreducible vertex $\Gamma^{\nu\nu'\omega}$ can be expressed in terms of the local quantities of the auxiliary impurity model (cf. Eq. (2.24))

$$\Gamma_c^{\nu\nu'\omega} = \left[\chi_c^{-1}\right]^{\nu\nu'\omega} - \left[\chi_0^{-1}\right]^{\nu\nu'\omega}, \tag{5.4}$$

where $\chi_c^{\nu\nu'\omega} = 2(\chi_{\uparrow\uparrow}^{\nu\nu'\omega} + \chi_{\uparrow\downarrow}^{\nu\nu'\omega})$, and $\chi_{\sigma\sigma'}^{\nu\nu'\omega}$ is defined in Eq. (2.17) [33]. Note that although in $d \to \infty$, Γ itself has a residual momentum dependence, this residual dependence vanishes if Γ is inserted into a BSE [171]. Hence, Eq. (5.4) can be used to rewrite Eq. (5.3) in the following way:

$$\chi_{\mathbf{q}}^{\omega} = \frac{1}{\beta^2} \sum_{\nu\nu'} \left[\left[\chi_c^{-1}\right]^{\nu\nu'\omega} + \left[\chi_{\mathbf{q}}^0\right]_{\nu\nu'\omega}^{-1} - \left[\chi_0^{-1}\right]^{\nu\nu'\omega} \right]^{-1}, \tag{5.5}$$

where the bubble term reads explicitly

$$\chi_{\mathbf{q}}^{0,\nu\nu'\omega} = \frac{-2\beta}{V} \sum_{\mathbf{k}} \frac{1}{\zeta_\nu - \epsilon_{\mathbf{k}}} \frac{1}{\zeta_{\nu+\omega} - \epsilon_{\mathbf{k}+\mathbf{q}}} \delta_{\nu\nu'}, \tag{5.6}$$

---

[3] In thermodynamics, the isothermal compressibility κ is defined as $\kappa_T = -\frac{1}{V}\frac{dV}{dp} = \frac{1}{n^2}\frac{dn}{d\mu}$. For an immediate comparison with $\chi_{\mathbf{q}=0}$, we define here $\kappa \equiv \frac{dn}{d\mu}$ in accordance with earlier literature [41, 161], see also Ref. [73]. This does not crucially affect the results, since the doping regions considered here are very close to half filling $n = 1$.

with $\zeta_v = iv + \mu - \Sigma(v)$ and $\epsilon_{\mathbf{k}} = -\frac{2t}{\sqrt{2d}} \sum_i^d \cos k_i$. The $\frac{1}{V}$-factor normalizes the momentum sum over the first Brillouin zone. Note also that the correct scaling of the hopping amplitude t for $d \to \infty$ is included in the dispersion relation $\epsilon_{\mathbf{k}}$ (cf. Sec. 2.3.1). We can reformulate the bubble terms with the Hilbert transform defined as:

$$\mathcal{H}(\zeta) = \int_{-\infty}^{+\infty} d\epsilon \, D(\epsilon) \frac{1}{\zeta - \epsilon} \, , \tag{5.7}$$

where $D(\epsilon)$ is the non-interacting density of states. By summing over all momenta $\mathbf{q}$ we obtain the local bubble term. Here, the sums over the two different momenta factorize and we get

$$\chi_0^{vv'\omega} = \frac{1}{V} \sum_{\mathbf{q}} \chi_{\mathbf{q}}^{0,vv'\omega} = -2\beta \mathcal{H}(\zeta_v) \mathcal{H}(\zeta_{v+\omega}) \delta_{vv'} \, . \tag{5.8}$$

In our case, the static charge response ($\mathbf{q} \to 0$, $\omega = 0$) is of interest, where the $\mathbf{q}$-dependent bubble reads

$$\begin{aligned}
\chi_{\mathbf{q}=0}^{0,vv'(\omega=0)} &= -2\beta \int_{-\infty}^{+\infty} d\epsilon \, D(\epsilon) \frac{1}{(\zeta - \epsilon)^2} \delta_{vv'} \\
&= 2\beta \frac{d\mathcal{H}(\zeta_v)}{d\zeta_v} \delta_{vv'}.
\end{aligned} \tag{5.9}$$

5.2.1 Bethe-lattice

For the Bethe-lattice with a semi-elliptic density of states the Hilbert transform simplifies to

$$\mathcal{H}(\zeta) = \frac{\zeta - \text{sgn}(\text{Im}\zeta)\sqrt{\zeta^2 - 4t^2}}{2t^2} \, , \tag{5.10}$$

and the difference between the two inverted bubble terms for $\omega = 0$ is equal to a constant [172] :

$$\left[\chi_{\mathbf{q}=0}^0\right]_{vv'}^{-1} - \left[\chi_0^{-1}\right]^{vv'} = \frac{t^2}{2\beta} \delta_{vv'} \, . \tag{5.11}$$

We note that this result does not depend on the frequency v or on the filling (or the chemical potential μ which is encoded in ζ).

The compact expression for the difference of the bubble inverses is inserted into Eq. (5.5). By recasting the resulting expression in the eigenbasis of the generalized susceptibility $\chi_c^{vv'}$, which is straightforward due to the $\delta_{vv'}$ frequency-dependence of Eq. (5.11), one obtains:

$$\kappa = \chi_{\mathbf{q}=0}^{\omega=0} = \sum_i \left(\frac{1}{\lambda_i} + \frac{\beta t^2}{2}\right)^{-1} w_i \, . \tag{5.12}$$

By a similar derivation, but inserting the particle-particle DMFT bubble at $\mathbf{q} = 0$ or the particle-hole bubble at $\mathbf{q} = (\pi, \pi, \pi, ...)$ into Eq. (5.11), one can show that one gets an additional minus sign for $\frac{t^2}{2\beta}$ [172] in Eq. (5.11) and correspondingly also in Eq. (5.12).
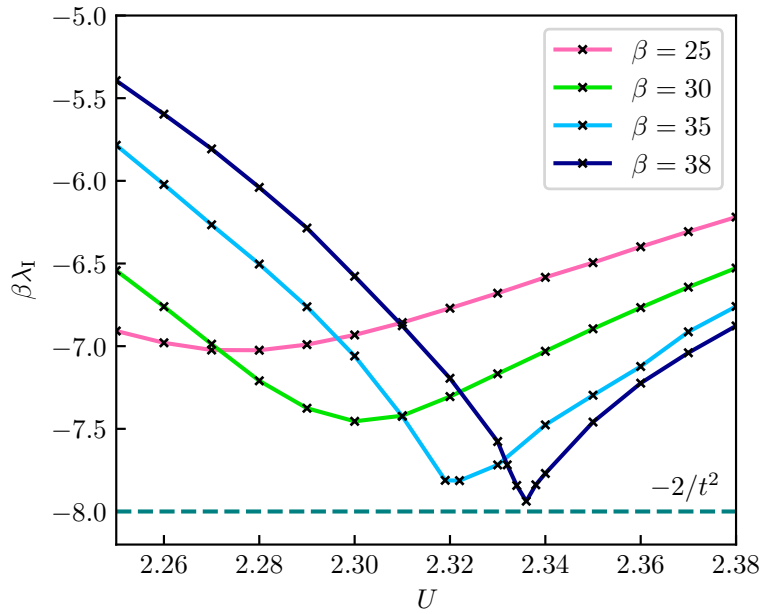
Figure 5.3: Lowest eigenvalue λ_{I} of $\chi_c^{\nu\nu'}$ for different temperatures, computed by DMFT on a half-filled Bethe lattice (solid lines), compared with the divergence condition $-\frac{2}{t^2}$ (dashed line) of the analytical expression for the uniform susceptibility [Eq. (5.12)].

Eq. (5.12) holds exactly for the Bethe-lattice case (here of half-bandwidth $D = 2t = 1$), independently of its filling. As we will explicitly discuss below, it also represents a very good approximation if the DMFT is performed on other, more realistic lattices (see further Appendix A.2.1).

A quick glance at Eq. (5.12) immediately shows that the *only* possibility for a divergence of κ is that the condition $\beta\lambda_i = -\frac{2}{t^2} < 0$ is verified for one eigenvalue of $\chi_c^{\nu\nu'(\omega=0)}$. Evidently, this locates necessarily such divergences of κ on the right side of the first vertex-singularity line (red curve in Fig. 5.2) and defines precise constraints, calling for a quantitative analysis.

5.3 The half-filled case

We consider first the (particle-hole symmetric) half-filled Bethe-lattice case, computing the evolution of the lowest eigenvalue $\lambda_{\mathrm{I}} < \lambda_{i\neq\mathrm{I}}$ as a function of U for different temperatures, shown in Fig. 5.3. We use a CT-QMC solver provided by the w2dynamics package [85] (cf. Sec. 2.3.1.2) to obtain the one- and two-particle quantities (for further numerical details see the supplemental material of Ref. [67]). As discussed in the literature [22, 26] (cf. Secs. 2.2.4.1 and 3.1.2) and at the beginning of this chapter, due to the high symmetry of this case, λ_{I} is associated with a real, antisymmetric eigenvector ($V_{\mathrm{I}}(\nu) = -V_{\mathrm{I}}(-\nu)$, hence $w_{\mathrm{I}} = 0$). From the data of Fig. 5.3, we clearly see that λ_{I} displays a minimum at intermediate U, in the *crossover region* of the Mott MIT. By reducing T the minimum gets sharper and progressively closer to the necessary condition of a divergence of κ (marked by the dashed line). Remarkably, the condition is fulfilled at the (second-order) critical

endpoint of the MIT (at $U \simeq 2.33$, $\beta \simeq 38$), where the minimum of λ_{I} becomes a cusp, before one starts observing a coexistence of two solutions at lower T (not shown). At half filling, however, the divergence of $(1/\lambda_{\mathrm{I}} + \beta t^2/2)^{-1}$ does not have *any* physical effect on κ, because the associated spectral weight w_{I} in Eq. (5.12) is always zero, due to the perfect antisymmetry of $V_{\mathrm{I}}(\nu)$. We note that this behavior can alternatively be understood from the critical properties of the MIT, as independently proven in a work by E. van Loon *et al.* [140]. The second lowest eigenvalue (λ_{II}), associated with a symmetric eigenvector ($V_{\mathrm{II}}(\nu) = V_{\mathrm{II}}(-\nu)$) becomes also negative (after the orange curve in Fig. 5.2), but it never reaches the critical condition $\beta\lambda_{\mathrm{II}} = -\frac{2}{t^2}$. In fact, as its spectral weight is positive, it contributes to a progressive suppression of κ.

5.4 Out of half filling

The results above crucially depend on the high-symmetry properties [26, 113] of the (non-frustrated) half-filled case. As soon as those are lifted, e.g. by doping the system and/or adding a next-to-nearest neighbor hopping term (t') striking changes are observed. Here, we consider explicitly the case of a hole doped system ($\mu - \frac{U}{2} < 0$, $n < 1$, $t' = 0$) on a square lattice[4](with half-bandwidth $D = 4t = 1$) in the *crossover* region of the phase separation near the critical endpoint of the half-filling MIT (i.e., $U = 2.4$, $\beta = 53$, as schematically indicated by the green arrow in Fig. 5.2).

In Fig. 5.4, we report the behavior of the local (χ_{loc}) and the uniform (κ) charge susceptibility as a function of the chemical potential, varying it toward half filling ($\mu = \frac{U}{2}$ on the right side). Our data show a clear *dichotomy* in the behavior of χ_{loc} and κ. While χ_{loc}, directly evaluated from Eq. (5.1), gets monotonically suppressed toward half filling, where correlations are stronger, κ, evaluated both as numerical derivative as well as from Eq. (5.3), displays a prominent maximum at a finite doping: This indicates that the parameters correspond to the crossover region[5], just slightly *above* the critical endpoint of the phase separation (dotted line in the sketch of Fig. 5.2).

5.5 Diagnostics of κ

A clear-cut theoretical insight into this phenomenology is obtained by decomposing χ_{loc} and κ, computed at several dopings, in terms of the contributions stemming from the different eigenvalues λ_i of $\chi_c^{\nu\nu'}$, in the spirit of Refs. [18, 58, 59, 122, 138, 153, 156, 173, 174]. Here, this procedure, which is always possible numerically, allows for a very transparent analytical understanding, based on the Bethe-lattice expression, Eq. (5.12). In fact, the

---

[4]In principle, one could have also chosen the Bethe lattice case out of half filling, obtaining similar results as those presented here. However, the choice of a two-dimensional square lattice allowed to perform a **q**-dependent analysis and also make closer contact with previous literature studies on the HM [10, 12, 19, 160].

[5]Note that this property of the chosen parameter set was carefully checked in various ways, see further Appendix A.2.2 and the supplemental material of Ref. [67]. In particular, when converging DMFT solutions as a function of μ from both limiting cases shown in Fig. 5.4, i.e.,half filling and $\mu - U/2 < -0.15$, always only a *single* solution could be converged [67].

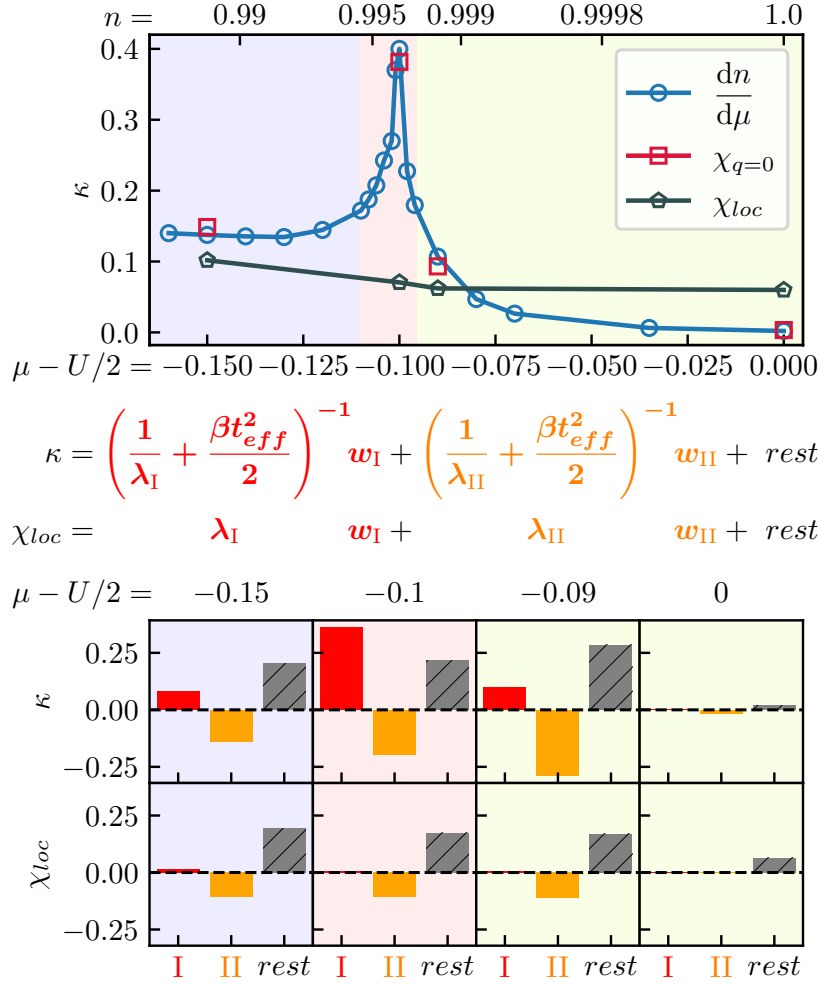Figure 5.4: Top: Compressibility κ (blue circles from the numerical derivative of n w.r.t. μ; red squares from the BSE for $\chi_{\mathbf{q}=0}$) and local charge susceptibility (χ_{loc}) of the Hubbard model computed in DMFT for $\beta = 53$ and $U = 2.4$ (on a square lattice with half-bandwidth $D = 1$). Bottom: Analysis of the contributions to κ and χ_{loc} arising from the lowest two *real* eigenvalues ("I" in red, "II" in orange) and from all the remaining terms ("*rest*" in grey) for four different dopings. The light background colors in the two panels are just a guide to the eye.

deviations found for the square lattice case are marginal in the parameter region of interest, see Appendix A.2.1. Eq. (5.12) can thus be exploited, in an approximated form ($t^2 \rightarrow t_{\text{eff}}^2$, where t_{eff} weakly depends on μ, cf. Appendix A.2.1), as a key to the interpretation.

We start by separating χ_{loc} in terms of the two lowest real λ_i-contributions and the rest to the sum in Eq. (5.1). As shown in the bottom panel of Fig. 5.4 at finite doping one observes a tiny *positive* contribution from λ_{I} (red bar) enhancing χ_{loc}, which fully disappears at half filling where its weight $w_{\text{I}} = 0$, due to symmetry. This is in contrast to the negative contribution from λ_{II}, which suppresses χ_{loc}, as in the half-filled case demonstrated in Fig. 5.1 [12]. The corresponding decomposition for κ shows, instead, that precisely the contribution originated from λ_{I} is responsible for its non-monotonous behavior as well as for the sharp maximum. By comparing the two decompositions, one immediately notes
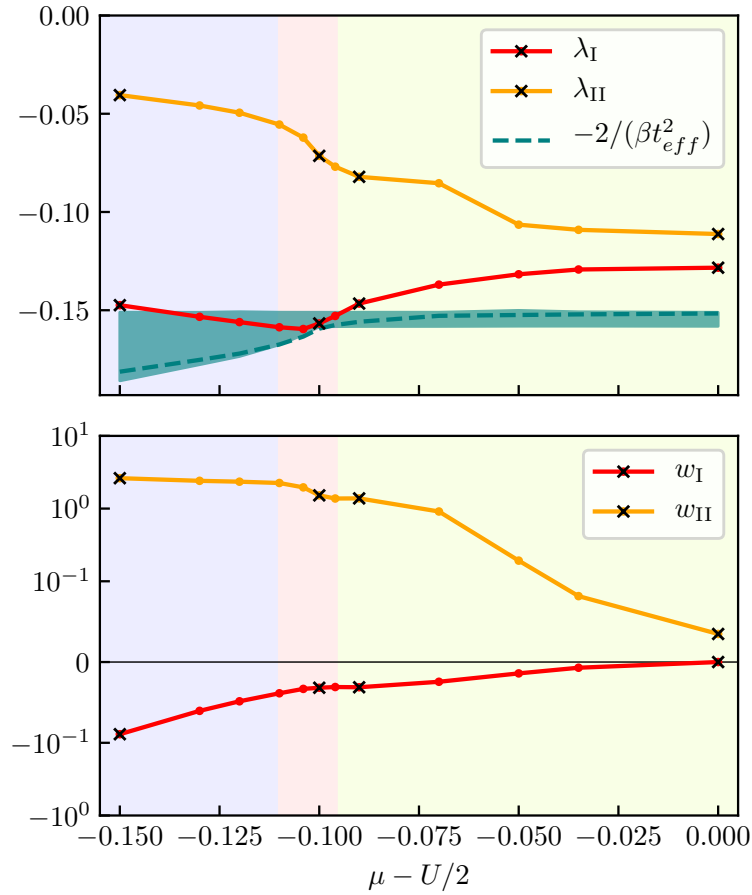
Figure 5.5: Top: Lowest two real eigenvalues (λ_I in red, λ_II in orange) of the local generalized charge susceptibility for the same parameters as Fig. 5.4; the weak frequency dependence of the difference of the inverse of the bubble terms for the square lattice case is marked, for each μ, by a blue-shaded area; the values of $^{-2}/_{\beta t^2_\mathrm{eff}}$ by a dashed line (see Appendix A.2.1). Bottom: corresponding spectral weights (w_I and w_II) on logarithmic y-axis.

how the dichotomy of the local and the uniform charge response is essentially controlled by the contributions (red bars) associated with the lowest real eigenvalue λ_I of $\chi_c^{\nu\nu'}$.

The outcome of our analysis can be readily understood in terms of Eq. (5.12), by studying the behavior of λ_I and w_I for different dopings, as reported in Fig. 5.5. If λ_I becomes negative enough, closely approaching the condition $\beta\lambda_\mathrm{I} \simeq -\frac{2}{t^2_\mathrm{eff}}$, a maximum of κ is observed. The difference w.r.t. the half-filled case is that the corresponding weight w_I is now *finite*, and actually *negative*, thus contributing to an overall enhancement of the charge response. Because of the small weight w_I, such an effect is generally mild, unless λ_I gets *negative enough* to trigger a strong enhancement or even the divergence of κ. Fig. 5.5 also shows that the weight associated with the second lowest real eigenvalue (λ_II) always remains positive, as at half filling. Hence, even if both $\lambda_\mathrm{I}, \lambda_\mathrm{II}$ are negative, the latter is responsible for a *suppression* of the charge response. In fact, it is the overall sign of $\lambda_i w_i$, which determines, in general, whether the net effect can be interpreted as
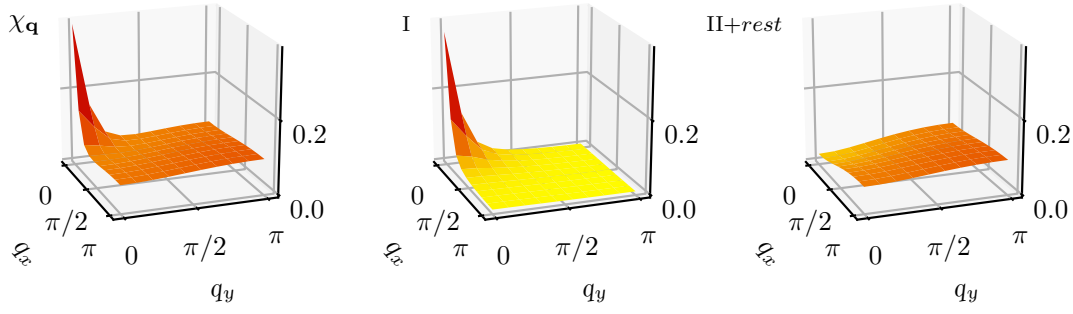
Figure 5.6: Left: Momentum-dependence of the charge susceptibility $\chi_{\mathbf{q}}$ computed in DMFT on a square lattice for $U = 2.4$, $\beta = 53$ for $\mu - U/2 = -0.1$, corresponding to the maximum of the compressibility κ. Center: contribution stemming from λ_{I}. Right: all other contributions summed.

repulsive or attractive in the charge sector, since the sign of w_i is no longer positive-definite (cf. Appendix A.2.3). This result impressively demonstrates the twofold effect that the negative eigenvalues, originated by the sign-flip associated with a vertex divergence, can have.

At the same time, the evolution of w_i of each λ_i, is smooth in the phase diagram (s. Fig. 5.5 and Appendix A.2.2). Hence, crossing the first divergence [10, 12, 19, 26] line of $\Gamma_c^{\nu\nu'}$, which is associated with a sign-change of λ_{I}, corresponds to flipping the net action of the corresponding contribution ($\lambda_{\mathrm{I}} w_{\mathrm{I}}$) to the charge response from suppressing to *enhancing*.

We stress that having $w_{\mathrm{I}} < 0$ is crucial both for the emergence of these strong-coupling phase-instabilities and for the dichotomy between the local and uniform response: The sum in Eq. (5.12) can be recast as

$$\kappa = \sum_i \frac{\chi_{\mathrm{loc}}^i}{1 + \beta J_{\mathrm{eff}}^i} \tag{5.13}$$

where $\chi_{\mathrm{loc}}^i = \lambda_i w_i$ and $J_{\mathrm{eff}}^i = \frac{t_{\mathrm{eff}}^2}{2 w_i} \chi_{\mathrm{loc}}^i$. All summands of Eqs. (5.1) and (5.13) are rather similar, except close to the critical endpoint of the phase separation where the difference between the local and uniform response is induced by the first term ($i = \mathrm{I}$) mainly. In that region, as $\chi_{\mathrm{loc}}^{\mathrm{I}} > 0$, $w_{\mathrm{I}} < 0$ implies a negative coupling ($J_{\mathrm{eff}}^{\mathrm{I}} < 0$) in the charge sector.

As a last point we extend our analysis to the entire momentum dependence of $\chi_{\mathbf{q}}$, performed at the same parameter set where the maximal κ is found. In the left panel of Fig. 5.6, $\chi_{\mathbf{q}}$ is plotted, where we observe a rather sharp peak at $\mathbf{q} = 0$. In the central and right panels, we decompose $\chi_{\mathbf{q}}$ into the contributions stemming from λ_{I} and the remaining eigenvalues, respectively. We immediately see that the nonperturbative enhancement of the charge response is confined to the small $\mathbf{q}$-sector. Further, we note that without the critical, effectively *attractive*, contribution from λ_{I}, the charge response would have a completely different shape, closely resembling the one at half filling, which is shown in

Fig. 5.7: a rather low $\chi_{\mathbf{q}}$ with a shallow maximum at $\mathbf{q} = (\pi, \pi)$. This selective enhancement of $\chi_{\mathbf{q}}$ around $\mathbf{q} = 0$ increases the corresponding correlation length ξ, which is necessary to ensure the second-order nature of the critical endpoints of the phase separation as well as for inducing the strong dichotomy between the local and the uniform response, discussed above (cf. Ref. [73]).
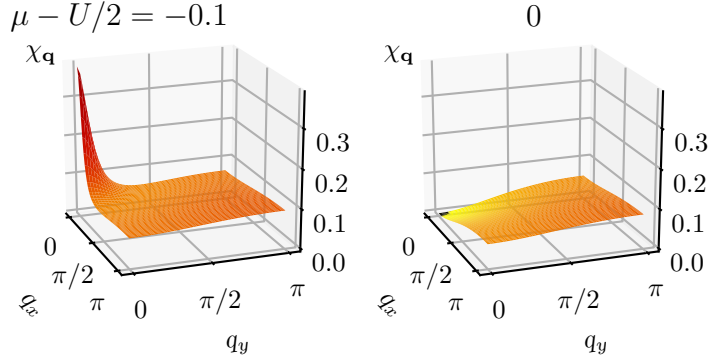

Figure 5.7: Comparison of the momentum dependence of $\chi_{\mathbf{q}}$ for the parameter set corresponding to the maximum of κ ($\mu - U/2 = -0.1$), see Fig. 5.6, and half filling (0).

We expect to find the same underlying mechanism along the entire, highly non-trivial, path of the phase-separation instability computed in the DMFT phase diagram of Ref. [163] (dotted blue line in Fig. 5.2). For specific examples at different parameter sets we refer to Ref. [73].

5.6 Discussion

In this chapter an important link between the appearance of vertex divergences and observable physical implications could be identified via the analysis of the corresponding eigenvalues of the local generalized susceptibility [12, 67]. In particular, the eigenvalues λ_i and weights w_i of $\chi_c^{\nu\nu'}$ (computed in DMFT) were *directly* connected to relevant physical quantities: the local (χ_{loc}) and the uniform ($\chi_{\mathbf{q}=0}$) charge susceptibility, whereas the latter corresponds to the isothermal compressibility κ.

For the local charge response χ_{loc}, suppressing and enhancing contributions were identified, depending on the overall sign of $\lambda_i w_i$. In this way, vertex divergence lines, which are characterized by positive w_i and symmetric eigenvectors at half filling, can be attributed to a *suppression* of χ_{loc}, as soon as sign-changes of the corresponding λ_i have occurred. The red divergence lines on the other hand (with antisymmetric eigenvectors at half filling), can be related to an *enhancing* effect, as the associated eigenvectors yield negative w_i as soon as particle-hole symmetry is broken.

As for the uniform susceptibility, depending on the sign of the corresponding weight w_i, the effect onto κ can be twofold, similarly as in the local case. A *sign-change* of λ_i corresponds to a *flipping* of the nature of the effective electronic interaction. In particular, if the weight is negative, as it happens out of half filling for the first red divergence line, the effective

interaction changes from repulsive to *attractive*. The origin of this effective attraction is thus directly related with the breakdown of self-consistent perturbation theory [12], formally marked by the first divergence of the irreducible vertex (cf. Appendix A.2.2). For a positive weight, such as the one characterizing the orange divergence lines at half filling, the associated negative eigenvalues have a suppressing effect onto κ.

This effective attraction due to negative eigenvalues (and weights) has significant physical and conceptual implications. In particular, we have demonstrated that *if* the lowest negative eigenvalue of the local charge susceptibility becomes *negative enough*, a divergence of the isothermal compressibility, and hence a thermodynamic instability of the systems toward a phase separation, will be triggered [67]. The specific details of the lattice system under investigation determine the negative value that needs to be reached (cf. Appendix. A.2.1).

It is insightful to generalize our considerations by further extending Eq. (5.12) to the other physical sectors, specifically to those which are mostly reactive to attractive interactions. One can show [172] that the corresponding DMFT expressions for the Bethe lattice for any static particle-hole susceptibility at $\mathbf{q} = \mathbf{\Pi} = (\pi, \pi, \pi, \dots)$ (describing charge-density-wave (CDW) instabilities in the charge or antiferromagnetic (AFM) instabilities in the magnetic sector), as well as of the pp susceptibility at $\mathbf{q} = 0$ (describing s-wave pairing instabilities) read

$$\chi_{\mathbf{q}=\mathbf{\Pi}} = \chi_{\mathbf{q}=0}^{pp} = \sum_i \left(\frac{1}{\lambda_i} - \frac{\beta t^2}{2} \right)^{-1} w_i, \tag{5.14}$$

independently of the filling.

The sign of the constant shift rules out the possibility of inducing CDW or *s*-wave pairing instabilities merely through a strong local repulsion: divergences of the corresponding responses can only originate from a *large* and *positive* λ_i, a typical hallmark [26] of preformed local pairs, and hence, of the presence of a bare attractive interaction $U < 0$. Here, we clearly see the difference between a bare (and frequency-independent) attractive interaction and an effective one, originating from nonperturbative mechanisms: The effect of the latter can be regarded as truly attractive only in specific sectors and parameter regions.

In this way, in the DMFT framework, *two* alternative routes for thermodynamic instabilities are identified, on the basis of the *perturbative* or *nonperturbative* mechanisms through which the corresponding transitions are realized. Fig. 5.8 summarizes and illustrates these two possibilities for a generic local generalized susceptibility.

The first kind of instabilities (right side in Fig. 5.8) are triggered when the *largest positive* eigenvalue λ_{max} of the generalized local susceptibility for the scattering channel under consideration (e.g. charge, magnetic, pp) becomes *large enough*, leading to a divergence of Eq. (5.14). Since for $U = 0$ (and $\omega = 0$), where $\chi_{\mathrm{loc}}^{\nu\nu'}$ reduces to the bare bubble term, all λ_α are positive, it is clear that these kind of transitions can also occur in the weak-coupling regime. Their description is indeed possible by means of perturbative schemes such as, e.g. the RPA, the fRG [98, 99] or the PA [55, 90–92, 96, 153–157]. One example for this mechanism is the antiferromagnetic instability for the repulsive Hubbard model [41, 98,

$$\chi_{q=0} = \sum_i \left(\frac{1}{\lambda_i} + \beta t^2 / 2\right)^{-1} w_i \qquad \chi_{q=\Pi} = \chi_{q=0}^{pp} = \sum_i \left(\frac{1}{\lambda_i} - \beta t^2 / 2\right)^{-1} w_i$$

⇓ ⇓

minimal negative λ_{min} maximal positive λ_{max}
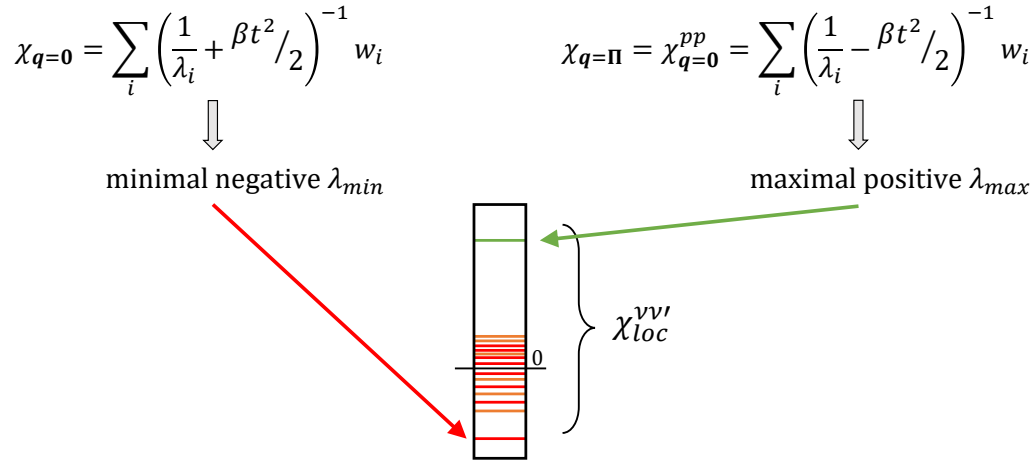
$\chi_{loc}^{\nu\nu'}$

0

Figure 5.8: Schematic representation of the different ways how a thermodynamic instability can be triggered in the framework of DMFT. On the left side Eq. (5.12) is stated for a general uniform particle-hole susceptibility. On the right side Eq. (5.14) is given. A generic local susceptibility with the corresponding eigenvalue spectrum is illustrated in the center, where the different key elements to trigger an instability are highlighted by the arrows.

106, 114, 175, 176] as well as the CDW or s-wave pairing instability in the attractive Hubbard model [102, 113, 115, 177–180].

The second kind of transitions are triggered when the *lowest negative* eigenvalue of the generalized local susceptibility $\lambda_{\min}$ becomes *negative enough*, leading to a divergence of Eq. (5.12). Such requirements would be applicable to the uniform response in all particle-hole sectors, describing the phase-separation instability studied here in the charge channel, or the ferromagnetic one in the magnetic sector.

As already discussed in Sec. 4.5 concerning the minimum of the charge response in the AIM, self-consistent perturbative methods lack the possibility of describing vertex divergences and hence also directly flipping the sign of the corresponding eigenvalues. This makes the condition $\lambda_{\min} < 0$ impossible to reach, starting from the perturbative regime close to half filling, as this requires to cross at least one divergence of the irreducible vertex in parameter space.

In this perspective, our analysis opens a new path to investigate phase transitions that have an intrinsic nonperturbative nature. These transitions, as described here in the DMFT framework, would be beyond the description of methods such as the fRG and the PA. However, a word of caution is still required at this stage. When starting from the local perspective, as DMFT does, Eqs. 5.12 and 5.14 determine the instabilities found in the lattice system under investigation. In this framework negative eigenvalues are crucially needed to trigger a corresponding instability, which is beyond the description of e.g., fRG and PA. However, these perturbative methods directly calculate the susceptibility of the lattice system under investigation $\chi_{\mathbf{q}}$, without starting from a local perspective, as DMFT does. Whether or to what extent, transitions of the same classes as those described here, might be triggered by different mechanisms in perturbative methods such as PA and fRG cannot be definitely answered yet. Nevertheless, these possible perturbative alternatives, even if

existing, are certainly not applicable for the description of the phase-separation instabilities in the proximity of the Mott MIT. This topic will be further discussed in Chapter 7.

Nevertheless, in the DMFT framework, our study provides a clear-cut positive answer to the third central question of this thesis: *Are there physical implications of the appearance of irreducible vertex divergences*? In fact, on a broader perspective, one could even suspect to find similar relations of negative eigenvalues of local generalized susceptibilities to other response functions. While these connections together with possible extensions of our analysis to cases beyond the DMFT framework will be addressed in Chapter 7, we briefly mention here a very immediate generalization: For parameter sets further in the crossover region of the MIT, e.g., at temperatures higher than $\beta = 53$ in the DMFT calculation considered in Sec. 5.4, neither a divergence nor a strong enhancement, but a *maximum* of κ as a function of μ (or U) at fixed T can be expected [73, 161, 165, 167–169, 181]. In fact, at finite doping, the maximum of κ for different values of μ (or equivalently n) and T in the crossover region is used to trace the so-called Widom line [166–169, 181, 182]. This concept, originally introduced for fluids, was first applied to strongly correlated electron systems in a work by G. Sordi *et al.* [166]. The Widom line emanates from the critical endpoint of a first order transition through the crossover regime, and hence can be used to identify a transition that might be hidden by a symmetry broken phase (e.g. superconductivity in the CDMFT applications of Refs. [181, 182]). For this parameter regime, at the maximum of κ, one can expect the distance between the lowest eigenvalue λ_{I} and the constant $\beta t_{\mathrm{eff}}^2/2$ term to be smallest, but not vanishingly small. This means, that the location of the Widom line throughout the crossover region could be traced by an analysis based on Eq. (5.12), similarly as above. Naturally, calculations which explicitly confirm this connection, should be performed in the future.

Possible workarounds

I'm dancing barefoot
In midair I spin
– Patti Smith

So far, we have discussed the problem of vertex divergences from several perspectives, including their appearance in different models, their physical origin, and eventually, the significant implications that the associated negative eigenvalues of the generalized charge susceptibility can have for the underlying physics. Instead, in this chapter, we focus on the *algorithmic* implications of the breakdown of the perturbative expansion and present possible strategies for circumventing them. We put a special emphasis on diagrammatic extensions of DMFT, specifically the combination of DMFT and fRG: the DMF^{2}RG. In particular, as an important building block for future developments of this method, we present a thorough analysis of the application of the recently introduced multiloop fRG to the AIM, representing the central part of this chapter.

In the last years, many approximation schemes were developed, aimed at treating complex many-electron problems in a wide range of physically relevant parameter regimes. Perturbative methods represent an important group of these approximation schemes, which include, among the most advanced ones, the truncated functional renormalization group method (fRG) as well as the parquet approximation (PA), both introduced in Sec. 2.3. While many of these methods benefit from a high level of physical transparency, they may be affected, to different extents, by the breakdown of the self-consistent perturbation expansion, as it occurs in the most fundamental models for strongly correlated systems. For instance, in the prominent case of the Hubbard model solved in DMFT (discussed also in Chapter 3) such a breakdown occurs already at intermediate values of the electron-electron coupling. More in general, in Chapters 3 to 5 we have discussed the appearance, the origin and the physical implications of the perturbative breakdown in great detail. Here instead, we focus on the crucial aspect of its *algorithmic* implications. In particular, we shed light onto the *way*

the perturbative breakdown has an effect on perturbative methods, and which strategies can be followed to circumvent these issues.

As discussed in Chapter 3, we briefly recall here that the perturbative breakdown manifests itself in two ways. On the one hand, it is directly associated with the multivaluedness of the Luttinger-Ward functional (LWF) [11, 12, 14–16, 19–21, 23, 24, 27, 28]. On the other hand, at the branching points of the LWF [12], divergences of the irreducible vertex functions are observed [10, 13, 17–19, 21–23, 25, 26]. At the beginning of this chapter, we discuss the implications of the multivaluedness of the Luttinger-Ward functional $\Phi[G]$ for numerical treatments, while the second part focuses on the algorithmic issues that arise in handling infinite vertex functions.

6.1 Multivaluedness of the LWF and algorithmic approaches

Concerning the multivaluedness of the LWF, let us briefly summarize here its manifestations (see the corresponding Sec. 3.2 for more details). The multivaluedness of $\Phi[G]$ has a peculiar implication: While the physical Green's function G is always unique, several non-interacting Green's functions G_0 exist that correspond to it, i.e., the map $G_0 \rightarrow G$ is not injective [11, 12, 14–16, 19–21, 23, 24, 28]. One of these G_0's represents the physical one whereas all other show unphysical behaviors, e.g. for the atomic limit (AL, cf. Sec. 2.1.1.1) at half-filling they may have a nonzero real part or violate the general relation $G_0(\nu) = G_0^*(-\nu)$, see Ref. [12]. Evidently, due to the (inverse) Dyson equation, the existence of these various G_0's is directly reflected in the existence of several corresponding self-energies Σ, of which only one is the physical one. In other words, the intrinsic multivaluedness of the LWF can be viewed, heuristically, as different "ways" to split the physical Green's function between the G_0- and the self-energy-terms consistent with the Dyson equation. However, the existence of unphysical solutions for G_0 and Σ would remain essentially irrelevant, if it was not for crossings between unphysical and the physical values of these quantities. In fact, there exist several parameter sets where one of the unphysical (or also multiple) and the physical branch of the LWF "touch", so-called branching points, which were discussed in great detail in Sec. 3.2 (see explicitly Fig. 3.27 and 3.30 for the AL). At such branching points the solution of numerical algorithms, e.g. the ones which directly sample the no longer single-valued $\Sigma[G]$, might jump onto the wrong branch. This would, in turn, lead to qualitatively incorrect results of calculations of physically observable quantities, e.g. an increase of the double occupation with increasing interaction U for the HA [11, 12]. The underlying issue is that the perturbative Feynman diagrammatic series turns out to be *not* absolutely convergent [11, 16]. In this respect, exploiting a dressed propagator, e.g., for self-consistently summing skeleton diagrammatic series (so-called "bold schemes"), corresponds to a specific reordering of the original series, which becomes highly problematic in the nonperturbative regime.

From an algorithmic perspective, the multivaluedness of the LWF presents a twofold challenge: On the one hand, one needs to handle (*a*) the *misleading* convergence aspect of the bold diagrammatic schemes [11], which means that without a warning the numerical

summation of a skeleton diagrammatic series might converge to an unphysical result. In the pioneering work by Kozik *et al.* [11] the bold diagrammatic Monte Carlo method [123, 124] for the atomic limit was investigated. In this work, the authors found that the bold diagrammatic resummation converged also beyond the first branching point of $\Phi[G]$, yielding an unphysical result. Without a "warning-signal", the numerical approach showed convergence in a regime where the summation of the skeleton diagrammatic series is no longer trustworthy. This issue evidently poses a huge problem to applications of these method to problems more complex than the AL, where the location of branching points is not known *a priori*. On the other hand (*b*), it is evidently crucial to find a way to apply the diagrammatic Monte-Carlo and other methods based on the summation of skeleton diagrammatic expansions also beyond the branching points of $\Phi[G]$. As it turns out in bold diagrammatic Monte Carlo calculations [11] as well as the so called nested cluster scheme [21] the numerical calculations jumps onto the unphysical branch after crossing the first branching point. This can be attributed to the unphysical solution becoming the attractive fix-point of an iterative scheme to e.g., calculate the self-energy $\Sigma[G]$ and the Green's function G [11]. During such a scheme, unlike in methods as DMFT, or its cluster extensions, the non-interacting G_0 is not fixed to the physical one, leading to noncausal hybridization functions and, eventually, to unphysical results [21].

Given the importance and versatility of diagrammatic series summations in the last years a huge effort was made to circumvent the algorithmic issues discussed above, which is briefly (and without claiming completeness) summarized in the following. Evidently, as for (*a*), the identification of a simple and practical criterion that signals the misleading convergence would be desirable. Important progress in this direction was made in a work by R. Rossi *et al.* [16], where, among other advancements, a specific criterion was introduced, based on which the reliability of a diagrammatic series can be determined. This criterion was used in a recent study of the bold diagrammatic Monte-Carlo to the two-dimensional Hubbard model [27], where the unphysical or physical character of the numerical solution was explicitly determined for different parameter sets. Moreover, based on the analysis of Ref. [16], further advancements were made in a work by K. Van Houcke *et al.* [28]. In an application to the Hubbard atom (i.e., the AL), the authors discuss a simplified criterion which signals the problematic *misleading* convergence behavior of the diagrammatic series, by means of a slight modification of it. The divergence of the modified series is a direct marker of misleading convergence of the original series. Problem (*b*) can be circumvented, instead, by using bare diagrammatic expansions, i.e., undressed propagators G_0 instead of full G's [11, 16, 19]. As a complementary route, in Ref. [16], the authors introduce a shifted-action approach which permits to devise a so-called "semibold" scheme, where the bold series is only performed up to a truncated finite order. We note that, regardless of the method chosen, there has been a immense effort in developing efficient algorithms to determine the expansion coefficients of the diagrammatic series for the observable under consideration [183–188] as well as techniques to properly treat its possibly divergent resummation [186, 189, 190], see also a recent work by A. J. Kim *et al.* [191] for an approach combining shifted-action and resummation techniques. We

refer the reader to Appendix D1 of Ref. [52] to obtain an overview of the current technical advances in this field.

By using the above-mentioned strategies the diagrammatic Monte Carlo method is able to overcome the perturbative breakdown, making it possible to apply this approach to cutting-edge problems, as exemplified by a subset of very recent Refs. [52, 192–195].

Throughout the remaining part of this chapter, we focus on the algorithmic challenges posed by the other, directly related, manifestation of the breakdown of perturbation theory: the appearance of divergences of irreducible vertex functions. To this end, we consider the so-called diagrammatic extensions of DMFT [51], as these use nonperturbative vertices of converged DMFT solutions as a main input.

6.2   Vertex divergences and diagrammatic extensions of DMFT

The heart of the algorithmic challenge posed by the divergences of the irreducible vertex functions can be summarized as follows: Since the irreducible vertex in channel r, Γ_r, as well as the fully irreducible vertex Λ diverge along infinitely many lines in the phase diagrams of many-electron models, methods that use these irreducible quantities are expected to fail along these divergence lines. Of course, in practice, calculations are performed at most in the proximity to a vertex divergence line, but typically not exactly at the parameter set, where the divergence occurs. Nevertheless, even in their proximity, the irreducible vertices will assume huge values, posing considerable problems to their numerical treatment (see e.g., Fig. 3.2, which shows $\Gamma_c^{\nu\nu'\omega=0}$ close to a vertex divergence). Additionally, one should also consider as additional difficulty the increasing "density" of divergence lines at larger interaction values, see, e.g., Fig. 3.20.

Evidently, diagrammatic methods that do not rely specifically on the irreducible vertices, but only on the full vertex F are, in principle, free of this issue.

It is worth noting a recent work by F. Krien *et al.* [137], where an alternative strategy for circumventing this issue for parquet-based methods was pushed forward. The main idea is to group the different classes of vertices according to another criterion for reducibility: This is no longer based on cutting two fermionic lines (two-particle reducibility), but on cutting one interaction line (U-reducibility). We discuss the details and advantages of this method in Sec. 6.2.2.

In the following we consider explicitly a subset of three pertinent examples of cutting-edge diagrammatic extensions of DMFT, discussing in particular, how these methods circumvent the problem posed by the ubiquitous presence of vertex divergences.

6.2.1   DΓA

The basic idea of the dynamical vertex approximation (DΓA) [95], as well as the QUADRILEX [196] approach, is to raise the central DMFT approximation to the next level of complexity. Instead of the one-particle irreducible vertex, i.e., the self-energy Σ, which is purely local in DMFT, it is the fully irreducible *two-particle* vertex which is assumed to be local (within
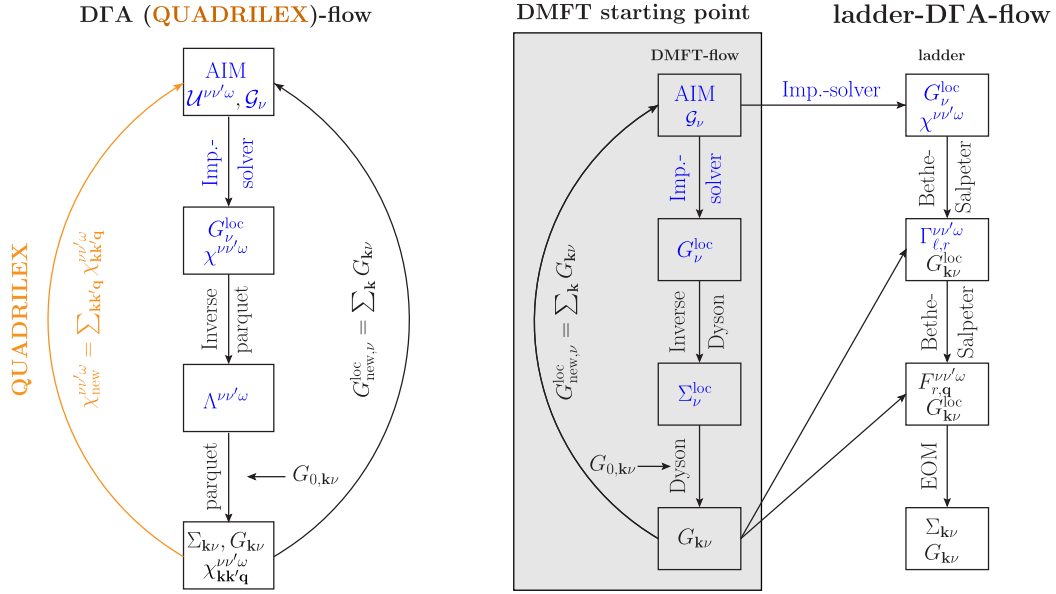
Figure 6.1: Algorithm flow diagrams of the diagrammatic extensions of DMFT, which explicitly use the *irreducible* vertex (fully or in channel r) of a DMFT solution as initial input. Left part, full/parquet DΓA and QUADRILEX schemes: While for the outer self-consistency of the DΓA approach (black arrow, right) only the Green's function is necessary, for the QUADRILEX method also the generalized susceptibility is used, ensuring the two-particle self-consistency. Right part, ladder DΓA approach: In the central grey box the DMFT algorithm (cf. Sec. 2.3.1) is sketched. In the rightmost part arrows (blue objects) highlight the input extracted from the DMFT solution (from the AIM). This figure was taken from Ref. [51] (see Fig. 11 therein).

QUADRILEX this is done in a functional-integral framework, which ensures a more advanced kind of self-consistency). While, for a recent review of these approaches, we refer the reader to Ref. [51], in the left panel of Fig. 6.1 we present a flow diagram, taken from Ref. [51], summarizing both approaches. Starting from an AIM corresponding to a self-consistent DMFT solution, an impurity solver (e.g. w2dynamics [85]), is used to obtain the local Green's function as well as the generalized susceptibility $\chi^{\nu\nu'\omega}$. Employing the inverse parquet equations the fully irreducible vertex $\Lambda^{\nu\nu'\omega}$ is calculated, which is the starting point for the parquet equations of the lattice system under investigation (whose dispersion is encoded in $G_{0,\mathbf{k}\nu}$). In this way, among other objects, a $\mathbf{k}$-dependent self-energy $\Sigma_{\mathbf{k}}$ is obtained at the end of a DΓA/QUADRILEX procedure, which includes all nonlocal correlations generated by the parquet diagrams on top of the DMFT solution.

While parquet (or full) DΓA calculations have been employed in some relevant cases [153, 156], the considerable numerical effort has made another flavor of DΓA, i.e., its ladder version [197, 198] more exploited for numerical applications [51]. This ladder version of the DΓA is illustrated in the right panel of Fig. 6.1. Here the nonlocal correlations beyond DMFT are only taken into account in selected channels r. The grey box represents a flow diagram, illustrating the DMFT algorithm used as a starting point. Instead of an inversion of the parquet equations, here the BSE are inverted to obtain the irreducible vertex in channel r, $\Gamma_r^{\nu\nu'\omega}$ (The l-index in Fig. 6.1 represents the particle-hole or particle-particle sectors).

Subsequently the BSE together with the equation of motion (EOM) is used to obtain $\Sigma_{\mathbf{k}}$.

Evidently, close to a vertex divergence, the crucial step of the inversion of the parquet or Bethe-Salpeter equations becomes problematic, hindering a reliable numerical treatment of all vertex functions in the following steps of the algorithms. To circumvent this issue, a reformulation of the corresponding equations would be necessary, *preventing* the explicit manipulation of irreducible vertices. So far no such reformulation has been found for the full/parquet DΓA or the QUADRILEX approach. The situation is more favorable for ladder DΓA, whose equations can be completely recast in terms of the full vertex F instead of Γ_r [51, 54].

This formal property has been exploited in a recent work by J. Kaufmann *et al.* [199], where the self-consistent version of the ladder DΓA algorithm was implemented and tested. As the authors explicitly showed, the reformulation using full vertices, instead of irreducible ones, allowed for applying a fully self-consistent version of ladder DΓA also at interaction values *larger* than those of the first vertex divergence lines. It should be noted, however, that just in the direct proximity of the divergence lines, the convergence of the self-consistent method could not be achieved, for reasons which are not fully clarified yet.

6.2.2 Dual fermion

The dual fermion approach [200–202] is based on rewriting the lattice problems in terms of a collection of Anderson impurity models, which are each numerically exactly solvable, and whose mutual coupling is treated in a perturbative manner [51]. To this end the original lattice action $\mathcal{S}$ is expressed in terms of a local reference action $\mathcal{S}_{\mathrm{loc}}$ and decoupled by introducing new fields, the so-called *dual* fermions. In particular, this is achieved by applying a Hubbard-Stratonovic transformation to the Gaussian part of $\mathcal{S}$. In order to obtain a generating functional W, which is completely expressed in terms of dual variables, W is expanded in terms of the local coupling between physical and dual fermions. This introduces the effective dual fermion interaction V_{eff}, which is fully determined by the *local* n-particle vertices of the impurity systems. In principle, V_{eff} includes interaction terms of higher particle order than the usual two-particle one. In practical applications, however, usually only the two-particle terms are retained. Using the generating functional W expressed in dual variables, relations between dual and original correlation functions can be identified, allowing one e.g. to obtain the physical self-energy from the dual one. The main advantage of this procedure lies in the improved starting point for perturbative expansions, which produces nonlocal correlations on top of the nonperturbative local ones already included via the auxiliary impurity models. The central approximation of the dual fermion method, beyond the choice of the dual interaction, is the diagrammatic expansion made in dual space. For a concise review of dual-fermion-based approaches we again refer the reader to Ref. [51].

Concerning the subject this thesis, the crucial advantage of the dual fermion method lies in the form of V_{eff}, where only the full local vertices enter, e.g., on the two-particle level, the full (one-particle-irreducible) local vertex F of an AIM, corresponding to a self-consistent DMFT solution. In this way the dual fermion approach automatically *circumvents*
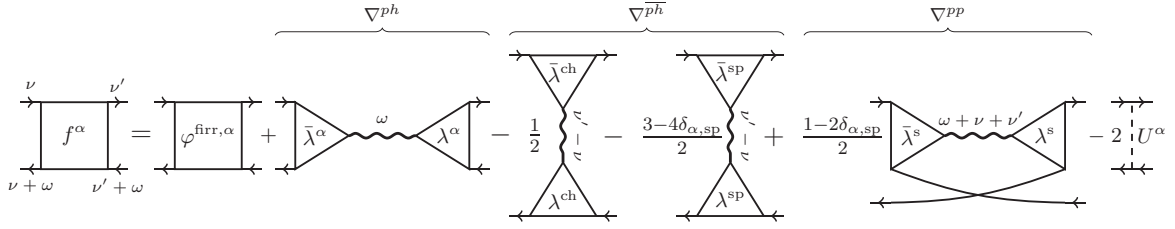
Figure 6.2: Single-boson exchange decomposition (SBE) [137] of the full vertex F^α in channels $\alpha = c, m$ into the fully U-irreducible vertex ($\varphi^{\text{firr},\alpha}$) and the U-reducible contributions from the three diagrammatic channels ($\nabla^{\text{ph}/\overline{\text{ph}}/\text{pp},\alpha}$), which are constructed upon the Hedin vertex λ^α and the screened interaction w^α (wiggly line). The last term is a double counting correction of the bare interaction. The figure is taken from Ref. [137] (see Fig. 1 therein) where the SBE is introduced. Note that f^α corresponds to F^α in our notation.

the explicit usage of irreducible vertex functions of the auxiliary AIM and, hence, all the related algorithmic problems posed by the appearance of vertex divergences.

While many flavors of the dual fermion method with different levels of approximations are known in the field [51], we want to focus here on a specific version, which was introduced only recently: The boson-exchange parquet solver for dual fermions (BEPS) [203]. This cutting-edge realization of the dual fermion approach has an important characteristic: The approach is based upon the so-called single-boson exchange (SBE) formulation, which we briefly sketch in the following.

The SBE [137] defines a convenient decomposition of the full vertex F, formally similar to the parquet decomposition (mentioned briefly in Sec. 3.1.4.2). However, instead of being based on the notion of two-particle reducibility by cutting two fermionic lines, it groups the diagrams contained in F according to reducibility with respect to the bare interaction — the so-called U-reducibility. This corresponds to the following equation (cf. Eq. (4) in Ref. [137]):

$$F^\alpha = \varphi^{\text{firr},\alpha} + \nabla^{\text{ph},\alpha} + \nabla^{\overline{\text{ph}},\alpha} + \nabla^{\text{pp},\alpha} - 2U^\alpha \quad . \tag{6.1}$$

Here, the full vertex in channels $\alpha = c, m$ is decomposed into a fully U-irreducible part $\varphi^{\text{firr},\alpha}$ and U-reducible diagrams ∇^α in the three different diagrammatic channels ph, $\overline{\text{ph}}$ and pp. These U-reducible diagrams are given by Hedin three-leg vertices λ^α and the screened interaction $w^\alpha = U^\alpha + \frac{1}{2}U^\alpha\chi^\alpha(\omega)U^\alpha$ [137]. The remaining term in Eq. (6.1) is a double-counting correction. In Fig. 6.2 we reproduce a figure from Ref. [137], illustrating the SBE decomposition. While the two-particle nature of the electronic interaction considered (here the Hubbard one) allows to directly relate the classes of 2P-reducible diagrams in the parquet decomposition to the corresponding U-reducible ones of the SBE one (the ph, $\overline{\text{ph}}$ and pp sectors respectively), the number of diagrams belonging to these classes is very different between the two decompositions. In particular, it can be easily verified that there are many diagrams which are two-particle reducible but not U-reducible. This leads to the fact that the U-irreducible vertex, $\varphi^{\text{firr},\alpha}$, contains much a larger number of Feynman diagrams than the fully irreducible vertex of the parquet decomposition [137]. Note that

similarly as for the parquet decomposition a system of self-consistent equations for a given $\varphi^{\text{firr},\alpha}$ can be defined [139] as well as simplified schemes based on approximations of $\varphi^{\text{firr},\alpha}$ can be formulated [204].

It is important to stress that in the SBE decomposition *all* vertices are obtained from algebraic relations, hence not requiring any kind of inversions [137]. In this way the SBE approach should be *protected* from the problem of vertex divergences, allowing for a decomposition of the full vertex also in the nonperturbative regime, as opposed to the parquet decomposition [18, 58, 59] (see Sec. 3.1.4.2).

In the BEPS method [203] the full vertex encoding the two-particle interaction between the dual fermions, is decomposed into SBE diagrams and the corresponding U-irreducible part, as discussed above. For the U-irreducible part the parquet equations are used, splitting it into multi-boson exchange processes and a remaining irreducible part. This formulation proved to be advantageous concerning the numerical performance, allowing for several interesting applications [205, 206] (for an formulation of this idea for real fermions see Ref. [207]). Among them the BEPS approach has recently offered a new viewpoint on the still highly controversial topic of the strong-coupling pseudogap in the 2D Hubbard model [206]. In particular this BEPS-based study allowed to identify the emergence of a non-negligible imaginary part of the spin-fermion coupling, which acts as a key player in the opening of the gap close to the antinodal point and, at the same time, in the protection of the Fermi arcs.

6.2.3 DMF^{2}RG

The DMF^{2}RG method [51, 208–211] is an extension of DMFT, which exploits the functional renormalization group approach, for a review see Ref. [98], as a means to systematically include nonlocal correlations on top of the nonperturbative local ones already included in the DMFT starting point.
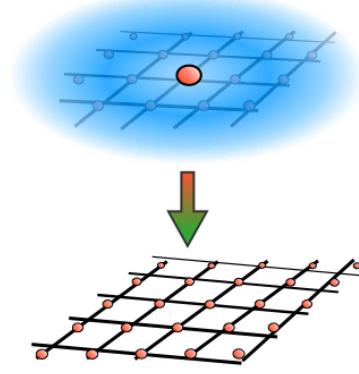
As summarized in Sec. 2.3.3, in the fRG method [98] a scale dependence Λ is introduced in the bare propagator and hence in the many-body action $\mathcal{S}^{\Lambda}$. This defines a Λ-dependent generating functional, which can be used to obtain an infinite hierarchy of coupled differential equations for one-particle irreducible quantities, the so-called Wetterich equations [98, 100]. In practical applications, this hierarchy is typically truncated at the two-particle level, i.e., only the differential equations for the self-energy Σ and the full vertex F are considered. These coupled equations are however not closed, because the latter still explicitly depends on the three-particle vertex. Different approximation schemes of the fRG approach usually concern the extent to which the three-particle vertex is included in the differential equation for F and Σ. For example, a commonly used scheme, the so-called one-loop (1ℓ) approximation, neglects the effect of the three-particle vertex entirely.

Eventually, once the set of differential equations is defined, it is solved starting from an initial condition, which often corresponds to an explicitly known limiting case. By doing so, the approximate fRG solution of the many-body problem under consideration is obtained. This process is often referred to as "flowing".

In the case of DMF^{2}RG the fRG method is formulated to represent the "turning on"

$$\mathcal{S} \overset{\Lambda = \Lambda_{\text{ini}}}{=} - \int_0^\beta d\tau d\tau' \sum_\sigma c_\sigma^\dagger(\tau) \mathcal{G}_{\text{AIM}}^{-1}(\mathbf{k}, \tau - \tau')^{-1} c_\sigma(\tau') + \ \mathcal{S}_{\text{int}}$$

$$\mathcal{G}_0^{\Lambda_{\text{ini}}}(\mathbf{k}, i\omega) = \mathcal{G}_{\text{AIM}}(i\omega)$$

$$\mathcal{S} \overset{\Lambda = \Lambda_{\text{fin}}}{=} - \int_0^\beta d\tau d\tau' \sum_{\mathbf{k}\sigma} c_{\mathbf{k}\sigma}^\dagger(\tau) \mathcal{G}_{\text{latt}}^{-1}(\mathbf{k}, \tau - \tau')^{-1} c_{\mathbf{k}\sigma}(\tau') + \ \mathcal{S}_{\text{int}}$$

$$\mathcal{G}_0^{\Lambda_{\text{fin}}}(\mathbf{k}, i\omega) = \mathcal{G}_{\text{latt}}(\mathbf{k}, i\omega)$$

Figure 6.3: Schematic representation of the DMF²RG method. At the scale Λ_{ini} the flow starts from the DMFT solution by using the bare local Green's function of the corresponding AIM, $\mathcal{G}_{\text{AIM}}(\nu)$, as bare propagator $\mathcal{G}_0^{\Lambda_{\text{ini}}}$ of the initial action $\mathcal{S}^{\Lambda = \Lambda_{\text{ini}}}$. As Λ_{fin} is reached, nonlocal correlations are included and the bare lattice Green's function ($\mathcal{G}_{\text{latt}}(\mathbf{k}, \nu)$) is fully included in the final action $\mathcal{S}^{\Lambda = \Lambda_{\text{fin}}}$. The figure is taken from Ref. [211] (see Fig. 2 therein).

of non-local correlations as Λ flows from the initial Λ_{ini} to the final value Λ_{fin} [208]. For instance, during the DMF²RG flow, the scale-dependent bare propagator $\mathcal{G}_0^\Lambda$ is turned from the one corresponding to the AIM of the self-consistent DMFT solution [$\mathcal{G}_{\text{AIM}}(\nu)$] to the one corresponding to the full lattice problem [$\mathcal{G}_{\text{latt}}(\mathbf{k}, \nu)$], as illustrated schematically in Fig. 6.3, reproduced from Ref. [211]. To avoid double-counting of local correlations $\mathcal{G}_0^\Lambda$ is chosen such that the following condition for the interacting Green's function is preserved throughout the flow [210, 211]:

$$G_{\text{loc}}^\Lambda(\nu)\big|_{\Sigma^\Lambda = \Sigma_{\text{DMFT}}} = \int_{\mathbf{k}} G^\Lambda(\mathbf{k}, \nu)\big|_{\Sigma^\Lambda = \Sigma_{\text{DMFT}}} = G_{\text{DMFT}}(\nu) \tag{6.2}$$

Importantly, similarly as in the dual fermion method, the DMF²RG requires the Green's function and the *full* vertex F of DMFT as an input. They provide the initial conditions for the differential equations describing the fRG flow of the self-energy and the one-particle irreducible vertex F. Evidently, in this way, the problem of vertex divergences is also automatically *circumvented*, as the irreducible vertex functions are never explicitly manipulated in any step of the procedure.

While the DMF²RG approach combines two very powerful methods, extending the applicability of truncated fRG to the strong coupling regime [208, 210, 211], its current implementations, exploiting the 1ℓ fRG, face an important limitation at low-temperatures. In particular, a magnetic instability is found below a so-called "pseudocritical" temperature,
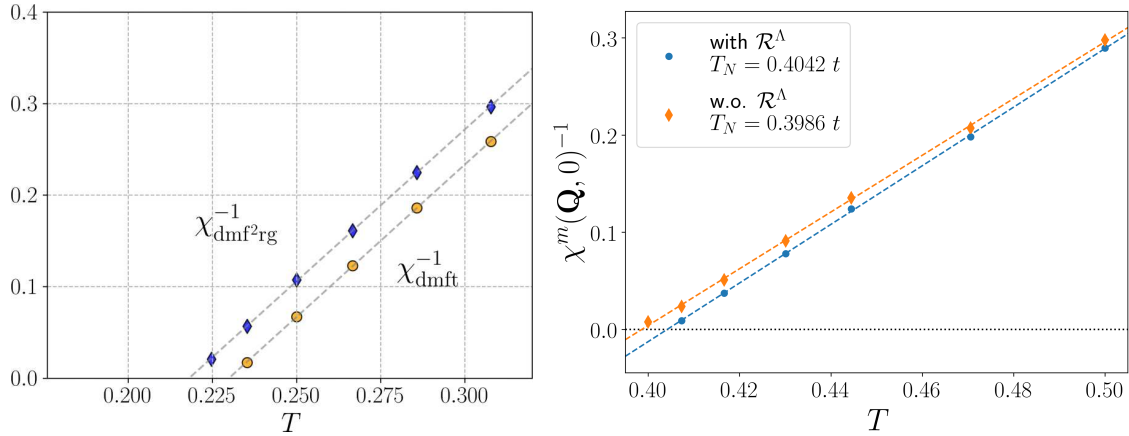
Figure 6.4: Inverse magnetic susceptibilities for $\omega = 0$ and $\mathbf{Q} = (\pi, \pi)$ of the 2D Hubbard model as obtained by DMFT and DMF²RG in two independent implementations. The left figure was taken from Ref. [210] (see Fig. 6 therein) and shows the case of $U = 4t$, the right figure has been extracted from Ref. [211] (see Fig. 9 therein) and refers to the case of $U = 8t$. While one of the main focuses of Ref. [211] was to investigate the effect of the inclusion of the restfunction of the SBE ($\mathcal{R}^\Lambda$) on the final results, for our discussion (s. text) the observation of a rather marginal reduction of T_N w.r.t. the corresponding one of the DMFT solution is mostly relevant.

which corresponds to a violation of the Mermin Wagner theorem [210, 211]. We recall that according to this theorem [212], in a purely two-dimensional system with short-ranged interactions, such as the Hubbard model, there should exist no finite-temperature phase transition associated with an order parameter of two or more components [51]. This means that critical temperatures, e.g., of antiferromagnetic orders, where the order parameter has three components, must be zero as long as the Mermin-Wagner theorem holds.

Recent studies applying the DMF²RG approach to study the 2D Hubbard model analyzed this aspect among many others. In Fig. 6.4 we reproduce the results of Ref. [210] (left) and Ref. [211] (right) showing finite values of T_N (both) and no significant reduction as compared to DMFT (left). Both studies used the 1ℓ implementation of the DMF²RG scheme, whereas the latter study, Ref. [211], incorporated also the SBE decomposition introduced above, which had crucial numerical advantages.

On a different note, a recently developed extension of the fRG, the so-called multiloop fRG (mfRG) [103–105], was formally proven to reconstruct the diagrammatics of the parquet approximation, which is expected to guarantee the fulfillment of the Mermin-Wagner theorem [213]. The mfRG implementation, which is utilized in the following section, is concisely introduced in Sec. 2.3.3. For a recent description of the mfRG approach based on the SBE formalism, rather than on parquet-like diagrams, we refer to Ref. [214]. As opposed to the 1ℓ scheme, in mfRG, a specific class of the three-particle vertex diagrams are included in the flow of Σ and F such that the corresponding differential equations represent a total derivative of the corresponding diagrammatic quantity. This way, all the diagrams of the PA are correctly reconstructed at the end of the mfRG flow. As another recent work by A. Tagliavini *et al.* [106] showed, applying the mfRG method to the 2D Hubbard model, has indeed allowed for a significant reduction of the pseudocritical temperatures. The
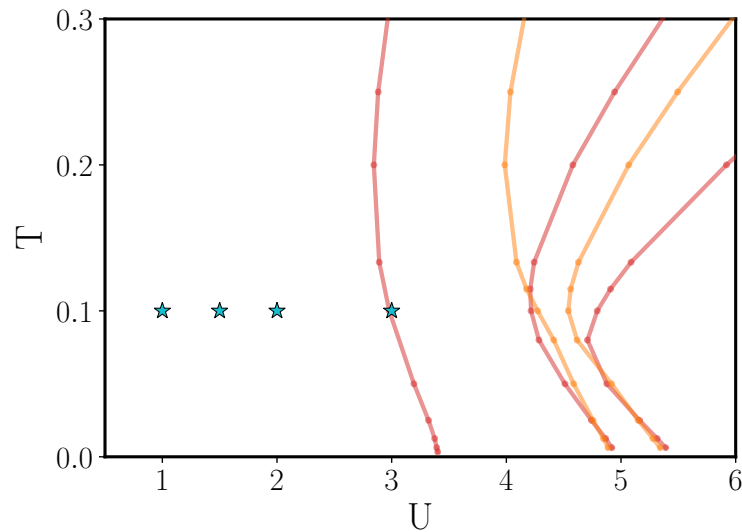
Figure 6.5: Parameters used for the mfRG calculations (turquoise stars) plotted in the T-U diagram of the specific AIM considered (see Sec. 2.1.1), where the corresponding divergences of the irreducible vertices (see the discussion in Chapter 3 and in particular Fig. 3.13) are reported as red and orange lines.

application of the mfRG method, without the self-energy Σ and the full vertex F of DMFT as a starting point, corresponds to the PA, and thus yields a quantitatively reliable weak-coupling approximation, which as shown in Ref. [94], displays remarkable agreement with exact methods in the weakly interacting regime.

6.3   Multiloop fRG

*Parts of this chapter, marked by a vertical bar, have already been published in the APS journal Phys. Rev. Research **4**, 023050 (2022)*

On the basis of the argumentation made above, it appears to be a very promising idea to extend the DMF^{2}RG approach, used so far at the 1ℓ level, to the multiloop case [105]. In particular, it can be argued that such a multiloop DMF^{2}RG solution would formally correspond to a parquet-DΓA solution [51]. Hence, by including all nonlocal correlations at the level of the parquet diagrams, this improved scheme would eliminate the issue of finite pseudocritical transition temperatures in the case of the 2D Hubbard model. In this way, the multiloop DMF^{2}RG would open a new path to diagrammatically extend the DMFT solution to the non-local case, with two important advantages w.r.t. similar other schemes: (*i*) The avoidance of manipulating the possibly divergent irreducible vertex functions at any point of the procedure, and (*ii*) the guarantee to fulfill the Mermin-Wagner theorem. In fact, this procedure could be regarded as an alternative way to recast the parquet equations for *real electrons* in terms of the full vertex F, without resorting to the dual fermion formalism.

In pursuing this goal, it is clear that many technical problems may arise, e.g. ranging from a sufficiently precise treatment of the **k**-grid, to the choice of a suitable regulator for

the flow, up to the performance of the mfRG loop resummation at intermediate to strong coupling.

As a crucial preliminary step, we investigate in the following how the simple mfRG scheme performs when applied to a fundamental case: the AIM, used throughout this work (see Sec. 2.1.1 for details) for increasing interaction values from weak to intermediate to strong coupling, as explicitly marked in Fig. 6.5 by turquoise stars. Regarding the choice of the model, we emphasize that using the AIM has the following advantages: (*i*) no further approximations for the application of the mfRG procedure are necessary. This is different w.r.t the Hubbard model case, where the mfRG algorithm needs to be adapted to account for an approximate treatment of the **k**-dependence, see further Ref. [94]; (*ii*) the numerically exact CT-QMC solution of the AIM provides a rigorous benchmark for the overall accuracy of the mfRG scheme. In this way our investigation allows for a systematic inspection of the multiloop convergence in different coupling regimes, which is a particularly important aspect for future applications of the DMF^{2}RG in the non-perturbative regime.

Beyond these mostly "practical" issues, we also investigate a more profound feature of the mfRG resummation and different loop-truncated versions of it (see Sec. 2.3.3): We analyze to which extent the solutions of these approximate methods fulfill fundamental properties of the exact solution, specifically sum rules associated with the *Pauli principle* as well as *Ward identities*. This investigation represents an important comparison not only in respect of future DMF^{2}RG applications, but also for approximate quantum many-body approaches in general.

Parts of the following section that are marked by a vertical bar, are taken from Ref. [215]. We note as a side remark that in this work a different convention for the diagrammatic channels as well as the sign of the vertex function was used. The parts, which are taken from this reference, have been adapted to match the conventions chosen in this thesis. Additionally, negative vertices (e.g., $-\Phi_m$) are shown in the following figures, to match more closely the plotting conventions of Ref. [215].

6.3.1   Multiloop fRG solution of the AIM

In this section, we present a detailed discussion of the results obtained by applying the mfRG approach, summarized in Sec. 2.3.3, to the half-filled AIM introduced in Sec. 2.1.1 at the inverse temperature $\beta = 10$. For further details on the implementation, we refer the reader to Refs. [96, 106]. We just note here that, for the reducible vertices, we adopt the parametrization $\Phi_r(\nu, \nu', \omega) = K_{1r}(\omega) + K_{2r}(\nu, \omega) + K_{2'r}(\nu', \omega) + K_{3r}(\nu, \nu', \omega)$ proposed in Ref. [96]. The K_{1r} and $K_{2^{(\prime)}r}$ functions with one and two frequency arguments, respectively, describe the high-frequency asymptotics, while the remaining full dependence, relevant at low frequencies, is contained in K_{3r}. This reduces the computational cost, allowing for the calculation of the vertices on a larger Matsubara frequency range (see Ref. [215] for computational details). The flowing susceptibilities are conveniently extracted through $\chi_r = -K_{1r}/U^2$.

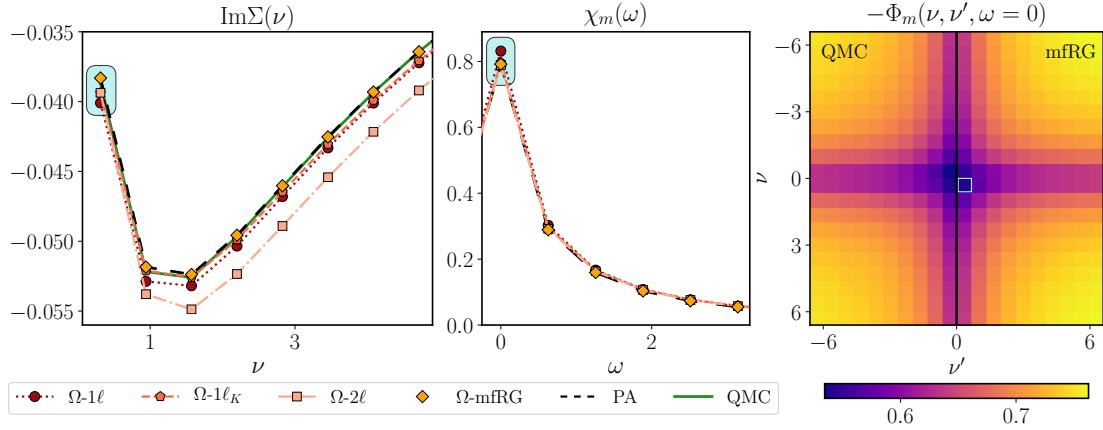We start the presentation of our numerical results by showcasing the central quanti-

Figure 6.6: Comparison of the results of different approaches for the self-energy $\mathrm{Im}\Sigma(\nu)$ (left), the magnetic susceptibility $\chi_m(\omega)$ (center), and the reducible vertex $\Phi_m = K_{1m} + K_{2m} + K_{2'm} + K_{3m}$ (right) of the half-filled AIM considered, for $U = 1$, $\beta = 10$. The fRG results shown here are computed with the Ω-flow, see Eq. (2.73). The shaded turquoise areas in the first two panels and the frame in the right one mark the specific frequencies used to study the loop convergence in Secs. 6.3.2 and 6.3.3.

ties of interest for this analysis, i.e. the self-energy Σ, the magnetic susceptibility χ_m, and the reducible vertex Φ_m of the impurity site in the magnetic channel, computed in the weak-coupling regime ($U = 1$) by means of the PA (see Sec. 2.3.2), the numerically exact QMC (see Sec. 2.3.1.2) and all fRG-based approaches introduced in Sec. 2.3.3. Figure 6.6 displays our results for Σ, χ_m and $-\Phi_m$ as a function of fermionic (bosonic) Matsubara frequencies. The corresponding numerical data would also allow one to estimate important physical quantities (e.g., the quasiparticle mass renormalization and life time) relevant for the description of the Fermi-liquid state of the impurity problem [9, 30, 146] as well as to quantify the temporal fluctuations of the local magnetic moment on the impurity site [61–63]. Consistent with the small U value of these illustrative calculations, all approaches yield qualitatively the same behavior and deviations to numerically exact QMC data are hardly visible. In particular, we note that the converged mfRG solution (orange squares), perfectly matches the PA (dashed black line) for all quantities, $\mathrm{Im}\Sigma$, χ_m, and Φ_m (not shown). The results at the highlighted Matsubara frequencies are then used in the following Sec. 6.3.2 for a quantitative study of the mfRG convergence as a function of loop order ℓ. There, we also showcase two hallmark qualities of the converged mfRG solution: (i) It is cutoff-independent, reflecting the fact that it reproduces the PA solution, which, as a self-consistent diagrammatic resummation, by construction is defined without reference to any cutoff. (ii) For quantities that can be computed either via their own RG flow equations, or via *post-processing* (PP) relations, the results agree. These PP relations refer to the Schwinger-Dyson equation of motion, which allows to obtain the self-energy Σ from the full vertex F (see Eq. (2.72)), as well as the Bethe-Salpeter equations, relating the generalized susceptibilities and the full vertex F, see Sec. 2.2.2. The magnetic response function χ_m is then obtained by summing all fermionic Matsubara frequencies (cf. Eq. (2.30)).

In Sec. 6.3.3, we extend our analysis to larger values of U.
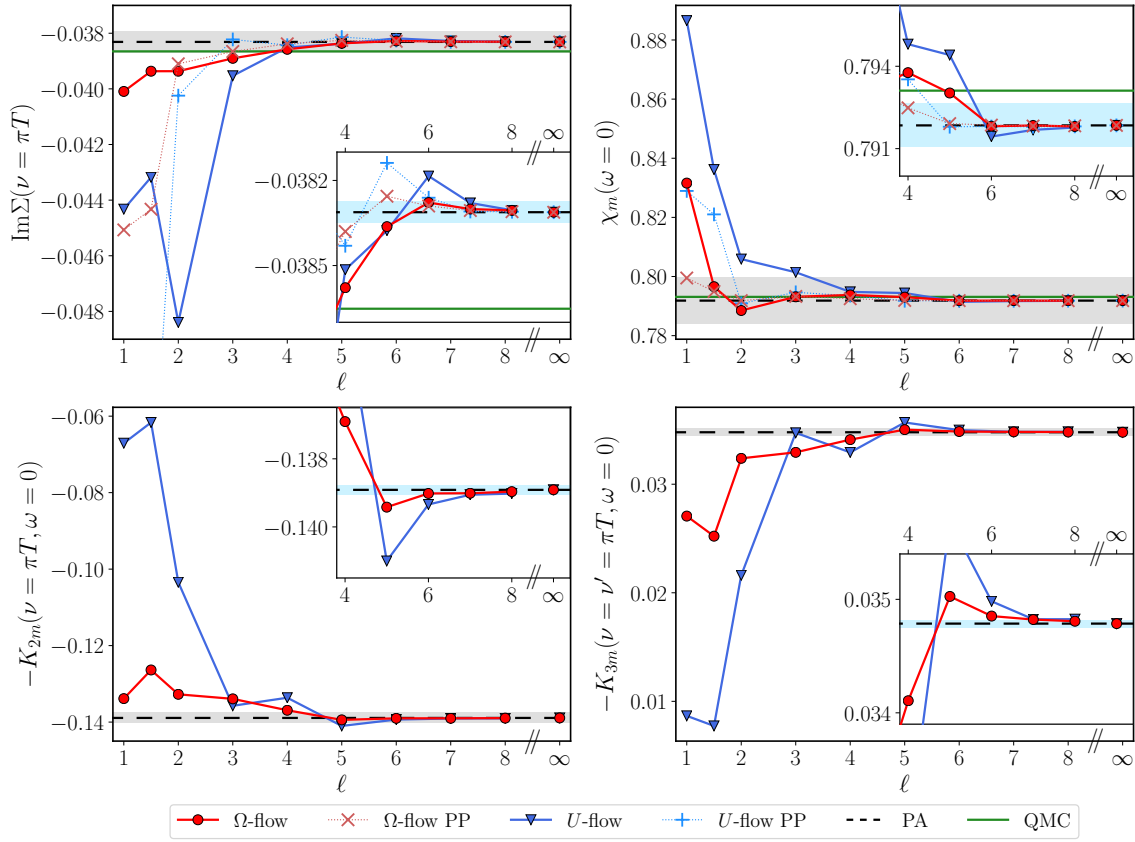
6.3.2   Multiloop convergence to PA

Figure 6.7: Ω-flow (red) and U-flow (blue) mfRG results as a function of loop order ℓ in comparison with the PA (black, dashed) and the numerically exact QMC data (green), for the half-filled AIM at $U = 1$. Upper panels: $\mathrm{Im}\Sigma(\nu = \pi T)$ and $\chi_m(\omega = 0)$, showing perfect agreement between post-processed (PP) and flowing results of both cutoffs and the PA result. Lower panels: asymptotic vertex functions K_{2m} and K_{3m} for the lowest Matsubara frequencies. Insets show a zoom for $\ell \geq 4$. The gray areas mark 1% deviation from the PA result, the blue ones in the insets 0.1%. The label '∞' represents the fully converged mfRG result. In this and similar figures below, the data points plotted between those at $\ell = 1$ and $\ell = 2$ represent the $1\ell_K$ results (Katanin substitution, see Sec. 2.3.3).

In Fig. 6.7, we analyze in detail the loop convergence of the mfRG flow for $U = 1$. The four panels display both the flowing and PP results for $\mathrm{Im}\Sigma(\nu = \pi T)$ and $\chi_m(\omega = 0)$ as well as the flowing results for $-K_{2m}(\nu = \pi T, \omega = 0)$ and $-K_{3m}(\nu = \nu' = \pi T, \omega = 0)$, as a function of loop order ℓ obtained with the two cutoffs, i.e., the Ω-flow, see Eq. (2.73) (red circles) and the U-flow, see Eq. (2.74) (blue triangles). For comparison, the PA (black dashed line) and QMC (green solid line) solutions are also reported. One readily notices that the mfRG solution for *both* cutoffs converges to the PA for all considered quantities. Throughout the paper, the label '∞' refers to the infinite loop-order mfRG solution, see [216]. The high quality of the mfRG convergence can be appreciated by looking at the corresponding insets, showing the data restricted to higher loop orders. While the gray area in the main
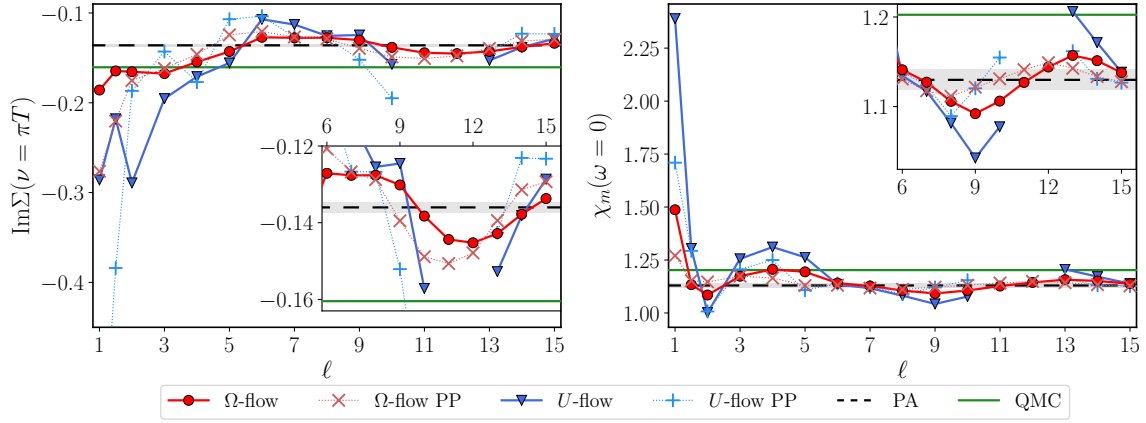
Figure 6.8: $\mathrm{Im}\Sigma(\nu = \pi T)$ and $\chi_m(\omega = 0)$ as in Fig. 6.7 but for the AIM at $U = 2$. Insets show a zoom for $\ell \geq 6$. The gray area indicates 1% deviation from the PA. For $\ell = 11, 12$ we were unable to converge the U-flow calculations.

panels marks 1% deviation with respect to the PA, the blue area in the insets corresponds to 0.1%.

It is worth stressing that for some quantities and specific values of ℓ, the mfRG and PA solution may be accidentally close, e.g. the 3ℓ Ω-flow result for $\chi_m(\omega = 0)$ or the 3ℓ U-flow result for $K_{3m}(\nu = \nu' = \pi T, \omega = 0)$. Of course, this does not mean that the mfRG procedure has already converged at 3ℓ: Full convergence implies the equivalence of mfRG and PA for *all* quantities and *both* cutoffs up to differences smaller than a given ϵ, e.g., here 0.1%. For the $U = 1$ calculations, this is clearly achieved for $\ell \geq 8$. Looking at the insets, the Ω-flow appears to converge systematically faster than the U-flow. We note that all U-flow results shown in the paper are obtained via a frequency extrapolation (see further the Appendix of Ref. [215]), which is required to achieve the highly precise convergence to PA demonstrated in the insets.

Another important property of the converged mfRG solution is the equivalence of the flowing and PP results, shown both for $\mathrm{Im}\Sigma(\nu = \pi T)$ and $\chi_m(\omega = 0)$ in the upper panels of Fig. 6.7. Except for the 1ℓ and $1\ell_K$ results for the self-energy, the PP data (dotted lines with '×' or '+' symbols) are always found to be closer to the PA than the flowing data (for the susceptibility, this trend was previously reported in Ref. [94]). For both cutoffs, flowing and PP results agree with the PA for $\ell \geq 8$, highlighting the perfect convergence of the mfRG scheme in this parameter regime. The loop convergence can also be seen from calculations with a single cutoff, as there are no more changes larger than a small ϵ in all quantities when going from ℓ to $\ell + 1$, and flowing and PP results agree with one another. Finally, let us note that adopting the PP procedure has also important implications for the fulfillment of sum rules, which are studied in Sec. 6.3.7.

6.3.3 Toward strong coupling

We now analyze how the convergence of the mfRG flow is affected by increasing the interaction U. In Figs. 6.8 and 6.9, we focus on the results for the physical quantities
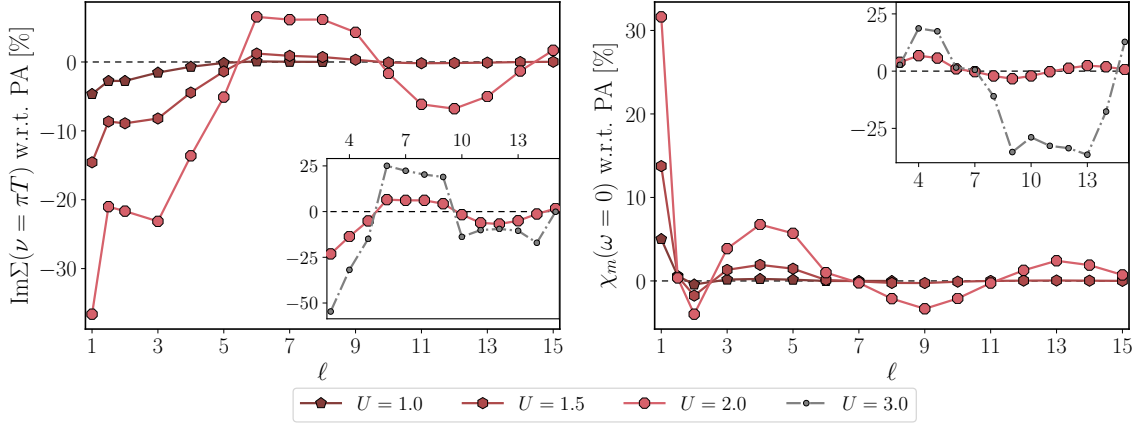
Figure 6.9: Relative difference between Ω-flow mfRG calculations (flowing) and the corresponding PA solutions for $\mathrm{Im}\Sigma(\nu = \pi T)$ (left) and $\chi_m(\omega = 0)$ (right), as a function of loop order ℓ and different values of the interaction U. Main panels show $U \leq 2$, insets $U \geq 2$.

$\mathrm{Im}\Sigma(\nu = \pi T)$ and $\chi_m(\omega = 0)$, but we also checked for convergence of $K_{2m}(\nu = \pi T, \omega = 0)$ and $K_{3m}(\nu = \nu' = \pi T, \omega = 0)$ (not shown).

For values of U slightly larger than $U = 1$, the convergence behavior is qualitatively the same (see Fig. A.10 in Appendix A.3 for $U = 1.5$), albeit with increasing interaction, as expected, more loop orders are required to reach convergence.

For $U = 2$, the dependence on loop order is shown in Fig. 6.8. While the mfRG solution quickly approaches the PA for low ℓ, the path toward full convergence for higher ℓ becomes visibly slower as the curves describing the loop dependence of the mfRG calculations keep oscillating around the PA solution. The Ω-flow results are generally found to be more accurate than the U-flow data (note that for the U-flow at $\ell = 11, 12$, no solution could be obtained; see further Ref. [215]). Yet, even with the Ω-flow, we did not reach *perfect* convergence up to $\ell = 40$. Different from the situation at $U = 1$ and $U = 1.5$, the results obtained by PP do not show a clear improvement. Instead, they seem to follow a slightly different oscillation pattern, somewhat shifted from the flowing data (see insets of Fig. 6.8).

Further insight on the oscillations characterizing the mfRG convergence with increasing interaction can be gained from Fig. 6.9. Here, we show the relative difference between the mfRG results and the corresponding PA solutions for different values of U. By comparing the (flowing) results of the Ω-flow for different interaction strengths $U = 1, 1.5$ and 2, one notices the presence of "nodes" in the multiloop oscillations, i.e., of loop orders at which mfRG and PA yield numerically very similar results for the quantity under consideration. The location of these nodes, however, depends on the observable. (While, e.g., $\ell = 7$ for $\chi_m(\omega = 0)$ is close to the PA for all values of U, for $\mathrm{Im}\Sigma(\nu = \pi T)$ this is not the case.) For larger interactions, the oscillations become stronger. Already for $U = 2$, the amplitude of the self-energy oscillations hardly decreases with increasing loop order, making a full convergence numerically challenging as discussed above. (The U-flow shows similar behavior, see Fig. A.12 in Appendix A.3.) This effect gets even more pronounced for
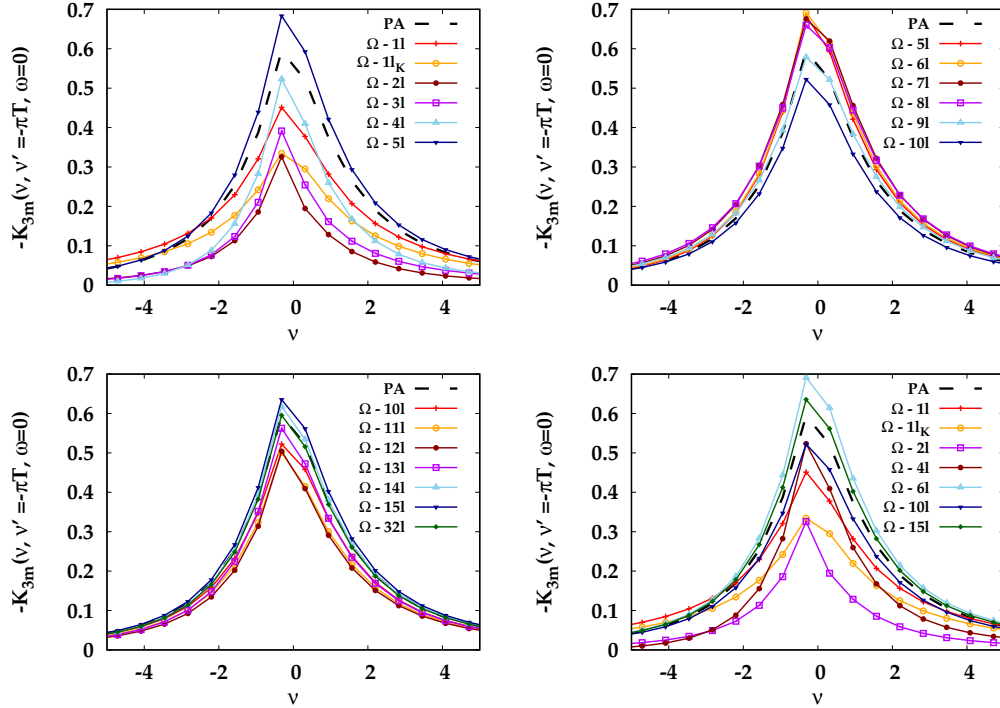
Figure 6.10: The restfunction $-K_{3m}(\nu, \nu', \omega)$ for fixed $\omega = 0$ and $\nu' = \pi T$ calculated from mfRG Ω-flow calculations of the AIM with different loop orders for the half-filled AIM at $U = 2$. To facilitate the comparison across different loop orders in the lower right panel a comparison across different ℓ is shown.

$U = 3$ displayed in the insets, together with $U = 2$ for comparison. There, higher loop orders, especially for $\chi_m(\omega = 0)$, yield a progressively enhanced deviation from the PA for increasing loop order. Therefore, we conclude that, within our current implementation and the given settings of the AIM, the mfRG loop resummation ceases to converge for $U = 3$. Such a lack of loop convergence serves as a built-in red-flag indicator that a parameter regime lies outside the zone of safe applicability of the approach. This outcome, however, is not entirely unexpected since, for the specific AIM considered, the interaction strength $U = 3$ already corresponds to the strong-coupling regime, where nonperturbative [11, 12, 67, 68] divergences of two-particle irreducible vertices [10, 13, 17, 19, 21, 23, 25, 26], which are—per construction—beyond the PA, were detected by means of QMC calculations [22, 68], as discussed in Chapter 3 and shown in Fig. 6.5.

As for the peculiar "node" structure of the multiloop oscillations, it should be noted that it is also observed, essentially unaltered, for different temperatures, see Appendix A.3.1 where we complement the discussion made above with results for $\beta = 5$. This might suggest that the occurrence of nodes in the multiloop oscillations is not a mere accidental feature of a specific parameter set.

6.3.4 "Breathing" of the rest function

In the previous section we discussed the way the multiloop oscillations affect the convergence of the mfRG scheme for $\mathrm{Im}\Sigma(\nu = \pi T)$ and $\chi_m(\omega = 0)$. In this section we present

more details on how the oscillations observed for $U = 2$ are reflected in the restfunction $K_{3m}(v, v', \omega)$ for $\omega = 0$, where the full fermionic frequency dependence is taken into account.

As a first step we fix $\omega = 0$ and $v' = -\pi T$ and show cuts in v for different loop orders using the Ω-flow in Fig. 6.10. Starting from the upper left panel it can be seen how the results oscillate as a function of loop order around the PA result (black dashed lines). The last loop order seen in each panel is replotted again in the following one for all panels but the last, where a comparison across several loop orders is shown. In the upper right panel the maxima and minima of the multiloop oscillations are particularly visible, as the loop orders $\ell = 5, 6, 7, 8$ almost coincide. In the lower left panel we also report the $\ell = 32$ result, which shows a convincing agreement with the PA for the rest function, but not for all other quantities such as $\text{Im}\Sigma(v = \pi T)$ (not shown), indicating that, as discussed before, the multiloop convergence is not fully reached.

As a second step we analyze the full fermionic frequency dependence of $K_{3m}(v, v', \omega)$. In Fig. 6.11 and 6.12 we present the results corresponding to the loop orders shown in the lower right panel of Fig. 6.10 as a function of both v and v' for $\omega = 0$. Fig. 6.11 exploits a color map, which is optimized for highlighting differences in the range of small values of $-K_{3m}(v, v', \omega = 0)$. This allows to easily identify the qualitative changes in v and v', where the shape of $K_{3m}(v, v', \omega = 0)$ changes from a diamond-like structure at low loop orders toward the butterfly-like structure of the PA solution. In Fig. 6.12, for a more quantitative analysis, we plot the differences of the Ω-flow results and the PA solution, i.e., $-\big(K_{3m}^{\text{mfRG}}(v, v', \omega = 0) - K_{3m}^{\text{PA}}(v, v', \omega = 0)\big)$. One readily notices that the trend observed in the fixed-v' cuts is coherent with the evolution of the full v, v' dependence of $K_{3m}(v, v', \omega = 0)$.

Overall we essentially obtain the same picture for the multiloop oscillations of $K_{3m}(v, v', \omega = 0)$ as for the ones of $\text{Im}\Sigma(v = \pi T)$ and $\chi_m(\omega = 0)$ discussed in the section above: One observes how the low-loop order results quickly approach the PA solution as well as the residual oscillations around it for larger loop orders. Since the entire $K_{3m}(v, v', \omega = 0)$ function oscillates around the PA result, we figuratively refer to these multiloop oscillations as "breathing" of the restfunction.

The corresponding plots for the U-flow calculations are shown in Appendix A.3.2, where qualitatively the same behavior is observed, albeit with quantitatively larger oscillations.

Our results of Figs. 6.10, 6.11 and 6.12, which demonstrate how the multiloop oscillations affect $K_{3m}(v, v', \omega = 0)$, have also important practical implications. Specifically, the usage of the high-frequency parametrization of the reducible vertex [96] allows for a speed-up of the numerical calculations as the full frequency-dependent restfunction needs to be taken into account only for a small finite frequency box (the so-called boxsize). In the choice of the number of frequencies to be included the "breathing" behavior of the restfunction needs to be carefully considered, since the boxsize might vary significantly during the multiloop procedure (see Ref. [215] for the specific choice made for this work).
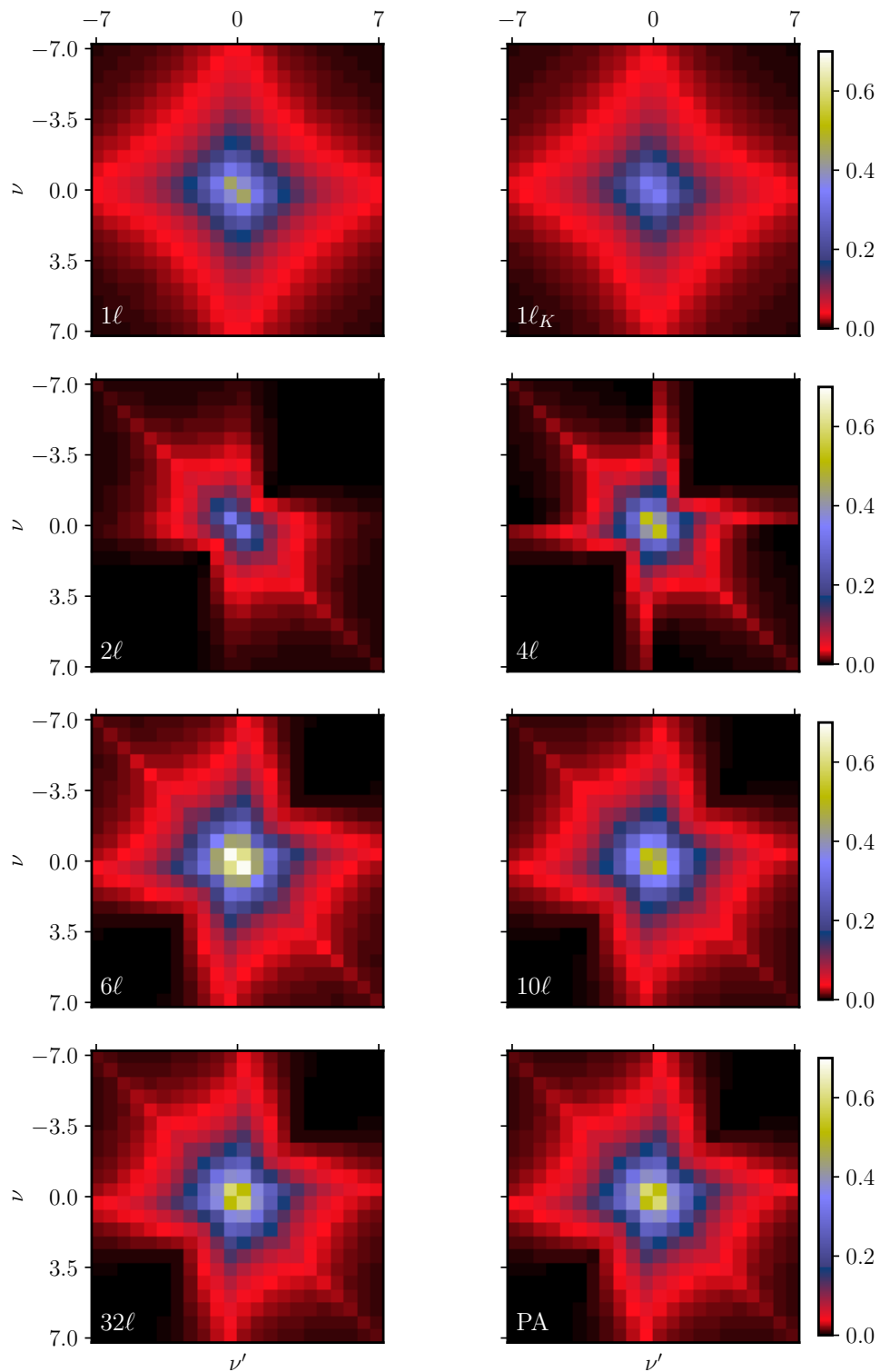
Figure 6.11: Ω-flow mfRG results for $-K_{3m}(\nu, \nu', \omega = 0)$ as a function of ν and ν' for the AIM with $U = 2$ and $\beta = 10$. The color map is optimized to better highlight the range of small values.
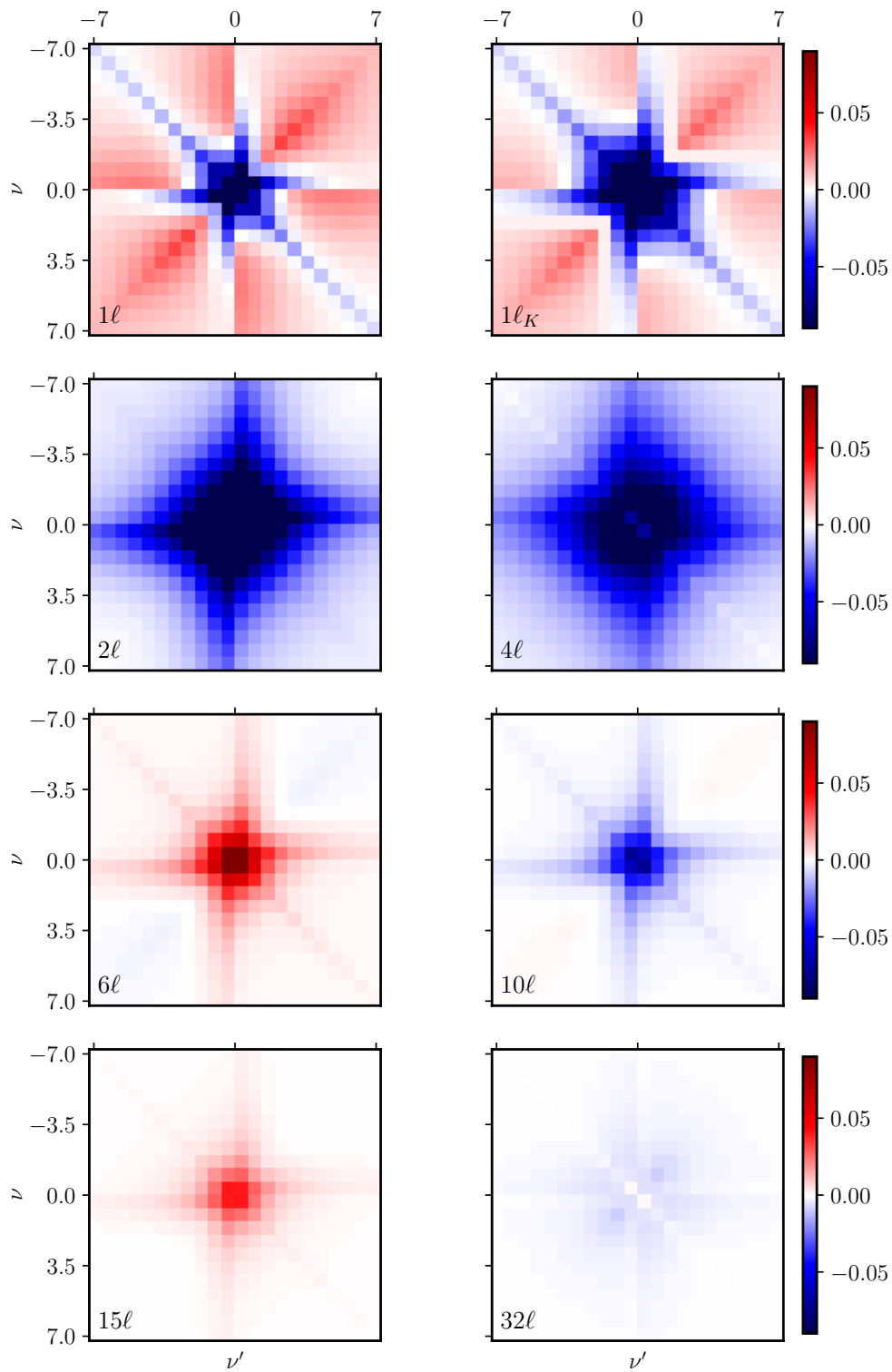
Figure 6.12: As in Fig. 6.11, showing the difference between Ω-flow calculations with different loop orders and the PA result, i.e., $-\left(K_{3m}^{\Omega-\mathrm{flow}}(\nu, \nu', \omega = 0) - K_{3m}^{\mathrm{PA}}(\nu, \nu', \omega = 0)\right)$.

6.3.5 Physical quantities: comparison from weak to strong coupling
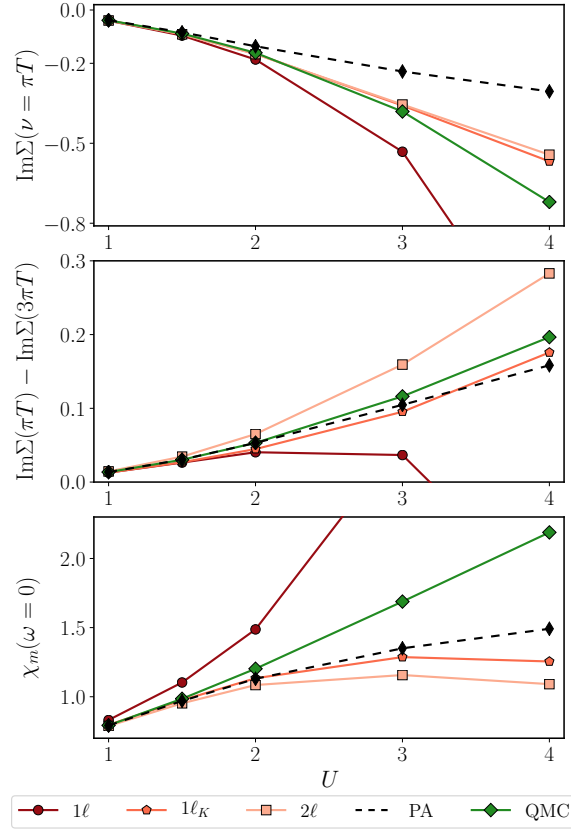
Figure 6.13: $\mathrm{Im}\Sigma(\pi T)$ (top), $\mathrm{Im}\Sigma(\pi T) - \mathrm{Im}\Sigma(3\pi T)$ (center) and $\chi_m(\omega = 0)$ (bottom) as a function of U, obtained from Ω-flows at low loop order, the PA, and QMC.

Here, we compare the results for some of the physical quantities considered, as a function of U for low loop order mfRG to the PA and the exact solution. Before we analyze the numerical data, it is worth noting that at very low values of U, the deviations of mfRG and PA schemes from QMC can be qualitatively understood from general perturbation-theory considerations. Already for $U > 1$, however, the interpretation becomes more complicated, and the accuracy of the different schemes depends on the observable considered. Among the Ω-flow results up to $U = 4$ in Fig. 6.13, the plain 1ℓ flow performs worst for all quantities. Comparing $1\ell_K$ and the PA to the exact QMC for large $U \geq 2$, we find the best results for $\mathrm{Im}\Sigma(\nu = \pi T)$ with $1\ell_K$, similar deviations for $\mathrm{Im}\Sigma(\nu = \pi T) - \mathrm{Im}\Sigma(\nu = 3\pi T)$ with $1\ell_K$ and the PA, and the best results for $\chi_m(\omega = 0)$ with the PA. This is consistent with the results of Chapter 4, where we discussed how the truncated fRG, mfRG or PA resummations of diagrams describe the formation of a local moment but without the intrinsic physical implications onto the charge channel. This can be regarded [68] as an insufficient transfer of information between the magnetic and the charge sector, formally corresponding to the impossibility of generating the irreducible vertex divergences in these approximate methods.

On a more general perspective, we note that the loop convergence of the mfRG procedure is mostly controlled by the ratio between the local interaction U and other relevant energy scales of the system under consideration (e.g., in the case of the AIM: $\pi\Delta$ or the temperature T) rather than by the ratio between the temperature and the Kondo temperature [68]. In future dedicated studies, it may be interesting to verify to what extent the grade of the loop convergence itself might be regarded as an additional independent marker of central physical aspects of the underlying exact solution of the problem.

After analyzing the performance of the multiloop scheme and its convergence behavior for the different parameter sets shown in Fig. 6.5, we now turn to the investigation of the fulfillment of fundamental properties of the exact solution in approximate methods.

6.3.6   Pauli principle and Ward identity

Both the Pauli principle and the Ward identities (WIs) are fundamental features of the many-electron physics. They are deeply rooted in quantum mechanics and pose important constraints on many-body correlation functions. An exact solution must evidently obey all such constraints. In approximate treatments, however, their fulfillment is not guaranteed *a priori*. It is commonly reckoned [55] that approximate many-body approaches either obey sum rules imposed by the Pauli principle *or* satisfy WIs. Hence, fulfilling both the Pauli principle and the WIs would represent a specific hallmark of the exact solution. On a more formal level, a pertinent example of such a trade-off in the context of parquet-based approximations can be obtained by exploiting explicit relations between the self-energy and four-point vertices [105, 217, 218] in the parquet formalism.

In the following, we utilize our converged numerical results for the AIM to analyze, on a quantitative level, to what extent the Pauli principle and WIs are fulfilled for the important class of approximate many-body approaches ranging from the conventional fRG to the mfRG and PA.

6.3.7   Pauli principle

Sum rule of $\chi^{\sigma\sigma}$: Formal aspects   — The Pauli exclusion principle states that two electrons cannot occupy the same quantum state. On the operator level, this corresponds to the fact that a fermionic occupation-number operator can only have eigenvalues zero and one. On the diagrammatic level, such a constraint affects the many-body correlation functions in several ways, e.g., through sum rules they must obey.

In this context, a relevant correlation function for the physics of the AIM is the equal-spin density-density susceptibility (cf. Sec. 2.2.3),

$$\chi^{\sigma\sigma}(\tau) = \langle T_\tau \hat{n}_\sigma(\tau)\hat{n}_\sigma \rangle - n_\sigma^2. \tag{6.3}$$

Here, $n_\sigma = \langle \hat{n}_\sigma \rangle$, and T_τ denotes (imaginary) time ordering, as discussed in Sec. 2.2 (for brevity, we omit here the particle-hole channel label). This susceptibility is directly affected

by the Pauli principle through the operator identity $\hat{n}_\sigma^2 = \hat{n}_\sigma$. Indeed, an evaluation at $\tau = 0$ yields

$$\chi^{\sigma\sigma}(\tau = 0) = \langle \hat{n}_\sigma^2 \rangle - n_\sigma^2 = n_\sigma(1 - n_\sigma), \tag{6.4}$$

a value, which is fully determined by the single-particle expectation value n_σ. Furthermore, as the equal-time correlator $\chi^{\sigma\sigma}(\tau = 0)$ is identical to the sum over all its Fourier components $\chi_\omega^{\sigma\sigma}$, the following sum rule [219] must hold:

$$\frac{1}{\beta} \sum_\omega \chi_\omega^{\sigma\sigma} = \chi^{\sigma\sigma}(\tau = 0) = n_\sigma(1 - n_\sigma). \tag{6.5}$$

At SU(2) spin symmetry and half filling, the result is 1/4.

For the purposes of the subsequent discussions, it is useful to elaborate on the quantum-field-theoretical relations which underlie Eq. (6.5). To this end, we recall that the Pauli principle can be translated from an operator identity ($\{\hat{c}_\sigma, \hat{c}_{\sigma'}\} = 0$, $\{\hat{c}_\sigma, \hat{c}_{\sigma'}^\dagger\} = \delta_{\sigma\sigma'}$) to the crossing symmetry of four-point correlators. For illustration, let us briefly use a compact notation where all arguments of an electronic operator are summarized in a single index i. Then, for $G_{2,i_1,i_2,i_3,i_4} \propto \langle T_\tau c_{i_1}^\dagger c_{i_2} c_{i_3}^\dagger c_{i_4} \rangle$ (cf. Eq. (2.13)), the crossing symmetry implies $G_{2,i_1,i_2,i_3,i_4} = -G_{2,i_3,i_2,i_1,i_4} = -G_{2,i_1,i_4,i_3,i_2}$.

Furthermore, the susceptibility can be represented through (full) propagators G and the (full) two-particle vertex F by

$$\chi_\omega^{\sigma\sigma} = -\frac{1}{\beta} \sum_\nu G_{\nu+\omega}^\sigma G_\nu^\sigma$$
$$- \frac{1}{\beta^2} \sum_{\nu\nu'} G_{\nu+\omega}^\sigma G_\nu^\sigma G_{\nu'+\omega}^\sigma G_{\nu'}^\sigma F_{\nu\nu'\omega}^{\sigma\sigma}, \tag{6.6}$$

see Sec. 2.2 for details. The first term of Eq. (6.6) summed over all frequencies ω, i.e., taken at $\tau = 0$, gives

$$\chi_{GG}^{\sigma\sigma}(\tau = 0) = -G^\sigma(\tau = 0^-)G^\sigma(\tau = 0^+). \tag{6.7}$$

Upon inserting $G^\sigma(\tau) = \langle T_\tau \hat{c}_\sigma^\dagger(\tau)\hat{c}_\sigma \rangle$, one finds

$$\chi_{GG}^{\sigma\sigma}(\tau = 0) = \langle c_\sigma c_\sigma^\dagger \rangle \langle c_\sigma^\dagger c_\sigma \rangle = (1 - n_\sigma)n_\sigma, \tag{6.8}$$

which yields already the *entire* sum rule, see Eq. (6.5). Consequently, the vertex contributions must vanish when summed over all frequencies ω. This is indeed guaranteed by the crossing symmetry, as we show below.

Consider the summed vertex contribution of Eq. (6.6),

$$\frac{1}{\beta} \sum_\omega \chi_{\text{vtx};\omega}^{\sigma\sigma} = -\frac{1}{\beta^3} \sum_{\omega\nu\nu'} G_{\nu+\omega}^\sigma G_\nu^\sigma G_{\nu'+\omega}^\sigma G_{\nu'}^\sigma F_{\nu\nu'\omega}^{\sigma\sigma}. \tag{6.9}$$

Figure 6.14: (a) The multiloop corrections to the flow of $\chi^{\sigma\sigma}$ do not vanish when summed over ω, since I_a itself is not crossing symmetric. (b) Totally irreducible 'envelope' vertex diagrams inserted into the standard self-energy flow contribute to the $1/\nu$ asymptote of Σ. Red colors indicate propagators that carry the large frequency ν.

For $F^{\sigma\sigma}$, the vertex with equal spins on all legs, the crossing symmetry simply gives $F^{\sigma\sigma}_{\nu\nu'\omega} = -F^{\sigma\sigma}_{\nu(\nu+\omega)(\nu'-\nu)}$ [54]. After inserting this into Eq. (6.9), we relabel the summation indices according to $\tilde{\omega} = \nu' - \nu$, $\tilde{\nu} = \nu + \omega$:

$$\frac{1}{\beta}\sum_{\omega}\chi^{\sigma\sigma}_{\text{vtx};\omega} = \frac{1}{\beta^3}\sum_{\omega\nu\nu'}G^{\sigma}_{\nu+\omega}G^{\sigma}_{\nu}G^{\sigma}_{\nu'}G^{\sigma}_{\nu'+\omega}F^{\sigma\sigma}_{\nu(\nu+\omega)(\nu'-\nu)}$$

$$= \frac{1}{\beta^3}\sum_{\tilde{\omega}\nu\tilde{\nu}}G^{\sigma}_{\tilde{\nu}}G^{\sigma}_{\nu}G^{\sigma}_{\tilde{\omega}+\nu}G^{\sigma}_{\tilde{\omega}+\tilde{\nu}}F^{\sigma\sigma}_{\nu\tilde{\nu}\tilde{\omega}}. \tag{6.10}$$

This reproduces the original expression for the summed vertex correction $\frac{1}{\beta}\sum_{\omega}\chi^{\sigma\sigma}_{\text{vtx};\omega}$ [Eq. (6.9)] with opposite sign, so that

$$\tfrac{1}{\beta}\sum_{\omega}\chi^{\sigma\sigma}_{\text{vtx};\omega} = -\tfrac{1}{\beta}\sum_{\omega}\chi^{\sigma\sigma}_{\text{vtx};\omega} \implies \tfrac{1}{\beta}\sum_{\omega}\chi^{\sigma\sigma}_{\text{vtx};\omega} = 0. \tag{6.11}$$

Sum rule of $\chi^{\sigma\sigma}$: Numerical results — As mentioned earlier, there are two ways [98, 106] of computing susceptibilities in fRG: (i) one can use Eq. (6.6) to obtain χ from Σ and F in a PP fashion, or (ii) one can deduce χ from its own flow equation (or that of K_1 as employed here). In the former approach the sum rule of $\chi^{\sigma\sigma}$ is fulfilled per construction, as long as the vertex used in the computation obeys the crossing symmetry, see Eqs. (6.8) and (6.11), while, in the latter scheme, this property is not guaranteed.

Not surprisingly, strategies (i) and (ii) then yield different results within 1ℓ fRG (see Figs. 6.7 and 6.8), suggesting that the susceptibility computed from a 1ℓ flow does not fulfill the sum rule. Indeed, one can easily convince oneself that the multiloop vertex corrections to the flow of $\chi^{\sigma\sigma}$ do not vanish when summing over all frequencies, cf. Fig. 6.14(a). On the other hand, we already noted that, for a converged mfRG calculation, both schemes of computing susceptibilities become equivalent [105, 106]. Therefore, the sum rule of $\chi^{\sigma\sigma}$ will be consistently fulfilled, no matter the strategy employed.

On the basis of these considerations, we now turn to our numerical mfRG data. In Fig. 6.15, we show the loop dependence of $\frac{1}{\beta}\sum_{\omega}\chi^{\sigma\sigma}_{\omega}$ for the flowing susceptibility (obtained in the Ω-flow) for different values of U. With increasing loop order, the fulfillment of the sum rule (see Eq. (6.5)), indicated by a dashed black line, is approached. Altogether, we observe a similar behavior as in Sec. 6.3: While, at low interaction values, the exact value is quickly reached, multiloop oscillations characterize the behavior at larger interaction
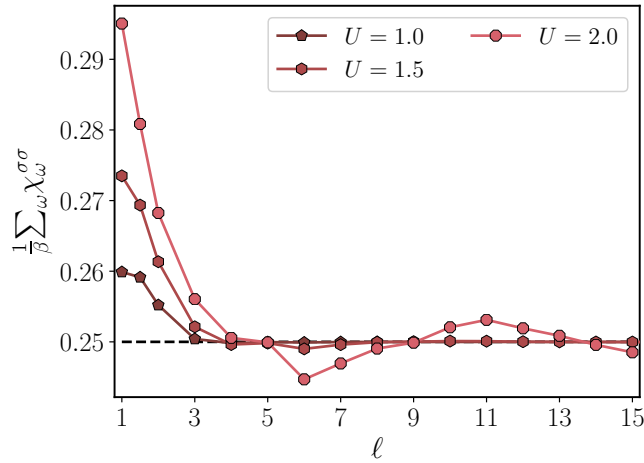
Figure 6.15: The frequency sum of $\chi_\omega^{\sigma\sigma}$ obtained for different values of U and loop order ℓ (in the Ω-flow). The multiloop corrections systematically improve the fulfillment of the sum rule [Eq. (6.5)]. Upon multiloop convergence, the sum rule is exactly fulfilled, as in the PA (dashed black line).

($U = 2$). Nevertheless, even for large U, the results at large ℓ are much closer to the fulfillment of the sum rule than the ones at low loop order. As for the PP susceptibility (not shown), we confirmed numerically that it fulfills the sum rule for all ℓ, consistent with the above explanations.

High-frequency asymptote of Σ: Formal aspects — Beside its natural link to the susceptibility, the Pauli principle also affects the self-energy, albeit more indirectly. From the moments of the single-particle spectral function, known through expectation values of operators, one can determine the high-frequency expansion of the propagator G, and thereby of the self-energy Σ [219]. One finds

$$\Sigma_\nu^\sigma = U n_{\bar\sigma} + \frac{U^2 n_{\bar\sigma}(1 - n_{\bar\sigma})}{i\nu} + O\left(\frac{1}{\nu^2}\right). \tag{6.12}$$

Next to the constant Hartree shift $U n_{\bar\sigma}$, the $1/\nu$ coefficient coincides with the r.h.s. of the sum rule for $\chi^{\bar\sigma\bar\sigma}$ (see Eq. (6.5)). Indeed, Eq. (6.12) can be equivalently rewritten [198] as

$$\Sigma_\nu^\sigma = U n_{\bar\sigma} + \frac{U^2}{i\nu} \frac{1}{\beta} \sum_\omega \chi_\omega^{\bar\sigma\bar\sigma} + O\left(\frac{1}{\nu^2}\right). \tag{6.13}$$

More insight about the quantum-field-theoretical relations underlying the asymptotic behavior of Σ can be gained from the Schwinger-Dyson equation (SDE) restated here,

$$\Sigma_\nu^\sigma = U n_{\bar\sigma} - \frac{U}{\beta^2} \sum_{\omega\nu'} G_{\nu+\omega}^\sigma G_{\nu'+\omega}^{\bar\sigma} G_{\nu'}^{\bar\sigma} F_{\nu\nu'\omega}^{\sigma\bar\sigma} , \tag{6.14}$$

see Sec. 2.2.1 for a diagrammatic representation. To this end, let us replace the vertex by
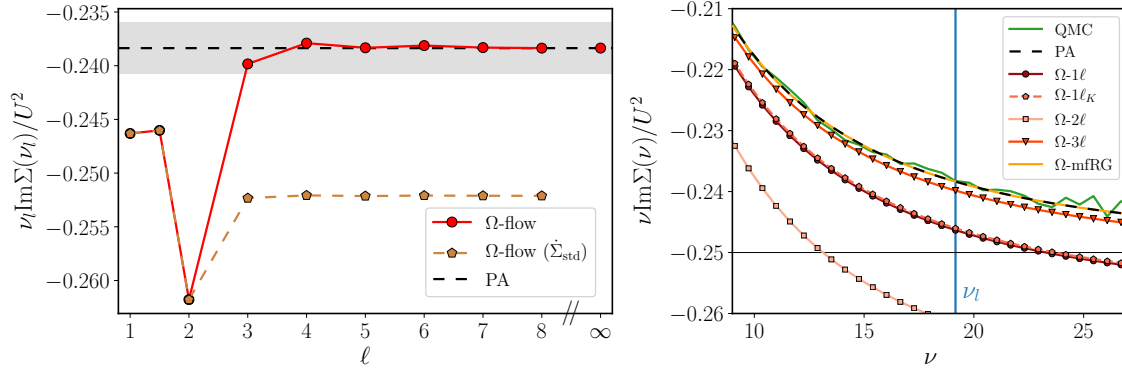
Figure 6.16: High-frequency asymptote of the self-energy, $\nu_l \mathrm{Im}\Sigma(\nu_l)/U^2$, for a large but finite frequency $\nu_l \approx 19.16$ ($\nu_l \mathrm{Im}\Sigma(\nu_l)/U^2 \to -\frac{1}{4}$ for $\nu_l \to \infty$), for $U = 1$. Left: Flowing result as a function of loop order, for an Ω-flow with (red circles) and without (gold pentagons) multiloop corrections to the self-energy flow, compared to the PA (black dashed). The gray area represents 1% deviation from PA. Right: Frequency dependence around ν_l for different methods, with QMC, PA, and mfRG following the exact asymptote.

its bare contribution, $F_0^{\sigma\bar{\sigma}} = U$, and use the first propagator in Eq. (6.14), $G_{\nu+\omega}^\sigma$, to factor out the dominant contribution for large $\nu \gg \omega$, $G_{\nu+\omega}^\sigma \sim 1/(i\nu)$. The remainder is a GG bubble summed over both frequencies ω and ν'. Hence, we find that the second-order contribution,

$$\Sigma_\nu^\sigma \overset{2^{\mathrm{nd}}}{\sim} \frac{-U^2}{i\nu} G^{\bar{\sigma}}(\tau=0^-) G^{\bar{\sigma}}(\tau=0^+) = \frac{U^2 n_{\bar{\sigma}}(1-n_{\bar{\sigma}})}{i\nu}, \qquad (6.15)$$

already provides the correct asymptotic behavior (6.12). This is similar to the sum rule of $\chi^{\sigma\sigma}$, where Eqs. (6.7)–(6.8) give the entire result, while the summed vertex corrections vanish (see Eq. (6.11)). Via Eq. (6.13), the same cancellation of vertex corrections occurs for the self-energy asymptote, as is explicitly shown in the Appendix of Ref. [215].

Within an fRG treatment, the standard flow equation for the self-energy $\dot{\Sigma}_{\mathrm{std}}$ in terms of the vertex F is *in principle* exact, as long as the exact vertex F is available. As this is almost never the case, the flow $\dot{\Sigma}_{\mathrm{std}}$ must be considered approximate. In mfRG, the multiloop corrections to the self-energy flow, see Sec. 2.3.3, effectively generate contributions to $\dot{\Sigma}_{\mathrm{std}}$ which *would* require—when using the term $\dot{\Sigma}_{\mathrm{std}}$ only—vertex diagrams beyond the PA (and thus beyond 1ℓ fRG). Indeed, one can generally show that vertex diagrams beyond the PA (and thus beyond 1ℓ fRG), such as the envelope diagram, do contribute to $\dot{\Sigma}_{\mathrm{std}}$ to order $1/\nu$ in the large-frequency limit (see Fig. 6.14(b)). Therefore, the Σ asymptote (Eq. (6.12)) is violated when using a 1ℓ or multiloop vertex flow while keeping the standard self-energy flow. This problem is circumvented by including the multiloop corrections to the self-energy flow [104], which guarantee a perfect equivalence to the SDE and, thereby, that the correct asymptote will be restored.

High-frequency asymptote of Σ: Numerical results   — In Fig. 6.16, we show (flowing) results for the asymptotic behavior of Σ as obtained from Ω-flow calculations for $U = 1$.

The left panel displays $\nu \mathrm{Im}\Sigma_\nu / U$ as a function of ℓ for a fixed, large value of $\nu_l \approx 19.16$. At this frequency, $\nu \mathrm{Im}\Sigma_\nu$ is expected to be slightly lower (in absolute value) than the corresponding asymptotic value of $-1/4$ for $\nu \to \infty$. The correct asymptotic description of the mfRG results (red circles) for large ℓ is demonstrated by their perfect match with the corresponding PA results, as the latter yield the correct high-frequency asymptotic by construction. As explained above, this would have not been the case without multiloop corrections to the self-energy flow. In fact, the gold pentagon line shows results which are obtained by $\dot\Sigma_{\mathrm{std}}$ without multiloop additions to the self-energy flow (these start at $\ell = 3$) and notably deviate from the correct value.

The right panel shows the frequency dependence of $\nu \mathrm{Im}\Sigma_\nu$ in a frequency window around ν_l (ν_l is represented by the vertical blue line). For fRG results at lower loop order, the high-frequency asymptote is incorrect, reflecting the fact that the SDE relation is not fulfilled. For the same reason, all approaches satisfying the SDE lie on top of each other, i.e., the PA (black dashed line), mfRG (orange solid line), and QMC (green line) yield the correct high-frequency behavior of Σ. Note that the QMC result was obtained using w2dynamics [85] with Worm sampling [87, 88] and symmetric improved estimators [89], designed to reduce the high-frequency noise. However, the noise cannot be suppressed completely, and thus the QMC result oscillates around the PA and mfRG solution. While the improvement of the high-frequency results is not monotonous for the lowest loop orders, we observe that rather accurate results are obtained already at the 3ℓ level, where the first multiloop corrections to the self-energy flow appear.

6.3.8 Ward identities

Formal aspects — The WIs play an essential role in the many-electron theory as they define how the information encoded in the continuity equations at a microscopical level is reflected onto response functions and macroscopic quantities. More specifically, a continuity equation is an operator relation of the form $\partial_\tau \hat\rho = -[\hat\rho, \hat H]$. If $\hat\rho$ is a symmetry of the Hamiltonian, $[\hat\rho, \hat H] = 0$, then $\hat\rho$ is a conserved quantity, $\partial_\tau \hat\rho = 0$. In this case, the continuity equation describes a conservation law. However, even if this is not the case, continuity relations can be used for deriving relevant WIs, in particular when $[\hat\rho, \hat H]$—albeit nonzero—yields a simple expression. Let us point out, that WIs are closely related with the Luttinger-Ward functional and the notion of Φ-deriveability, see Sec. 2.2.5.

In practice, WIs can be derived for n-point correlation functions of arbitrary n. If $\hat\rho$ and $[\hat\rho, \hat H]$ involve n_1 and $n_2 = n_1 + \delta n$ fermionic operators, respectively, then

$$\langle T_\tau \hat c_1 \cdots \hat c_{n-n_1}^\dagger \partial_\tau \hat\rho \rangle = -\langle T_\tau \hat c_1 \cdots \hat c_{n-n_1}^\dagger [\hat\rho, \hat H] \rangle \tag{6.16}$$

relates an n to an $(n+\delta n)$-point function. Typically, one mostly considers the WI connecting two- and four-point functions (i.e., the WIs ensuring the physical consistency between the one- and the two-particle description) and restricts oneself to the (local or global) charge or spin operators, substituting them for $\hat\rho$. A recent derivation, applicable to lattice and
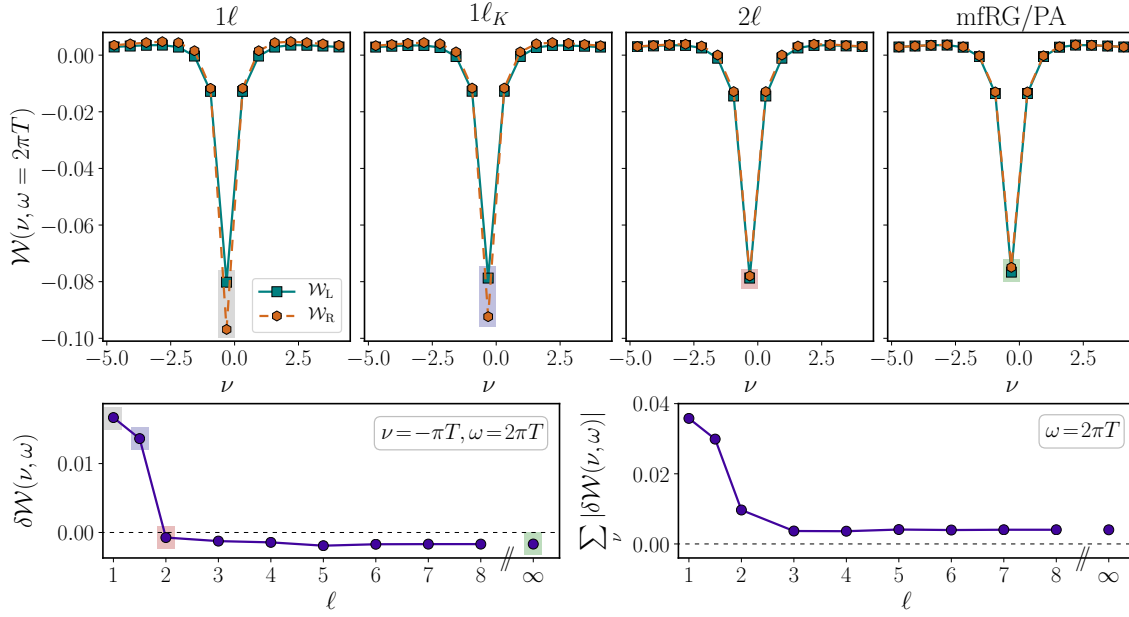
Figure 6.17: Top: Comparison of the left side $\mathcal{W}_L$ (teal, squares) and the right side $\mathcal{W}_R$ (brown, hexagons) of the WI (6.17) for Ω-flow mfRG calculations, as a function of ν for $\omega = 2\pi T$ and $U = 1$ ($\beta = 10$ throughout). Bottom: Fulfillment of the WI estimated by $\delta\mathcal{W} = \mathcal{W}_L - \mathcal{W}_R$ as a function of loop order, for $\nu = -\pi T$ (left) and for ν summed over a finite box (right, see text). Colored areas in the upper and lower left panel mark equivalent data points.

impurity systems, as well as references to prior work can be found in Refs. [56, 220]. Here, we consider explicitly the (local) charge, $\hat{\rho} = \sum_\sigma \hat{n}_\sigma$, as done in several preceding works [101, 221]. The resulting WI for the AIM reads

$$\underbrace{\Sigma_{\nu+\omega} - \Sigma_\nu}_{\mathcal{W}_L} = \underbrace{\frac{1}{\beta} \sum_{\nu'} \Gamma^c_{\nu\nu'\omega}(G_{\nu'+\omega} - G_{\nu'})}_{\mathcal{W}_R}. \tag{6.17}$$

We introduce the short-hand $\mathcal{W}_L(\nu, \omega)$ for the left and $\mathcal{W}_R(\nu, \omega)$ for the right side of the above equation. For a more general formulation of the WI, which remains valid also for cases with broken SU(2) symmetry, as well as a diagrammatic representation, we refer to Ref. [215].

Numerical results — Since the Pauli principle is preserved in the PA as well as (loop-converged) mfRG, one expects—on general grounds—these approximate schemes to violate the WIs to a certain extent. Arguably, the size of such violation should increase for increasing interaction strength, driven by the leading terms of the exact solution (where all fundamental relations are fulfilled) which are neglected in either approximate approach. Furthermore, it is known [98, 222] that the 1ℓ truncation leads to violations of the WIs. Katanin [101] proposed schemes to mitigate this deficiency. In particular, the $1\ell_K$ flow is widely used and often argued to better fulfill WIs. However, no explicit numerical studies were presented thus far. Here, we intend to fill this gap and investigate *quantitatively* the
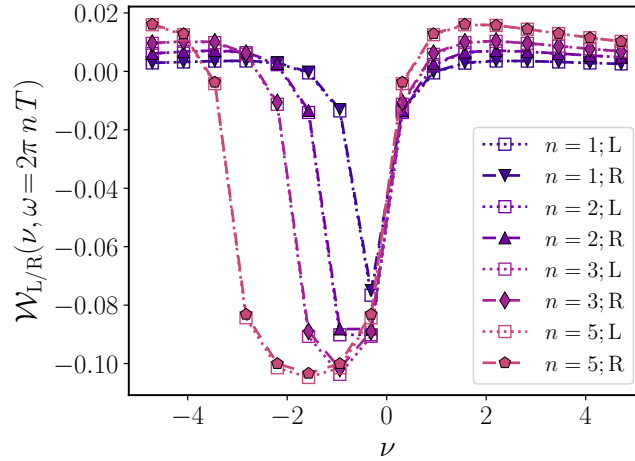
Figure 6.18: $\mathcal{W}_{\mathrm{L}}$ (dotted lines, empty squares) and $\mathcal{W}_{\mathrm{R}}$ (dashed lines, filled symbols) of the loop-converged mfRG solution, as a function of ν, at $U = 1$ and for different values of $\omega = 2\pi nT$. The absolute discrepancy is largest for ν around $-\omega/2$.

fulfillment of WIs in fRG using our numerical results for the AIM. We focus on flowing (m)fRG results obtained with the Ω-flow, in order to avoid the frequency extrapolation required for the U-flow (see further Ref. [215]).

We start with Fig. 6.17, where the top row shows $\mathcal{W}_{\mathrm{L}}(\nu, \omega)$ (squares) and $\mathcal{W}_{\mathrm{R}}(\nu, \omega)$ (hexagons) for $\omega = 2\pi T$ as a function of ν for $U = 1$, as obtained from the flow. We find that the 1ℓ result exhibits the *strongest deviation* in the WI for all ν; $1\ell_K$ yields already a visible improvement at the lowest Matsubara frequency. However, the 2ℓ and mfRG/PA results show an overall much more accurate description of the WI for all frequencies. In particular, we note that while, at the lowest Matsubara frequency, the deviation in 2ℓ is smaller than in mfRG/PA, the trend is reversed for larger frequencies.

To better quantify the deviations between both sides of the WI, we focus on the quantity $\delta\mathcal{W}(\nu, \omega) = \mathcal{W}_{\mathrm{L}}(\nu, \omega) - \mathcal{W}_{\mathrm{R}}(\nu, \omega)$ at $\omega = 2\pi nT$ ($n \in \mathbb{N}$) for two different choices for ν: In the first case, we fix ν to $\nu_s = -\lceil n/2 \rceil 2\pi T + \pi T$, which gives the fermionic frequency closest to the symmetry axis $\nu = -\omega/2$, where the largest absolute deviations are found (e.g. $\nu_s = -\pi T$ for $\omega = 2\pi T$ in Fig. 6.17, see also Fig. 6.18 discussed below). In the second case, we sum $|\delta\mathcal{W}|$ for ν in a finite frequency box. Specifically, we sum over 11 frequencies to the left and 11 frequencies to the right of the symmetry axis, adding also the contribution right at $\nu = -\omega/2$ if n is odd. In this way, we incorporate the behavior at larger frequencies, while avoiding numerical inaccuracies from the finite-frequency box effect of the high-frequency parametrization in our implementation [96] (see also Ref. [215]). When comparing results for different transfer frequency $\omega = 2\pi nT$, we divide by n to obtain more comparable results. The bottom row of Fig. 6.17 shows $\delta\mathcal{W}$ for the $n = 1$ data reported at the top. The plot confirms that, at weak-coupling, already the first multiloop corrections strongly improve the fulfillment of the WI. In particular, the minimal value for $\delta\mathcal{W}$ at $\nu = -\pi T$ (left panel) is found at $\ell = 2$ and for $|\delta\mathcal{W}|$ summed over ν (right panel) at $\ell = 3$. Hence,
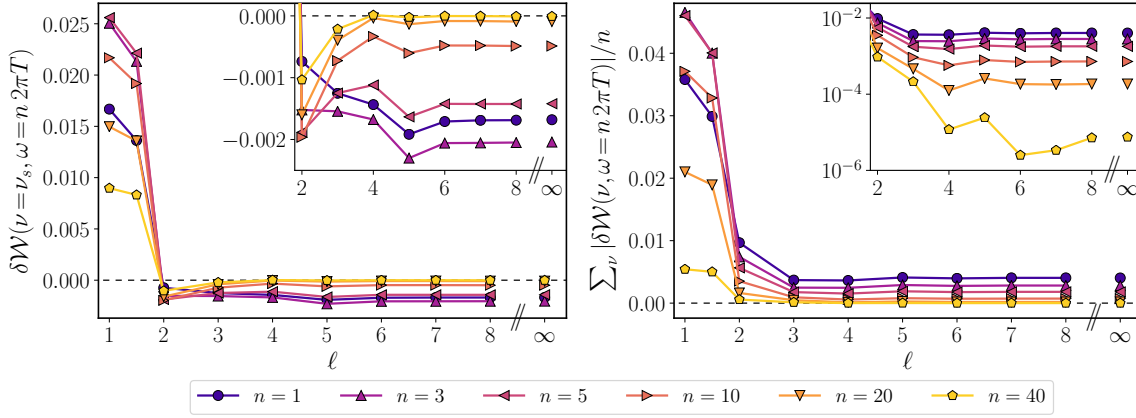
Figure 6.19: $\delta\mathcal{W}$ in mfRG as a function of loop order at $U = 1$ for different values of $\omega = 2\pi nT$ and different choices for ν. Left: $\nu = \nu_s = -\lceil n/2 \rceil 2\pi T + \pi T$, which gives the fermionic frequency closest to the symmetry axis $\nu = -\omega/2$ where the largest absolute deviation is found. Right: ν is summed over a finite box (see text). Larger values of ω are shown in yellow, smaller ones in violet. The insets show a zoom starting at $\ell = 2$, using a linear (logarithmic) scale for the left (right) panel.

our $U = 1$ calculations show that the finite deviation from the exact fulfillment of the WI expected to occur in the loop-converged mfRG/PA results is notably smaller in comparison to 1ℓ or $1\ell_K$, and that it quantitatively represents a marginal effect in the weak-coupling regime. This trend is also confirmed regarding relative deviations $|\delta_r\mathcal{W}| = |\delta\mathcal{W}/\mathcal{W}_L|$, as explicitly shown in the Appendix of Ref. [215].

Next, we extend the analysis to larger values of $\omega = 2\pi nT$ and show in Fig. 6.18 loop-converged mfRG results for $1 \le n \le 5$. The plot demonstrates that the mfRG data provide satisfactory agreement between $\mathcal{W}_L$ (empty squares) and $\mathcal{W}_R$ (filled symbols) for all values of ω and ν, and that the largest absolute deviation indeed occurs for ν around ν_s, i.e. the frequency closest to the symmetry axis $\nu = \omega/2$ (see above). Figure 6.19 presents $\delta\mathcal{W}$ as a function of ℓ for n up to 40. Again, the fulfillment of the WI is slightly improved when going from 1ℓ to $1\ell_K$ and strongly improved starting from 2ℓ, for all values of ω. However, the details in the change from $\ell = 2$ to ∞ depend on ω. In general, we observe that the WI is better fulfilled for larger values of ω. In fact, a perfect match is given for $\omega \to \infty$ and $\ell \to \infty$, since the WI reproduces the SDE for $\omega \to \infty$ (see Appendix of Ref. [215]), which is exactly fulfilled in mfRG and the PA. This can be clearly seen in both insets of Fig. 6.19. The inset of the right panel uses a logarithmic scale, where one can also spot the onset of oscillations in the multiloop convergence, in spite of their small amplitude.

Finally, we analyze the effects of the interaction strength, by progressively increasing its value up to $U = 4$. In Fig. 6.20, we examine $\delta\mathcal{W}$ for $\omega = 2\pi nT$ at $n = 1$ and $n = 11$, comparing results of (m)fRG flows at low loop order with the PA. At large interaction, the pure 1ℓ flow is evidently unreliable, violating the WI with very large values of $\delta\mathcal{W}$. The situation visibly improves in $1\ell_K$, 2ℓ, and PA. In particular, for $U \le 2$, $1\ell_K$ is farther off than 2ℓ and PA. Interestingly, however, the $1\ell_K$ deviations display a highly non-trivial behavior with increasing U—they are non-monotonous in the top left panel and have a decreasing
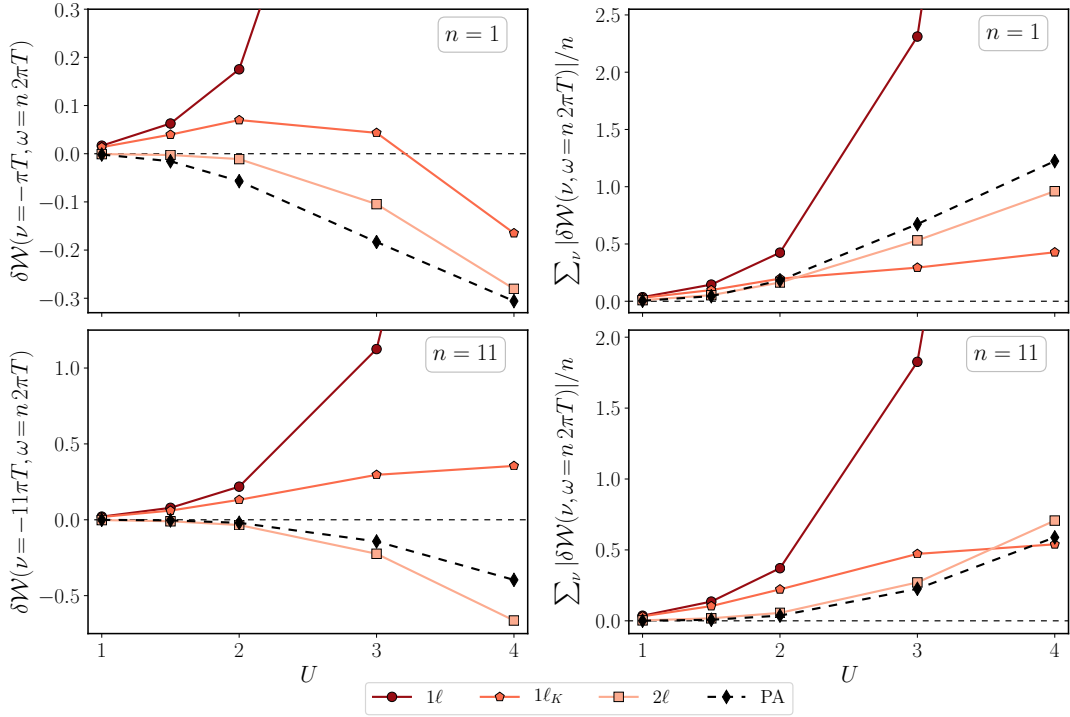
Figure 6.20: $\delta\mathcal{W}$ for increasing U obtained with different methods. Solid lines in shades of red denote (m)fRG schemes (Ω-flow) at low loop order; the PA solution is shown in dashed black. In the top (bottom) panels, $\omega = 2\pi nT$ is fixed at $n = 1$ ($n = 11$). In the left panels, we use $\nu = -\pi T$ ($\nu = -11\pi T$). In the right panels ν is summed over a finite box.

slope in the other panels—and thereby yield comparatively small values of $\delta\mathcal{W}$ at larger U. By contrast, for the PA results, $|\delta\mathcal{W}|$ starts rather small but increases monotonously with increasing U.

For the $n = 1$ case the individual calculations for the different U values are shown for the $1\ell_K$ (upper row) and the PA (lower) case in Fig. 6.21. The pink circles represent $\delta\mathcal{W}(\nu, \omega = 2\pi T)$ as a function of ν. In the upper row one readily notices that the frequency structure of $\delta\mathcal{W}(\nu, \omega = 2\pi T)$ changes significantly for the $1\ell_K$ solution as U is increased. In particular, the sign change of $\delta\mathcal{W}(\nu, \omega = 2\pi T)$ at low frequencies, observed between $U = 3$ and $U = 4$, corresponds to the non-monotonous trend of the $1\ell_K$ data shown in Fig. 6.20. For the PA instead, the frequency structure of $\delta\mathcal{W}(\nu, \omega = 2\pi T)$ does not display significant qualitative changes for different values of U, instead it quantitatively grows with increasing U, as one would expect.

To summarize, we observe that at intermediate to strong coupling, the $1\ell_K$ shows the smallest deviations in the fulfillment of the WI at small frequencies, e.g., for $n = 1$ [215]. The PA and mfRG solution instead provide a more accurate description for larger frequencies, see e.g., the results for $n = 11$ [215]. Further details on the individual deviations of $\mathcal{W}_L$ and $\mathcal{W}_R$ in comparison with the conserving exact solution can be found in the Appendix of Ref. [215].
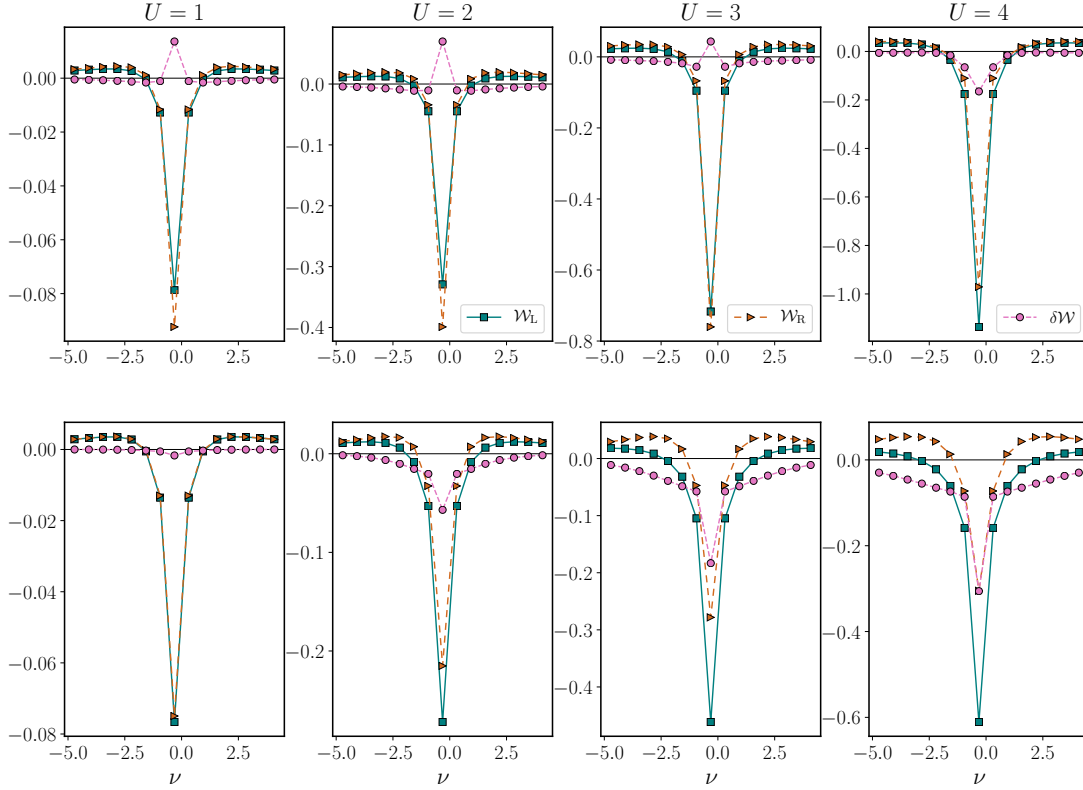
Figure 6.21: Comparison of $\mathcal{W}_L(\nu, \omega = 2\pi T)$ (teal, squares), $\mathcal{W}_R(\nu, \omega = 2\pi T)$ (brown, hexagons) and $\delta\mathcal{W}(\nu, \omega = 2\pi T)$ (pink, circles) for different values of U for $1\ell_K$ (upper row) and PA (lower) calculations of the AIM.

As a last step, we compare the numerical deviations $\delta\mathcal{W}$ as a function of U focusing on small interaction values $U < 1$. Figure 6.22 shows $\delta\mathcal{W}$, similarly as in Fig. 6.20, but on a log-log scale. Using a $f(x) = \alpha\, x + d$ fit, we extract the exponents of the deviations of the WI, $\delta\mathcal{W} \sim U^\alpha$, for the (m)fRG flow and PA scheme. Our analysis shows perfect agreement with the theoretical predictions of Ref. [101]: the 1ℓ scheme displays deviations that grow with the third power of U ($\alpha \approx 3$, solid lines), and the 2ℓ results are in agreement with a U^4 growth ($\alpha \approx 4$, dotted lines). The $1\ell_K$ results at small U also manifest $O(U^3)$ deviations. This is in agreement with the analytic arguments of Ref. [101] since, for the commonly used $1\ell_K$ scheme, only part of the 2ℓ corrections are included by substituting $S \rightarrow \dot{G}$. Hence, some terms violating the WI at $O(U^3)$ remain, as seen in our numerical data in Fig. 6.22 ($\alpha \approx 3$, dashed-dotted lines). Note that the behavior at larger interaction values, as discussed above, is beyond the reach of the present analysis applicable at small values of U.

Further, concerning the loop-converged mfRG/PA results, we find deviations of the WI, which behave as $O(U^5)$ (dashed lines). In general, one expects the PA/mfRG schemes to deviate from the exact solution as $O(U^4)$. However, at half filling, the combination of the particle-hole symmetry and spin symmetry of our problem causes the contributions to the WI from the forth-order "envelope" diagrams to exactly cancel, as can be shown explicitly (see the Appendix of Ref. [215]). For completeness, we also note that the same
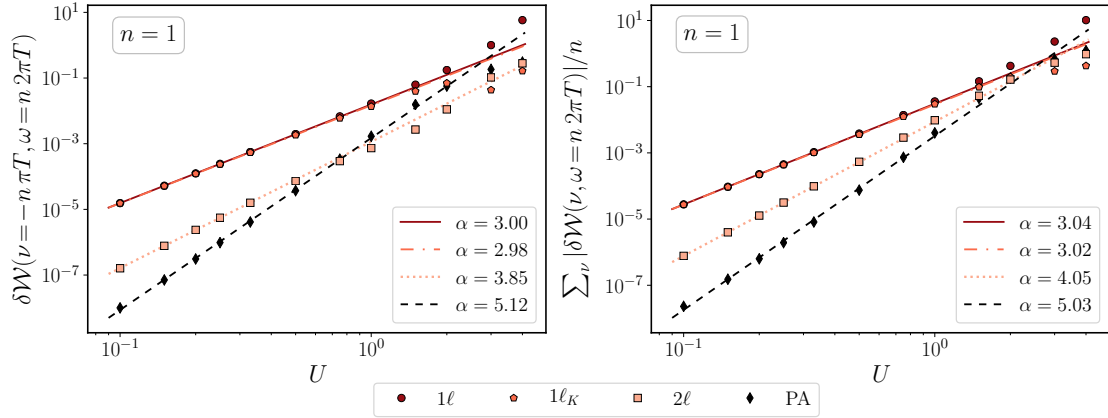
Figure 6.22: Same as Fig. 6.20 for $n = 1$, but including data for very small interaction values $U < 1$, using a log-log scale. The straight lines correspond to $f(x) = \alpha x + d$ fits using the first data points between $U = 0.1$ and $U = 0.5$, yielding the exponents of the $\sim U^\alpha$ behavior.

behavior as in Fig. 6.22 is found for other frequency choices as well (e.g. for $n = 11$ used in the lower panel of Fig. 6.20).

6.3.9 Discussion

Our thorough investigation of the performance of the mfRG scheme has ranged from the weak- up to the strong-coupling regime, where the first divergences of the irreducible vertex functions appear in the exact QMC solution of the problem, as shown in Fig. 6.5. In the former case, the convergence of the mfRG scheme could be achieved quickly within few loop orders and a perfect match with the corresponding PA results was found. At stronger coupling multiloop oscillations appeared, eventually hampering the mfRG convergence at high loop orders.

Beyond this purely numerical study, we also investigated fundamental properties that characterize the exact solution of the many-body problem highlighting important features of the mfRG scheme: As opposed to flowing results of loop-truncated approximations, the full mfRG solution, as well as the PA, preserve the Pauli principle and the corresponding sum rules. As detailed above, this also relates to the fact that the self-energy exhibits the proper high-frequency behavior in the mfRG/PA case. As for the Ward identities the non-conserving nature of all approximation schemes investigated became apparent. Nevertheless for weak interaction a systematic improvement of the fulfillment of WIs for the PA/mfRG solution was found in comparison with other loop truncated approximations. At larger interaction values a more diverse picture emerged, as the magnitude of the WI violation depends crucially on the considered bosonic frequency ω.

Our results are relevant in light of future DMF^{2}RG applications, since they allow to foresee possible issues one might have to face. In particular, the following considerations can be made: On the one hand, by choosing the DMFT solution as a starting point for intermediate-to-strong coupling applications, one is closer to the exact solution of the lattice problem than one would be starting from the non-interacting case [208, 209]. Indeed,

the flow of the DMF^{2}RG scheme, see Sec. 6.2.3, is generating non-local correlations on top of the local ones already included in the DMFT starting point. Consequently, one could expect that a swift convergence in loop order is found, in all cases where non-local correlations remain reasonably well treatable by an advanced perturbative approach, even in a context of strong (nonperturbative) local correlations. Evidently, this might boost the applicability of truncated fRG methods well beyond the regime of small-to-intermediate U. On the other hand, by increasing U and/or reducing the temperature, one might encounter similar oscillation patterns as a function of loop order, since the local DMFT vertices on which the DMF^{2}RG is build are large compared to the bare interaction U. It remains to be seen in practical calculations, which scenario will be eventually realized. Nevertheless let us emphasize that, even in the case of multiloop oscillations and slow convergence in loop order, the multiloop scheme leads to systematic improvements of fundamental properties of the approximative solution, as clearly observed in our case for the sum rule at intermediate coupling in Sec. 6.3.7.

Conclusion and Outlook

> *... Take a walk on the wild side*
> – Lou Reed

In this thesis, significant aspects of the divergences of irreducible local vertex functions were thoroughly discussed, including their occurrence in several fundamental many-electron models, their connection to the multivaluedness of the Luttinger-Ward functional (LWF), their physical origin, and, finally, their physical and algorithmic implications. Based on the presentation made, the following conclusion can certainly be drawn: *Irreducible vertex divergences are more than a mere mathematical peculiarity of the QFT formalism applied for describing correlated electron systems.* In fact, at the beginning of this thesis, one could have had the misconception that the main topic was essentially hunting mathematical ghosts [223] without any deeper physical meaning or impact. In the end, however, one is certainly convinced of the opposite (or at least the author hopes so).

In this respect, let us summarize the essential insights gained throughout this work by concisely answering the central questions of this thesis, which were posed in the Introduction.

- *In which cases are the different manifestations of the breakdown of perturbation theory (irreducible vertex divergences and crossings of solutions of the LWF) appearing, and how are they connected*?

  Following the detailed discussion in **Chapter** 3, one would be almost tempted to answer: *Everywhere, where there is correlation*. Indeed, after the analysis of several fundamental many-electron models in cases with and without particle-hole symmetry, the following systematic seems to emerge: On the two-particle level, in channels whose local fluctuations are *suppressed* by the electronic interaction, this suppression is reflected in the decrease of eigenvalues of the local generalized susceptibilities. Depending on zero or nonzero imaginary parts of the *singular* eigenvalues, divergences of the corresponding irreducible vertices are triggered or not. This scenario is, however, not the whole story since a second kind of irreducible vertex divergences exists, which can even affect the *dominant* fluctuation channel. While at perfect particle-

hole symmetry, these divergences are decoupled from the corresponding physical response, out of half filling they are related to its *enhancement*.

Moreover, the divergences of the irreducible vertex functions are related to the multivaluedness of the LWF [11]. The corresponding branching points, i.e., crossings of unphysical and physical solutions, were similarly observed ubiquitously throughout all models studied in this thesis [11, 19, 21]. For half filling, the connection among these nonperturbative manifestations is even understood on an analytic level [12]. Out of half filling, an analytic proof is still missing, but overwhelming hints to a possible underlying connection are found [21].

- *What is the underlying physical mechanism that triggers the perturbative breakdown*?

  Here, a clear-cut picture emerges from **Chapter** 4: On the local level for repulsive interaction, the formation of the local moment is reflected in a characteristic frequency structure of the generalized charge susceptibility–its *fingerprint*: strongly suppressed diagonal entries and an emerging off-diagonal structure. This is the way how the local moment formation originates the appearance of negative eigenvalues in the charge channel and, hence, the associated irreducible vertex divergences. Additionally, thanks to this investigation, another characteristic frequency structure–labeled as the "*onion*" structure–could be identified and related to the screening of the local moment in the Kondo regime. Based on this analysis, an alternative criterion for the determination of the Kondo temperature T_K on the two-particle level in the *charge* channel could be identified.

- *Are there physical implications of the appearance of irreducible vertex divergences*?

  Yes! The associated negative eigenvalues of the local generalized susceptibilities are *crucial* for the correct description of the local physical response function, as pointed out in **Chapters** 4 and 5. Even more so, these negative eigenvalues can trigger a strong enhancement and ultimately the divergence of the *uniform* charge response of correlated electrons on a lattice. In particular, in **Chapter** 5, the divergence of the isothermal compressibility in the proximity of the Mott-MIT of the Hubbard model [161] (solved by DMFT) could be directly linked to a *negative enough* eigenvalue of the local generalized charge susceptibility. Such an effect can be interpreted, to a certain extent, as a sign flip of the effective interaction in the charge channel, from repulsive to attractive, representing a mechanism of purely nonperturbative nature.

- *What are the algorithmic implications of the breakdown of the perturbative expansions, and are there possible strategies for circumventing them*?

  While the multivaluedness of the LWF poses significant hurdles to the application of corresponding bold diagrammatic resummation techniques [11], the associated divergences of the irreducible vertices hinder their direct usage for diagrammatic extensions of DMFT [51]. Concerning the former, working with *bare* propagators instead, allows to go beyond the many branching points of the LWF [11]. For the diagrammatic extensions of DMFT, the solution can be summarized briefly as:

"*do not open Pandora's box*"–i.e., rewrite or base the diagrammatic approach upon the *full* one-particle irreducible vertex F, instead of its irreducible counterparts. In **Chapter** 6, several examples of approaches that *circumvent* the explicit usage of the irreducible vertices were presented, with a particular focus on the DMF^{2}RG method [208]. In this respect, the performance of the multiloop fRG [103, 104], as applied to the AIM, was thoroughly analyzed, as it can represent an important basis for possible applications of a multiloop DMF^{2}RG method [105] (or D(MF)^{2}RG) in the future.

The considerations of all these results outline, for the local case with repulsive interaction, the emergence of a well defined mechanism associated to nonperturbative physics, which we refer to as "**the circle of suppression and enhancement**".

The circle of suppression and enhancement   Enhanced magnetic fluctuations[1] are reflected in a suppressed local charge response with associated suppressed positive or even negative eigenvalues of the generalized charge susceptibility. The communication between these channels is "transmitted" via irreducible vertices, which diverge if the corresponding eigenvalues are real and undergo a sign change. These negative eigenvalues of the local generalized susceptibility, after becoming negative enough, can trigger an instability in the uniform charge response, representing a *nonperturbative* pathway to phase transitions.

In this way, a true nonperturbative *feat*, or similarly, another "perfect espresso" of strong local electronic correlation, could be identified throughout this thesis.

7.1   Outlook

In this section, we elaborate on possible future investigations, which are directly inspired by the different results presented throughout this work.

Beyond DMFT   The intuitive picture of the "circle of suppression and enhancement" we have presented above naturally calls for extensions to cases beyond the DMFT treatment of the single-band HM.

On the one hand, one can think to include nonlocal correlations on top of DMFT. As a pertinent example, let us consider the two-dimensional (2D) HM solved by cluster extensions of DMFT, e.g., CDMFT or DCA [121]. In these cases, several studies have highlighted the crucial role played by antiferromagnetic fluctuations for the physics of the 2D HM [51, 52, 58, 59, 122, 173, 174, 224–226]. In this particular case, also all other basic "ingredients" for the mechanism described above are present: (*a*) In the study by J. Vučičević *et al.* [21], which was summarized in Sec. 3.1.4.2, the occurrence of irreducible vertex divergences in the charge channel at intermediate coupling was identified in a CDMFT treatment. Similarly, in the DCA analysis performed in Ref. [18], negative eigenvalues in the generalized

---

[1]Here, this role is played by the local moment formation, which effectively increases the magnitude of $\chi_{\uparrow\downarrow}$, see Fig. 4.5. In this way, the magnetic response ($\chi_m = \chi_{\uparrow\uparrow} - \chi_{\uparrow\downarrow}$) is increased and, at the same time, the charge response is suppressed ($\chi_c = \chi_{\uparrow\uparrow} + \chi_{\uparrow\downarrow}$), due to the overall negative sign of $\chi_{\uparrow\downarrow}$.

momentum-dependent charge susceptibility were found, and related to corresponding divergences of irreducible vertex functions. At the same time, (*b*) CDMFT calculations for the 2D HM have shown a strong increase of the compressibility κ in the proximity of the corresponding MIT, see e.g. Refs. [166–168]. Based on these cornerstones, one can safely assume to find an extension of the "circle of suppression and enhancement" to cases where strong nonlocal correlations are included.

On the other hand, extending the study to a multiorbital system, where the Hund's coupling can be taken into account, certainly represents another case where strong local magnetic fluctuations can be expected [61, 227, 228]. As the Refs. [229, 230] have shown, also in these situations, an increase of the compressibility can be observed in the proximity of the Hund's-Mott MIT. Hence, the study of a multiorbital HM would represent another possible extension of the "circle of suppression and enhancement".

Let us underline that one should not limit these investigations to the charge sector and the associated phase-separation instabilities only: The impact of negative eigenvalues, occurring also in the particle-particle sector, should be also systematically inspected in all cases where nonlocal correlations beyond DMFT or multiorbital systems are considered.

Some of these possible extensions are currently being worked on by Matthias Reitner in the group of Alessandro Toschi, aiming to identify the link between phase instabilities and negative eigenvalues of the local or short-ranged generalized susceptibility in the more general situations. In this context, we also want to stress that for both cases an analysis of the frequency and the momentum/orbital structures of the generalized susceptibilities would certainly be of interest. In this way, a similar identification of characteristic structures might be pursued, as the ones presented in this work.

On a more general perspective, it would be interesting to see, whether the "circle of suppression and enhancement" really is a pathway to phase transitions of purely *nonperturbative* nature. In this respect, one would need to analyze the fully **k**-dependent case, without starting from a local/short-ranged perspective. Here, one needs to clarify whether a situation of a diverging *negative* eigenvalue with a corresponding negative weight of the fully **k**-dependent generalized susceptibility, leading to an instability of a general **q**-dependent response $\chi_{\mathbf{q}}$, would be imaginable. This naturally seems likely, following also the discussion of the case of cluster extensions of DMFT made above. As a second step, it would be necessary to check if such negative eigenvalues $\lambda_{\alpha}^{\mathbf{q}}$ could be, in principle, obtained in a self-consistent perturbative treatment such as, e.g., fRG or PA. In particular, one would need to investigate whether such negative eigenvalues are *always* preceded by a divergence of the corresponding momentum- and frequency-dependent irreducible vertex. From the analysis presented so far, this seems indeed possible. As another hint for the existence of this mechanism for the fully **k**-dependent case, without using DMFT as a starting point, consider also Fig. 4 of Ref. [11]. Here, unphysical solutions, i.e., the existence of branching points of the LWF, are observed in the fully **k**-dependent result obtained by bold diagrammatic Monte-Carlo calculation for a 2D-HM at half-filling. This result underlines that the multivaluedness, and likely also the divergences of irreducible vertex functions, will indeed affect also the fully **k**-dependent solution of e.g., the 2D-HM.

Physical implications of vertex divergences – Widom line and Fermi-Liquid theory   As already discussed at the end of Chapter 5, the connection of negative eigenvalues of the local generalized charge susceptibility to the maximum of the isothermal compressibility for temperatures further in the crossover region, which defines the Widom line [166–169, 181, 182], would be an interesting extension of the work presented there. As another possible future project, let us also mention the Fermi-Liquid parameters of the AIM [30]: It would be interesting to clarify on a fundamental theoretical level, whether in these quantities an impact of negative eigenvalues of $\chi_c^{\nu\nu'}$ could be identified. This investigation would follow the direction of defining a distinction between a perturbative and a nonperturbative Fermi-Liquid.

Fingerprints of the local moment formation – unequivocally identifying the culprit
While at the moment, fluctuation diagnostic techniques are mostly defined and applied to the electronic self-energy [58, 59, 122], one could exploit the single-boson exchange decomposition [137] (introduced briefly in Sec. 6.2.2), to analyze directly, how the diagonal ($\nu = \nu'$) as well as the counter-diagonal ($\nu = -\nu'$) of $\chi_c^{\nu\nu'(\omega=0)}$ are determined by the different diagrammatic channels. The goal here would be to relate $\chi_c^{\nu=\pm\nu'(\omega=0)}$ to the physical magnetic response function $\chi_m(\omega = 0)$, in which the local moment formation is explicitly encoded. In this way, the impact of the progressive enhancement of $\chi_m(\omega = 0)$ as the local moment is formed, could be directly connected with the appearance of negative entries in the diagonal of $\chi_c^{\nu\nu'}$. Further, one could also attempt to identify the microscopic processes responsible for the increase of the off-diagonal elements of $\chi_c^{\nu=-\nu'(\omega=0)}$, which was shown for the first Matsubara frequency ($\chi_c^{(\nu=\pi T)(\nu'=-\pi T)(\omega=0)} = \chi^O$) in Figs. 4.3 and A.4. In an upcoming work by Severino Adler, working in the group of Alessandro Toschi, several aspects of this question will be investigated.

Irreducible vertex divergences – extending the "zoo"   Chapter 3 already discussed the appearance of irreducible vertex divergences in many situations – representing a diverse "zoo" of nonperturbative manifestations throughout various many-electron models in different physical channels. However, it would be intriguing to extend the analysis to more complex cases. Here we have in mind: (*i*) a more focused study of the case of broken particle-hole symmetry, for example, at different temperatures or larger values of U (e.g. what happens to the multiple negative eigenvalues seen in Fig. 3.20, when the half filling constraint is lifted). In this respect, let us also note the relevant extension of the proof linking a crossing of the physical with unphysical solutions to the occurrence of vertex divergences [12] to cases out of half filling. This goes hand in hand with a closer inspection of the boundaries of the nonperturbative regime, as identified by bold resummation techniques [11, 21, 28], and the different divergence lines observed for this case.

On a more general perspective (*ii*), a systematic investigation of vertex divergences for symmetry broken phases (e.g., the antiferromagnetic solution of the HM in DMFT) would be very intriguing, which is currently being worked on by Matthias Reitner.

Finally, let us in this respect also mention (*iii*) the idea to investigate vertex divergences

directly on the real frequency axis, as already outlined at the end of Sec. 3.1.3. Here, the pioneering Refs. [141] and [142], certainly play an important role as a possible starting point.

Two-particle criterion for T_K   Naturally, it would be also interesting to investigate whether the two-particle criterion for T_K can be adapted and applied to more complex cases, e.g., out of half filling, multiorbital systems, or even cases of nonlocal correlations, all discussed at the beginning of this section (hand in hand with the hunt for possible fingerprints, see "Beyond DMFT"). Here, the temperature identified by this criterion would most likely provide an estimate of the coherence temperature. More generally, an analytic foundation of the two-particle criterion pinpointed in Chapter 4 in the general QFT formalism would be most desirable, as already discussed at the end of Sec. 4.6. Here a possible connection to the full vertex F could represent a first step, also in light of the NRG results presented in Fig. 9 of Ref. [141].

Existence of the minimum of the charge response in the perturbative regime   Following the analysis made in Chapter 4 and the latest results of Ref. [158], the question arises whether a more strict statement about the presence of vertex divergences and the minimum of the local charge response χ_c as a function of T can be made. In particular: At which interaction value does the minimum of χ_c as a function of T vanish and is this related to the lowest U value where irreducible vertex divergences are found?

Multiloop DMF^{2}RG   A clear future perspective of the mfRG analysis presented in Sec. 6.3 is to perform multiloop DMF^{2}RG calculations for, e.g., the two-dimensional Hubbard model. Based on the arguments presented in Secs. 6.2 and 6.3, one should expect a significant decrease of the pseudocritical temperatures with increasing loop orders. First steps into this direction are currently made by Aiman Al-Eryani and Sarah Heinzelmann in the group of Sabine Andergassen, by applying the mfRG (without a DMFT starting point) to the attractive Hubbard model.

    As a much more speculative outlook (following mainly the author's gut feeling), it would also be interesting to investigate further the "node"-structure of the multiloop oscillations described in Sec. 6.3.3. On the one hand, one could analyze how robust the position of the "nodes" is as the parameters of the system change, e.g., the temperature (in a broader range than discussed in Chapter 6). On a more general level, however, the question arises whether resummation techniques [16, 191], introduced to handle divergent resummations of bare diagrammatic series (see Sec. 6.1), could be in some way applied to the multiloop series. Here, the challenge would certainly be to connect these resummation techniques, which work mainly on the level of the action $\mathcal{S}$ and concern summations of diagram orders, to a summation of loop orders on the level of one-particle irreducible vertices Σ and F.

This rich and multifaceted list of possible future research developments, inspired by the investigations made in this work, highlights the significance of the results obtained for the forefront description of correlated many-electron systems and their puzzling but fascinating physics.

Additional results and considerations

In order to provide an insightful and focused reading experience of the main text, some supplemental results and additional considerations are shown in this Appendix.

A.1   Additional results for Chapter 4

*Parts of this chapter, marked by a vertical bar, have already been published in the APS journal Phys. Rev. Lett. **126**, 056403 (2021), specifically as the corresponding supplemental material.*

A.1.1   Frequency structures in $\tilde{\chi}_c^{\nu\nu'}$

In this section, additional results on the frequency structures of $\tilde{\chi}_c^{\nu\nu'}$, discussed in the main text, are provided. First, the fingerprints of the local moment formation and the Kondo regime are shown for the case of the AIM at a different value of U than the one considered in Chapter 4. Second, the presence of the characteristic Matsubara frequency structures is confirmed also for the cases of the PAM and the HM. Finally, the particular structure of the partial summation of $\tilde{\chi}_c^{\nu\nu'}$, which was discussed in Sec. 4.1, is reported also for the lowest-T (T_{cold}) case shown in Fig. 4.11.

We start by showing in Fig. A.1 a similar analysis as made in Sec. 4.2, but for a different value of $U = 7.25$ ($U/\Delta \approx 11.54$). As the temperature is reduced, the same characteristic qualitative changes of the Matsubara frequency structure of $\tilde{\chi}_c^{\nu\nu'}$ are observed, confirming the generality of our discussion made in the main text. We note that for this interaction value, the Kondo temperature is $T_K = 1/158$, which is very close to the calculation of $\beta = 160$ shown in central bottom panel of Fig. A.1, where the equality of the 2×2 submatrix elements of $\tilde{\chi}_c^{\nu\nu'}$ can be seen immediately. For temperatures slightly below T_K ($\beta = 200$, bottom row right panel), the onion structure is still clearly visible.

As already mentioned in Chapter 4, the specific frequency features, coined *fingerprints*, can also be observed for the PAM and the HM, as shown in Fig. A.2. The top panels display the results for the generalized charge susceptibility $\tilde{\chi}_c^{\nu\nu'}$ (again normalized by T^2) at intermediate temperatures ($U/D/V > T_{\text{int}} > T_K$), the bottom panels nicely show the
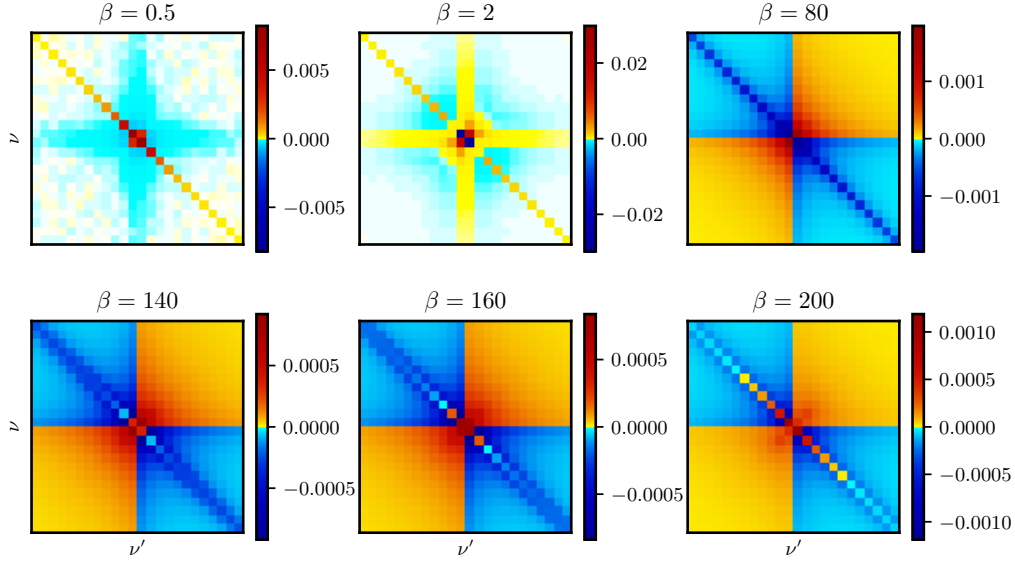
Figure A.1: Similarly as Fig. 4.3 of the main text, $T^2 \tilde{\chi}_c^{\nu\nu'}(\omega = 0)$ for the AIM at different inverse temperatures $\beta = 1/T$ and fixed $U = 7.25$, where $T_K = 1/158$.

"onion-structure" observed for both, the PAM (left column) and the HM (right column), in the Kondo regime ($T_{low} \approx T_K$).

The precise parameters of the DMFT calculations for the HM and the PAM shown in Fig. A.2 are the following: For the PAM the hybridization constant was fixed to $V = 0.91t$ and $T_{int} = 1/52$, $T_{low} = 1/100$. For the HM on the Bethe-lattice the interaction was fixed to $U = 2.2$ in units of the half-bandwidth D, and $T_{int} = 1/40$, $T_{low} = 1/50$.

Finally, in Fig. A.3, the result of a partial summation of $\tilde{\chi}_c^{\nu\nu'}$, as defined in Sec. 4.2, is shown for the T_{cold} case presented in Sec. 4.6. As discussed therein, the fingerprints of the suppression of the charge channel due to the local moment are no longer directly visible in $\tilde{\chi}_c^{\nu\nu'}$. Nevertheless, as Fig. A.3 shows, the overall suppression due to negative eigenvalues is still present, and distinguishes the T_{cold} case clearly from perturbative cases, e.g. the one of T_{high} discussed in Sec 4.2.

A.1.2 Low-frequency criterion of $\tilde{\chi}_c^{\nu\nu'}$ for T_K

As we discussed in the main part, at $T \approx T_K$ the generalized charge susceptibility acquires a typical "onion"-structure. Beyond this qualitative feature, the value of T_K can be extracted for large interaction values, by a precise condition on the lowest frequency entries of $\tilde{\chi}_c^{\nu\nu'}$: $\tilde{\chi}^D = \tilde{\chi}^O$, where $\tilde{\chi}^D = T^2 \tilde{\chi}_c^{\pi T, \pi T}$ and $\tilde{\chi}^O = T^2 \tilde{\chi}_c^{\pi T, -\pi T}$. We note in passing, that a practical quality of this criterion resides in the possibility of performing a bisection.

Since the singularity of the innermost 2×2 submatrix of $\tilde{\chi}_c^{\nu\nu'}$ is a precise reference-point on the two-particle level, T_K can be obtained either by a scan in temperature for fixed interaction values (as shown in the lower panel of Fig. 4.3), or vice versa. The second possibility is shown in Fig. A.4, where the temperature is fixed to $T = 1/80 = 0.0125$, and the interaction value is varied in a broad range. By monitoring the value of $\tilde{\chi}^D - \tilde{\chi}^O$ (black
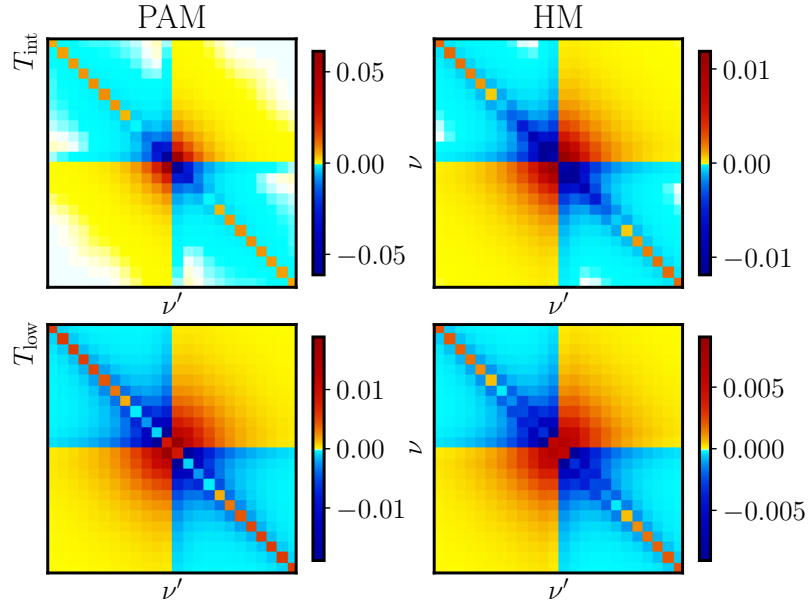
Figure A.2: Comparison of the frequency structure of $T^2 \tilde{\chi}^{\nu\nu'}$ for the PAM (left column) and the HM (right column). At intermediate temperatures $T_{\text{int}} > T_K$ (top panels) one observes the local moment structure, described above for the AIM. The same holds for the $T_{\text{low}} \approx T_K$ regime (bottom panels), where one recognizes for both cases the characteristic "onion-structure".

line) as a function of U, one can readily identify the singularity of the 2×2 submatrix of $\tilde{\chi}_c^{\nu\nu'}$ (black triangle), see also the inset, where a zoom around U(T_K) (blue vertical line) is shown. The value U(T_K) refers in this context to the interaction value where T_K is equal to the temperature $T = 0.0125$.

As mentioned in Sec. 4.3, the condition $\tilde{\chi}^D = \tilde{\chi}^O$ turns out to be the most accurate one to match the value of T_K for large interaction values and low-temperatures. Here, we compare the criterion (*i*) $\tilde{\chi}^D = \tilde{\chi}^O$ to other reasonable low-frequency criteria one could think of, in particular (*ii*) $\tilde{\chi}^D = -\tilde{\chi}^O$ and (*iii*) $\tilde{\chi}^D = 0$. The results of this comparison are shown in Fig. A.5. The second singularity of the 2×2 submatrix, $\tilde{\chi}^D = -\tilde{\chi}^O$, is represented by the grey plus symbols. We note that, for high temperatures, this coincides with the singularity of the whole matrix $\tilde{\chi}_c^{\nu\nu'}$, which leads to the second vertex divergence observed in the AIM (orange divergence line, cf. Fig. 3.13 or 3.14). At the same time, the brown diamonds denote the parameter set where $\tilde{\chi}^D = 0$ holds, which lies in between (*i*) and (*ii*). As one notices readily in the inset shown in Fig. A.5, all these low-frequency criteria are fairly close to the Kondo temperature for large interaction values and low-temperatures. However they can be clearly distinguished from $\tilde{\chi}^D = \tilde{\chi}^O$, which lies *on-top* of T_K.
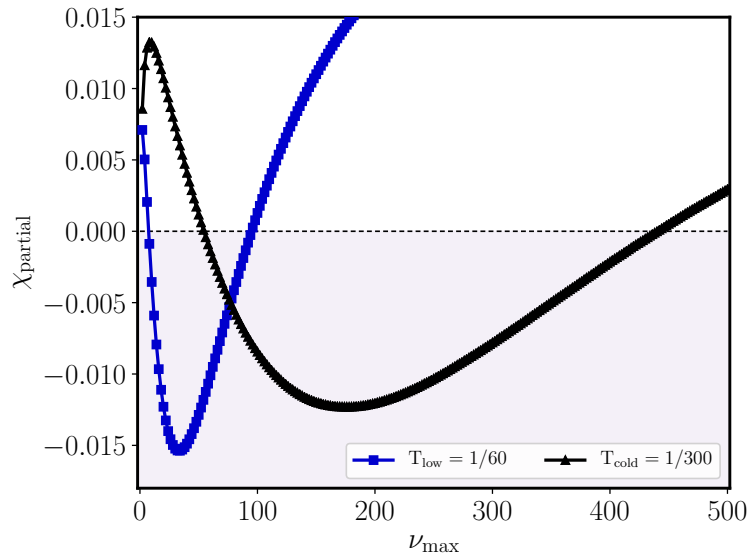
Figure A.3: Result of a partial summation of $\tilde{\chi}_c^{\nu\nu'}$ of the AIM, as in Fig. 4.4 for $U = 5.75$, but for $T_{\text{cold}} = 1/300 \ll T_K$. As a comparison, also the result for $T_{\text{low}} \gtrsim T_K$ of Fig. 4.4 is reproduced.
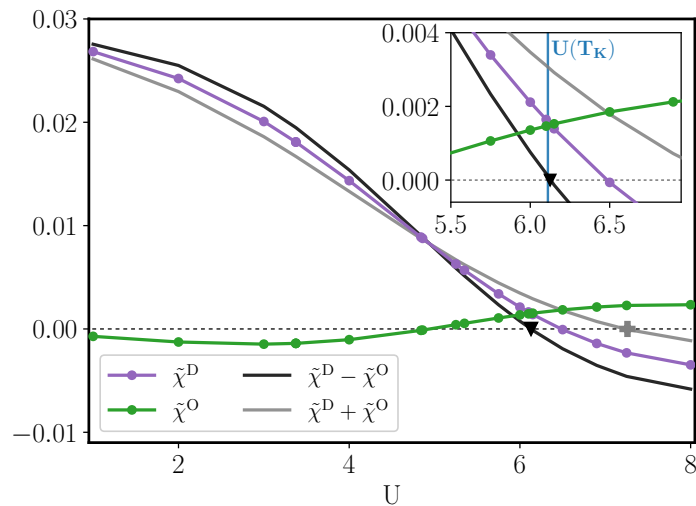

Figure A.4: Behaviour of $\tilde{\chi}^D$ (violet) and $\tilde{\chi}^O$ (green) as a function of U for $T = 0.0125$ for the AIM. The black line represents the first eigenvalue of the 2×2 submatrix of $\tilde{\chi}_c^{\nu\nu'}$ ($\tilde{\chi}^D - \tilde{\chi}^O$), which is singular (black triangle) closely to $U(T_K)$. The second low-frequency criterion obtained from the second eigenvalue ($\tilde{\chi}^D + \tilde{\chi}^O$) is shown as a grey line.
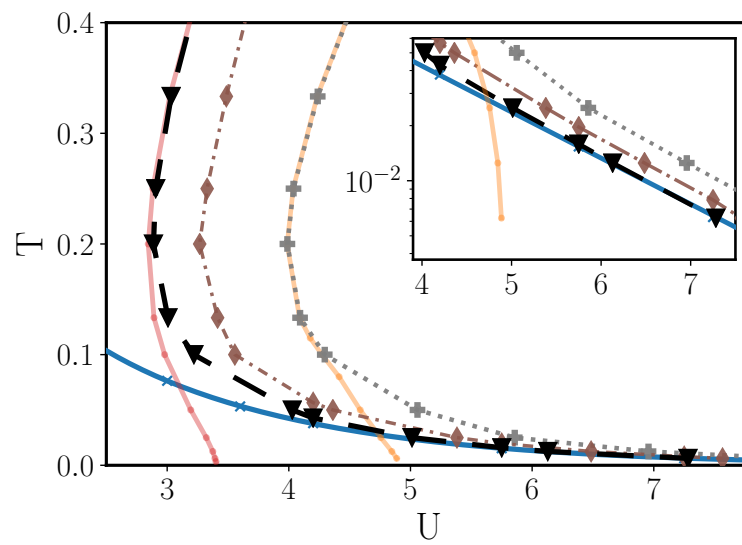
Figure A.5: $T - U$ diagram of the AIM, the blue solid line represents the Kondo temperature T_K. Several low-frequency criteria are shown: (*i*) $\tilde{\chi}^D = \tilde{\chi}^O$ (black triangles), (*ii*) $\tilde{\chi}^D = -\tilde{\chi}^O$ (grey plus symbols) and (*iii*) $\tilde{\chi}^D = 0$ (brown diamonds). Only the first criterion (*i*) lies on-top of T_K for large interaction values and low-temperatures, as discussed in the main part. The others are close, but not on-top, see the logarithmic inset. The first and the second vertex divergence line for the AIM are shown as red and orange line, respectively, which coincide with conditions (*i*) and (*ii*) for high-temperatures.
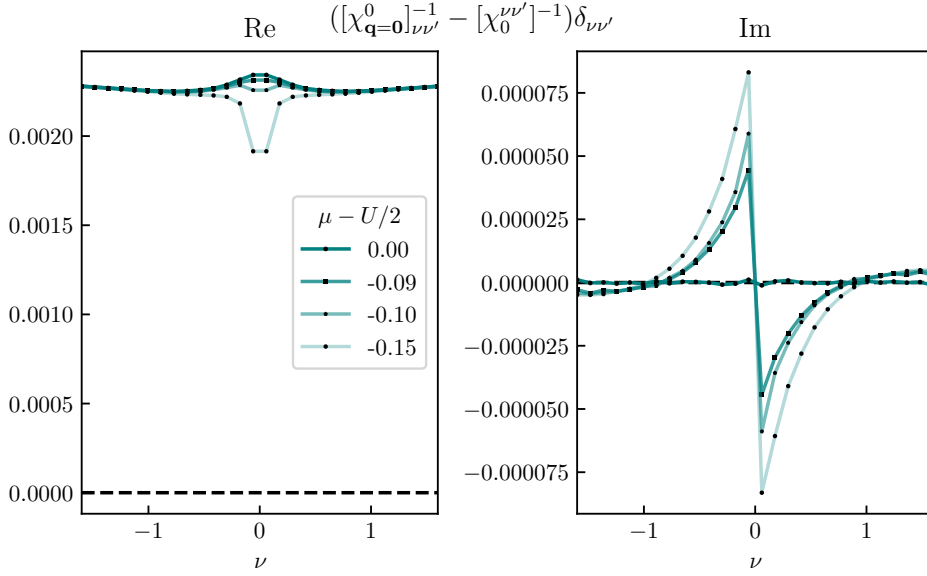
Figure A.6: The difference between the inverse of the static limit of the momentum dependent and the local bubble term ($[\chi^0_{\mathbf{q}=0}]^{-1}_{\nu\nu'} - [\chi^{-1}_0]^{\nu\nu'}$) at different chemical potential ($\mu - U/2$) and as function of fermionic Matsubara frequency ν, showing an almost constant behavior. Left: real part. Right: imaginary part.

A.2 Additional considerations for Chapter 5

*Parts of this chapter, marked by a vertical bar, have already been published in the APS journal Phys. Rev. Lett. **125**, 196403 (2020) and the corresponding supplemental material.*

A.2.1 Square lattice

As discussed in the main text, the results for the one-band Hubbard model on a square lattice can be readily understood using Eq. (5.12) of the main text, where $t^2 \to t^2_{\text{eff}}$. In this section we discuss the validity of this approach for our parameter set.

In Sec. 5.2.1 we demonstrated that the term $[\chi^0_{\mathbf{q}=0}]^{-1}_{\nu\nu'} - [\chi^{-1}_0]^{\nu\nu'}$ of Eq. 5.5 is equal to the constant $\frac{t^2}{2\beta}\delta_{\nu\nu'}$ for the Bethe-lattice (cf. Eq. (5.11)). Using the approximation $t^2 \to t^2_{\text{eff}}$ hence boils down to assuming that the difference of the **q**-dependent and local inverted bubble terms for the square lattice is constant in Matsubara frequency space. Furthermore, other than for the Bethe-lattice case, the difference of the inverted bubble terms is in principle also depending on the filling. The behaviour of $[\chi^0_{\mathbf{q}=0}]^{-1}_{\nu\nu'} - [\chi^{-1}_0]^{\nu\nu'}$ is explicitly shown in Fig. A.6 (we recall that this quantity only depends on one Matsubara frequency ν since both matrices are diagonal in the fermionic frequency space). The results of these calculations are illustrated in the upper panel of Fig. 5.5 of the main text. There, for each μ, the variation of the real part of $[\chi^0_{\mathbf{q}=0}]^{-1}_{\nu\nu'} - [\chi^{-1}_0]^{\nu\nu'}$ as a function of Matsubara frequency ν is represented by the blue-shaded area. It can clearly be seen that this variation is small with respect to the difference of the two lowest real eigenvalues of $\chi^{\nu\nu'(\omega=0)}_c$ (which are central to our study). This allows us to restrict the analysis of the phase-separation instability in DMFT
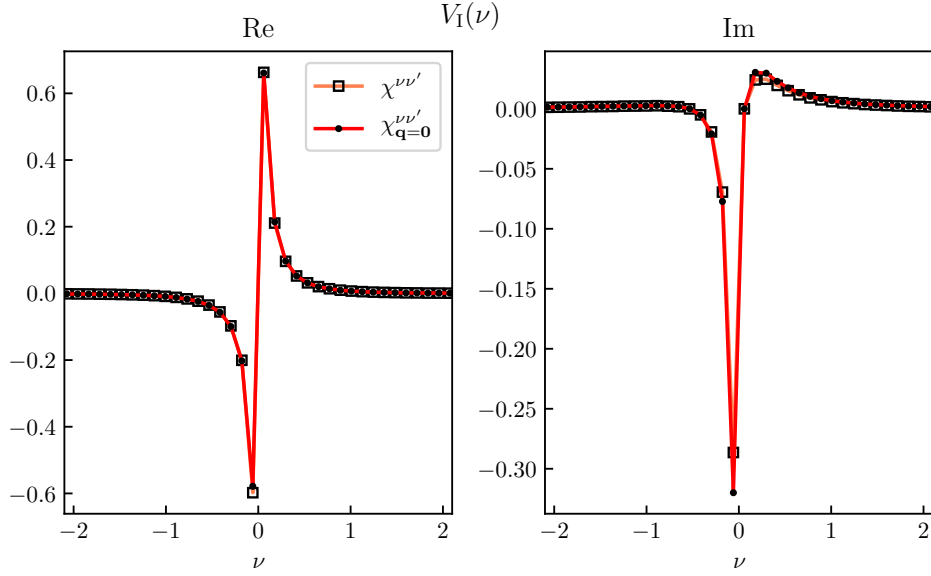
Figure A.7: Comparison of the eigenvectors $V_I(\nu)$ of the lowest real eigenvalue of $\chi_c^{\nu\nu'}(= \chi^{\nu\nu'})$ and $\chi_{\mathbf{q=0}}^{\nu\nu'}$ at the maximum of κ ($U = 2.4, \beta = 53, \mu - U/2 = -0.1$). Left: real part. Right: imaginary part.

to the lowest eigenvalue λ_I. In the right panel of Fig. A.6 one can also clearly see that the imaginary part (zero in the Bethe lattice case) is nonzero, but vanishingly small and therefore negligible. These considerations demonstrate that using Eq. (5.12) of the main text as a basis for the explanation is a valid approach.

This assessment can be further strengthened by comparing the eigenvectors $V_i(\nu)$ of the local $\chi_c^{\nu\nu'(\omega=0)}$ and the uniform generalized charge susceptibility $\chi_{\mathbf{q=0}}^{\nu\nu'(\omega=0)}$, where $\kappa = \frac{1}{\beta^2} \sum_{\nu\nu'} \chi_{\mathbf{q=0}}^{\nu\nu'(\omega=0)}$. The comparison is made for the parameters corresponding to the maximum of κ and focused on the eigenvector corresponding to λ_I, i.e. the eigenvector associated to the most negative eigenvalue of $\chi_{\mathbf{q=0}}^{\nu\nu'(\omega=0)}$ (as discussed in the main text). A perfect agreement of the two eigenvectors is obviously only found in the Bethe-lattice case, but as it is shown in Fig. A.7, also for the square lattice the agreement is very convincing.

In this context, where one restricts the analysis to the lowest eigenvalues of $\chi_c^{\nu\nu'(\omega=0)}$, it is possible to provide a precise definition of $\beta t_{\text{eff}}^2/2$: For each value of μ, we determine the value of $\widetilde{\lambda}_I$, that *would* trigger $\kappa(\widetilde{\lambda}_I \in \mathbb{R}) \to \infty$ by using the BSE (Eq. (5.5)). Then the value of t_{eff} is determined from: $1/\widetilde{\lambda}_I - \beta t_{\text{eff}}^2/2 = 0$.

This definition is used to mark the blue dashed line in the upper panel of Fig. 5.5 of the main text. Evidently the physical maximum of κ corresponds to the minimal difference between λ_I and the value of $-2/(\beta t_{\text{eff}}^2)$. Since λ_I never reaches this condition, we confirm our statement in the main text that for $\beta = 53, U = 2.4$ we are just slightly above the onset of the phase separation (see further section II of the supplemental material of Ref. [67]). It is interesting to note that the value $\beta t_{\text{eff}}^2/2$ corresponds, with a satisfying level of agreement to the value of $[\chi_{\mathbf{q=0}}^0]_{\nu\nu'}^{-1} - [\chi_0^{\nu\nu'}]^{-1}$ for the lowest Matsubara frequency (not shown). This is consistent with the observation that the eigenvector $V_I(\nu)$ of λ_I (see Fig. A.8 below) is
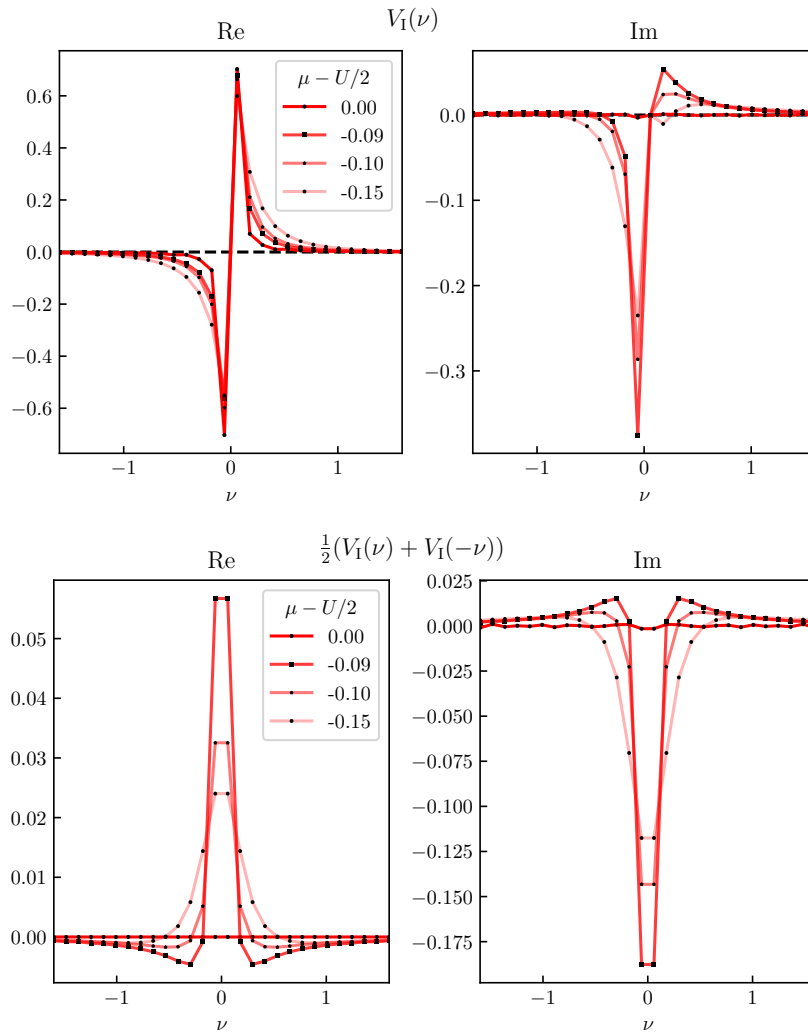
Figure A.8: Upper: Gradual evolution of the eigenvector $V_{\mathrm{I}}(\nu)$, corresponding to λ_{I}, from half filling ($\mu - U/2 = 0$) to finite doping ($\mu - U/2 = -0.15$). Lower: Evolution of the symmetrized eigenvector $\frac{1}{2}(V_{\mathrm{I}}(\nu) + V_{\mathrm{I}}(-\nu))$, corresponding to λ_{I}, highlighting the antisymmetry of $V_{\mathrm{I}}(\nu)$ at half filling. At finite doping, the condition $V_{\mathrm{I}}(\nu) = -V_{\mathrm{I}}(-\nu)$ is violated, and the symmetrized eigenvector shows non-zero values. Left: corresponding real parts. Right: corresponding imaginary parts.

extremely localized in the frequency domain.

As both, the overall frequency dependence and the μ-dependence are weak compared to $|\lambda_{\mathrm{I}} - \lambda_{\mathrm{II}}|$ the approximation based on the Bethe-lattice expression works reasonably well for the square lattice. As a result, the fulfilment of the condition for the enhancement/divergence of κ matches to a good approximation the minimum value of λ_{I}.

A.2.2 Correspondence with vertex divergences

In this section we demonstrate that the eigenvalues λ_{I} and λ_{II}, discussed in the main text, are directly related to the first and second vertex divergence lines of the Hubbard model, respectively (line I and II in Fig. 5.2 of the main text).

A first indication is the smooth behaviour of $\lambda_{\mathrm{I/II}}$ and $w_{\mathrm{I/II}}$, seen in Fig. 5.5. Nevertheless,
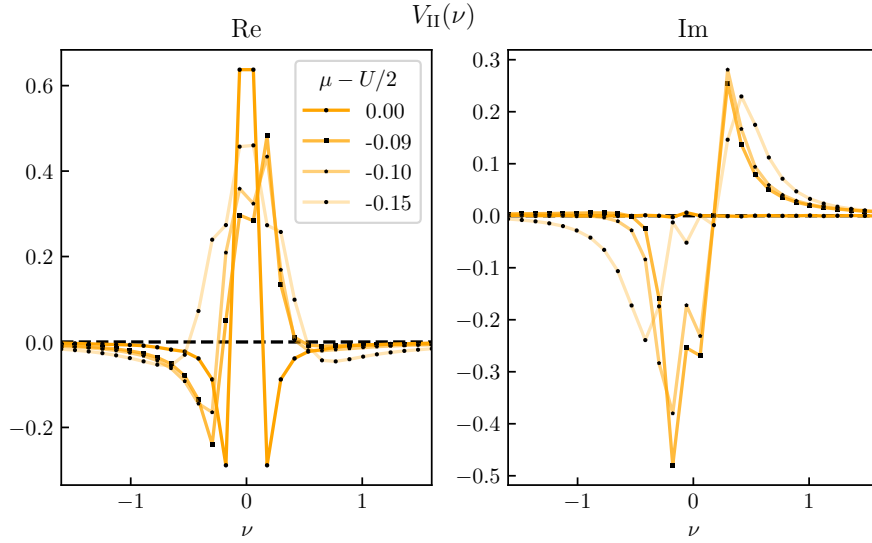
Figure A.9: Gradual evolution of the eigenvector $V_{\mathrm{II}}(\nu)$, corresponding to λ_{II}, from half filling ($\mu - U/2 = 0$) to finite doping ($\mu - U/2 = -0.15$). Left: real part. Right: imaginary part.

to make a definite connection, we study the continuous evolution of the eigenvectors $V_{\mathrm{I/II}}(\nu)$ (corresponding to the eigenvalues $\lambda_{\mathrm{I/II}}$) of the local charge susceptibility $\chi_c^{\nu\nu'(\omega=0)}$ as a function of filling, see Fig. A.8 and A.9. As stated in the main text, at half filling, i.e. $\mu - U/2 = 0.0$, $\chi_c^{\nu\nu'(\omega=0)}$ is a real, bisymmetric matrix. This implies [26] that the eigenvectors $V_{\mathrm{I/II}}(\nu)$ are real and either symmetric, or antisymmetric, with respect to $\nu \leftrightarrow -\nu$ (see Secs. 2.2.4.1 and 3.1.2). Fig. A.8 readily shows that the real part of $V_{\mathrm{I}}(\nu)$ is antisymmetric at half filling (left panels), whereas the imaginary part is vanishing (right panels). The same holds for $V_{\mathrm{II}}(\nu)$ (see Fig. A.9), whereas it is symmetric at half filling. As discussed in several works [22, 23, 26] on the appearance of vertex divergences in fundamental models of many-electrons systems, the first divergence line is associated with an antisymmetric eigenvector, the second line with a symmetric one (cf. Sec. 3.1). For high- and intermediate temperatures [19, 22, 26] the eigenvector of the first divergence line resembles the one of the atomic limit [19, 23] ($\frac{1}{\sqrt{2}}(\delta_{\nu\bar{\nu}} - \delta_{\nu\bar{\nu}})$), where $\bar{\nu} = \pi T$ (cf. Sec. 3.1.1.1). This is clearly recognizable in Fig. A.8. On the other hand the eigenvector of the second divergence line [22, 26] has similarities with the symmetric combination ($\frac{1}{\sqrt{2}}(\delta_{\nu\bar{\nu}} + \delta_{\nu\bar{\nu}})$) (cf. Fig. 3.17), also apparent in Fig. A.9. Hence, the eigenvalues λ_{I} and λ_{II} and their corresponding eigenvectors $V_{\mathrm{I}}(\nu)$ and $V_{\mathrm{II}}(\nu)$ are those that also originate the divergence lines I and II at lower values of U at half filling.

As a last point, let us also point out the overall similarity between $V_{\mathrm{I/II}}(\nu)$ and the eigenvectors of the first two divergence lines in the charge channel of AIM out of half filling, see Fig. 3.22, which is an additional confirmation of the assessment made above.

A.2.3 Negative weights

In Sec. 2.2.4.2 the nature of the generalized susceptibility in the ph-channels for cases out of half filling was discussed in detail. As pointed out there, the eigenvalues can either be

real or form complex conjugate pairs, due to the centrohermitian property of $\chi_c^{\nu\nu'(\omega=0)}$ [72] (cf. Eq. (2.58)). At the same time, the corresponding weights are either real (non necessarily positive) or complex conjugates.

Hence, we briefly discuss, which terms originate the *negative* weights.

Focusing on the case of a real eigenvalue λ_I its real weight [67] reads:

$$
\begin{aligned}
w_I = {}& \mathrm{Re}\Big[\sum_\nu V_I^{-1}(\nu) \Big] \mathrm{Re}\Big[\sum_{\nu'} V_I(\nu') \Big] \\
& - \mathrm{Im}\Big[\sum_\nu V_I^{-1}(\nu) \Big] \mathrm{Im}\Big[\sum_{\nu'} V_I(\nu') \Big] ,
\end{aligned}
\tag{A.1}
$$

and is thus determined by both, the real as well as the imaginary part of the corresponding eigenvector. In the numerical calculations, both parts were found to yield negative contributions, where the imaginary part was found to be the dominant one (not shown), see further Ref. [73].
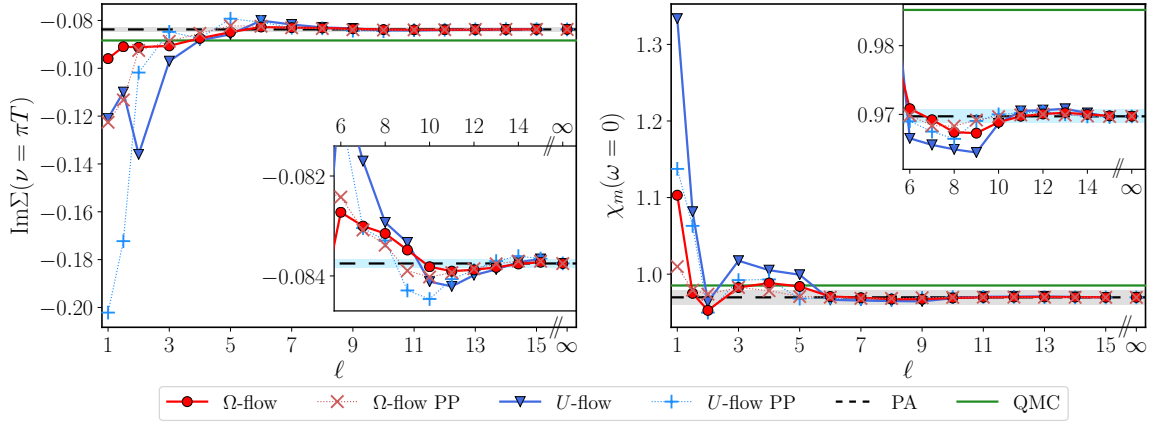
Figure A.10: $\text{Im}\Sigma(\nu = \pi T)$ and $\chi_m(\omega = 0)$ as in Fig. 6.7 but for $U = 1.5$. Insets show a zoom for $\ell \geq 6$. The gray (blue) area indicates 1% (0.1%) deviation from the PA.

A.3 Additional results for Chapter 6

Parts of this section, marked by a vertical bar, have already been published
*in the APS journal Phys. Rev. Research **4**, 023050 (2022)*

In this part we provide additional results for Chapter 6, especially calculations for $\beta = 5$ (Sec. A.3.1) and results for the U-flow (Sec. A.3.2), completing the discussion made in earlier sections.

In Fig. A.10, we report the results for $U = 1.5$ ($\beta = 10$, half-filling), which were anticipated in Sec. 6.3.3. For this parameter set, too, the mfRG scheme converges perfectly in loop order. For $\ell \geq 15$, both regulators lead to identical results for all quantities, and the PP (dotted lines with '$\times$' or '$+$' symbols) and flowing data coincide. As stated in the main text, no qualitative difference in the convergence behavior is observed, apart from the fact that, for $U = 1.5$, more loop orders are necessary to reach it.

A.3.1 β=5

In Fig. A.11 we show a direct comparison of $\beta = 5$ and $\beta = 10$ data, obtained from Ω-flow calculations with respect to the corresponding PA solution for $U = 2$. The plot is done in a similar fashion as Fig. 6.9. Also for the higher temperature $\beta = 5$ one finds multiloop oscillations. Surprisingly, not only the "node"-structure remains the same, but also the amplitude of the oscillations seems to be almost temperature independent. We note, however, that this comparison was only done for a quantitatively different temperature, not one where a qualitatively different physical situation is to be expected.

A.3.2 U-flow

In Fig. A.12, the relative comparison between U-flow results and the PA for $U = 1, 1.5, 2$ is shown in the same fashion as in Fig. 6.9 for the Ω-flow. While there is no qualitative difference, quantitatively the U-flow shows larger relative differences with respect to the

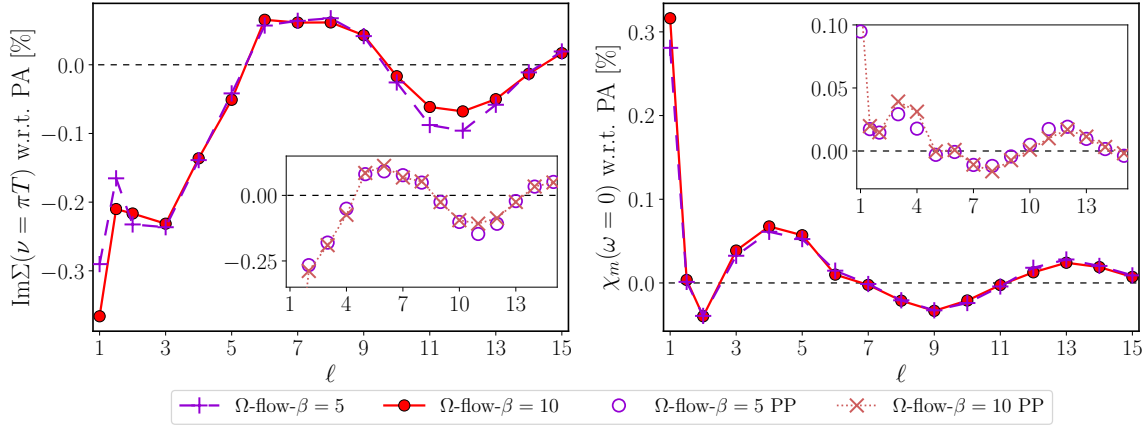Figure A.11: Ω-flow calculations for different loop orders for $\beta = 5$ (violet) and $\beta = 10$ (red) at $U = 2$. Each data set is shown in comparison with the corresponding PA result, similarly as in Fig. 6.9. The PP data is shown in the insets.
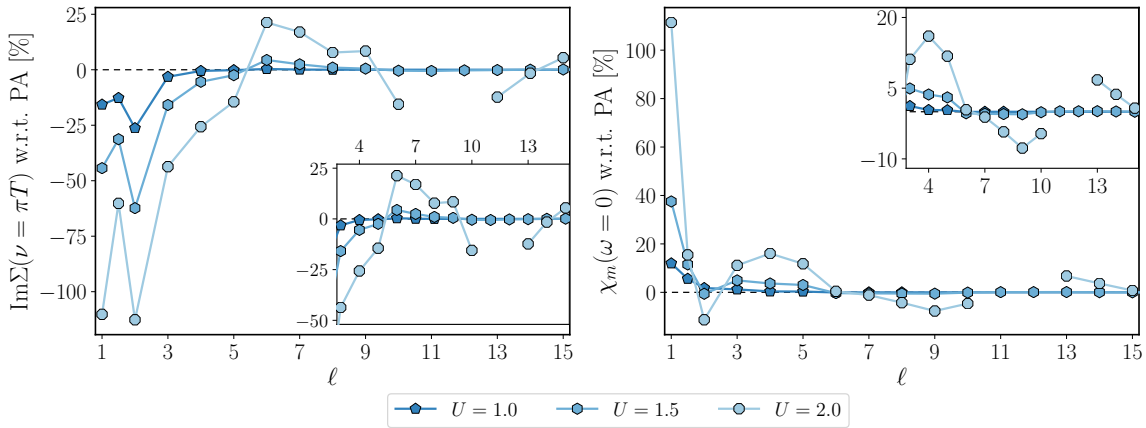

Figure A.12: Relative difference between U-flow mfRG calculations and the corresponding PA solutions for $\text{Im}\Sigma(\nu = \pi T)$ (left) and $\chi_m(\omega = 0)$ (right), as a function of loop order ℓ and different values of the interaction U, as in Fig. 6.9. Insets show a zoom for $\ell \geq 3$.

PA. Note that we were unable to converge the U-flow calculation for $\ell = 11, 12$; see further Ref. [215].

In Figs. A.13–A.15, we show the "breathing" of the restfunction for the U-flow in the same way as shown in Sec. 6.3.4 for the Ω-flow. The trend, as already anticipated in the corresponding section, continues to the restfunction. For high loop orders, qualitatively the same "breathing" is observed, with quantitatively larger amplitudes of the multiloop oscillations. At low loop order a sign change in $-K_{3m}^{U\text{-flow}}(\nu, \nu' = -\pi T, \omega = 0)$ is observed, which is absent in the PA result.
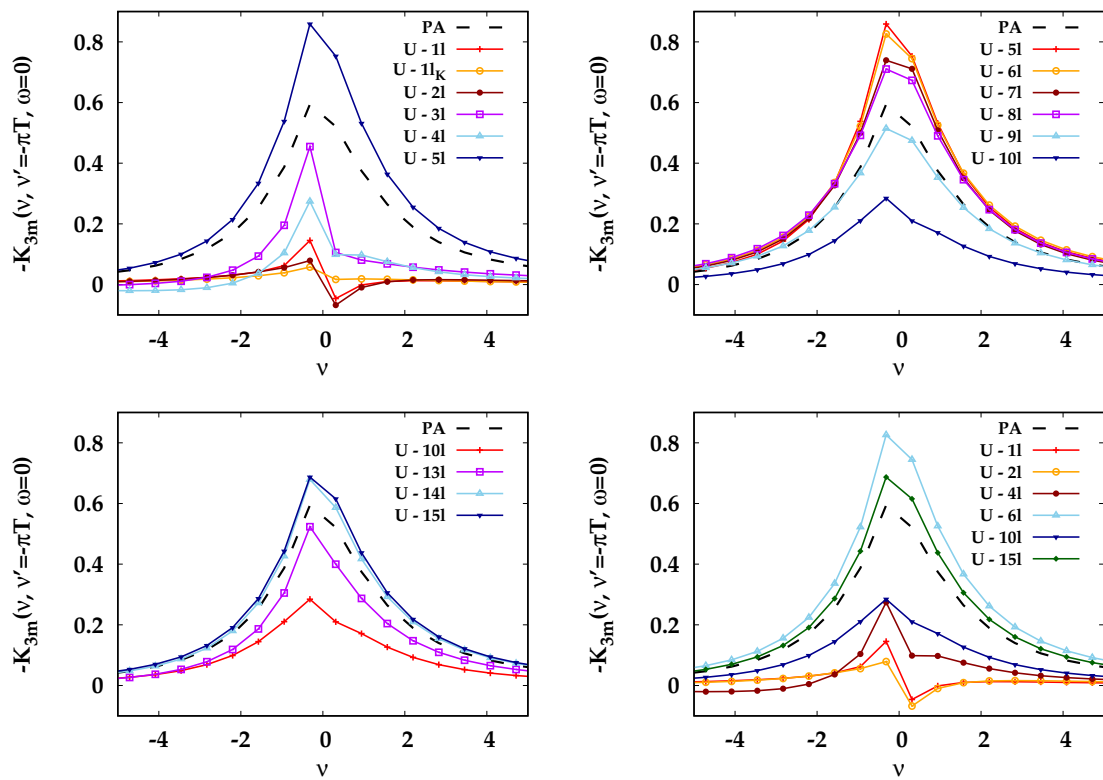
Figure A.13: As Fig. 6.10 for U-flow calculations. By comparing the two figures the larger amplitudes of the multiloop oscillations in the U-flow can be readily seen.
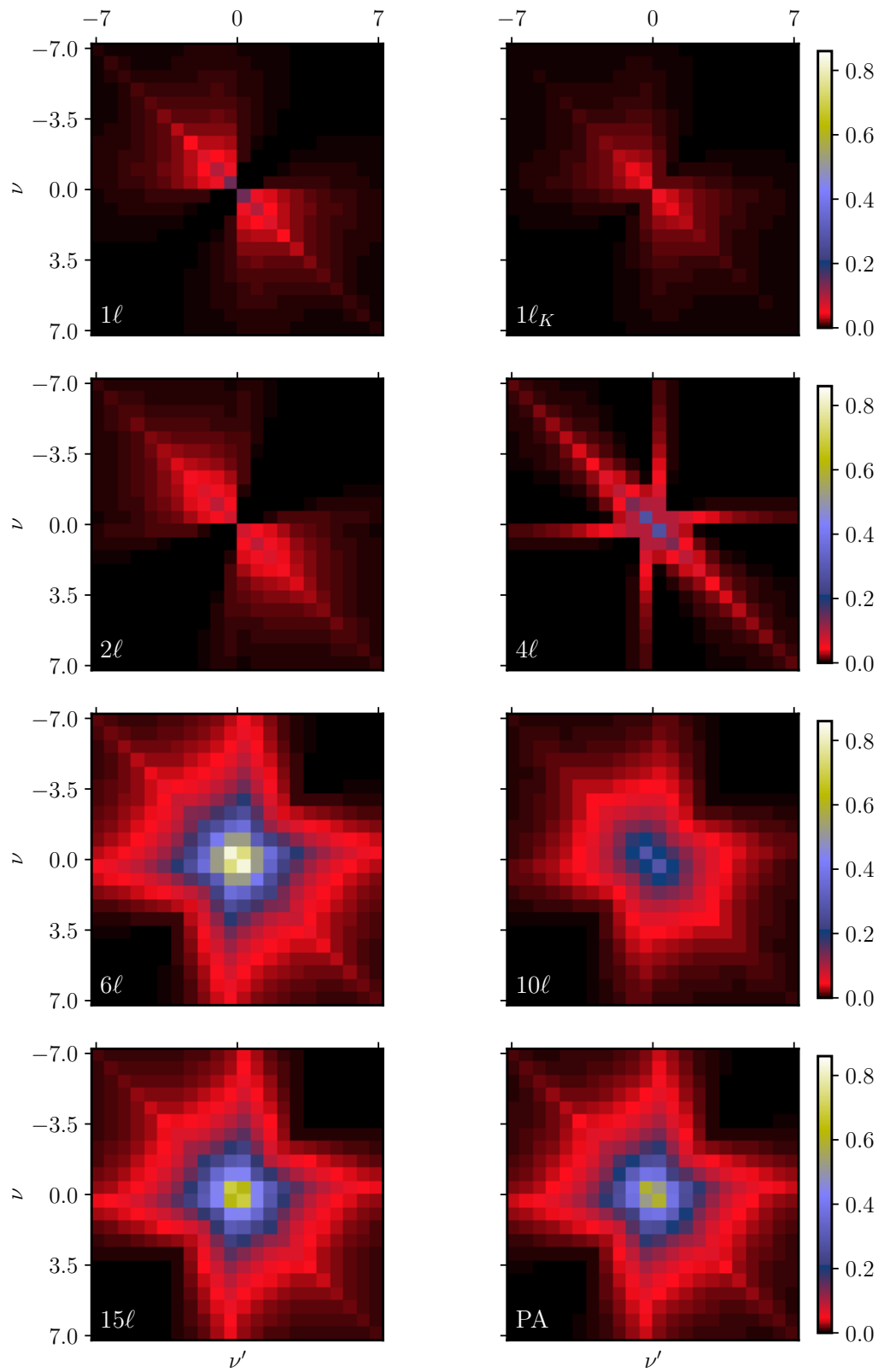
Figure A.14: *U*-flow results for $-K_{3m}(\nu, \nu', \omega = 0)$ as a function of ν and ν', as for Fig. 6.11 for the Ω-flow. The color map is optimized to highlight the small value ranges.
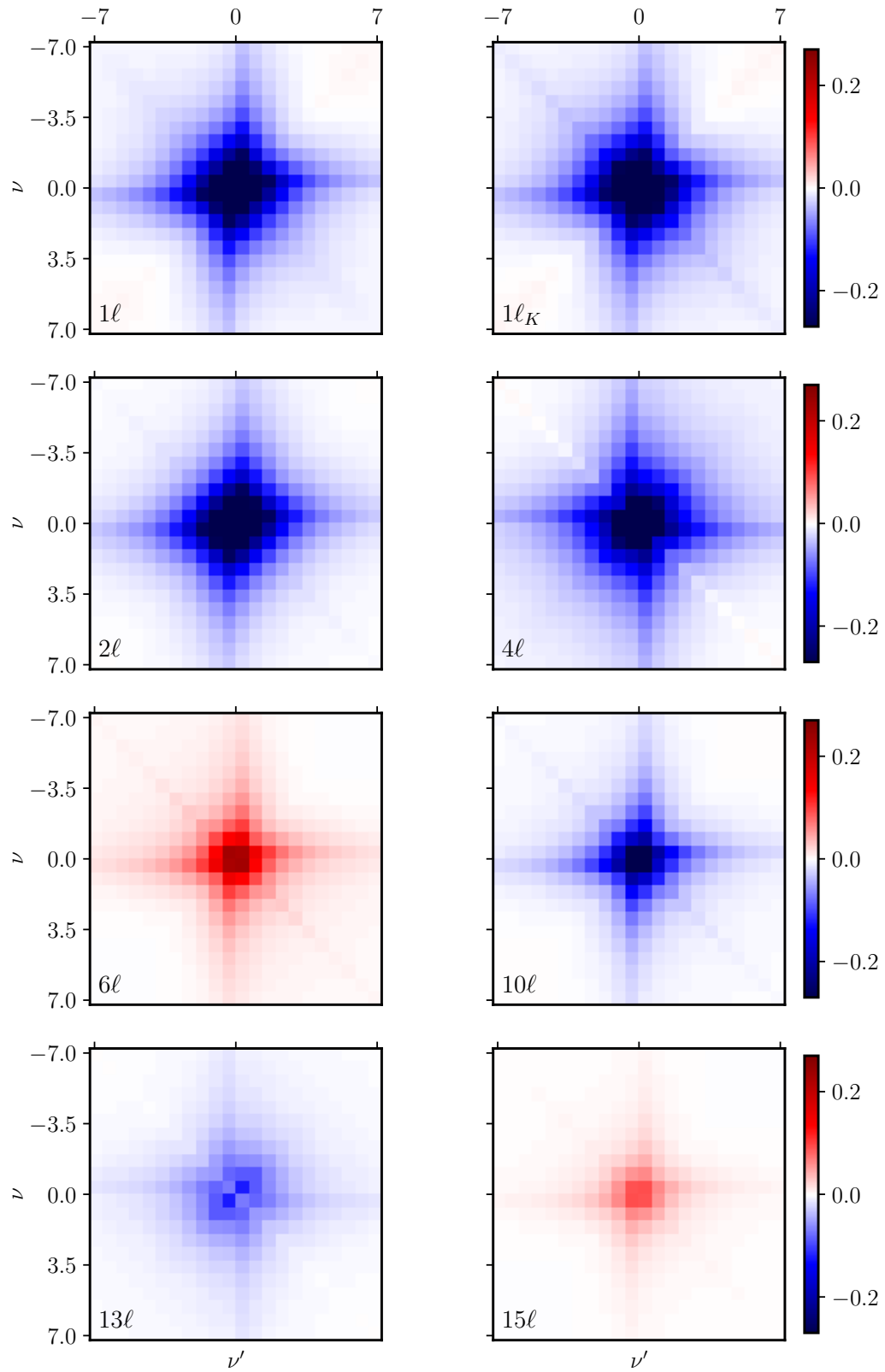
Figure A.15: As Fig. A.14, showing the difference between U-flow calculations with different loop orders and the PA result, i.e. $-K_{3m}^{U-\text{flow}}(\nu, \nu', \omega = 0) + K_{3m}^{\text{PA}}(\nu, \nu', \omega = 0)$.

Bibliography

[1]   Anderson, P. W. More Is Different. *Science* **177,** 393–396 (1972).

[2]   Dagotto, E. Complexity in Strongly Correlated Electronic Systems. *Science* **309,** 257–262 (2005).

[3]   Lee, P. A., Nagaosa, N. & Wen, X.-G. Doping a Mott insulator: Physics of high-temperature superconductivity. *Rev. Mod. Phys.* **78,** 17–85 (2006).

[4]   Bednorz, J. G. & Müller, K. A. Possible high T_C superconductivity in the Ba–La–Cu–O system. *Zeitschrift für Physik B Condensed Matter* **64,** 189–193 (1986).

[5]   Chubukov, A. & Hirschfeld, P. J. Iron-based superconductors, seven years later. *Physics Today* **68,** 46–52 (2015).

[6]   Abrikosov, A. A., Gorkov, L. P. & Dzyaloshinski, I. E. Methods of Quantum Field Theory in Statistical Physics (Dover, New York, 1975).

[7]   Zagoskin, A. M. Quantum Theory of Many-Body Systems (eds Birman, J. L., Lynn, J. W., Silverman, M. P., Stanley, H. E. & Voloshin, M.) (Springer-Verlag New York, Inc., 1998).

[8]   Mahan, G. D. Many-Particle Physics (Kluwer Academic/Plenum Publishers, New York, 2000).

[9]   Coleman, P. Introduction to Many-Body Physics (Cambridge University Press, 2015).

[10] Schäfer, T. *et al.* Divergent Precursors of the Mott-Hubbard Transition at the Two-Particle Level. *Phys. Rev. Lett.* **110,** 246405 (2013).

[11] Kozik, E., Ferrero, M. & Georges, A. Nonexistence of the Luttinger-Ward Functional and Misleading Convergence of Skeleton Diagrammatic Series for Hubbard-Like Models. *Phys. Rev. Lett.* **114,** 156402 (2015).

[12] Gunnarsson, O., Rohringer, G., Schäfer, T., Sangiovanni, G. & Toschi, A. Breakdown of Traditional Many-Body Theories for Correlated Electrons. *Phys. Rev. Lett.* **119,** 056402 (2017).

[13] Janiš, V. & Pokorný, V. Critical metal-insulator transition and divergence in a two-particle irreducible vertex in disordered and interacting electron systems. *Phys. Rev. B* **90,** 045143 (2014).

[14] Stan, A., Romaniello, P., Rigamonti, S., Reining, L. & Berger, J. A. Unphysical and physical solutions in many-body theories: from weak to strong correlation. *New J. Phys.* **17,** 093045 (2015).

[15] Rossi, R. & Werner, F. Skeleton series and multivaluedness of the self-energy functional in zero space-time dimensions. *Journal of Physics A: Mathematical and Theoretical* **48,** 485202 (2015).

[16] Rossi, R., Werner, F., Prokof'ev, N. & Svistunov, B. Shifted-action expansion and applicability of dressed diagrammatic schemes. *Phys. Rev. B* **93,** 161102 (2016).

[17] Ribic, T., Rohringer, G. & Held, K. Nonlocal correlations and spectral properties of the Falicov-Kimball model. *Phys. Rev. B* **93,** 195105 (2016).

[18] Gunnarsson, O. *et al.* Parquet decomposition calculations of the electronic self-energy. *Phys. Rev. B* **93,** 245102 (2016).

[19] Schäfer, T. *et al.* Non-perturbative landscape of the Mott-Hubbard transition: Multiple divergence lines around the critical endpoint. *Phys. Rev. B* **94,** 235108 (2016).

[20] Tarantino, W., Romaniello, P., Berger, J. A. & Reining, L. Self-consistent Dyson equation and self-energy functionals: An analysis and illustration on the example of the Hubbard atom. *Phys. Rev. B* **96,** 045124 (2017).

[21] Vučičević, J., Wentzell, N., Ferrero, M. & Parcollet, O. Practical consequences of the Luttinger-Ward functional multivaluedness for cluster DMFT methods. *Phys. Rev. B* **97,** 125141 (2018).

[22] Chalupa, P., Gunacker, P., Schäfer, T., Held, K. & Toschi, A. Divergences of the irreducible vertex functions in correlated metallic systems: Insights from the Anderson impurity model. *Phys. Rev. B* **97,** 245136 (2018).

[23] Thunström, P., Gunnarsson, O., Ciuchi, S. & Rohringer, G. Analytical investigation of singularities in two-particle irreducible vertex functions of the Hubbard atom. *Phys. Rev. B* **98,** 235107 (2018).

[24] Kim, A. J. & Sacksteder, V. Multivaluedness of the Luttinger-Ward functional in the fermionic and bosonic system with replicas. *Phys. Rev. B* **101,** 115146 (2020).

[25] Melnick, C. & Kotliar, G. Fermi-liquid theory and divergences of the two-particle irreducible vertex in the periodic Anderson lattice. *Phys. Rev. B* **101,** 165105 (2020).

[26] Springer, D., Chalupa, P., Ciuchi, S., Sangiovanni, G. & Toschi, A. Interplay between local response and vertex divergences in many-fermion systems with on-site attraction. *Phys. Rev. B* **101,** 155148 (2020).

[27] Kim, A. J., Werner, P. & Kozik, E. Strange Metal Solution in the Diagrammatic Theory for the 2d Hubbard Model. 2020. arXiv: `2012.06159 [cond-mat.str-el]`.

[28] Houcke, K. V., Kozik, E., Rossi, R., Deng, Y. & Werner, F. Physical and unphysical regimes of self-consistent many-body perturbation theory. 2021. arXiv: `2102.04508 [cond-mat.str-el]`.

[29] Chalupa, P. Irreducible vertex divergences in strongly correlated metallic systems : the case of the Anderson impurity model. MA thesis (TU Wien, 2017).

[30] Hewson, A. The Kondo Problem to Heavy Fermions (Cambridge University Press, 1993).

[31] Martin, R. M., Reining, L. & Ceperley, D. M. Interacting Electrons: Theory and Computational Approaches (Cambridge University Press, 2016).

[32] Anderson, P. W. Localized Magnetic States in Metals. *Phys. Rev.* **124,** 41–53 (1961).

[33] Rohringer, G., Valli, A. & Toschi, A. Local electronic correlation at the two-particle level. *Phys. Rev. B* **86,** 125114 (2012).

[34] Kondo, J. Resistance Minimum in Dilute Magnetic Alloys. *Progress of Theoretical Physics* **32,** 37–49 (1964).

[35] Abrikosov, A. A. Electron scattering on magnetic impurities in metals and anomalous resistivity effects. *Physics Physique Fizika* **2,** 5–20 (1965).

[36] Anderson, P. W. A poor man's derivation of scaling laws for the Kondo problem. *Journal of Physics C: Solid State Physics* **3,** 2436–2441 (1970).

[37] Wilson, K. G. The renormalization group: Critical phenomena and the Kondo problem. *Rev. Mod. Phys.* **47,** 773–840 (1975).

[38] Nozières, P. A "fermi-liquid" description of the Kondo problem at low temperatures. *Journal of Low Temperature Physics* **17,** 31–42 (1974).

[39] Krishna-murthy, H. R., Wilson, K. G. & Wilkins, J. W. Temperature-Dependent Susceptibility of the Symmetric Anderson Model: Connection to the Kondo Model. *Phys. Rev. Lett.* **35,** 1101–1104 (1975).

[40] Krishna-murthy, H. R., Wilkins, J. W. & Wilson, K. G. Renormalization-group approach to the Anderson model of dilute magnetic alloys. I. Static properties for the symmetric case. *Phys. Rev. B* **21,** 1003–1043 (1980).

[41] Georges, A., Kotliar, G., Krauth, W. & Rozenberg, M. J. Dynamical mean-field theory of strongly correlated fermion systems and the limit of infinite dimensions. *Rev. Mod. Phys.* **68,** 13 (1996).

[42] Bruus, H. & Flensberg, K. Many-body quantum theory in condensed matter physics: an introduction (Oxford Univ. Pr., Oxford, 2006).

[43] Borzenets, I. *et al.* Observation of the Kondo screening cloud. *Nature* **579,** 210–213 (2020).

[44] Schäfer, T., Katanin, A. A., Kitatani, M., Toschi, A. & Held, K. Quantum Criticality in the Two-Dimensional Periodic Anderson Model. *Phys. Rev. Lett.* **122,** 227201 (2019).

[45] Hubbard, J. Electron Correlations in Narrow Energy Bands. *Proceedings of the Royal Society of London. Series A, Mathematical and Physical Sciences* **276,** 238–257 (1963).

[46] Kanamori, J. Electron correlation and ferromagnetism of transition metals. *Progress of Theoretical Physics* **30,** 275–289 (1963).

[47] Gutzwiller, M. C. Effect of Correlation on the Ferromagnetism of Transition Metals. *Phys. Rev. Lett.* **10,** 159–162 (1963).

[48] The Hubbard Model - A Reprint Volume (ed Montorsi, A.) (World Scientific, Singapore, 1992).

[49] DMFT: From Infinite Dimensions to Real Materials (eds Pavarini, E., Koch, E., Lichtenstein, A. & Vollhardt, D.) ISBN: 978-3-95806-313-6. https://juser.fz-juelich.de/record/852559 (Forschungszentrum Jülich GmbH Zentralbibliothek, Verlag, Jülich, 2018).

[50] LeBlanc, J. P. F. *et al.* Solutions of the Two-Dimensional Hubbard Model: Benchmarks and Results from a Wide Range of Numerical Algorithms. *Phys. Rev. X* **5,** 041041 (2015).

[51] Rohringer, G. *et al.* Diagrammatic routes to nonlocal correlations beyond dynamical mean field theory. *Rev. Mod. Phys.* **90,** 025003 (2018).

[52] Schäfer, T. *et al.* Tracking the Footprints of Spin Fluctuations: A MultiMethod, MultiMessenger Study of the Two-Dimensional Hubbard Model. *Phys. Rev. X* **11,** 011058 (2021).

[53] Qin, M., Schäfer, T., Andergassen, S., Corboz, P. & Gull, E. The Hubbard model: A computational perspective. 2021.

[54] Rohringer, G. New routes towards a theoretical treatment of nonlocal electronic correlations. PhD thesis (Vienna University of Technology, 2013).

[55] Bickers, N. Theoretical Methods for Strongly Correlated Electrons (eds Sénéchal, D., Tremblay, A.-M. & Bourbonnais, C.) 237–296 (Springer-Verlag New York Berlin Heidelberg, 2004).

[56] Krien, F. *et al.* Conservation in two-particle self-consistent extensions of dynamical mean-field theory. *Phys. Rev. B* **96,** 075155 (2017).

[57] Krien, F., van Loon, E. G. C. P., Katsnelson, M. I., Lichtenstein, A. I. & Capone, M. Two-particle Fermi liquid parameters at the Mott transition: Vertex divergences, Landau parameters, and incoherent response in dynamical mean-field theory. *Phys. Rev. B* **99,** 245128 (2019).

[58] Rohringer, G. Spectra of correlated many-electron systems: From a one- to a two-particle description. *Journal of Electron Spectroscopy and Related Phenomena* **241,** 146804 (2020).

[59] Schäfer, T. & Toschi, A. How to read between the lines of electronic spectra: the diagnostics of fluctuations in strongly correlated electron systems. *Journal of Physics: Condensed Matter* **33,** 214001 (2021).

[60] Toschi, A., Arita, R., Hansmann, P., Sangiovanni, G. & Held, K. Quantum dynamical screening of the local magnetic moment in Fe-based superconductors. *Phys. Rev. B* **86,** 064411 (2012).

[61] Watzenböck, C., Edelmann, M., Springer, D., Sangiovanni, G. & Toschi, A. Characteristic Timescales of the Local Moment Dynamics in Hund's Metals. *Phys. Rev. Lett.* **125,** 086402 (2020).

[62] Watzenböck, C., Fellinger, M., Held, K. & Toschi, A. Long-term memory magnetic correlations in the Hubbard model: A dynamical mean-field theory analysis. *SciPost Phys.* **12,** 184 (2022).

[63] Gaspard, L. & Tomczak, J. M. Timescale of local moment screening across and above the Mott transition. 2021. arXiv: `2112.02881 [cond-mat.str-el]`.

[64] DMFT at 25: Infinite Dimensions (eds Pavarini, E., Koch, E., Vollhardt, D. & Lichtenstein, A.) ISBN: 978-3-89336-953-9. `https://juser.fz-juelich.de/record/155829` (Forschungszentrum Jülich Zentralbibliothek, Verlag (Jülich), Jülich, 2014).

[65] Held, K., Hörbiger, F., Kauch, A., Tomczak, J. & Toschi, A. Lecture notes of the quantum-field theory for many-particle systems course. IFP TU Wien. 2022.

[66] Wilcox, R. M. Bounds for the Isothermal, Adiabatic, and Isolated Static Susceptibility Tensors. *Phys. Rev.* **174,** 624–629 (1968).

[67] Reitner, M. *et al.* Attractive Effect of a Strong Electronic Repulsion: The Physics of Vertex Divergences. *Phys. Rev. Lett.* **125,** 196403 (2020).

[68] Chalupa, P. *et al.* Fingerprints of the Local Moment Formation and its Kondo Screening in the Generalized Susceptibilities of Many-Electron Problems. *Phys. Rev. Lett.* **126,** 056403 (2021).

[69] Weaver, J. R. Centrosymmetric (Cross-Symmetric) Matrices, Their Basic Properties, Eigenvalues, and Eigenvectors. *The American Mathematical Monthly* **92,** 711–717 (1985).

[70] Reid, R. M. Classroom Note: Some Eigenvalue Properties of Persymmetric Matrices. *SIAM Review* **39,** 313–316 (1997).

[71] Abu-Jeib, I. Centrosymmetric matrices: properties and an alternative approach. *The Canadian Applied Mathematics Quarterly* **10** (Jan. 2002).

[72] Lee, A. Centrohermitian and skew-centrohermitian matrices. *Linear Algebra and its Applications* **29.** Special Volume Dedicated to Alson S. Householder, 205–210 (1980).

[73] Reitner, M. Dychotomy between local and uniform compressibility in correlated systems: the role of the irreducible vertex. MA thesis (TU Wien, Wien, 2020).

[74] Luttinger, J. M. & Ward, J. C. Ground-State Energy of a Many-Fermion System. II. *Phys. Rev.* **118,** 1417–1427 (1960).

[75] Potthoff, M. Non-perturbative construction of the Luttinger-Ward functional. *Condensed Matter Physics* **9,** 557 (2006).

[76] Baym, G. & Kadanoff, L. P. Conservation Laws and Correlation Functions. *Phys. Rev.* **124,** 287–299 (1961).

[77] Janiš, V. & Vollhardt, D. Comprehensive mean-field theory for the Hubbard model. *International Journal of Modern Physics B* **06,** 731–747 (1992).

[78] Kotliar, G. & Vollhardt, D. Strongly Correlated Materials: Insights from Dynamical Mean-Field Theory. *Physics Today* **57,** 53 (2004).

[79] Vollhardt, D. Dynamical mean-field theory for correlated electrons. *Annalen der Physik* **524,** 1–19 (2012).

[80] Metzner, W. & Vollhardt, D. Correlated Lattice Fermions in $d = \infty$ Dimensions. *Phys. Rev. Lett.* **62,** 324–327 (Jan. 1989).

[81] Georges, A. & Kotliar, G. Hubbard model in infinite dimensions. *Phys. Rev. B* **45,** 6479–6483 (1992).

[82] Kotliar, G. *et al.* Electronic structure calculations with dynamical mean-field theory. *Rev. Mod. Phys.* **78,** 865 (2006).

[83] Held, K. Electronic structure calculations using dynamical mean field theory. *Advances in Physics* **56,** 829–926 (2007).

[84] Pelz, M. Investigation of the highly non-perturbative nature of the Mott-Hubbard metal insulator transition: Vertex divergences in the coexistence region. MA thesis (TU Wien, 2022).

[85] Wallerberger, M. *et al.* w2dynamics: Local one- and two-particle quantities from dynamical mean field theory. *Computer Physics Communications* **235,** 388–399 (2019).

[86] Gull, E. *et al.* Continuous-time Monte Carlo methods for quantum impurity models. *Rev. Mod. Phys.* **83,** 349 (2011).

[87] Gunacker, P. *et al.* Continuous-time quantum Monte Carlo using worm sampling. *Phys. Rev. B* **92,** 155102 (2015).

[88] Gunacker, P. *et al.* Worm-improved estimators in continuous-time quantum Monte Carlo. *Phys. Rev. B* **94,** 125153 (2016).

[89] Kaufmann, J., Gunacker, P., Kowalski, A., Sangiovanni, G. & Held, K. Symmetric improved estimators for continuous-time quantum Monte Carlo. *Phys. Rev. B* **100,** 075119 (2019).

[90] Yang, S. X. *et al.* Parquet approximation for the 4×4 Hubbard cluster. *Phys. Rev. E* **80,** 046706 (2009).

[91] Tam, K.-M. *et al.* Solving the parquet equations for the Hubbard model beyond weak coupling. *Phys. Rev. E* **87,** 013311 (2013).

[92] Li, G., Wentzell, N., Pudleiner, P., Thunström, P. & Held, K. Efficient implementation of the parquet equations: Role of the reducible vertex function and its kernel approximation. *Phys. Rev. B* **93,** 165103 (2016).

[93] Eckhardt, C. J., Honerkamp, C., Held, K. & Kauch, A. Truncated unity parquet solver. *Phys. Rev. B* **101,** 155104 (2020).

[94] Hille, C. *et al.* Quantitative functional renormalization group description of the two-dimensional Hubbard model. *Phys. Rev. Research* **2,** 033372 (2020).

[95] Toschi, A., Katanin, A. A. & Held, K. Dynamical vertex approximation; A step beyond dynamical mean-field theory. *Phys Rev B* **75,** 045118 (2007).

[96] Wentzell, N. *et al.* High-frequency asymptotics of the vertex function: Diagrammatic parametrization and algorithmic implementation. *Phys. Rev. B* **102,** 085106 (2020).

[97] Dupuis, N. *et al.* The nonperturbative functional renormalization group and its applications. *Physics Reports* **910.** The nonperturbative functional renormalization group and its applications, 1–114 (2021).

[98] Metzner, W., Salmhofer, M., Honerkamp, C., Meden, V. & Schönhammer, K. Functional renormalization group approach to correlated fermion systems. *Rev. Mod. Phys.* **84,** 299–352 (2012).

[99] Platt, C., Hanke, W. & Thomale, R. Functional renormalization group for multi-orbital Fermi surface instabilities. *Advances in Physics* **62,** 453–562 (2013).

[100] Wetterich, C. Exact evolution equation for the effective potential. *Physics Letters B* **301,** 90–94 (1993).

[101] Katanin, A. A. Fulfillment of Ward identities in the functional renormalization group approach. *Phys. Rev. B* **70,** 115109 (2004).

[102] Eberlein, A. Fermionic two-loop functional renormalization group for correlated fermions: Method and application to the attractive Hubbard model. *Phys. Rev. B* **90,** 115125 (2014).

[103] Kugler, F. B. & von Delft, J. Multiloop Functional Renormalization Group That Sums Up All Parquet Diagrams. *Phys. Rev. Lett.* **120,** 057403 (2018).

[104] Kugler, F. B. & von Delft, J. Multiloop functional renormalization group for general models. *Phys. Rev. B* **97,** 35162 (2018).

[105] Kugler, F. B. & von Delft, J. Derivation of exact flow equations from the self-consistent parquet relations. *New Journal of Physics* **20,** 123029 (2018).

[106] Tagliavini, A. *et al.* Multiloop functional renormalization group for the two-dimensional Hubbard model: Loop convergence of the response functions. *SciPost Physics* **6,** 009 (2019).

[107] Domazetovski, L. Divergences of the irreducible vertex beyond particle-hole symmetry: an Anderson Impurity Model study. Project thesis. 2022.

[108] Yang, S.-X. *et al.* Dual Fermion Dynamical Cluster Approach for Strongly Correlated Systems. *arXiv:1104.3854v1.* Appendix A (2011).

[109] Yang, S.-X. *et al.* Dual fermion dynamical cluster approach for strongly correlated systems. *Phys. Rev. B* **84,** 155106 (2011).

[110] Schäfer, T. Classical and quantum phase transitions in strongly correlated electron systems. PhD thesis (TU Wien, 2016).

[111] Shiba, H. Thermodynamic Properties of the One-Dimensional Half-Filled-Band Hubbard Model. II: Application of the Grand Canonical Method. *Progress of Theoretical Physics* **48,** 2171–2186. ISSN: 0033-068X (Dec. 1972).

[112] Micnas, R., Ranninger, J. & Robaszkiewicz, S. Superconductivity in narrow-band systems with loca nonretarded attractive interactions. *Rev. Mod. Phys.* **62,** 113 (1990).

[113] Del Re, L., Capone, M. & Toschi, A. Dynamical vertex approximation for the attractive Hubbard model. *Phys. Rev. B* **99,** 045137 (2019).

[114] Taranto, C. *et al.* Signature of antiferromagnetic long-range order in the optical spectrum of strongly correlated electron systems. *Phys. Rev. B* **85,** 085124 (2012).

[115] Tagliavini, A., Capone, M. & Toschi, A. Detecting a preformed pair phase: Response to a pairing forcing field. *Phys. Rev. B* **94,** 155114 (2016).

[116] Efron, B. & Stein, C. The Jackknife Estimate of Variance. *The Annals of Statistics* **9,** 586–596 (1981).

[117] Schattauer, C. Irreducible Vertex Divergences of the "Zero Bandwidth" Anderson Impurity Model. Project thesis. 2018.

[118] Fus, D. R. Bachelor thesis. unpublished.

[119] Reitner, M. et al. in preparation.

[120] Eßl, H. Project thesis. unpublished.

[121] Maier, T., Jarrell, M., Pruschke, T. & Hettler, M. H. Quantum Cluster Theories. *Rev. Mod. Phys.* **77,** 1027 (2005).

[122] Gunnarsson, O. *et al.* Fluctuation Diagnostics of the Electron Self-Energy: Origin of the Pseudogap Physics. *Phys. Rev. Lett.* **114,** 236402 (2015).

[123] Van Houcke, K., Kozik, E., Prokof'ev, N. & Svistunov, B. Diagrammatic Monte Carlo. *Physics Procedia* **6,** 95–105 (2010).

[124] Kozik, E. *et al.* Diagrammatic Monte Carlo for correlated fermions. *EPL (Europhysics Letters)* **90,** 10004 (2010).

[125] Damascelli, A., Hussain, Z. & Shen, Z.-X. Angle-resolved photoemission studies of the cuprate superconductors. *Rev. Mod. Phys.* **75,** 473–541 (2003).

[126] Binnig, G. & Rohrer, H. Scanning tunneling microscopy—from birth to adolescence. *Rev. Mod. Phys.* **59,** 615–625 (1987).

[127] Fischer, Ø., Kugler, M., Maggio-Aprile, I., Berthod, C. & Renner, C. Scanning tunneling spectroscopy of high-temperature superconductors. *Rev. Mod. Phys.* **79,** 353–419 (2007).

[128] Hayden, S. M. Neutron Scattering and the Magnetic Response of Superconductors and Related Compounds (eds Bennemann, K. H. & Ketterson, J. B.) 993–1029. `https://doi.org/10.1007/978-3-540-73253-2_18` (Springer Berlin Heidelberg, Berlin, Heidelberg, 2008).

[129] Johnston, D. C. The puzzle of high temperature superconductivity in layered iron pnictides and chalcogenides. *Advances in Physics* **59,** 803–1061 (2010).

[130] Kuneš, J. Efficient treatment of two-particle vertices in dynamical mean-field theory. *Phys. Rev. B* **83,** 085102 (2011).

[131] Hafermann, H. Self-energy and vertex functions from hybridization-expansion continuous-time quantum Monte Carlo for impurity models with retarded interaction. *Phys. Rev. B* **89,** 235128 (2014).

[132] Kaufmann, J., Gunacker, P. & Held, K. Continuous-time quantum Monte Carlo calculation of multiorbital vertex asymptotics. *Phys. Rev. B* **96,** 035114 (2017).

[133] Tagliavini, A. *et al.* Efficient Bethe-Salpeter equation treatment in dynamical mean-field theory. *Phys. Rev. B* **97,** 235140 (2018).

[134] Stepanov, E. A. *et al.* Effective Heisenberg Model and Exchange Interaction for Strongly Correlated Systems. *Phys. Rev. Lett.* **121,** 037204 (2018).

[135] Van Loon, E. G. C. P., Krien, F., Hafermann, H., Lichtenstein, A. I. & Katsnelson, M. I. Fermion-boson vertex within dynamical mean-field theory. *Phys. Rev. B* **98,** 205148 (2018).

[136] Stepanov, E. A., Huber, A., Lichtenstein, A. I. & Katsnelson, M. I. Effective Ising model for correlated systems with charge ordering. *Phys. Rev. B* **99,** 115124 (2019).

[137] Krien, F., Valli, A. & Capone, M. Single-boson exchange decomposition of the vertex function. *Phys. Rev. B* **100,** 155149 (2019).

[138] Stepanov, E. A., Harkov, V. & Lichtenstein, A. I. Consistent partial bosonization of the extended Hubbard model. *Phys. Rev. B* **100,** 205115 (2019).

[139] Krien, F. & Valli, A. Parquetlike equations for the Hedin three-leg vertex. *Phys. Rev. B* **100,** 245147 (2019).

[140] Van Loon, E. G. C. P., Krien, F. & Katanin, A. A. Bethe-Salpeter Equation at the Critical End Point of the Mott Transition. *Phys. Rev. Lett.* **125,** 136402 (2020).

[141] Kugler, F. B., Lee, S.-S. B. & von Delft, J. Multipoint Correlation Functions: Spectral Representation and Numerical Evaluation. *Phys. Rev. X* **11,** 041006 (2021).

[142] Lee, S.-S. B., Kugler, F. B. & von Delft, J. Computing Local Multipoint Correlators Using the Numerical Renormalization Group. *Phys. Rev. X* **11,** 041007 (2021).

[143] Fisk, Z. *et al.* Heavy-Electron Metals: New Highly Correlated States of Matter. *Science* **239,** 33–42 (1988).

[144] Dagotto, E. Correlated electrons in high-temperature superconductors. *Rev. Mod. Phys.* **66,** 763–840 (1994).

[145] Lee, P. A., Nagaosa, N. & Wen, X.-G. Doping a Mott insulator: Physics of high-temperature superconductivity. *Rev. Mod. Phys.* **78,** 17–85 (2006).

[146] Coleman, P. Heavy Fermions: electrons at the edge of magnetism. Handbook of Magnetism and Advanced Magnetic Materials. Edited by H. Kronmuller and S. Parkin. Vol 1: Fundamentals and Theory. (John Wiley and Sons). 2007.

[147] Andergassen, S., Meden, V., Schoeller, H., Splettstoesser, J. & Wegewijs, M. R. Charge transport through single molecules, quantum dots and quantum wires. *Nanotechnology* **21,** 272001 (2010).

[148] Rohringer, G. *et al.* LadderDΓA code. *github.com/ladderDGA.* https://github.com/ladderDGA/ladderDGA (2018).

[149] Terletska, H., Vučičević, J., Tanasković, D. & Dobrosavljević, V. Quantum Critical Transport near the Mott Transition. *Phys. Rev. Lett.* **107,** 026401 (July 2011).

[150] Vučičević, J., Terletska, H., Tanasković, D. & Dobrosavljević, V. Finite-temperature crossover and the quantum Widom line near the Mott transition. *Phys. Rev. B* **88,** 075143 (2013).

[151] Janiš, V. & Augustinský, P. Analytic impurity solver with Kondo strong-coupling asymptotics. *Phys. Rev. B* **75,** 165108 (2007).

[152] Janiš, V. & Augustinský, P. Kondo behavior in the asymmetric Anderson model: Analytic approach. *Phys. Rev. B* **77,** 085106 (2008).

[153] Valli, A. *et al.* Dynamical vertex approximation in its parquet implementation: Application to Hubbard nanorings. *Phys. Rev. B* **91,** 115115 (2015).

[154] Janiš, V., Zalom, P., Pokorný, V. & Klíč, A. Strongly correlated electrons: Analytic mean-field theories with two-particle self-consistency. *Phys. Rev. B* **100,** 195114 (2019).

[155] Janiš, V. & Klíč, A. in *Proceedings of the International Conference on Strongly Correlated Electron Systems (SCES2019)* (2019). https://journals.jps.jp/doi/abs/10.7566/JPSCP.30.011124.

[156] Kauch, A. *et al.* Generic Optical Excitations of Correlated Systems: π-tons. *Phys. Rev. Lett.* **124,** 047401 (2020).

[157] Janiš, V., Klíč, A., Yan, J. & Pokorný, V. Curie-Weiss susceptibility in strongly correlated electron systems. *Phys. Rev. B* **102,** 205120 (2020).

[158] Mazitov, T. B. & Katanin, A. A. Local magnetic moment formation and Kondo screening in the half-filled single-band Hubbard model. *Phys. Rev. B* **105,** L081111 (2022).

[159] Stepanov, E. A., Brener, S., Harkov, V., Katsnelson, M. I. & Lichtenstein, A. I. Spin dynamics of itinerant electrons: Local magnetic moment formation and Berry phase. *Phys. Rev. B* **105,** 155151 (2022).

[160] Nourafkan, R., Côté, M. & Tremblay, A.-M. S. Charge fluctuations in lightly hole-doped cuprates: Effect of vertex corrections. *Phys. Rev. B* **99,** 035161 (2019).

[161] Kotliar, G., Murthy, S. & Rozenberg, M. J. Compressibility Divergence and the Finite Temperature Mott Transition. *Phys. Rev. Lett.* **89,** 046401 (2002).

[162] Werner, P. & Millis, A. J. Doping-driven Mott transition in the one-band Hubbard model. *Phys. Rev. B* **75,** 085108 (2007).

[163] Eckstein, M., Kollar, M., Potthoff, M. & Vollhardt, D. Phase separation in the particle-hole asymmetric Hubbard model. *Phys. Rev. B* **75,** 125103 (2007).

[164] Sordi, G., Haule, K. & Tremblay, A.-M. S. Finite Doping Signatures of the Mott Transition in the Two-Dimensional Hubbard Model. *Phys. Rev. Lett.* **104,** 226402 (2010).

[165] Sordi, G., Haule, K. & Tremblay, A.-M. S. Mott physics and first-order transition between two metals in the normal-state phase diagram of the two-dimensional Hubbard model. *Phys. Rev. B* **84,** 075161 (2011).

[166] Sordi, G., Sémon, P., Haule, K. & Tremblay, A.-M. S. Pseudogap temperature as a Widom line in doped Mott insulators. *Scientific reports* **2,** 547 (2012).

[167] Walsh, C., Sémon, P., Sordi, G. & Tremblay, A.-M. S. Critical opalescence across the doping-driven Mott transition in optical lattices of ultracold atoms. *Phys. Rev. B* **99,** 165151 (2019).

[168] Sordi, G., Walsh, C., Sémon, P. & Tremblay, A.-M. S. Specific heat maximum as a signature of Mott physics in the two-dimensional Hubbard model. *Phys. Rev. B* **100,** 121105 (2019).

[169] Walsh, C., Sémon, P., Poulin, D., Sordi, G. & Tremblay, A.-M. S. Entanglement and Classical Correlations at the Doping-Driven Mott Transition in the Two-Dimensional Hubbard Model. *PRX Quantum* **1,** 020310 (2020).

[170] Van Loon, E. G. C. P., Hafermann, H., Lichtenstein, A. I. & Katsnelson, M. I. Thermodynamic consistency of the charge response in dynamical mean-field based approaches. *Phys. Rev. B* **92,** 085106 (2015).

[171] Del Re, L. & Toschi, A. Dynamical vertex approximation for many-electron systems with spontaneously broken SU(2) symmetry. *Phys. Rev. B* **104,** 085120 (2021).

[172] Del Re, L. & Rohringer, G. Fluctuations analysis of spin susceptibility: Néel ordering revisited in dynamical mean field theory. *Phys. Rev. B* **104,** 235128 (2021).

[173] Wu, W., Ferrero, M., Georges, A. & Kozik, E. Controlling Feynman diagrammatic expansions: Physical nature of the pseudogap in the two-dimensional Hubbard model. *Phys. Rev. B* **96,** 041105 (2017).

[174] Dong, X., Del Re, L., Toschi, A. & Gull, E. Mechanism of Superconductivity in the Hubbard Model at Intermediate Interaction Strength. 2022. arXiv: `2205.06286 [cond-mat.str-el]`.

[175] Sangiovanni, G. *et al.* Static versus dynamical mean-field theory of Mott antiferromagnets. *Phys. Rev. B* **73,** 205121 (2006).

[176] Rohringer, G., Toschi, A., Katanin, A. & Held, K. Critical Properties of the Half-Filled Hubbard Model in Three Dimensions. *Phys. Rev. Lett.* **107,** 256402 (2011).

[177] Keller, M., Metzner, W. & Schollwöck, U. Dynamical Mean-Field Theory for Pairing and Spin Gap in the Attractive Hubbard Model. *Phys. Rev. Lett.* **86,** 4612–4615 (2001).

[178] Capone, M., Castellani, C. & Grilli, M. First-Order Pairing Transition and Single-Particle Spectral Function in the Attractive Hubbard Model. *Phys. Rev. Lett.* **88,** 126403 (2002).

[179] Toschi, A., Barone, P., Capone, M. & Castellani, C. Pairing and superconductivity from weak to strong coupling in the attractive Hubbard model. *New J. Phys.* **7,** 7 (2005).

[180] Toschi, A., Capone, M. & Castellani, C. Energetic balance of the superconducting transition across the BCS-Bose Einstein crossover in the attractive Hubbard model. *Phys. Rev. B* **72,** 235118 (2005).

[181] Sordi, G., Sémon, P., Haule, K. & Tremblay, A.-M. S. Strong Coupling Superconductivity, Pseudogap, and Mott Transition. *Phys. Rev. Lett.* **108,** 216401 (2012).

[182] Sordi, G., Sémon, P., Haule, K. & Tremblay, A.-M. S. c-axis resistivity, pseudogap, superconductivity, and Widom line in doped Mott insulators. *Phys. Rev. B* **87,** 041101 (2013).

[183] Rossi, R. Determinant Diagrammatic Monte Carlo Algorithm in the Thermodynamic Limit. *Phys. Rev. Lett.* **119,** 045701 (2017).

[184] Moutenet, A., Wu, W. & Ferrero, M. Determinant Monte Carlo algorithms for dynamical quantities in fermionic systems. *Phys. Rev. B* **97,** 085117 (2018).

[185] Rossi, R. Direct sampling of the self-energy with Connected Determinant Monte Carlo. 2018. arXiv: `1802.04743 [cond-mat.str-el]`.

[186] Šimkovic, F. & Kozik, E. Determinant Monte Carlo for irreducible Feynman diagrams in the strongly correlated regime. *Phys. Rev. B* **100,** 121102 (2019).

[187] Rossi, R., Šimkovic, F. & Ferrero, M. Renormalized perturbation theory at large expansion orders. *EPL (Europhysics Letters)* **132,** 11001 (2020).

[188] Šimkovic, F., Rossi, R. & Ferrero, M. Efficient one-loop-renormalized vertex expansions with connected determinant diagrammatic Monte Carlo. *Phys. Rev. B* **102,** 195122 (Nov. 2020).

[189] Van Houcke, K. *et al.* Feynman diagrams versus Fermi-gas Feynman emulator. *Nature Physics* **8,** 366–370 (2012).

[190] Rossi, R., Ohgoe, T., Van Houcke, K. & Werner, F. Resummation of Diagrammatic Series with Zero Convergence Radius for Strongly Correlated Fermions. *Phys. Rev. Lett.* **121,** 130405 (2018).

[191] Kim, A. J., Prokof'ev, N. V., Svistunov, B. V. & Kozik, E. Homotopic Action: A Pathway to Convergent Diagrammatic Theories. *Phys. Rev. Lett.* **126,** 257001 (2021).

[192] Šimkovic, F. *et al.* Extended Crossover from a Fermi Liquid to a Quasiantiferromagnet in the Half-Filled 2D Hubbard Model. *Phys. Rev. Lett.* **124,** 017003 (2020).

[193]   Kim, A. J., Simkovic, F. & Kozik, E. Spin and Charge Correlations across the Metal-to-Insulator Crossover in the Half-Filled 2D Hubbard Model. *Phys. Rev. Lett.* **124,** 117602 (2020).

[194]   Lenihan, C., Kim, A. J., Šimkovic IV., F. & Kozik, E. Entropy in the Non-Fermi-Liquid Regime of the Doped 2D Hubbard Model. *Phys. Rev. Lett.* **126,** 105701 (2021).

[195]   Šimkovic, F., Rossi, R. & Ferrero, M. The Weak, the Strong and the Long Correlation Regimes of the Two-Dimensional Hubbard Model at Finite Temperature. 2021. arXiv: `2110.05863 [cond-mat.str-el]`.

[196]   Ayral, T. & Parcollet, O. Mott physics and collective modes: An atomic approximation of the four-particle irreducible functional. *Phys. Rev. B* **94,** 075159 (2016).

[197]   Katanin, A. A., Toschi, A. & Held, K. Comparing pertinent effects of antiferromagnetic fluctuations in the two- and three-dimensional Hubbard model. *Phys. Rev. B* **80,** 075104 (2009).

[198]   Rohringer, G. & Toschi, A. Impact of non-local correlations over different energy scales: A Dynamical Vertex Approximation study. *Phys. Rev. B* **94,** 125144 (2016).

[199]   Kaufmann, J. *et al.* Self-consistent ladder dynamical vertex approximation. *Phys. Rev. B* **103,** 035120 (2021).

[200]   Rubtsov, A. N., Katsnelson, M. I. & Lichtenstein, A. I. Dual fermion approach to nonlocal correlations in the Hubbard model. *Phys. Rev. B* **77,** 033101 (2008).

[201]   Rubtsov, A. N., Katsnelson, M. I., Lichtenstein, A. I. & Georges, A. Dual fermion approach to the two-dimensional Hubbard model: Antiferromagnetic fluctuations and Fermi arcs. *Phys. Rev. B* **79,** 045133 (2009).

[202]   Hafermann, H. *et al.* Efficient Perturbation Theory for Quantum Lattice Models. *Phys. Rev. Lett.* **102,** 206401 (2009).

[203]   Krien, F. *et al.* Boson-exchange parquet solver for dual fermions. *Phys. Rev. B* **102,** 195131 (2020).

[204]   Harkov, V., Lichtenstein, A. I. & Krien, F. Parametrizations of local vertex corrections from weak to strong coupling: Importance of the Hedin three-leg vertex. *Phys. Rev. B* **104,** 125141 (2021).

[205]   Krien, F., Lichtenstein, A. I. & Rohringer, G. Fluctuation diagnostic of the nodal/antinodal dichotomy in the Hubbard model at weak coupling: A parquet dual fermion approach. *Phys. Rev. B* **102,** 235133 (2020).

[206]   Krien, F., Worm, P., Chalupa, P., Toschi, A. & Held, K. Spin scattering turns complex at strong coupling: the key to pseudogap and Fermi arcs in the Hubbard model. 2021. arXiv: `2107.06529 [cond-mat.str-el]`.

[207]   Krien, F., Kauch, A. & Held, K. Tiling with triangles: parquet and $GW\gamma$ methods unified. *Phys. Rev. Research* **3,** 013149 (2021).

[208]   Taranto, C. *et al.* From Infinite to Two Dimensions through the Functional Renormalization Group. *Phys. Rev. Lett.* **112,** 196402 (2014).

[209] Wentzell, N., Taranto, C., Katanin, A., Toschi, A. & Andergassen, S. Correlated starting points for the functional renormalization group. *Phys. Rev. B* **91,** 045120 (2015).

[210] Vilardi, D., Taranto, C. & Metzner, W. Antiferromagnetic and *d*-wave pairing correlations in the strongly interacting two-dimensional Hubbard model from the functional renormalization group. *Phys. Rev. B* **99,** 104501 (2019).

[211] Bonetti, P. M., Toschi, A., Hille, C., Andergassen, S. & Vilardi, D. Single-boson exchange representation of the functional renormalization group for strongly interacting many-electron systems. *Phys. Rev. Research* **4,** 013034 (2022).

[212] Mermin, N. D. & Wagner, H. Absence of Ferromagnetism or Antiferromagnetism in One- or Two-Dimensional Isotropic Heisenberg Models. *Phys. Rev. Lett.* **17,** 1307–1307 (1966).

[213] Bickers, N. E. & Scalapino, D. J. Critical behavior of electronic parquet solutions. *Phys. Rev. B* **46,** 8050–8056 (1992).

[214] Gievers, Marcel, Walter, Elias, Ge, Anxiang, Delft, Jan von & Kugler, Fabian B. Multiloop flow equations for single-boson exchange fRG. *Eur. Phys. J. B* **95,** 108 (2022).

[215] Chalupa-Gantner, P. *et al.* Fulfillment of sum rules and Ward identities in the multiloop functional renormalization group solution of the Anderson impurity model. *Phys. Rev. Research* **4,** 023050 (2022).

[216] The ∞-loop mfRG solution refers to a solution of the mfRG scheme where no maximum loop order ℓ is used. Instead, throughout the flow, at each integration step Λ_i, higher loop orders are calculated until the changes, when comparing loop order $\ell + 1$ with ℓ in all quantities, decrease below a given ϵ. More details, such as the precise loop orders needed for the different parameter sets and the specific values used for ϵ can be found in the Appendix of Ref. [215].

[217] Smith, R. A. Planar version of Baym-Kadanoff theory. *Phys. Rev. A* **46,** 4586–4597 (1992).

[218] Janiš, V., Kauch, A. & Pokorný, V. Thermodynamically consistent description of criticality in models of correlated electrons. *Phys. Rev. B* **95,** 045108 (2017).

[219] Vilk, Y. M. & Tremblay, A.-M. S. Non-Perturbative Many-Body Approach to the Hubbard Model and Single-Particle Pseudogap. *J. Phys. I France* **7,** 1309–1368 (1997).

[220] Krien, F. Conserving dynamical mean-field approaches to strongly correlated systems. PhD thesis (Universität Hamburg, 2018). https://ediss.sub.uni-hamburg.de/handle/ediss/7726.

[221] Hafermann, H., van Loon, E. G. C. P., Katsnelson, M. I., Lichtenstein, A. I. & Parcollet, O. Collective charge excitations of strongly correlated electrons, vertex corrections, and gauge invariance. *Phys. Rev. B* **90,** 235105 (Dec. 2014).

[222] Enss, T. Renormalization, Conservation Laws and Transport in Correlated Electron Systems. PhD thesis (University of Stuttgart, 2016).

[223] Pickem, M. & Chalupa-Gantner, P. Private Communications, (2017-2022).

[224] Gull, E., Werner, P., Wang, X., Troyer, M. & Millis, A. J. Local order and the gapped phase of the Hubbard model: A plaquette dynamical mean-field investigation. *EPL (Europhysics Letters)* **84,** 37009 (2008).

[225] Fratino, L., Charlebois, M., Sémon, P., Sordi, G. & Tremblay, A.-M. S. Effects of interaction strength, doping, and frustration on the antiferromagnetic phase of the two-dimensional Hubbard model. *Phys. Rev. B* **96,** 241109 (2017).

[226] Wú, W., Wang, X. & Tremblay, A.-M. Non-Fermi liquid phase and linear-in-temperature scattering rate in overdoped two-dimensional Hubbard model. *Proceedings of the National Academy of Sciences* **119,** e2115819119 (2022).

[227] Haule, K. & Kotliar, G. Coherence-incoherence crossover in the normal state of iron oxypnictides and importance of Hund's rule coupling. *New Journal of Physics* **11,** 025021 (2009).

[228] De'Medici, L., Mravlje, J. & Georges, A. Janus-Faced Influence of Hund's Rule Coupling in Strongly Correlated Materials. *Phys. Rev. Lett.* **107,** 256401 (2011).

[229] De'Medici, L. Hund's Induced Fermi-Liquid Instabilities and Enhanced Quasiparticle Interactions. *Phys. Rev. Lett.* **118,** 167003 (2017).

[230] Chatzieleftheriou, M., Berović, M., Villar Arribi, P., Capone, M. & de'Medici, L. Enhancement of charge instabilities in Hund's metals by breaking of rotational symmetry. *Phys. Rev. B* **102,** 205127 (2020).

Acknowledgements

A PhD truly is a great effort, in my opinion impossible without the support of many people, which I want to thank in the following.

First of all, I want to thank my supervisor **Alessandro Toschi**, who guided me in this scientific endeavor. His enthusiasm and dedication to science always impressed me and were a great source of motivation. In particular, I was always inspired by his profound conviction that there *exist* relevant physical aspects to the irreducible vertex divergences, apart from their fascinating appearances throughout several fundamental many-electron models – and I'm extremely happy and proud that we managed to identify them in the end. In the last years, Alessandro was not only a great supervisor but also a great teacher of the Italian language, the culture, the cuisine, and also the politics. I am most grateful for our always very enjoyable Italian sessions! Ale, ci sono mille cose per cui ringraziarti, ne ho scelto una come rappresentante: grazie mille per avermi fatto vedere *le viuzze che seguono i ciglioni, discendono tra i ciuffi delle canne e mettono negli orti, tra gli alberi dei limoni.*

I also want to thank Alessandro's close scientific network, which has almost become a scientific "family": Grazie mille to **Giorgio Sangiovanni**, for all the great discussions, the invitations to Würzburg and Campello, and always creating a cheerful atmosphere (for example, the "attractive effects of ..."). Grazie mille to **Sabine Andergassen**, for giving me the opportunity to work in the field of fRG, for organizing research visits to Tübingen, and for the many fruitful discussions and research projects. Grazie mille to **Sergio Ciuchi**, for his great scientific intuition and the invitation to la Città Eterna. I am also most grateful to **Thomas Schäfer** for the many great discussions we had in several instances (including the special ones on the vertex). He was always a great inspiration to me (including also his excellent taste in music). Further, I want to thank **Georg Rohringer**, whose pedagogic style and profound understanding of many-body physics made our discussions always most productive and stimulating. Let me also thank **Daniel Springer** and **Lorenzo del Re**, from whom I could learn a lot about physics (and also about proper punctuation). My gratitude also extends to **Philipp Hansmann** for the insightful discussions we had.

Throughout the years, I have had the pleasure to meet and discuss with many great physicists (apart from the ones already mentioned). Starting with the colleagues from Vienna, I want to thank **Karsten Held**, **Sebastian Huber**, **Jan Tomczak**, and **Markus Wallerberger** for the discussions we had in the last years. In particular, I am grateful to **Anna Kauch** and **Friedrich Krien**, who always impressed me with their profound understanding of fundamental physical concepts. I really enjoyed working with them! I am also

indebted to **Antoine Georges** for his invitation to the CCQ, which was a wonderful experience, the opportunity to give a seminar talk at the Collége de France, and his encouraging words after my talk in Amalfi. Let me also thank **Olivier Parcollet**, **Gabi Kotliar**, **Hugo Strand**, and **Martin Eckstein** for the discussions at the CCQ. Further, I want to thank **Alexander Lichtenstein** for the great discussions we had in the last years. Let me also express my gratitude to **Massimo Capone** (one of the "doctorfathers" of my supervisor), for inviting me to give a seminar talk in Trieste, and for the insightful exchange of ideas.

A great part of my thesis was devoted to applying the mfRG scheme to the AIM. Here, I want to thank **Agnese Tagliavini** for her patient introduction into the field of multiloop fRG, **Cornelia Hille** for always helping me with any code related issues and hurdles I faced, and **Fabian Kugler** for the many great discussions we had. His understanding of the fRG and many-body physics in general was truly inspiring to me. Let me also express my gratitude to **Jan von Delft**, for inviting me to München and the many fruitful discussions.

Concerning practical issues one faces during a PhD, let me also thank **Patrik Gunacker**, **Andreas Hausoel**, and **Josef Kaufmann**, who were almost like a "w2dynamics fire brigade" to me. Thank you for always helping me out, improving the code if needed, and for your great and patient explanations.

At this point, I want to thank the younger people/people of the theory groups at the IFP (AG Held, Kuneš and Toschi) who I have met over the years, and in part, had the pleasure of co-supervising. Many thanks to **Matthias Pickem** for being a great office colleague. I always enjoyed our discussions about physics, politics, and life in general. Let me also thank **Clemens Watzenböck** – I'll never forget our scientific trips! I also want to thank **Matthias Reitner**, whom I co-supervised during his Master thesis. I greatly enjoyed working with him (still do), and having a great cup of coffee. Also, I want to thank **Severino Adler** and **Andriy Smolyanyuk** for being great office colleagues and for creating a nice atmosphere in the group. Lastly, I thank **Mathias Pelz**, **Christoph Schattauer**, and **Alexander Vock**, whom I co-supervised. It was a great pleasure to work with you!

Finally, let me also thank the personnel of the secretary's office of the Institute for Solid State Physics, in particular **Helga Frank**. Her creativity in finding solutions for complicated bureaucratic problems knows no limits.

To finish a PhD, also the support of people outside one's scientific community is greatly needed. Here, I want to thank my family for their support throughout all the years. I also want to thank all my friends for accompanying me through my student- and PhD years.

In addition, I want to thank the Viennese coffee house culture for providing a great workplace apart from the office. To me, working in the coffee house was an essential part of finishing all my publications and this thesis itself. Let me mention here several great examples: Café Nest, Café in der Burggasse 24, Kaffeefabrik, Café Hummel, Tachles, and das Möbel. In particular, I want to thank the **Knockbox** for providing great coffee on days where the hours passed (almost too) quickly. Above all, I want to thank **Carl Ludwig Café** – in my opinion, a café that provides truly the best combination of a relaxing atmosphere, fueling one's creativity, fantastic coffee, and probably the best "Schanigarten"

of all of Vienna.

Lastly, and most importantly, I want to thank my wife, **Franziska**, for her endless support. I am most grateful for sharing this PhD adventure with her. Thank you for the many incredible pep talks!

List of Publications

In the following, a list of publications is provided. The items marked by a "○"-symbol are only briefly mentioned in this thesis.

Peer-reviewed journal publications:

- P. Chalupa, P. Gunacker, T. Schäfer, K. Held, and A. Toschi, *Divergences of the irreducible vertex functions in correlated metallic systems: Insights from the Anderson impurity model*, Phys. Rev. B **97**, 245136 (2018).

- D. Springer, P. Chalupa, S. Ciuchi, G. Sangiovanni, and A. Toschi, *Interplay between local response and vertex divergences in many-fermion systems with on-site attraction*, Phys. Rev. B **101**, 155148 (2020), featured as Editor's Suggestion.

- M. Reitner*, P. Chalupa*, L. Del Re, D. Springer, S. Ciuchi, G. Sangiovanni, and A. Toschi, *Attractive Effect of a Strong Electronic Repulsion: The Physics of Vertex Divergences*, Phys. Rev. Lett. **125**, 196403 (2020), the authors marked by a "*" symbol contributed equally to this work.

  See also the popular article of the TU press office: *Sticky Electrons: When Repulsion turns into Attraction* (English) or *Klebrige Elektronen: Aus Abstoßung wird Anziehung* (Deutsch).

- Friedrich Krien, Angelo Valli, Patrick Chalupa, Massimo Capone, Alexander I. Lichtenstein, and Alessandro Toschi, *Boson-exchange parquet solver for dual fermions*, Phys. Rev. B **102**, 195131 (2020).

- P. Chalupa, T. Schäfer, M. Reitner, D. Springer, S. Andergassen, and A. Toschi, *Fingerprints of the Local Moment Formation and its Kondo Screening in the Generalized Susceptibilities of Many-Electron Problems*, Phys. Rev. Lett. **126**, 056403 (2021).

  See also the popular article of the TU press office: *Tatort Festkörper: Die Fingerabdrücke der Quanteneffekte* (Deutsch) or the article of the "attempto" magazine of the Universität Tübingen *Quantenphysiker identifizieren „Fingerabdrücke" fundamentaler physikalischer Effekte* (Deutsch and English).

- Patrick Chalupa-Gantner, Fabian B. Kugler, Cornelia Hille, Jan von Delft, Sabine Andergassen, and Alessandro Toschi, *Fulfillment of sum rules and Ward identities in the multiloop functional renormalization group solution of the Anderson impurity model*, Phys. Rev. Research **4**, 023050 (2022).

Preprints:

- Friedrich Krien, Paul Worm, Patrick Chalupa, Alessandro Toschi, and Karsten Held, *Spin scattering turns complex at strong coupling: the key to pseudogap and Fermi arcs in the Hubbard model.* arXiv:2107.06529 (2021); accepted for publication in Commun. Phys. on August 8th, 2022

Personal contributions to publications

In the following, I summarize my personal contributions to the publications listed above.

Divergences of the irreducible vertex functions in correlated metallic systems: Insights from the Anderson impurity model [Phys. Rev. B **97**, 245136 (2018)] In this work, I performed all the CT-QMC calculations for obtaining the one- and two-particle quantities of interest. Further, I analyzed the data to search for singular eigenvalues of the generalized susceptibilities in order to trace the vertex divergence lines throughout the parameter space of the Anderson impurity model, as well as to study the temperature evolution of the associated singular eigenvectors. I also contributed to the interpretation of the results and the identification of the scaling behavior of the singular eigenvectors. In the writing and revision process, I contributed mainly to the results sections of the work.

Interplay between local response and vertex divergences in many-fermion systems with on-site attraction [Phys. Rev. B **101**, 155148 (2020)] In this work, I mainly contributed to the analysis of the symmetry properties, which underlie the perfect mapping of the divergence lines. I managed to prove the perfect mirroring based on the centrosymmetric properties of the generalized susceptibilities. In the writing process, I mainly contributed to those parts of the paper that concern the underlying symmetry properties (Sec. III B and Appendices A and B).

Attractive Effect of a Strong Electronic Repulsion: The Physics of Vertex Divergences [Phys. Rev. Lett. **125**, 196403 (2020)] For this work, Matthias Reitner and myself shared the workload for obtaining the DMFT quantities of interest. While I performed the one-particle DMFT calculations, converging close to the critical point, he computed the corresponding two-particle quantities and analyzed the data. I also contributed to the overall design of the research project and the interpretation of the results. Further, I was involved in the writing and revision process of the article.

Boson-exchange parquet solver for dual fermions   [Phys. Rev. B **102**, 195131 (2020)] For this work, I calculated the quantities for the DMFT starting point of the BEPS approach. This concerns the one- and two-particle Green's functions as well as two-leg (χ_ω^α) and three-leg quantities ($\lambda_{\nu\omega}^\alpha$).

Fingerprints of the Local Moment Formation and its Kondo Screening in the Generalized Susceptibilities of Many-Electron Problems   [Phys. Rev. Lett. **126**, 056403 (2021)] In this work, I contributed in conceiving the research project, devising also the different comparisons of interest. I performed all numerical calculations to obtain the one- and two-particle quantities of interest, apart from the ones for the periodic Anderson model. Moreover, I was involved in the interpretation of the results, the writing of the article, and revising the manuscript during the review process.

Fulfillment of sum rules and Ward identities in the multiloop functional renormalization group solution of the Anderson impurity model   [Phys. Rev. Research **4**, 023050 (2022)] In this work, I have obtained and analyzed all the numerical data, using an existing code. Specific algorithmic extensions, required for the project, were performed by Cornelia Hille or by myself under her guidance. The more formal parts of the paper, including in particular most of the proofs and diagrammatic arguments, were formulated by Fabian B. Kugler. In the writing process, I was mostly involved with the description of the numerical results, and I have also significantly contributed to reviewing the manuscript along the line of the referee reports, conceiving new analyses and performing the related numerical calculations.

Spin scattering turns complex at strong coupling: the key to pseudogap and Fermi arcs in the Hubbard model   [arXiv:2107.06529 (2021)] For this work, together with Paul Worm, I provided the quantities of the DMFT starting point needed for the subsequent BEPS calculation.

Curriculum Vitae

Personal Information

Name:	Patrick Chalupa-Gantner
Mail:	chalupa.patrick@gmail.com
Date of birth:	29.01.1992
Nationality:	Austrian

Education

2017 - present:	PhD in Physics, TU Wien
2015 - 2017:	M. Sc. in Technical Physics (with distinction), TU Wien
2011 - 2015:	B. Sc. in Technical Physics (with distinction), TU Wien
2010:	Matura, BRG Gröhrmühlgasse Wr. Neustadt

Academic Employment and Teaching

08/2017 - 07/2021:	Project Assistant (FWF), TU Wien
2013 - 2017:	Teaching Assistant for several courses of the Bachelor program "Technical Physics" at the TU Wien (Mathematische Methoden der Theoretischen Physik, Elektrodynamik I, Quantenmechanik I, Statistische Physik I, Laborübungen III)

Co-Supervision of Students

2020:	Matthias Reitner, *Dichotomy Between Local and Uniform Compressibility in Correlated Systems: The Role of the Irreducible Vertex*, Master thesis (TU Wien)
2019:	Alexander Vock, *Quantum criticality with dynamical mean-field theory*, Master thesis (TU Wien)
2018:	Mathias Pelz, *Comparison of Mott-Hubbard-transition on the Bethe-lattice and the 2D-square-lattice*, Bachelor thesis (TU Wien)
2018:	Christoph Schattauer, *Irreducible Vertex Divergences of the "Zero Bandwidth" Anderson Impurity Model*, Project work (TU Wien)

International Research Activity

Research Stays 02/2020; Universität Würzburg (Germany). Research stay with Prof. Giorgio Sangiovanni.

01/2019-03/2019; Center for Computational Quantum Physics (CCQ) at the Flatiron Institute in New York City (USA). Research stay with Prof. Antoine Georges and Prof. Olivier Parcollet.

06/2019; LMU München (Germany). Research stay with Prof. Jan von Delft and Fabian Kugler.

07/2018; Universität Tübingen (Germany). Research stay with Prof. Sabine Andergassen.

01/2018; La Sapienza Roma (Italy). Research stay with Prof. Sergio Ciuchi.

Invited Talks 04/2022; *Nonperturbative feats of strong electronic correlation*; Electronic Correlations, Emergent Phenomena, and Quantum Materials-conference (Lectiones Amalfitanae), Amalfi (Italy)

06/2021; *Sticky electrons: When repulsion turns into attraction*; Correlations in Novel Quantum Materials Workshop, Stuttgart (Germany); online

06/2020; *The nonperturbative feats of electronic correlations: a two-particle perspective*; Seminar in Condensed Matter Physics at the Collège de France, Paris (France); online

08/2018; *Irreducible vertex divergences: Insights from the Anderson Impurity Model*; Lectiones Clitumnaliae on electronic correlations, Campello sul Clitunno (Italy)

Talks 01/2021; *Fingerprints of the local moment formation and its Kondo screening in the generalized susceptibilities of many-electron problems*; Seminar on Condensed Matter Physics (SCQM-EKUT), Stuttgart (Germany); online

07/2020; *The nonperturbative feats of electronic correlations: a two-particle perspective*; Seminar talk in the group of Prof. M. Capone, Trieste (Italy); online

06/2020; *The nonperturbative feats of electronic correlations: a two-particle perspective*; Seminar talk in the group of Prof. S. Andergassen, Tübingen (Germany); online

03/2019; *Divergences of the irreducible vertex functions in correlated metallic systems: Insights from the Anderson Impurity Model*; APS March Meeting, Boston (USA)

03/2018; *Divergences of the irreducible vertex functions in correlated metallic systems: Insights from the Anderson Impurity*; DPG spring meeting, Berlin (Germany)

03/2017; *Breakdown of the many-body perturbation theory: Vertex divergences in the Anderson Impurity Model*; DPG spring meeting, Dresden (Germany)

Posters	08/2019; Emergent Phenomena in Correlated Quantum Matter - Summerschool IES Cargese, Cargese (France)
	09/2018; Workshop on "Quantum Many-Body Methods in Condensed Matter Systems", Jülich (Germany)
	09/2018; Autumn School on Correlated Electrons 2018, Jülich (Germany)
	07/2018; CECAM School "Bandstructure meets quantum field theory", Vienna (Austria)
	04/2018; From Electrons to Phase Transitions (ViCom Conference), Vienna (Austria)
	02/2018; Simons Collaboration on the Many Electron Problem Annual Meeting 2018, New York (USA)
	09/2017; Autumn School on Correlated Electrons 2017, Jülich (Germany)

Additional Information

Languages	German (mother tongue), English (C1), Italian (advanced level), French (beginner's level)
Awards	Awardee of the "Sigfried Ludwig Stiftung" scholarship
	Awardee of the "Windhag" scholarship by the government of Lower Austria
	Awardee of the student scholarships of the Faculty for Physics of the TU Wien for excellent achievement
	Awardee of the "Christiana Hörbiger" prize
Others	Member of the organizational team of the TUtheTOP-Alumni club